Author:
Knapp-Wilson, Amber L

Title:
The impact of respiratory complex dysfunction in Caenorhabditis elegans

The impact of respiratory complex dysfunction in *Caenorhabditis elegans*

Amber Knapp-Wilson

A dissertation submitted to the University of Bristol in accordance with the requirements of the Doctor of Philosophy in the Faculty of Life Sciences

School of Biochemistry
Faculty of Life Sciences
University of Bristol
United Kingdom

June 2019

Word count = 39 000

Abstract

Mitochondria are essential organelles of eukaryotic cells, responsible for the generation of the majority of the energy carrier molecule ATP. This essential process of energy production is achieved by oxidative phosphorylation (OXPHOS), facilitated by a set of proteins collectively named the electron transport chain (ETC). Loss of mitochondrial function has devastating effects on the cell and is usually associated with a disease state.

The model organism *Caenorhabditis elegans (C. elegans)* is genetically tractable, has large progeny broods and provides information on a whole animal level. In recent years, it has become an established model organism for identifying connections between mitochondrial dysfunction and lifespan. Using bioinformatics combined with protein modelling, the *C. elegans* B0491.5 protein has been identified as the homologue of NDUFA11, a key mammalian component of the electron transport chain complex I accessory subunit. NDUFA11 is linked to complex assembly and stabilisation; loss of NDUFA11 results in a reduction of complex I and metabolic perturbation.

The research presented in my thesis investigates the impact of reducing B0491.5 activity on whole animal physiology and mitochondrial biochemistry. I have shown through a genetic knockout that *b0419.5* is an essential gene, and using RNAi to suppress *b0491.5* expression, that in its absence animal growth is delayed and reproductive capabilities severely reduced. Depleting B0491.5 also has a significant impact on mitochondrial physiology, disrupting respiration activity and seemingly limiting animals to achieve only minimum energy demands. Mitochondrial biochemistry establishes B0491.5 enrichment in mitochondria, in addition to validating the protein's association with complex I. Furthermore, evidence is presented suggesting B0491.5 participates in the formation of complex I containing supercomplexes. When B0491.5 is reduced, there is disruption to supercomplex formation and decreased levels of complex I, proteome wide changes to cytosolic and mitochondrial proteins, as well as morphological and physiology mitochondrial perturbation. These changes are thought to be due to atypical cellular respiration, linked to a disruption of complex organisation within the ETC, due to the role NDUFA11 has to play within complex I and the respirasome.

Acknowledgements

I would like to thank Prof. Ian Collinson for giving me the opportunity to join the M-floor team in the first place, and for both his and Prof. Patty Kuwabara's continuous support throughout my PhD. They have provided endless patience, motivation, and knowledge which shaped my learning, and their imparted wisdom will stay with me as I continue in education and research. I would also like to express gratitude to my progression panel members Dr. Paul Curnow and Prof.Mark Szczelkun, for their insightful comments and encouragement, but also for the hard questioning which drove me to focus my research.

The whole team on M-floor created a supportive, encouraging and enjoyable environment, which was hugely influential during my project, and for which I am very thankful. Very special mentions to Gonçalo Pereira, Robin Corey, Andy Richardson and Remy Martin, who gave extensive amounts of their time helping me, in all aspects of my work. It really was a wonderful group to carry out my PhD in, and I will cherish many memories! I am also grateful to many university staff, including; Chris Neal, Paul Verkade, Kate Heesom, Phil Lewis and Vicki Gold (University of Exeter), for their support and assistance, and, the University of Bristol for funding my PhD.

Thank you to my family and friends for their unwavering support throughout my project, the past four years have come with both highs and lows, and I have been very grateful to share those experiences with loved ones. I am especially thankful to Ben, who champions me in every way, inspires me to be the best I can, and who I am incredibly lucky to have in my life.

Finally, my eternal gratitude to the "powerhouse of the cell", without which I would not have had the potential to carry out my research.

Declaration

I declare that the work in this dissertation was carried out in accordance with the requirements of the University's Regulations and Code of Practice for Research Degree Programmes and that it has not been submitted for any other academic award. Except where indicated by specific reference in the text, the work is the candidate's own work. Work done in collaboration with, or with the assistance of, others, is indicated as such. Any views expressed in the dissertation are those of the author.

SIGNED: .....

DATE:.....

Contents

List of Figures

List of Tables

Abbreviations

AA	antimycin A
ADP	adenosine diphosphate
ATP	adenosine triphosphate
BCA	bicinchoninic acid
BF	bright field
BLAST	Basic Local Alignment Search Tool
BN PAGE	Blue Native Polyacrylamide Gel Electrophoresis
bp	base pairs
CI	NADH-ubiquinone oxidoreductase
CII	succinate dehydrogenase
CIII	coenzyme Q : cytochrome *c* – oxidoreductase
CIV	cytochrome *c* oxidase
CV	ATP synthase
CL	cardiolipin
CGC	Caenorhabditis Genetics Center
CMC	critical micelle concentration
CoA	coenzyme A
COSMIC	Catalogue Of Somatic Mutations In Cancer
CDP-DAG	cytidinediphosphate-diacylglycerol
CoQ	coenzyme Q_{10}
CRISPR	clustered regularly interspaced short palindromic repeats
CryoET	electron cryotomography
DOPE	Discrete Optimised Protein Energy
dsRNA	double stranded RNA
DTT	1,4-Dithiothreitol
EM	electron microscopy
EMBL-EBI	European Bioinformatics Institute
ER	endoplasmic reticulum

ETCS	electron transport chain supercomplex
FAD	flavin adenine dinucleotide
FC	fold change
Fe-S	iron–sulfur
FET	forward electron transference
FMN	flavin mononucleotide
FUdR	5-Fluoro-2' -deoxyuridine
G-250	Coomassie blue G-250
GPX	glutathione peroxidase-1
IMM	inner mitochondrial membrane
IMS	intermembrane space
kDa	kilodaltons
KO	knockout
mtDNA	mitochondrial DNA
MD	molecular dynamics
MW	molecular weight
NAD	nonlinear anisotropic diffusion
NADH/NAD^+	nicotinamide adenine dinucleotide
OMM	outer mitochondrial membrane
OXPHOS	oxidative phosphorylation
PA	phosphatidic acid
PAGE	polyacrylamide gel electrophoresis
PC	phosphatidylcholine
PCR	polymerase chain reaction
PE	phosphatidylethanolamine
PMF	proton motive force
PS	phosphatidylserine
psi-BLAST	Position-Specific Iterative Basic Local Alignment Search Tool
PVDF	polyvinylidene difluoride
RCR	respiratory control ratio

RET	reverse electron transference
ROS	reactive oxygen species
RNAi	RNA interference
RSMF	root-mean-square fluctuation
RMSD	root-mean-square deviation
TEM	transmission electron microscopy
TIM	translocase on the inner membrane
TMH	transmembrane helix
TMRM	tetramethylrhodamine methyl ester
TMT	tandem mass tagging
TOM	translocase of the outer membrane
TX-100	Triton X-100

Chapter 1

General Introduction

1.1 Mitochondria

Mitochondria are essential, semi-autonomous eukaryotic organelles, born out of a symbiotic event of a non-respiring eukaryotic cell and invading prokaryotic cell (Wilkins and Holliday, 2009). They serve as metabolic hubs which produce more than 95% of cellular energy in the form of the molecular unit adenosine triphosphate (ATP) (Zimmerman et al., 2011) through aerobic respiration. ATP acts as an energy currency that can be redeemed universally in exchange for cellular processes by hydrolysis of a phosphate bond (Cole, 2016). There are many cellular metabolic processes that are able to regenerate ATP; however, oxidative phosphorylation (OXPHOS) is responsible for the majority of this activity. This project focuses on the constituent protein machinery of the OXPHOS pathway. The first part of the introduction will describe mitochondria morphology and physiology in relation to their cellular respiratory function, to demonstrate how each component contributes to the system.

1.1.1 Mitochondrial morphology

Mitochondria exhibit high morphological variability. They exist within dynamic membrane networks, that are reshaped by fusion and fission events (Scharwey et al., 2013), they are capable of changing shape and subcellular distribution (Hubbard and Greenstein, 2000). Within the cellular environment mitochondria are relatively large organelles, with an area commonly reported between 0.75 to 3 μm^2

in size (Wiemerslage and Lee, 2016) they are generally only exceeded in size by the nucleus within mammalian cells. Mitochondria structures have high heterogeneity, varying from tissue to tissue and even within the same cellular environment. For example, in cardiac muscle tissue, the mitochondria are highly packed along the muscle fiber, presented as long interconnected networks (Palmer et al., 1977). Whereas in liver tissue, the mitochondrial network is found to be less connected, with a more spherical mitochondria (de Kroon et al., 1997).

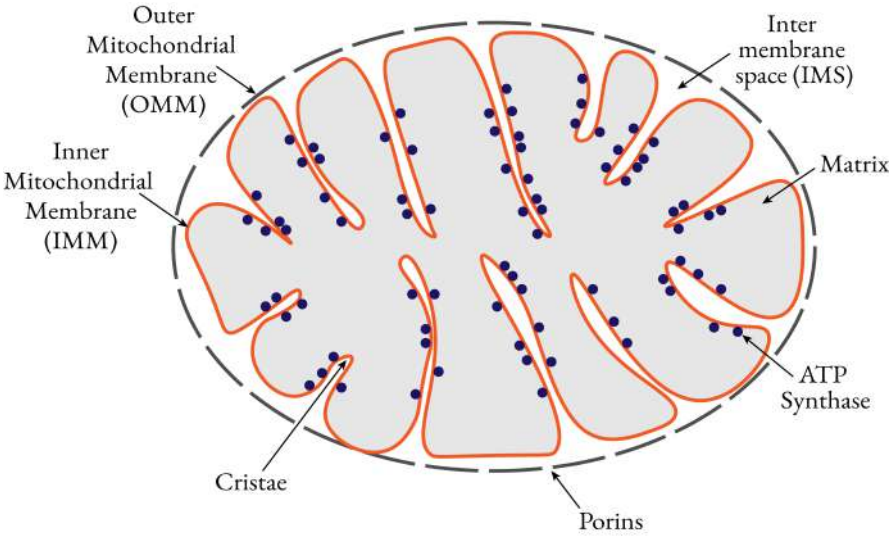

Figure 1.1: Schematic Representation of a typical mitochondrion - The outer mitochondrial membranes (OMM) is visualised by a dashed line, with the gaps representing porins that allow the membrane to be highly permeable. The inner mitochondrial membrane (IMM) is visualised in orange and folded into structures called cristae. The dots represent the distribution of the ATP synthase machinery distributed along the cristae

The basic structure of a mitochondrion is highlighted in Figure 1.1, a schematic representation of a classical mitochondrial cross section, although it is a simplification of actual structures, it serves to highlight the basic key features. The organelle is defined by a double membrane system, consisting of an outer mitochondrial membrane (OMM) and inner mitochondrial membrane (IMM), which divides it into four distinct compartments, each with well defined roles. The outer membrane contains pro-

tein channels, termed porins, which act non-specifically for solutes less than 10 kDa, making it freely permeable to ions and the majority of metabolites (Cole et al., 2010). The porous nature of the OMM is represented in Figure 1.1, by the dashed line. The outer membrane exacts some specificity for larger molecules, particularly proteins, that are imported through specific translocases (Dekker et al., 1998). In contrast, the inner membrane is impermeable except through specific channels (Lemasters, 2007). This is a crucial feature, as the impermeability allows the proton gradient to be generated across the IMM, which is utilised to drive ATP synthesis. The IMM is arranged as folds called cristae, this increases the surface area and acts to facilitate a greater volume of respiration machinery that is located within the membrane along the cristae.

The intermembrane space (IMS), one of two aqueous environments within a mitochondrion, is located between the outer and inner membrane. This compartment plays a pivotal role in coordinating mitochondrial activities with other cellular processes. The processes include, but are not limited to; facilitating the exchange of lipids, proteins and ions between the cytosol and the matrix, regulation of signalling pathways regulating respiration and control of mitochondrial morphogenesis (Herrmann and Riemer, 2010). The mitochondrial matrix, the innermost compartment and second aqueous environment, is defined by a high pH of 7.9-8. This is due to the pumping of protons by the respiratory complexes from the mitochondrial matrix into the IMS. The compartment has an incredibly high protein density (≈500 mg/ml), which reflects the numerous enzymatic reactions that are carried out, such as oxidation of pyruvate, the Krebs cycle and the beta oxidation of fatty acids (Nicholls and Ferguson, 2013).

1.1.1.1 Lipids in the mitochondrial membrane

Biological membranes, comprised by phospholipid bilayers, play an important role in all living cells and organelles by acting to divide and differentiate two different environments. The permeability of the membrane, predominately governed by protein membrane channels, dictates which molecules are able to pass through. This allows the accumulation of functionally important biological molecules within a particular compartment.

Mitochondria have a varied lipid composition consisting of six different lipids, see Table 1.1. The biogenesis and transport of these lipids happens by tightly controlled processes involving the endoplasmic reticulum (ER) and the mitochondria themselves, with cross-talk and lipid transfer between the two organelles essential for a healthy cell (Flis and Daum, 2013). The ER is the predominant lipid-synthesising organelle within the cell (Scharwey et al., 2013), where once synthesised, lipids are transported through contact sites called mitochondrial-associated ER membranes (Levine, 2004). However, mitochondria play an important role in the synthesis of a subset of key membrane phospholipids, with lipid precursors produced on the ER being transferred across the mitochondrial IMS for synthesis in the IMM. One such lipid is phosphatidylethanolamine (PE), produced from ER synthesised precursor phosphatidylserine (PS). A second is the signature mitochondrial lipid cardiolipin (CL), synthesised in the IMM by precursor phosphatidic acid (PA) (Clancey et al., 1993; Mesmin, 2016).

Despite a large morphological variance across different populations of mitochondria, the composition of mitochondrial phospholipids varies minimally, suggesting that major changes cannot be tolerated and the lipid composition is integral to the function of the mitochondria (Wang et al., 2012). In fact, a variety of human disease states have been linked to altered phospholipid levels or phospholipid damage, in particular the lipid cardiolipin (Wang et al., 2012; Joshi et al., 2009). The two mitochondrial membranes vary considerably in their individual composition, as shown in Table 1.1, reflecting the diversity in the roles they play within the organelle (Daum and Vance, 1997; Zinser et al., 1991)

	Mammalian Cells (Rat Liver)		Plant Cells (Cauliflower)		Yeast (*Saccharomyces cerevisiae*)	
	OMM	IMM	OMM	IMM	OMM	IMM
	mg/mg protein					
Phospholipid	0.45	0.20	0.63	0.41	0.91	0.15
	% of total phospholipids					
PC	54	40	47	42	46	38
PE	29	34	27	38	33	24
PI	13	5	23	5	10	16
PS	2	3	-	-	1	4
CL	<1	18	3	15	6	16
PA	1	-	-	-	4	2

Table 1.1: Lipid composition of the outer (OMM) and inner (IMM) mitochondrial membrane. Phospholipids are; Phosphatidylcholine (PC), Phosphatidylethanolamine (PE), Phosphatidylinositol (PI), Phosphatidylserine (PS), Cardiolipin (CL), Phosphatidic acid (PA). Data from Daum and Vance (Daum and Vance, 1997) and Zinser et al. (Zinser et al., 1991)

.

The lipid composition within the IMM and OMM is detailed in Table 1.1, (Horvath and Daum, 2013; Daum and Vance, 1997; Zinser et al., 1991), showing that overall, the OMM has a greater amount of phospholipid, mg/mg protein, than the IMM. In mammalian cells, the OMM has just over double the phospholipid content, 0.45 (mg/mg protein), than the IMM, which has 0.20 (mg/mg protein). A similar pattern is seen in plant cells, with about a third more phospholipid in the OMM, and yeast demonstrates an even greater proportional difference, with a six-fold increase of phospholipid in the OMM, 0.91 and 0.15 for the OMM and IMM respectively.

The mitochondrial outer membrane forms a smooth lipid rich surface with high membrane fluidity (Horvath and Daum, 2013) that hosts proteins with a diverse range of functions. These include, enzymes involved in amino acid and fatty acid metabolism, complexes facilitating protein import, systems for signal transduction and proteins controlling morphology (de Kroon et al., 1997).In contrast, the mitochondrial inner membrane is highly folded and, compared to the OMM, has an elevated protein level and lower lipid content. This composition is reflective of the high level of activity that takes place across the IMM, including metabolite transport, protein transport and respiration. The IMM has a distinctive phospholipid composition, integral for protein packing in the membrane and structural stability of proteins. The IMM is defined by the presence of the lipid CL, shown in Table 1.1 to be predominately found in the IMM, where it plays an important role in the energy transducing membrane, explained in more detail in the next section.

1.1.1.2 Cardiolipin

Cardiolipin is the only known dimeric glycerophospholipid. Almost exclusively located in the inner mitochondrial membrane (Paradies et al., 2014; Houtkooper and Vaz, 2008), it plays a major role in the the energy transducing membrane maintaining the function of membrane-associated proteins (Horvath and Daum, 2013). Within the IMM, there is an increase in the proportion of non-bilayer forming lipids, PE and CL, as shown in Table 1.1. Considering the small head group and long chain of unsaturated fatty acids, CL presents itself in a conical shape which promotes the formation of hexagonal phases in lipid membranes and induces negative curvature in the membrane.

The role of PE is currently not well understood, however CL has been shown to play a central role in the formation of respiratory supercomplexes and the enzymatic activity of the electron transport chain complexes, as well as playing an important role in maintaining membrane potential (Paradies et al., 2014; Zhang et al., 2002; Böttinger et al., 2012). It has also been hypothesised that the negative charge of CL allows the protons pumped into the IMS by the respiratory complexes to stay associated on the outer-leaflet of the IMM. Therefore allowing for more efficient channelling of protons towards the ATP synthase machinery, compared to if they remained in the bulk phase (Gasanov et al., 2018).

CL synthesis occurs in the IMM, as discussed in above in Section 1.1.1.1, by a two-step process. The first step produces non-mature CL from phosphatidylglycerol and cytidinediphosphate-diacylglycerol (CDP-DAG). In the second step, the mature acyl chain composition of CL is achieved through a combination of at least two remodelling mechanisms, resulting in a molecule of PA bound to PG to form a singular CL molecule. (Houtkooper and Vaz, 2008; Schlame, 2008).

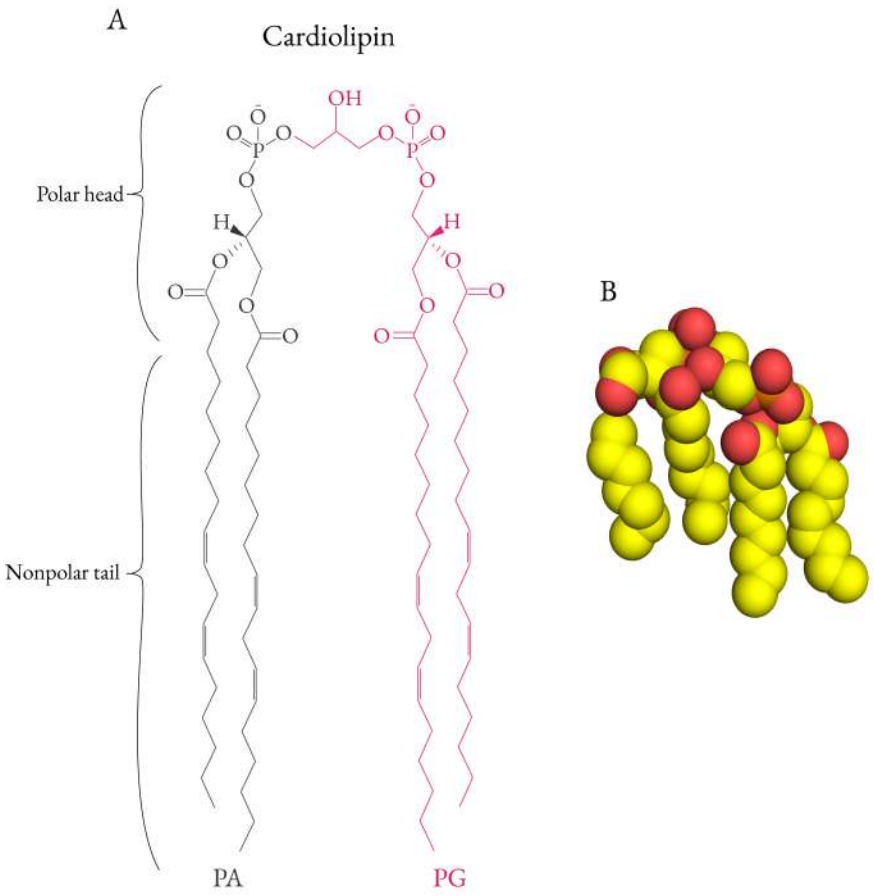

Figure 1.2: Cardiolipin - (A) Molecular structure of cardiolipin showing it is a dimer of phosphatidylglycerol (PG) and phosphatidic acid (PA) and is comprised of four acyl chains and two phosphate groups. (B) Model of cardiolipin displayed in spherical form generated in PyMOL, represented as follows; yellow = carbon, oxygen = red and phosphate = orange

The distinctive structure of CL (Figure 1.2), is unique among phospholipids. It has a conical structure (Mileykovskaya and Dowhan, 2014), leading to its non-bilayer forming nature, as mentioned previously in this section. At physiological pH, one of the phosphate groups is deprotonated, making cardiolipin a negatively-charged phospholipid. The negative charge and bulky head-group are features that are potentially influential in the lipids protein binding specificity.

CL has been shown to bind with high affinity to a large number of IMM proteins, and is necessary for optimal activity of many of the mitochondrial respiratory chain complexes (Mileykovskaya and Dowhan, 2014) . This is in addition to the role the lipid plays in the organisation and stabilisation of higher order supercomplexes. Overall it can be said that CL is critical for competent respiration in mitochondria. Perturbation of CL synthesis alters mitochondrial bioenergetics, leading to reduced membrane potential, less effective coupling of respiration, and ultimately decreased ATP synthesis (Patil et al., 2013) (Raja et al., 2017; Yin and Zhu, 2012; Chicco and Sparagna, 2007; Schug and Gottlieb, 2009).

However, knowledge of how CL is incorporated into the protein complexes, the mechanism by which it modulates enzymatic activity and the role it plays in complex organisation and stability is currently a matter of debate. Therefore, it is a continued area of interest to investigate the relationship between CL and the respiratory protein complexes. Making subunits which have been shown to interact with CL, such as the protein of interest in this project, particularly interesting.

1.1.2 Mitochondrial physiology

Mitochondria serve as semi-autonomous hubs which carry out a wide range of biological processes. Their main function revolves around supplying cellular energy, carrying out a multitude of processes including; oxidative phosphorylation, Krebs cycle, fatty acid oxidation, ketogenesis, gluconeogenesis and the urea cycle, which all contribute to energy production (Nicholls and Ferguson, 2013). However, mitochondria are also involved in signalling, cellular differentiation and apoptosis (Wang and Youle,

2009), as well as playing a crucial role in the control of the cell cycle and cell growth (Antico Arciuch et al., 2012; Finkel and Hwang, 2009; Osellame et al., 2012). Further roles include calcium handling (Granatiero et al., 2017) and lipid transfer (Flis and Daum, 2013). For the interest of this project the mitochondrial physiology relating to cellular respiration, specifically the oxidative phosphorylation (OXPHOS) pathway, will be explored in more detail.

As detailed in the Section 1.1.1 on mitochondria morphology, the organelle is separated into four distinct compartments, creating a variety of contrasting environments within mitochondria where processes are carried out in specific compartments optimised for that reaction. This section will explore the mitochondrial genome and how nuclear encoded proteins are transported into the mitochondria, as well as provide an overview of the stages that make up the cellular respiration pathway, leading into a more comprehensive explanation of oxidative phosphorylation in Section 1.1.3. Figure 1.3 provides a simplified overview, highlighting processes that begin outside the mitochondria, and feed into mitochondrial physiology.

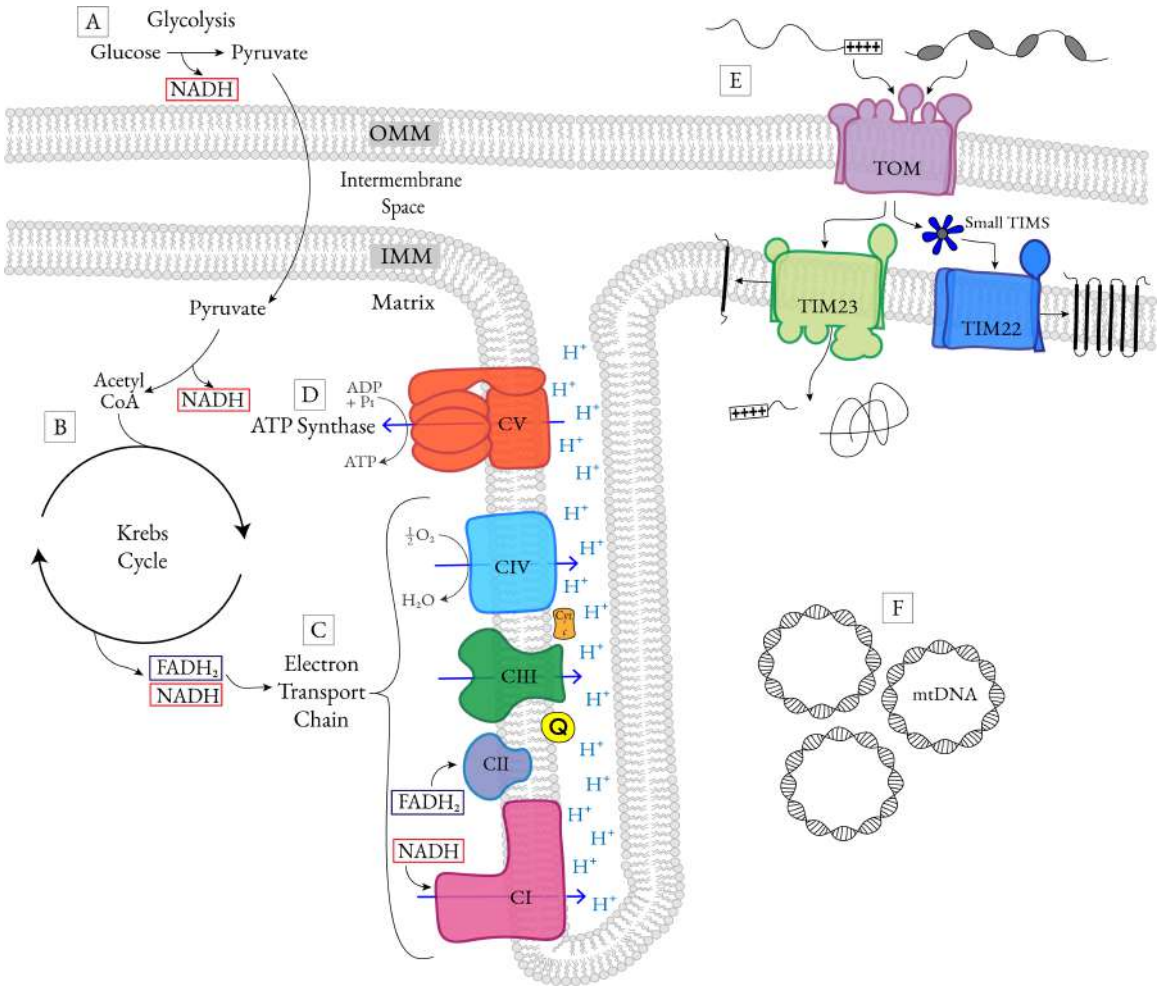

Figure 1.3: Mitochondria physiology overview - A schematic representation of the mitochondrial membranes, outlining particular key features relevant to the work carried out in this project. (A) Glycolysis (B) Krebs cycle (C) electron transport chain, consisting of complexes I-IV, showing the oxidation of reduced electron carriers NADH and $FADH_2$ at complexes I and II respectively and reduction molecular oxygen at complex IV. Simultaneously the ETC pumps protons into the IMS (D) ATP synthase utilising the proton gradient in the IMS to synthesise ATP from ADP and Pi (E) Protein import via TIM/TOM complexes, these complexes transport 99% of mitochondrial proteins that are encoded on the nuclear genome (E) Mitochondrial genome which encodes for 37 genes, including 13 polypeptides, all of which encode for subunits of the ETC.

1.1.2.1 Mitochondrial genome and protein import machinery

Mitochondria contain their own double-stranded, circular molecules of mitochondrial DNA (mtDNA), consisting of ≈16,500 base pairs (bp) in mammalian mitochondria, of which each cell generally contains several copies, Figure 1.3 (F). It encodes a total of 37 genes; 22 tRNAs, two rRNAs, and 13 polypeptides (Taanman, 1999). The polypeptides encoded in the mtDNA are all subunits of enzyme complexes in the OXPHOS metabolic pathway; seven of complex I, one of complex III, three of complex IV and two of ATP synthase. Complex II is the only respiratory complexes which has all its subunits (four) encoded by the nuclear DNA. This results in assembly of the already complex multimeric OXPHOS machinery requiring co-ordination between nuclear and mitochondrial encoded subunits.

The vast majority of mitochondrial proteins, including the remaining subunits of the respiratory complexes, are encoded by the nuclear genome, requiring them to be translocated into the organelle (Wiedemann and Pfanner, 2017). The protein machineries that facilitate this process are the translocase of the outer membrane (TOM) and translocase of the inner membrane (TIM) complexes, indicated by 'E' in Figure 1.3. Proteins being transported from the cytosol have four potential destinations; the outer membrane, the intermembrane space, the inner membrane or the matrix.

Significant advances have been made in recent decades deciphering how protein translocation works and the mechanism by which proteins are delivered to their final destination in a "specific" manner. Proteins containing a positively charged N-terminal signal sequence are targeted to TIM23, which is responsible for delivery of matrix proteins. However, there is a sub-set of proteins in this category which contain a hydrophobic domain which halts translocation on TIM23 channel, leading to protein insertion into the IMM. Proteins targeted to TIM complex TIM22 contain signal sequences within the transmembrane regions and are inserted into the IMM, and lastly, small proteins with twin cysteine motifs are delivered into the IMS via the Mia40 pathway (Mordas and Tokatlidis, 2015). However, there are still some nuclear encoded proteins where the transport method is not fully understood.

1.1.2.2 Cellular respiration

The cellular respiration pathway can be broken down into four basic stages; glycolysis, pyruvate oxidation, Krebs cycle and oxidative phosphorylation. Glycolysis occurs independently, whereas pyruvate oxidation and the Krebs cycle are driven by oxidative phosphorylation (Nicholls and Ferguson, 2013).

Glycolysis, indicated by 'A' in Figure 1.3, is an oxygen-independent metabolic pathway carried out in the cytosol, with the breakdown of one glucose molecule producing two molecules each of; pyruvate, ATP, NADH and water. Pyruvate is able to be transported into the mitochondrial matrix via a pyruvate carrier, where it is oxidised before feeding into the Krebs cycle. The NADH that is produced by glycolysis, on the other hand, cannot cross the inner mitochondrial membrane, however it can be utilised by the malate-aspartate shuttle. In this mechanism, a compound is reduced in the cytosol by NADH, the compound is then able to cross the membrane into the matrix, where it regenerates NADH by reducing NAD^+, and can then by utilised by the electron transport chain (Lunt and Vander Heiden, 2011).

Oxidation of pyruvate links glycolysis to the remaining cellular respiration pathway, and occurs in the mitochondria matrix. Pyruvate is converted from a three-carbon molecule to a two-carbon molecule before undergoing an oxidation reaction where a coenzyme A (CoA) molecule is attached producing acetyl-CoA, as well as producing a reduced molecule of NADH.

Acetyl CoA is the entry molecule for the Krebs cycle, indicated by 'B' in Figure 1.3. It is also known as the citric acid or TCA cycle (Akram, 2014), and is a central component of cellular respiration, generating reduced electron carriers in the form of $FADH_2$ and NADH that subsequently feed electrons into the electron transport chain. The cycle is a series of redox reactions, in a closed loop that harvests the bond energy of the intermediates (David L Nelson, 2017).

This outlines the first three steps of cellular respiration, which in themselves produce small amounts ATP; two molecules of ATP from glycolysis and a further two from the Krebs cycle per molecule of glucose. However the reduced electron carriers produced by these processes, two NADH in glycolysis,

two NADH from the oxidation of pyruvate to acetyl CoA and a further six NADH and two $FADH_2$ from the Krebs cycle (per molecule of glucose), transfer electrons to the electron transport chain, indicated by 'C' in Figure 1.3, which ultimately generates a further 26-28 ATP molecules through the OXPHOS pathway, which is coupled to the ATP synthase machinery, indicated by 'D' (Nicholls and Ferguson, 2013; Akram, 2014). This process will be covered in more depth in the following section.

1.1.3 Mitochondrial energy production by oxidative phosphorylation

The final stage in cellular respiration is the metabolic pathway of oxidative phosphorylation, first proposed as the chemiosmotic theory in 1961 by Mitchell (Mitchell, 2011). It theorised that multimeric redox enzymes facilitate the coupling of substrate oxidation to the regeneration of ATP. The free energy released from the downhill transfer of electrons is utilised to pump protons across the IMM and create a proton gradient. This electrochemical gradient is then sufficient to drive ATP synthesis.

The pathway has many components that work together to drive energy production, an overview of the various elements will be discussed in this section, supported by the schematic diagram in Figure 1.4. If one element becomes dysfunctional, it can have a system-wide impact, and a comprehensive understanding of the system as a whole is vital to interpret alterations in physiology.

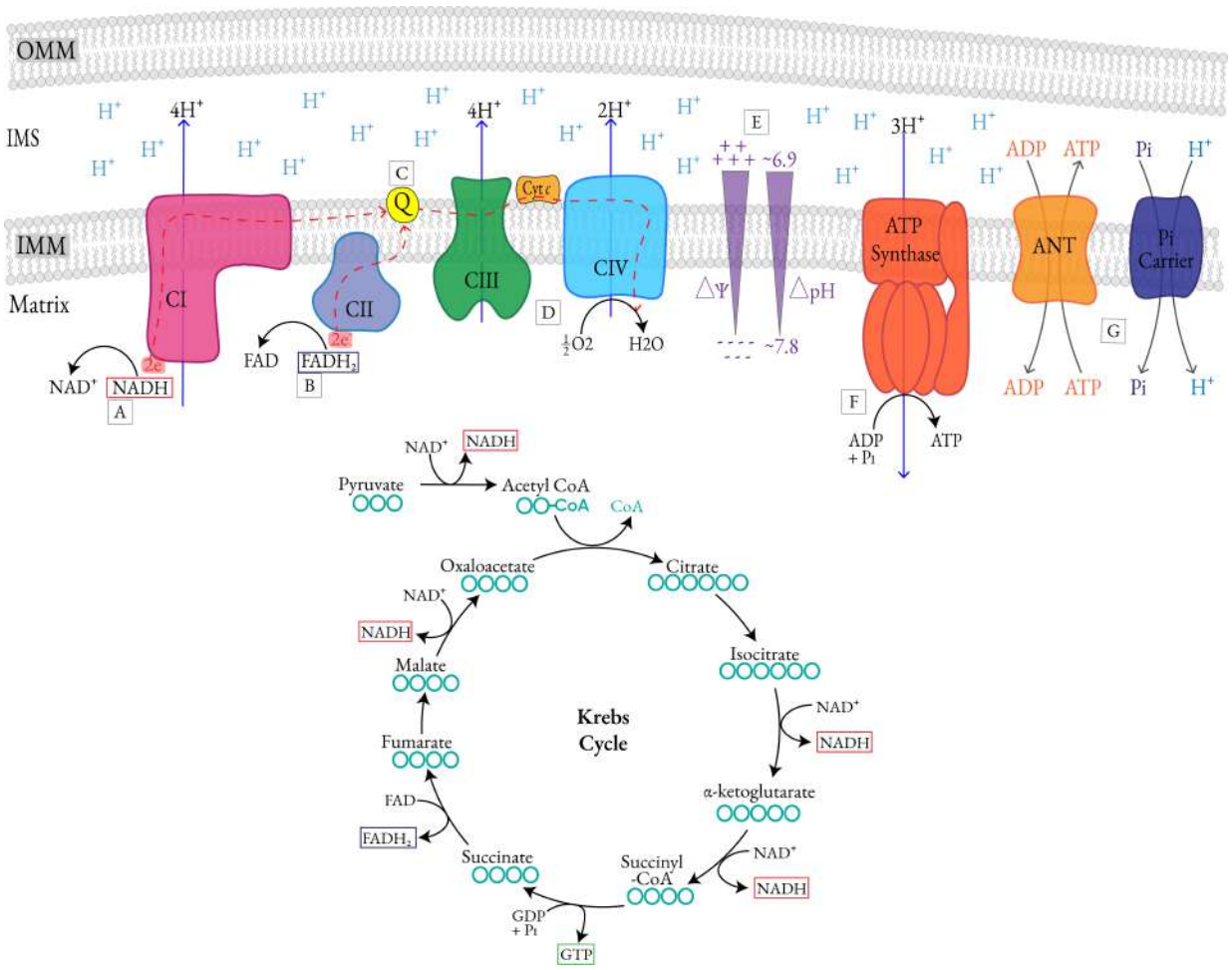

Figure 1.4: Overview of oxidative phosphorylation - Schematic representation of components of the OXPHOS pathway. The Krebs cycle is represented in the bottom part of the figure, with each component annotated with a string of circles representing the number of carbons in that molecule. (A) complex I-linked respiration, CI accepting electrons from NADH (B) CII-linked respiration, CII accepting electrons from $FADH_2$ (C) quinone molecule which links the entry redox complexes to CIII in the pathway (D) CIII, cytochrome c, CIV and final electron acceptor, molecular oxygen (E) use of free energy to create an electrochemical proton gradient, membrane potential ($\Delta\Psi$) and pH gradient (ΔpH) make up the PMF. pH values used as found on bionumbers, the database of useful biological numbers (Porcelli et al., 2005). IMS pH as referenced is 6.88 pH Range: ±0.09, and matrix 7.78 pH, Range: ±0.17 pH (F) ATP synthase utilising the proton gradient to drive ATP synthesis (G) transporters complementing OXPHOS machinery

The energy-transducing membrane system works by a series of proton pumps and channels working in opposite directions: the electron transport chain (ETC) (complexes I-IV) contain pumps that actively move protons into the IMS, driven by the downhill transfer of electrons. This is tightly coupled to the controlled movement of protons down a channel in ATP synthase. The system is comprised by several components, subdivided into molecular or chemical entities. The molecular entities comprise the respiratory complexes and all other carriers and enzymes that allow substrate entry and oxidation in the mitochondrial matrix. The chemical entities which comprise of the different components of the proton-motive force: the charge separation (membrane potential) and pH gradient across the IMM (Nicholls and Ferguson, 2013), (Hatefi, 1985), (Mitchell, 1961).

There are two entries to the ETC, one route is via NADH:ubiquinone oxidoreductase (complex I), shown in Figure 1.4 at point A, where electrons are fed in by the electron carrier NADH; a molecule produced at multiple stages in cellular respiration, as detailed earlier. Making complex I-linked respiration the major entry component of the oxidative system. Additionally, four protons are translocated by complex I. The second point of entry is at succinate:ubiquinone oxidoreductase, also known as succinate dehydrogenase (complex II), point B in Figure 1.4. Here $FADH_2$ is used as the redox cofactor, generated from succinate being converted to fumarate in the Krebs cycle. During complex II-linked respiration, less protons are pumped per electron transferred as, unlike complex I, succinate dehydrogenase does not transfer any protons.

The electrons fed into the entry complexes CI and CII transfer electrons to a quinone compound (Figure 1.4, C), which acts to continue the downhill transfer of electrons to complexes CIII, cytochrome *c* and CIV and the final electron acceptor molecular oxygen (Figure 1.4, D).

Figure 1.4 E, represents the proton electrochemical gradient ($\Delta\widetilde{\mu}H^{+}$), which is comprised of two components. The first, resulting from the difference in proton concentration across the membrane is ΔpH. The other component, due to the difference in electrical potential between the IMS and matrix compartments, is the membrane potential $\Delta\Psi$. When expressing ($\Delta\widetilde{\mu}H^{+}$) it is conventional to convert it into units of electrical potential, represented by the symbol Δp and otherwise known as the proton motive force (PMF). Of the two components in a mitochondrion $\Delta\Psi$ is dominant,

contributing ≈180 mV to the PMF. As large changes in pH would be detrimental to the function of proteins in the IMS, the ΔpH contributes ≈30 mV (Mitchell, 2011; Nicholls and Ferguson, 2013; Nicholls, 2010; Liberman et al., 1969).

Figure 1.4 (G) shows transporters that work in complement with the OXPHOS machinery. Carriers supply the matrix with ADP and Pi allowing coupled respiration, as the PMF is utilised by ATP synthase in the presence of ADP and Pi to drive ATP synthesis, Figure 1.4 F. Active ATP synthesis causes depolarisation of the PMF, which drives ETC respiration, leading to increased electron transfer and proton pumping to maintain the membrane potential. This section has provided an overview of the oxidative phosphorylation system and the energetic process, the components of the ETC will now be looked at in more functional depth (Nicholls, 2010).

1.1.4 Components of the electron transport chain

The ETC consists of over 80 different subunits, distributed across four different multimeric complexes (CI-CIV), with CI having the greatest number of subunits at 44, and CII the smallest at only four. Coupled to the ETC is the complex ATP synthase, which is comprised of an additional 20 subunits. As previously discussed in Section 1.1.3, electrons enter the ETC at complexes I and II, where they flow through the complexes due to different redox potentials. Naturally, they flow from the highest to the lowest redox potential, as that is more thermodynamically favourable (Meyer et al., 2019).

As electron flow is coupled with primary proton pumps, in complex I, III and IV, the PMF is generated as a consequence of electron flow through the complexes. Therefore, the PMF is not created because the ETC uses the electrons; instead, the PMF is the consequence of electron flow, proton pumping and the highly impermeable IMM (Nicholls and Ferguson, 2013; Mitchell, 2011).

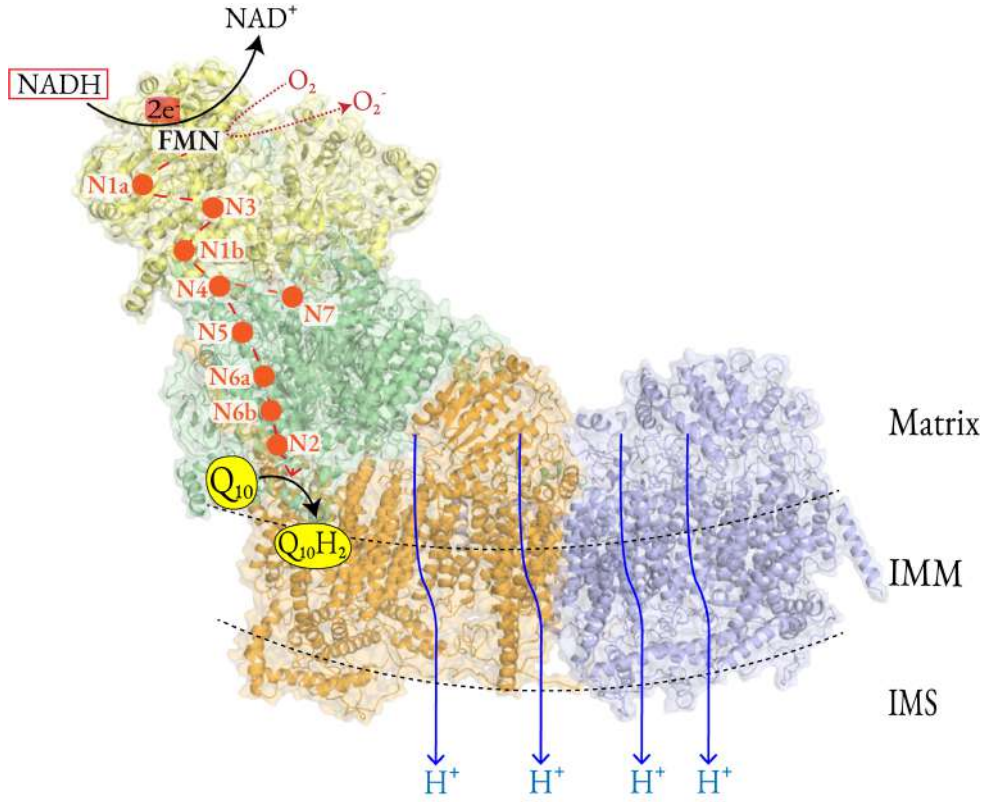

Figure 1.5: Schematic overview of complex I - In the top module (coloured in yellow), NADH is oxidised by a flavin mononucleotide (FMN), generating the release of two electrons (2e) which enter a chain of seven iron–sulfur (Fe-S) clusters (represented by orange circles). At this stage, the reduced FMN cofactor also reacts with O_2 to form ROS. The terminal Fe-S cluster (N2) transfers the electrons to a ubiquinone molecule (Q_{10}) which gets reduced ($Q_{10}H_2$). Conformations changes, induced by the reduction of ubiquinone, allow proton-translocation across the two P modules (coloured in orange and blue) via long chains of charged residues through the membrane arm. Pumping four protons from the matrix to the IMS. Schematic CI model is made from a electron cryo-microscopy structure of complex I from *Bos taurus* ((Zhu et al., 2016); PDB 5LDW)

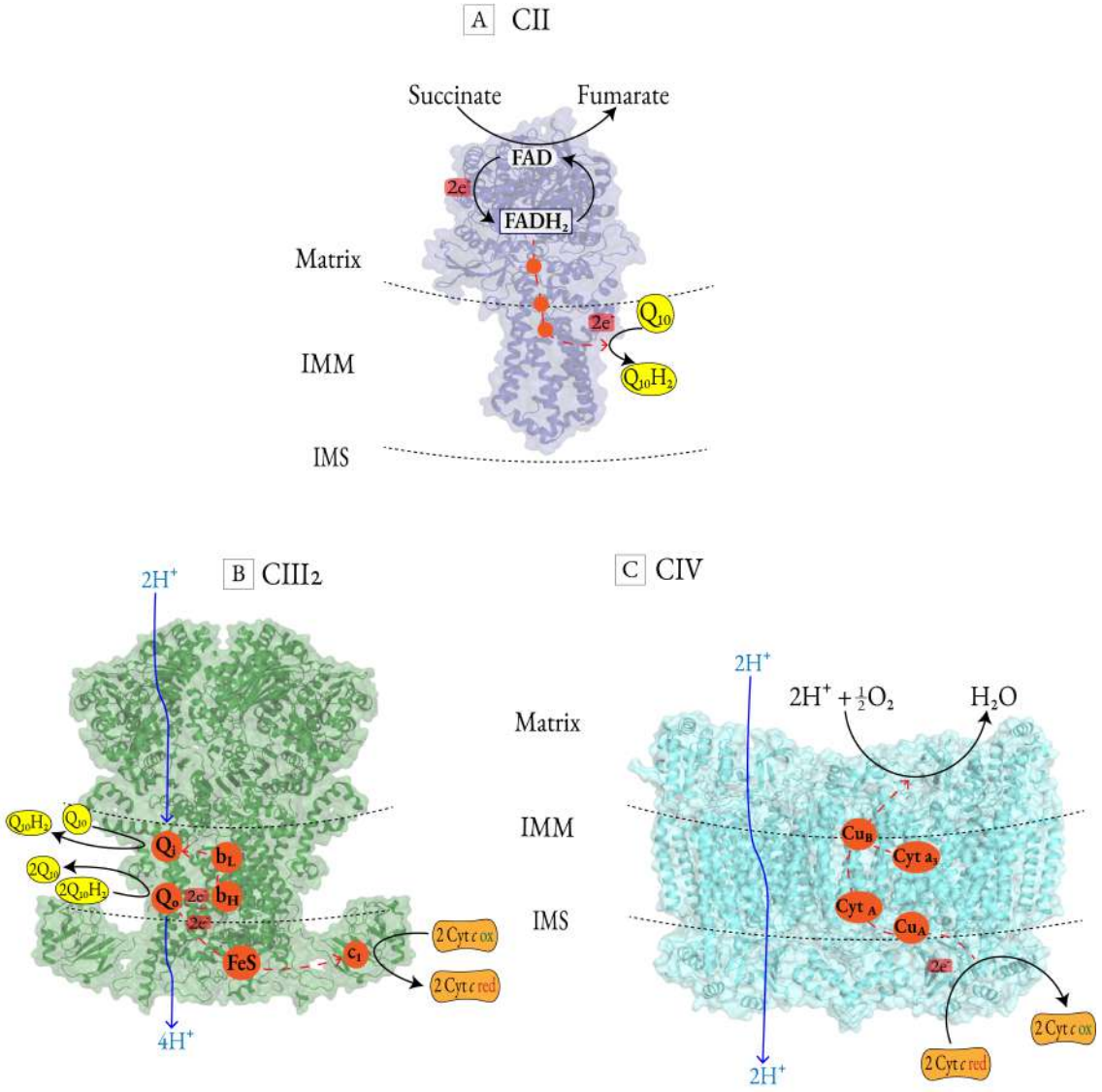

Figure 1.6: Schematic overview of complexes I, III and IV - highlighting the role coenzyme Q_{10} and cytochrome c playing mediating electron transfer between the ETC complexes. Complex cofactors are shown in orange within the structure, highlighting how electron transfer is mediated within the complex **(A)** Succinate dehydrogensae (CII), **(B)** Ubiquinol:cytochrome-c oxidoreductase (CIII), **(C)** cytochrome-c: oxygen oxidoreductase (complex IV). Further details in the text. (PDB 1NEK (CII)(Yankovskaya et al., 2003), 1NTZ(CIII)(Gao et al., 2003), 1OCC(CIV)(Tsukihara et al., 1996) Structure images created from PyMOL.)

1.1.4.1 NADH:ubiquinone oxidoreductase

NADH:ubiquinone oxidoreductase, also known as complex I (CI), is the largest ETC complex, and indeed, one of the largest membrane-bound enzymes found in the cell. The mammalian complex consists of 45 subunits, of these 14 are considered core subunits which facilitate the catalytic activity of the enzyme (Sazanov, 2015). These subunits have been found to be highly conserved across species, representative of their essential role in the OXPHOS pathway (Zhu et al., 2016). Additionally, the complex has 31 supernumerary subunits, which although referred to as mammalian-specific (Sazanov, 2015; Hirst et al., 2003), have been found to have homologous proteins in other subsets of the animal kingdom, such as the phylum Nematoda, discussed in more detail in Section 1.2.2. Eukaryotic CI is organised into four functional modules (coloured independently in Figure 1.5). The peripheral arm extends up into the mitochondrial matrix, where it facilitates the electron flow, whereas the membrane arm catalyses proton transport across the IMM (Sazanov, 2015).

The first of two entry points to the ETC, complex I is thought to provide about 40% of the PMF (Sazanov, 2015). As detailed in Figure 1.5, NADH is oxidised to NAD^+, feeding electrons via iron–sulfur (Fe-S) clusters to the electron carrier coenzyme Q_{10}, ubiquinone. Coupled to the flow of electrons, as previously mentioned, is the translocation of four protons from the matrix to the IMS (Sazanov, 2015; Hirst, 2013). Conformation changes induced by the reduction of ubiquinone, allow proton-translocation across the two P modules (coloured in orange and blue in Figure 1.5) via long chains of charged residues through the membrane arm. In addition to pumping protons, the transfer of electrons can generate superoxide ($O_2^{\bullet -}$) reactive oxygen species (ROS), discussed in more detail in Section 1.1.5.1.

Complex I and disease

Complex I deficiency is the most frequently occurring mitochondrial disorder presenting in childhood, accounting for ≈30% of cases. The deficiency is characterised by clinical and genetic heterogeneity (Kirby et al., 1999). This could be attributed to the fact that CI is the largest enzyme of the OXPHOS system, with subunits that are encoded on both the nuclear and mitochondrial genome. Clinical presentation of CI deficiency is extremely heterogeneous (Rodenburg, 2016; Fassone and Rahman, 2012), including; fatal infantile lactic acidosis (Kirby et al., 2004), Leigh syndrome (Rah-

man et al., 1996), leukoencephalopathy (Ogilvie et al., 2005) and cardiomyopathy (Ruiter et al., 2007). Genetic complexity, in addition to clinical heterogeneity mentioned, leads to significant difficulties in establishing genetic diagnoses for patients with CI deficiency (Fassone and Rahman, 2012). Genetic screening of patients from around the world has shown a consistent prevalence of mtDNA mutations in 20%–30% of complex I deficiencies (Lebon et al., 2003). Additionally, mutations in all seven of the nuclear-encoded core units and ten of the accessory subunits have been associated with CI deficiency (Fassone and Rahman, 2012).

1.1.4.2 Succinate:ubiquinone oxidoreductase

Succinate:ubiquinone oxidoreductase, otherwise known as succinate dehydrogenase or complex II (CII), is a IMM-bound four subunit enzyme (Yankovskaya et al., 2003). CII facilitates a second point at which electrons can enter the ETC, shown in Figure 1.6 (A). However, it is sometimes considered a non-integral component of the ETC, partly due to the fact that the electron transfer activity of the enzyme is not coupled to a corresponding translocation of a proton (Rutter et al., 2010). This is because substrate electron transfer through CII generates potential energy close to 0 mV, therefore, thermodynamically incompatible with proton translocation (Nicholls and Ferguson, 2013). In addition, the primary role of CII is within the Krebs cycle, converting succinate to fumarate. Further compounding the idea of CII not forming an integral part of the ETC, is that supercomplex organisation of CI, CIII and CIV is well established (Section 1.1.6.2), with no validated structures showing CII interaction. However, it has been hypothesised that CII may interact in a so called 'electron transport chain supercomplex' (ETCS), but this is yet to be validated (Guo et al., 2017).

Transferring electrons to CoQ pool is an additional role the complex is able to carry out, due to its membrane bound nature and cofactors (Rich and Maréchal, 2010). The active site, within the subunit furthest from the membrane, has a covalently bound flavin adenine dinucleotide (FAD). When succinate is oxidised, electron transfer flows through FAD to CoQ, mediated by three FeS clusters (Rich and Maréchal, 2010).

1.1.4.3 Ubiquinol:cytochrome-c oxidoreductase

Ubiquinol:cytochrome-c oxidoreductase, also known as cytochrome bc_1 complex or complex III (CIII), is located at a 'mid point' in the ETC, facilitating the transfer of electrons which have entered the ETC through CI/II, and passed via CoQ to CIII, onto the final complex for oxygen reduction, via cytochrome *c*. The complex is composed by 11 subunits, including one which is mitochondrial-encoded (cytochrome b), and only functions as a dimer. The complex is supported by four cofactors, which facilitate electron transfer (Crofts, 2004), shown in Figure 1.6 (B). A net addition of four protons are contributed to the PMF, for every two electrons that flow through the complex.

1.1.4.4 Cytochrome-c: oxygen oxidoreductase

Cytochrome-c:oxygen oxidoreductase, also known as cytochrome-*c* oxidase or complex IV (CIV), is the final enzyme in the ETC, and facilitates the reduction of O_2 to water. Consisting of 13 subunits, of which, three catalytic subunits are encoded by the mitochondrial genes (Rich and Maréchal, 2010). Complex IV contributes to the PMF, through consuming protons and electrons from opposite sites of the IMM, but additionally, through pumping four protons from the matrix to the IMS, per reduced oxygen (Kadenbach et al., 1987). Electrons are transferred to Complex IV via cytochrome *c*, in the IMS, while protons are acquired from the matrix side. To reduce to one molecule of oxygen, to two of water, four electrons and four protons are required. CIV is thought to act as the rate limiting step of the ETC, and its activity, consumption of oxygen, can be measured as an indicator of the oxidative capacity of the mitochondria (Srinivasan and Avadhani, 2012).

1.1.5 Reactive oxygen species

Reactive oxygen species (ROS) describes various reactive molecules and free radicals that are derived from molecular oxygen. An electron structure consisting of atomic oxygen, two unpaired electrons in separate orbits in its outer electron shell, makes oxygen susceptible to radical formation (Phaniendra

et al., 2015). Two examples of ROS, superoxide and hydrogen peroxide, which have relevance to the mitochondrial respiratory machinery, can be see in detail in Figure 1.4. Superoxide anions are very reactive and quite unstable, and therefore will react in the vicinity where they are created. On the contrary, H_2O_2 is a relatively stable molecule, with a long life-time and therefore is able to travel around the cell, even across membranes. These characteristics of H_2O_2 can be utilised in experimental methods to measure ROS production (Dickinson and Chang, 2011).

Oxidative stress occurs when there is an excess of ROS or oxidants, above the cells antioxidant capability (Ray et al., 2012). During times of oxidative stress ROS can potentially damage lipids, DNA, RNA and proteins; in addition, ROS and the damage carried out to the aforementioned biomolecules can potentially drive a number of pathological processes such as ageing, apoptosis and ischemic injury (Chen et al., 2003). However, ROS also have a physiologically relevant role in cell signalling in cellular processes such as; apoptosis, gene expression and the activation of signalling cascades (Feissner et al., 2009).

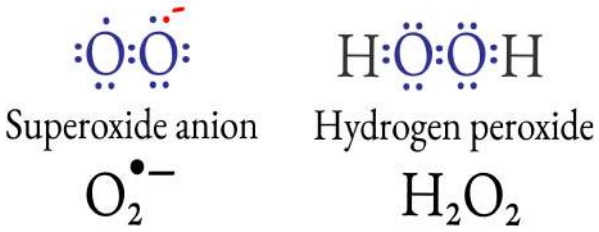

Figure 1.7: Reactive oxygen species - Electron structures of two common ROS. Each structure is paired with its name and chemical formula.

During normal metabolism, the mitochondrial ETC is a major source of reactive oxygen species (Jastroch et al., 2010). Initial discoveries in the field found that isolated mitochondria were a source of H_2O_2 (Loschen et al., 1971), this developed into an understanding that H_2O_2 arose from the dismu-

tation of superoxide ($O_2^{\bullet -}$), which is the proximal mitochondrial ROS (Murphy, 2009) (Echtay et al., 2002; Kussmaul and Hirst, 2006). Under certain pathologic conditions, such as hypoxia, ischemia, ageing, and chemical inhibition of respiration, the rate of ROS production from mitochondria can increase (Jastroch et al., 2010).

It is worth noting however, that in addition to mitochondrial contribution to cellular ROS, there are several other redox systems capable of producing significant levels of ROS. These systems include; cytochrome P450 in microsomes; fatty acid oxidation and urate oxidase in peroxisomes and nitric oxide synthase and lipoxygenases in the cell cytosol (Brown and Borutaite, 2012). The individual contributions of each system will likely differ between cell type, species of ROS and the conditions of the cellular environment.

1.1.5.1 ROS in mitochondria

In the mitochondrial system there are at least nine oxidoreductase complexes capable of one-electron reduction of oxygen, generating superoxide anion species. A few include; cytochrome b5 reductase, monoamine oxidases, succinate dehydrogenase (complex II) and *alpha*-ketoglutarate dehydrogenase complex. The amount of mitochondrial ROS produced by any individual complex under physiological conditions is not yet known, and defining a single "main" source of ROS proves difficult to establish (Brown and Borutaite, 2012).

Within the electron transport chain, respiratory complexes I and III are the predominant enzymes capable of producing significant levels of ROS, as such they will be explored in more detail. However, it seems that under normal physiological conditions, the amount of ROS produced by the enzymes is generally low, with higher levels attributed to malfunction in the system or non-physiological conditions.

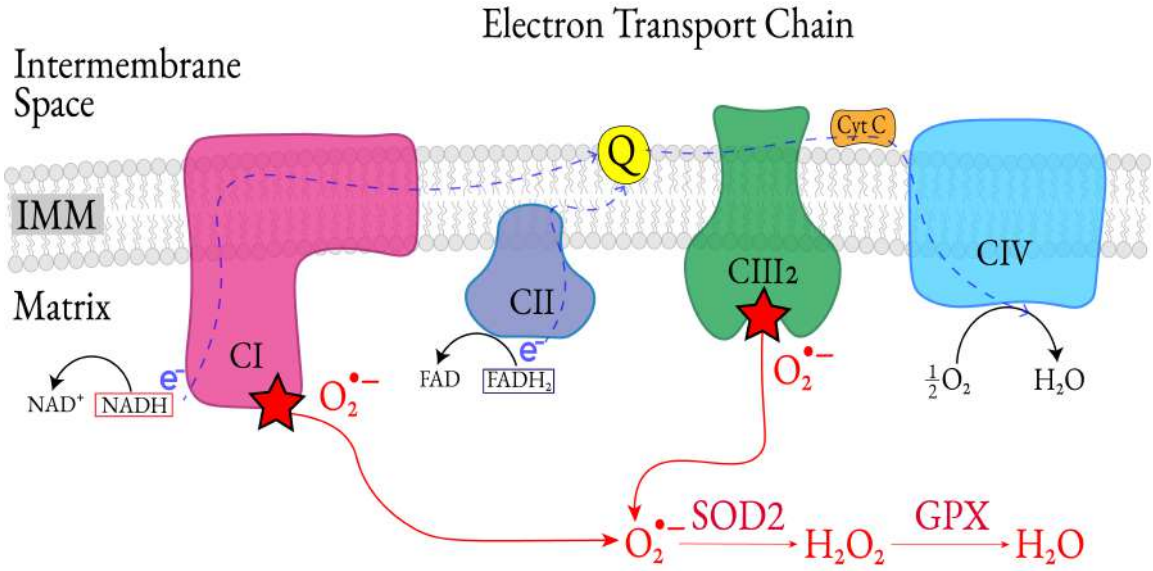

Figure 1.8: Reactive oxygen species and the electron transport chain - schematic diagram showing the four complexes of the ETC (CI-CIV). The red stars denote the two complexes (CI and CIII) which are the majority contributors to mitochondria ROS. The diagram also details how the superoxide anions are converted by superoxide dismutase 2 (SOD2) to H_2O_2

Complex I

It is thought that CI produces ROS at three distinct sites, FMN, FeS clusters and the CoQ binding site (Zorov et al., 2014; Feissner et al., 2009; Hirst et al., 2008), with Figure 1.5 detailing these sites, but only annotating ROS production at the FMN. Within CI, there are two pathways that produce ROS, forward electron transference (FET) and reverse electron transference (RET).

The RET pathway has been found to be active under the presence of succinate sustained respiration, which leads to a high PMF and a reduced Q-pool, reversing the electron flow and driving electrons thermodynamically upwards, into CI, causing reduction of NAD^+. In in-vitro systems, this pathway is thought to be how the majority of ROS species from CI are produced. Within the experimental system it can be inhibited by rotenone and uncouplers, and increased by antimycin A (Aon et al., 2010; Andreyev et al., 2005). However, the RET pathway is not thought to be hugely physiologically relevant, as CII is not the primary entry of electrons for the ETC in vivo. Furthermore, the

PMF is considerably lower in cellular mitochondria due to the constant demand and production of ATP (Aon et al., 2010; Murphy, 2009; Lambert and Brand, 2009).

The FET pathway is typically observed in the presence of NAD^+-linked substrates, although, it is thought that the amount of ROS produced through this route is considerably negligible (Andreyev et al., 2005). An increase in ROS production is seen in the presence of inhibitors, but still not as much as in RET (Lambert and Brand, 2009). The FET pathway is highly influenced by the $NADH/NAD_+$ ratio, which is critical in determining the proportion of reduced FMN in the complex. High levels of reduced flavin leads to electrons entering the complex with a diminished capacity to exit through the normal route, increasing the likelihood of electron slip and the production of ROS, due to the increased time the complex spends in the reduced form (Murphy, 2009).

Complex III

Under normal conditions, ROS production at CIII is at a similar magnitude as in the CI FET pathway, and significantly lower than in RET (Lambert and Brand, 2009). However, in the presence of antimycin A, a significant increase in ROS production is found. Electrons still enter CIII, but the Q-cycle of the enzyme is disrupted, increasing the likelihood of electron slip occurring and partial reduction of O_2 (Lambert and Brand, 2009; Murphy, 2009). Therefore, although CIII can be induced to produce high levels of ROS through antimycin A inhibition, under normal physiological conditions the production of CIII-linked ROS is small (Murphy, 2009).

1.1.5.2 Cardiolipin and reactive oxygen species

Cardiolipin molecules are particularly susceptible to ROS-induced oxidation (Esterbauer, 1993). Firstly, they are sensitive to ROS-induced oxidation due to the presence of a glycerol bridge between two double bonds of CL fatty acids. Secondly, CL molecules are located near to ROS production sites in the electron transport chain, namely complex I and complex III as discussed above (Feissner et al., 2009;

Chen et al., 2003). Oxidative damage to CL may have deleterious effect on respiratory chain complex activity and mitochondrial function. As discussed previously, CL molecules are required for functional activity of a number of inner mitochondrial membrane proteins, including respiratory chain complexes involved in OXPHOS (Paradies et al., 2001; Petrosillo et al., 2001).

It has been theorised that free radical oxidation of CL likely has a significant impact on a wide range of biological processes, such as apoptosis and mitochondrial function, potentially contributing to a number of mitochondrial diseases, such as ageing and neurodegeneration (Yin and Zhu, 2012; Chicco and Sparagna, 2007; Schug and Gottlieb, 2009). Exactly how the respiratory complexes are affected by CL oxidation is currently not understood, however, multiple studies indicate that peroxidised CL is unable to support normal activity of the respiratory enzymes (Musatov, 2006; Paradies et al., 2004, 2002). Furthermore, it has been shown the CL plays an important role in the stabilisation of the supercomplexes (Zhang et al., 2002; Pfeiffer et al., 2003; Schägger, 2002), discussed in Section 1.1.1.2. It is also thought that when CL oxidation is increased, it may lead to an overall decrease in the amount of CL overall (McLean et al., 1993). This could feasibly cause destabilisation of the supercomplexes, but there has yet to be any conclusive evidence of CL mediated supercomplex loss as of ROS.

1.1.5.3 Antioxidant machinery

Within the mitochondrial environment, in normal conditions, ROS will not be accumulated, as they are promptly scavenged by antioxidant machinery. Mitochondria employ many mechanisms to reduce ROS, this section will introduction two of those processes, the first being the action of mitochondrial antioxidant enzymes and the second, the 'mild uncoupling theory' (Starkov, 1997). The capacity of the mitochondrial antioxidant is finite, and once exhausted, ROS levels will progressively increase.

Mitochondrial antioxidant enzymes, such as SOD2, otherwise known as manganese-dependent superoxide dismutase (MnSOD), is exclusively found in the mitochondrial matrix (Murphy, 2009),

rapidly convert superoxide anion to H_2O_2, referenced in Figure 1.8. H_2O_2 is able to easily diffuse across membranes, to be quickly reduced to water by mitochondrial and cytoplasmic peroxiredoxins, catalases, and glutathione peroxidases (Murphy, 2009; Forkink et al., 2010).

A strong correlation exists between the PMF and the production of ROS (Korshunov et al., 1997), the 'mild uncoupling' theory (Starkov, 1997), suggests that a small decrease of $\Delta\Psi$, of about 10%, causes a decrease in ROS formation by the ETC. Uncoupling of OXPHOS is akin to a "short circuiting" of the system, allowing leak of protons from the IMS to the matrix, bypassing ATP synthase, and causing a decrease in PMF. It has been found that a small increase in $\Delta\Psi$ can induce ROS formation, whereas, slight decreases can significantly reduce ROS production (Mailloux and Harper, 2011). Therefore, it was suggested that the 'mild uncoupling' of mitochondria may occur as a first line of defence against oxidative stress (Brand and Esteves, 2005). This is an interesting theory, when considering findings that partial mitochondrial respiration impairment has been found to increase the lifespan of some organisms, discussed in more detail in Section 1.2.2.2.

1.1.6 Respiratory supercomplexes

Supercomplex formation, and understanding the factors that govern their formation and stability are important in relation to the investigations of this project. However, their very existence has been a matter of debate, as theories of how the four electron transport chain proteins are organised within the mitochondrial inner membrane have changed with time (Lobo-Jarne and Ugalde, 2018). A summary of different organisations can be seen in Figure 1.9, split between the "fluid-state" and "solid-state" model organisations, expanded on below.

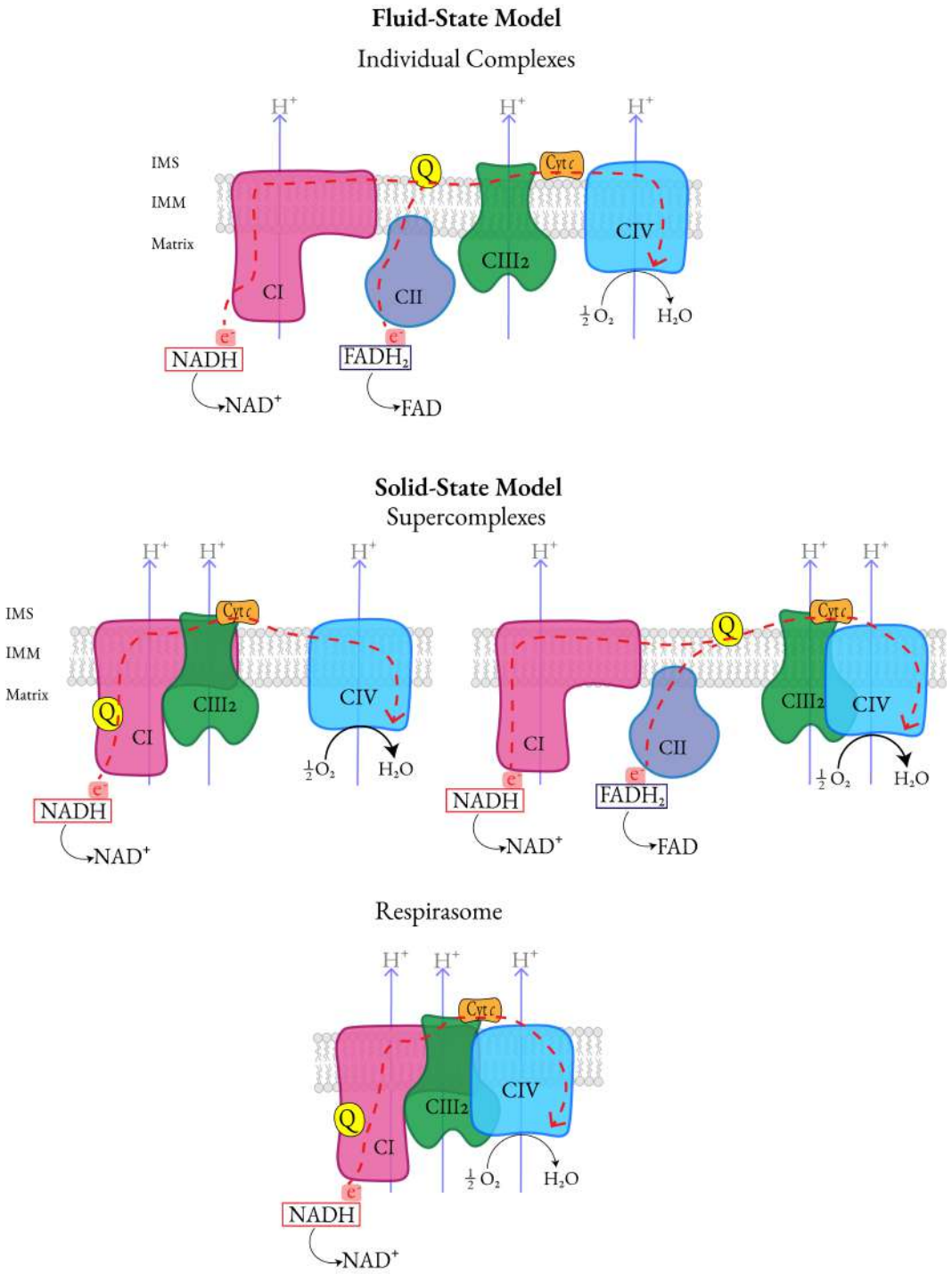

Figure 1.9: Schematic of electron transport chain compositions - original fluid state model, respirasome of all three complexes and supercomplexes of combinations of either CI:III or CIII:IV (Hackenbrock et al., 1986; Schägger, 2002)

1.1.6.1 Fluid-state and solid-state model

The initial theory, proposed by Hackenbroock (Hackenbrock et al., 1986), describes a fluid-state or random collision model, where each component of the ETC are independent units and diffuse individually in the the IMM, shown in Figure 1.9, top panel. Electron transfer relies on random collision events between the four complexes and two smaller electron carriers, coenzyme Q_{10} (CoQ) and cytochrome *c* (Hackenbrock et al., 1986; Dudkina et al., 2010; Paradies et al., 2014). This model is supported by the fact that all of the individual ETC protein complexes can be homogenously purified, and still be found enzymatically active (Dudkina et al., 2010).

This theory was challenged by Schägger's solid-state model (Schägger, 2002), which proposed that interactions between the OXPHOS complexes are stabilised in higher order entities named supercomplexes, Figure 1.9 bottom panels. The organisation of CI:CIII:CIV has been specifically labelled the "respirasome" for clarity going forward, as to distinguish it from other CI:III and CIII:IV supercomplexes, however it is still under the class of a supercomplex.

1.1.6.2 Evidence supporting the solid-state model

Blue native gels

Evidence supporting the solid-state model and existence of supramolecular organisation of the ETC exists from a wide range of experimental findings, including both functional and structural studies. A well established method of resolving supercomplexes is by blue native polyacrylamide gel electrophoresis (Jha et al., 2016), furthermore, within the BN gels the activities of the supercomplexes can be shown by in-gel assays (Suthammarak et al., 2010, 2009; Jha et al., 2016). These in-gel assays, combined with mass spectrometry techniques allows the composition of the blue native bands to be confidently identified and varying compositions of supercomplexes to be elucidated.

Flux control analysis

Experiments investigating flux control distinguish between the two theories on the basis that in the fluid-state model each individual enzyme would likely be deferentially rate-controlled, whereas in the solid-state model, the whole respiratory pathway would behave as a single entity, therefore inhibition of its components would generate the same flux control. This has been investigated for NADH oxidation, looking at complexes of I:III:IV and also for succinate oxidation, II:III:IV in bovine mitochondria (Bianchi et al., 2004) and ubiquinone and cytochrome *c* in yeast (Boumans et al., 1998). Both studies suggest the components of the OXPHOS metabolic pathway are working as combined functional units, supporting supramolecular organisation, as opposed to them operating as discrete entities.

Genetic experiments

Genetic experiments have shown that point mutations in genes encoding particular subunits of one of the OXPHOS complexes, affects the stability of other complexes in the system ((Lapuente-Brun et al., 2013). More specifically, research has shown in mouse and human cell cultured mitochondria that when the mtDNA encoded CIII gene cytochrome b is mutated, this leads to CIII assembly being impeded, and this goes on to cause a significant reduction in the amount of CI (Acín-Pérez et al., 2004). Conversely, if CI was removed, this did not influence CIII stability (Acín-Pérez et al., 2004). Furthermore, work in mouse fibroblasts found that, in rapidly dividing cells, CIV is necessary for CI assembly and stability (Diaz et al., 2006). These findings suggest inter-complex interactions may be required for normal function for some of the respiratory complexes.

Electron microscopy structures

Developments in the field of electron microscopy (EM) have had a large influence on our understanding of mitochondrial supercomplexes. Low resolution structures provided some evidence of supercomplex organisation, (Dudkina et al., 2005; Schäfer et al., 2006; Heinemeyer et al., 2007). However, from 2016 a wave of high resolution structures of mitochondrial supercomplexes were published, providing a deeper insight into the supramolecular entities, including phospholipid molecules mediating complex organisation and potential interaction points (Wu et al., 2016; Gu et al., 2016; Letts et al., 2016; Sousa et al., 2016; Guo et al., 2017).

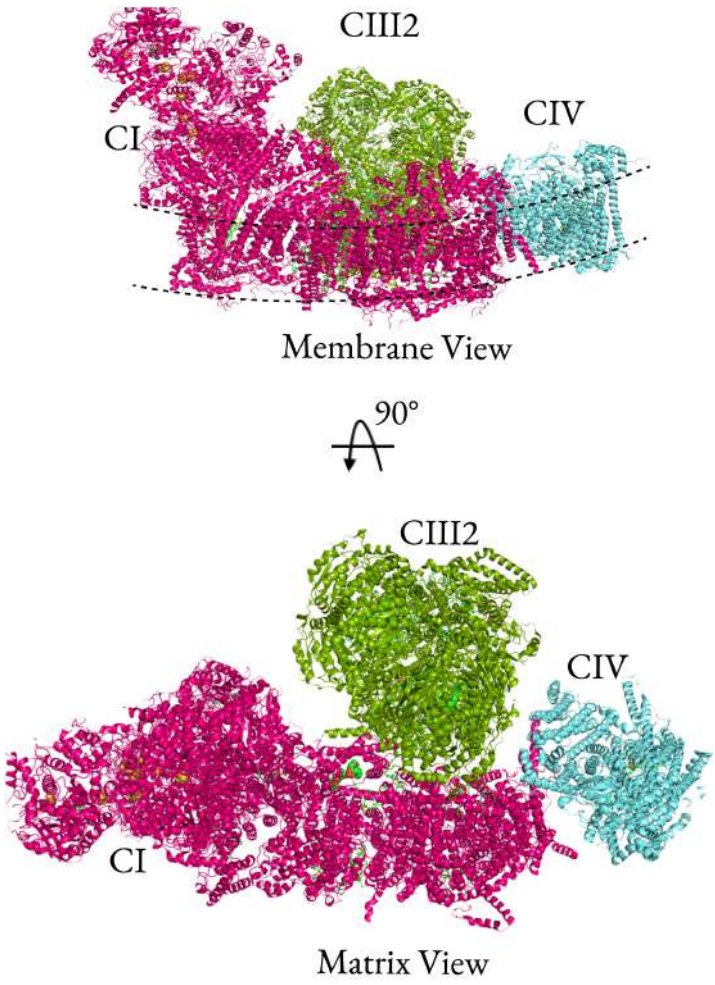

Figure 1.10: Structure of human respirasome - PDB structure 5XTH, purified from HEK293 cell line (Guo et al., 2017). Complex I is shown in pink, complex III dimer in green and complex IV in blue. Showing the arrangement of CIII sitting along the membrane arm of CI with CIV at the end of arm of CI. The structure is consistent with other structures of the respirasome from porcine and ovine mitochondria (Wu et al., 2016; Letts et al., 2016). Images created in PyMOL.

Supercomplex structures are now available from the mitochondria of human (Guo et al., 2017), pig (Wu et al., 2016; Gu et al., 2016), cow (Sousa et al., 2016) and sheep (Letts et al., 2016). There has been a high level of consistency between the structures, with the predominant form of supercomplex organisation, the respirasome ($CI_1CIII_2CIV_1$) being solved independently by multiple groups (Guo et al., 2017; Wu et al., 2016; Gu et al., 2016; Letts et al., 2016; Sousa et al., 2016). Additionally, structures were solved for supercomplexes of varying stoichiometries; CI_1CIII_2 (Letts et al., 2016), $CIII_2CIV_1$

(Rathore et al., 2019), and a megacomplex $CI_2CIII_2CIV_2$ albeit at 17.4 Å, that had been previously hypothesised when the respirasome was established. A potential supercomplex of $CI_2CII_2CIII_2CIV_2$ deemed the electron transport chain supercomplex (ETCS), discussed briefly in Section 1.1.4.2, has also been proposed but further investigation is needed to verify the speculative model (Guo et al., 2017). This would be the first structure to verify complex II involvement in a supercomplex.

Interestingly, it has been found that cardiolipin is required for the formation and stability of some supercomplexes (Zhang et al., 2002; Pfeiffer et al., 2003; Schägger, 2002). These findings, in conjunction with EM structures, allow the binding sites of lipids to be characterised within supercomplexes. The importance of CL in the mitochondria inner membrane, particularly in relation to the organisation of the respiratory complexes, is a rapidly developing field. Structural data can can be used to provide further mechanistic understanding of protein: CL interactions. The supercomplex structures also shine light on conformational changes, with some groups finding a 'tight' and 'loose' variation of $CI_1CIII_2CIV_1$ (Letts et al., 2016).

1.1.6.3 Potential roles of supercomplexes

Although providing a plethora of structural information, there is still limited quantifiable evidence of functional benefits of supercomplexes, measured as distinct entities as compared to respiration through individual complexes. Furthermore, as supercomplexes are dynamic entities, the absolute amount of any one species at any given time is very difficult to define. Supercomplex formation has been linked to the assembly and stability of the individual components (Lobo-Jarne and Ugalde, 2018). Functionally, it has been suggested that the supramolecular structure facilitates enhancement of electron flow between complexes due to reduced distance between the electron carriers, ubiquinone and cytochrome c, or due to substrate channelling between associated ETC complexes (Schagger, 2001; Kühlbrandt, 2015; Althoff et al., 2011).

Supercomplex formation was suggested to be important in preventing excess oxygen radical formation. A growing number of studies suggest that ROS levels are correlated with a decrease in supercomplex assembly (Milenkovic et al., 2017; Acín-Pérez and Enríquez, 2014; Maranzana et al., 2013). It has been proposed that a decline in mitochondrial respiratory function with age is connected to a decrease in the amount of supercomplexes (Gómez and Hagen, 2012). In contrast with these findings, but still linked to ROS production, it was found that in rat skeletal muscle the older animals had the highest level of supercomplexes (Lombardi et al., 2009). It was theorised that this could perhaps be due to a mechanism that enhances the catalytic activity of the respirasome, by better channelling of fuels and by preventing ROS generation (Lombardi et al., 2009; Kühlbrandt, 2015; Althoff et al., 2011).

Until relatively recently the fluid-state model was the widely accepted model for ETC organisation in the field of bioenergetics. However, a multitude of evidence now exists supporting the existence of higher order structures, although some scepticism still exists around them having a physiological function. A growing body of research is suggesting supercomplexes, or more specifically the loss of them could be responsible for a range of pathological states (Milenkovic et al., 2017; Jang and Javadov, 2018; Porras and Bai, 2015). These discoveries are particularly interesting when analysing results in this project, and although not fully characterised yet, it is a mechanism to keep in mind.

1.1.7 Assembly subunit of complex I NDUFA11

The focus of the project is a unique accessory subunit of complex I, NDUFA11, also known as B14.7. Nuclear encoded with an acetylated N terminus and no detectable presequence, much of the research pertaining to NDUFA11 was carried out before its structure was solved within complex I in 2016 (Zhu et al., 2016). The structure confirmed the hypothesised protein conformation of a four transmembrane helix (TMH), the four-helix bundle is shown to sit roughly parallel with the TMHs in the middle of the membrane arm of complex I, with a short N terminal helix and a C terminal loop region (Gu et al., 2016), shown in Figure 1.9 (D). Further structural information, provided by the supercomplex structures discussed in Section 1.1.6 (Wu et al., 2016; Gu et al., 2016; Letts et al., 2016; Guo et al., 2017),

positions NDUFA11 at the interface between complex I and III in the respirasome, as shown in Figure 1.9 (B) of the human respirasome (Guo et al., 2017). Within the respirasome, NDUFA11 is found with a CL lipid molecule bound between the THM 'pore like' structure and the arm of complex I (Guo et al., 2017; Wu et al., 2016).

Mammalian NDUFA11 is homologous to complex I subunit 21.3b in *Neurospora crassa* and B14.7 in some plant species. Interestingly, NDUFA11 is also homologous to mitochondrial import protein TIM17 and belongs to the TIMM17-TIMM22-TIMM23 mitochondrial protein translocase family, shown previously in Figure 1.3 (E) (Žárský and Doležal, 2016; Stroud et al., 2016). Indications that NDUFA11 was an important subunit for complex I function came initially in 1992 when studies in *Neurospora crassa* found that disruption of the protein resulted in incomplete assembly of complex I (Nehls et al., 1992). Further interest arose from the presence of a disease-causing mutation discussed in Section 1.1.7.4, which, although the role of NDUFA11 was still not fully characterised provided further evidence that it was important for complex I to function properly (Mimaki et al., 2012; Hoefs et al., 2008).

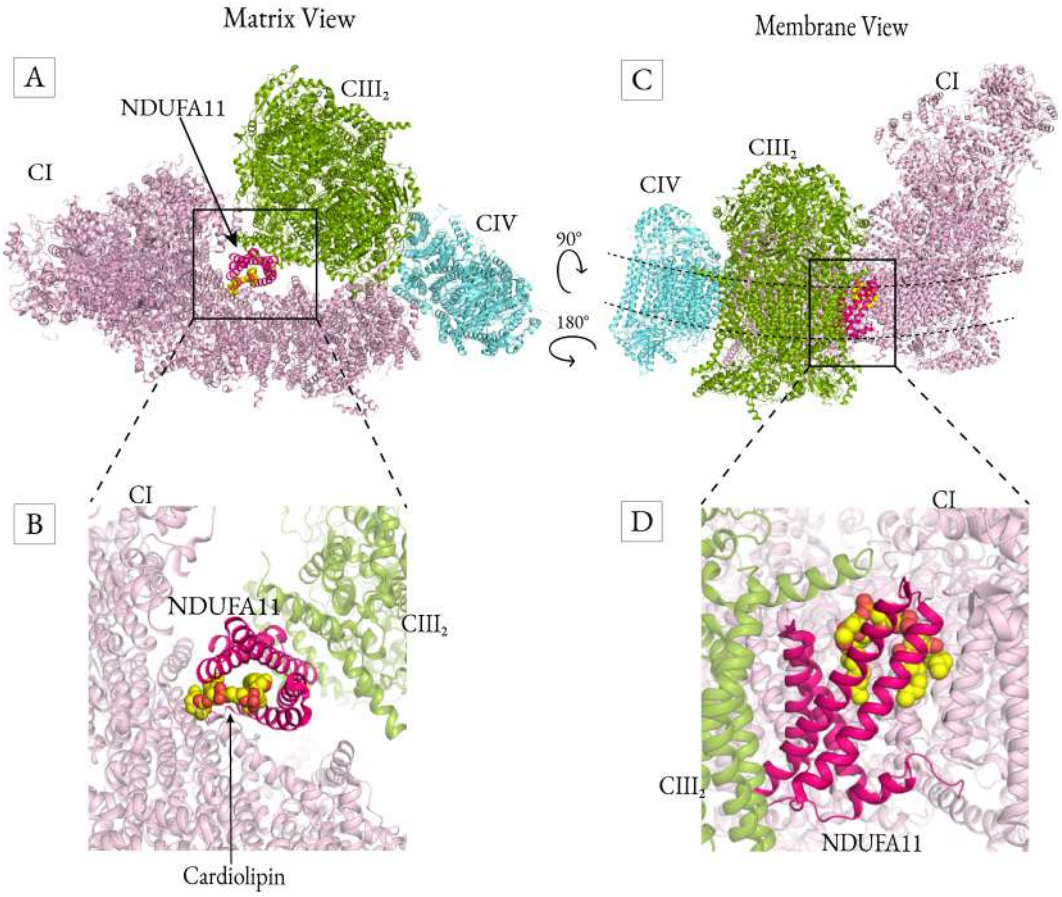

Figure 1.11: Complex I subunit NDUFA11 in the human respirasome - Structure used is 5XTH (Guo et al., 2017). Complex I is shown in light pink, CIII2 in green and CIV in blue. NDUFA11 in hot pink, CL in yellow. (A) shows a matrix view of the whole respirasome, (B) is a zoomed in view as indicated by the boxed area in A with some of the helices surrounding NDUFA11 slabbed away. (C) membrane view of the whole respirasome, rotated 90º and 180º to have the CI arm at the back of the image, (D)is a zoomed in view as indicated by the boxed area in C. Images created in PyMOL.

1.1.7.1 Relationship to the import machinery

The complexes of the mitochondrial electron transport chain and protein translocase machinery have an interlinked relationship. To transport the nuclear-encoded proteins, which includes the majority of OXPHOS subunits, across the inner mitochondrial membrane requires the PMF which is generated by the respiratory complexes themselves (Dudek et al., 2013). Creating a symbiotic scenario where the import machinery is integral in the biogenesis of the ETC, whilst the active assembled complexes are fundamental for the functioning of protein import machinery (Kulawiak et al., 2013). Moreover, several other links have been made between the ETC and the translocase machinery, although the exact roles the interactions perform is not well understood. In yeast a TIM23 complex subunit, Tim21 has been found to interact directly with complex III (Wiedemann et al., 2007; Dienhart and Stuart, 2008) and Tim proteins have also been found associated with complex I.

The role NDUFA11 has in relation to this cooperative system is not currently well understood, but is likely linked to its role as an assembly factor, which is explored in more detail in the next section. In plants, an association between import subunit Tim23–2 and complex I subunit B14.7 (NDUFA11) has been found (Wang et al., 2012). As mentioned previously, NDUFA11 has been established that the mammalian orthologue NDUFA11 belongs to the TIMM17-TIMM22-TIMM23 protein family (Žárský and Doležal, 2016; Stroud et al., 2016), alongside a second complex I assembly factor, TIMMDC1, that belongs in the same family.

1.1.7.2 Role of NDUFA11 within complex I

It was established that NDUFA11 is not a core subunit of complex I, and, as mentioned above, there was evidence from experiments in *Neurospora crassa* that disruption of the NDUFA11 homologue causes incomplete assembly of complex I (Nehls et al., 1992), categorising NDUFA11 relatively early on as a supernumerary or assembly subunit of complex I. The assembly of CI is thought to happen in a series of sub-complexes, or modules, that come together, however the mechanism by which NDUFA11 works within this system to facilitate complex I assembly is not understood. Some studies have found that

NDUFA11 was not able to be definitively associated with a particular assembly module and instead it was suggested it may reside at module interfaces (Stroud et al., 2016). Likewise, in pulse-chase experiments following the steps of assembly for sub-complexes, NDUFA11 was the only subunit unable to be allocated to a stage of assembly and it was stated that it remained unclear at which step it is inserted (Sánchez-Caballero et al., 2016).

Further support of NDUFA11's role as an assembly factor is found from experiments in human cell line 143B, which found that suppressed expression of NDUFA11 disrupted complex I assembly, with the amount of intact complex I being significantly reduced and sub-complexes of 815 and 550 kDa accumulating (Andrews et al., 2013). Further investigation of the suppression found that complex I-linked cellular oxygen consumption was reduced by two-thirds and the mitochondrial network became fragmented. This evidence led the author to suggest that NDUFA11 has the characteristics of an intrinsic assembly factor and that it was required for the assembly and/or potentially the structural integrity of complex I and that NDUFA11, along with other assembly factors participates in the construction of the membrane arm of CI. Furthermore, the association of NDUFA11 with the TIM17 family of import proteins could suggest a potential role for the subunit inserting hydrophobic proteins into the complex I membrane arm (Andrews et al., 2013).

The notion that NDUFA11 could perform a stabilisation role, as well as, or instead of, a role in complex assembly also has evidence to support the idea. Some authors have hypothesised that the subunit has a role anchoring the peripheral arm to the inner membrane (Berger et al., 2008) and that the four TMHs of NDUFA11 support other subunits of complex I and anchor them each other (Zhu et al., 2016). Furthermore, a recent study in 2017 found that NDUFA11 was added to complex I in the final step of assembly, which the authors described as forming a 'lid' covering the TMH which anchors the lateral helix of subunit ND5, concluding that NDUFA11 binds only when others assembly factors have left with the function to stabilise the complex (Guerrero-Castillo et al., 2017). Figure 1.10 highlights the complex I subunits NDUFA11 is in contact with, highlighting and the 'lid' formed across the helix of ND5 in the middle panel and showing the C terminus in contact with ND2, ND4 and NDUFB5 on IMS facing side of the membrane arm in the black box in the bottom panel.

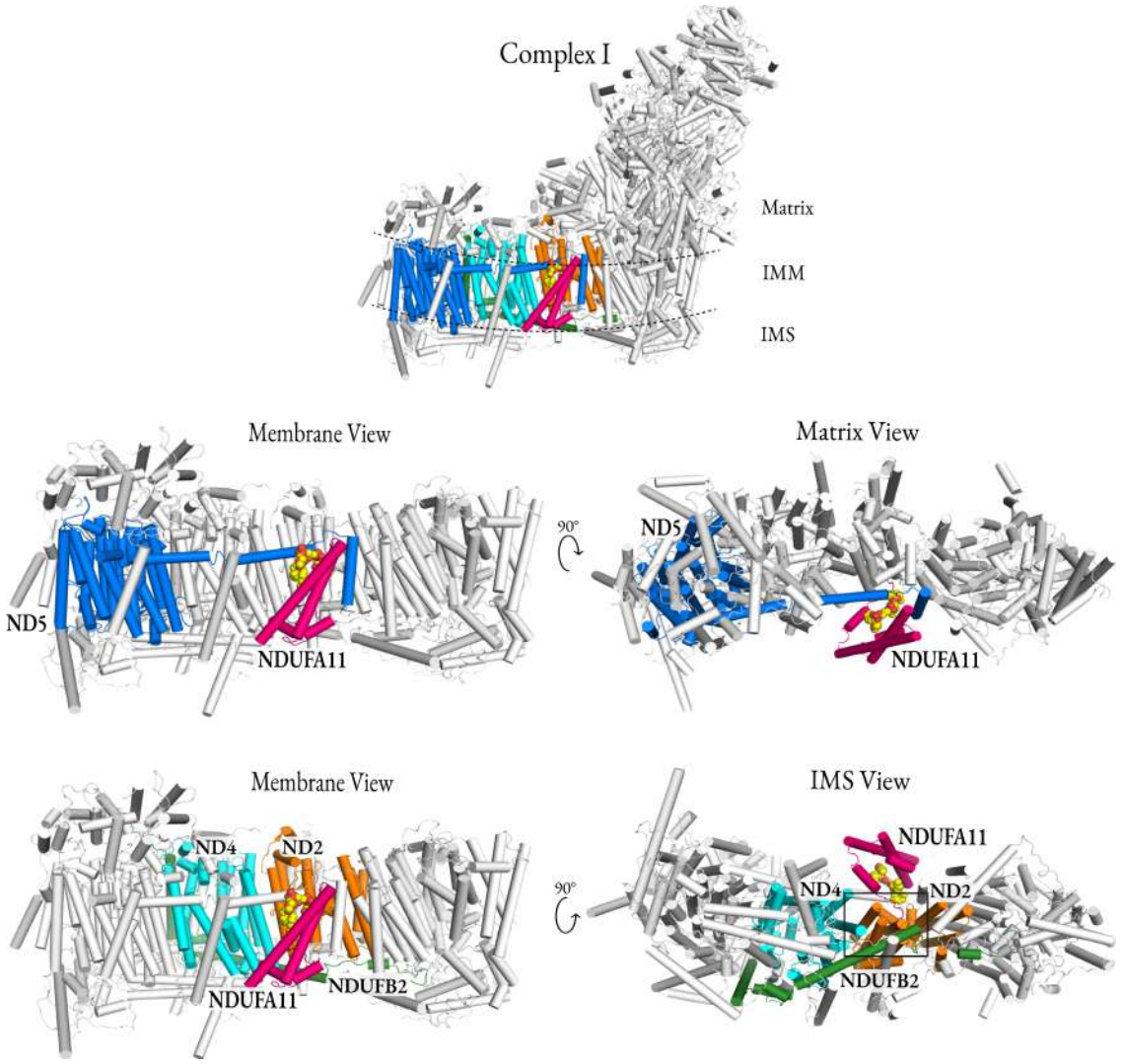

Figure 1.12: NDUFA11 contacts in complex I - Structure used is 5XTH (Guo et al., 2017). **Top panel**: Complex I is shown in white with highlighted subunits NDUFA11 in hot pink, ND5 in marine, ND2 in orange, ND4 in cyan and NDUFB2 in forest green. **Middle panel**: Membrane arm of complex I only, highlighting only NDUFA11 (hot pink) and ND5 (marine), illustrating the contact NDUFA11 makes across the lateral helix of ND5. **Bottom panel**: Illustrating the C terminal region of NDUFA11 (hot pink) making contact with ND2 (orange), ND4 (cyan) and NDUFB2 (forest green). The region is surrounded by a black box. Images created in PyMOL.

In addition to the conjecture that the binding placement of NDUFA11 and the timing of the subunit joining the complex supports a stabilisation function for the protein, the fact that NDUFA11 interacts with a CL molecule should also be taken into consideration. It is generally acknowledged that CL plays a role in stabilisation with integral membrane proteins (such as complex I) (Mileykovskaya and Dowhan, 2014) and more specifically a central role in the formation and stability of supercomplexes (Mileykovskaya and Dowhan, 2014). This is supported by research in mammalian cells where the authors concluded there was evidence that confirmed CL has a direct role in the supramolecular organisation of the mitochondrial ETC (Mileykovskaya and Dowhan, 2014).

1.1.7.3 Structural position in the respirasome

As advances in cryo-EM have facilitated multiple high resolution structures of the respiratory complexes, this has simultaneously provided more structural information in regards to NDUFA11. This provides particular value within the supercomplex setting, as it may elicit potential functions of NDUFA11 that are not possible to observe from a stand alone complex I structure, if in fact the role of NDUFA11 is linked to supercomplex formation. Across all architectures of the respirasome, which were discussed in more detail in Section 1.1.5, there is reported consistency between the position and interactions of NDUFA11 which adds support for the protein playing a functional role in the supramolecular organisation of the ETC.

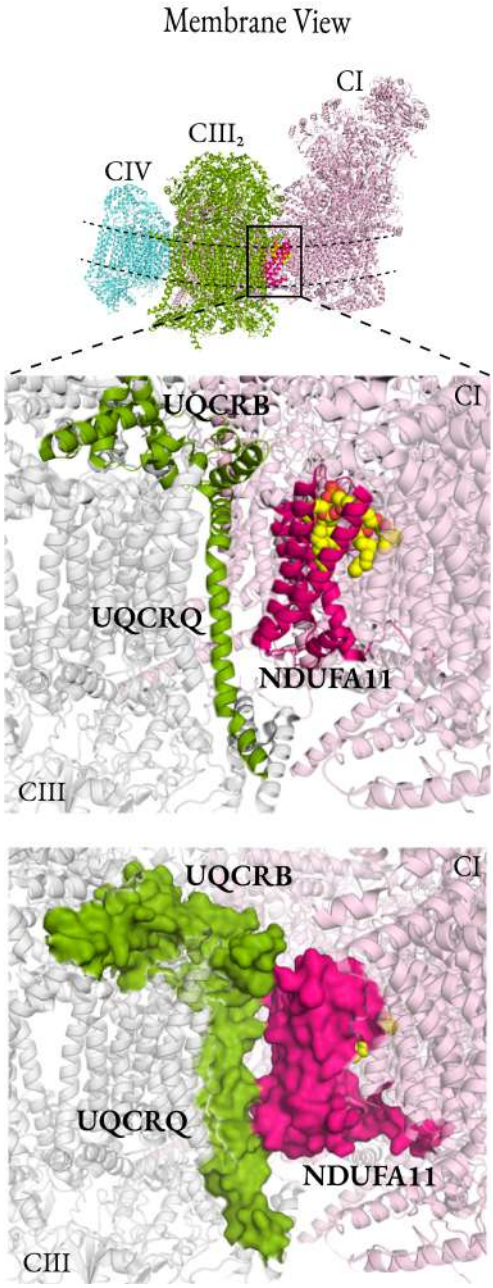

Figure 1.13: NDUFA11 interaction with complex III - Structure used is 5XTH (Guo et al., 2017). **Top panel**: Complex I is shown in light pink, CIII2 in green and CIV in blue. NDUFA11 in hot pink, CL in yellow. **Middle panel**: Exploring the interaction between CI subunit NDUFA11 (hot pink) and CIII subunits UQCRB and UQCRQ (green) in cartoon representation. **Bottom panel**: same orientation as the middle but representing the subunits of interest in the surface view to show potential points of contact between the two. Images created in PyMOL.

Interactions between NDUFA11 and CIII subunits UQCRB and UQCRQ can be seen in Figure 1.13. All analyses in response to the respirasome structures make reference to NDUFA11 in the membrane arm of complex I interacting directly with subunits in complex III, with these interactions being one of nine sites that contribute to the oligomerization of the two complexes (Wu et al., 2016; Gu et al., 2016; Letts et al., 2016; Sousa et al., 2016; Guo et al., 2017), furthermore some authors go as far to say that NDUFA11 clearly plays a major role in the formation and stability of the respirasome (Sousa et al., 2016).

As previously mentioned in relation to the function of NDUFA11 within CI, it has been established that regions of the protein interact with other subunits of CI, namely the HL helix, ND2, ND4 and ND5. When looking within the setting of the respirasome, NDUFA11 also faces the transmembrane region of one monomer of CIII, coming into contact with subunits UQCRB and UQCRQ of CIII (Gu et al., 2016; Letts et al., 2016; Guo et al., 2017). One author suggests that NDUFA11 contributions to CI: CIII stabilisation could be mediated by a combination of direct protein-protein interactions and phospholipid molecule interactions (Wu et al., 2016), specific interactions between NDUFA11 and CL are explored in more detail in section 4.10. Taking into account information from Section 1.1.1.2 on CL and the role it plays in membranes it could play a stabilisation role in the respirasome, potentially mediated by interactions with NDUFA11.

1.1.7.4 NDUFA11 in disease

Impaired cellular respiration can be catastrophic, clinically manifesting in the form of Leigh syndrome, neonatal lactic acidosis, and disorders in the cardiac, renal and hepatic systems. As discussed in Section 1.1.4.1, complex I deficiency is the most common respiratory chain defect, accounting for one third of patients with dysfunctional respiration (Kirby et al., 1999), it also displays an extensive range of defects and clinical heterogeneity due to the size and complexity of the complex (Haack et al., 2012). Of the patients that have complex I deficiency, only 20% were found to have mutations in mtDNA encoded genes, suggesting that the majority of deficiencies are caused by mutations in nuclear encoded subunits (Lebon et al., 2003; McFarland et al., 2004).

NDUFA11 has been found to have two disease variants, with the most recent discovery only published in 2019 (Peverelli et al., 2019). The two disease variants are genetically distinct from each other and manifest with different clinical presentations.

NDUFA11 splice variant

The original NDUFA11 disease variant was detailed by (Berger et al., 2008) and all information presented in this section pertains to this publication. Six patients from three unrelated families were discovered to each hold a splice-site mutation in the NDUFA11 gene, discovered after they presented with either encephalocardiomyopathy or fatal infantile lactic acidemia within the first few months of their lives, which was attributed to a complex I deficiency. NDUFA11 is the first complex I deficiency gene mutant to be associated with fatal infantile lactic acidemia.

The single mutation in NDUFA11 disrupts the splicing efficiency at the exon 1 junction, leading to the expression of two variants of NDUFA11, a wild-type and mutant version, with the mutant version predicted to cause the elimination of the first transmembrane domain of the protein. When analysing patient fibroblasts a ratio of 2:1 wild-type to mutant transcripts was found, suggesting the mutant/wild-type ratio dictates the phenotype, which varies across respective tissues. All six patients were found to be homozygous for the mutation, with immediate members of the families found to be heterozygote carriers of the mutation, but displaying no symptoms. Among a control sample of 52 ethnicity-matched subjects, no carriers of the mutation were detected.

As well as clinically present symptoms, enzymatic activities of the four ETC complexes and ATP synthase were determined from patient samples. Activity of complex I was reduced in all cases, whereas the activities of the other OXPHOS complexes were within the reference range. The authors hypothesised that the gene mutation, which caused a heterogeneous population of NDUFA11 (wild-type and mutant), ultimately led to a complex I deficiency disease state due to destabilisation of complex I.

NDUFA11 missense variant

The second disease variant of NDUFA11, found over ten years after the discovery of the splice mutant described previously, was uncovered in a patient who first presented symptoms at 65 years old and was found to be a compound heterozygote for two novel and rare variants of NDUFA11 (Peverelli et al., 2019).

A genetic screen led to the identification of two gene mutations in NDUFA11, with the two variants being on different alleles. Furthermore, the two variants were only present in the alternative isoform 2 of NDUFA11, with the production of isoform 1 unimpaired. The patient displayed a late onset mild neuromuscular phenotype, with a reduction in muscle complex I activity. This clinical manifestation may be explained by the genotype and overall dominance of NDUFA11 isoform one, explaining the mildness of the symptoms compared to the splice mutant where severe symptoms presented from a young age. Moreover, the muscle specific symptoms of the patient may be due to potential predominant expression of isoform 2 in skeletal muscle tissue.

The discovery of a second NDUFA11 mutant furthers the understanding of the clinical phenotype associated with NDUFA11 deficiency. The emergence of multiple disease variants of NDUFA11 and an understanding of the potentially severe implications it can have on the overall health of a person makes it an important respiratory subunit to investigate. Combining the knowledge of NDUFA11s potential to cause a disease state, along with academic structural and biochemical information available in relation to supercomplex assembly and respiration activity means that further investigation into the subunit could elucidate an explanation of the role NDUFA11 plays within the ETC, and provide a deeper understanding of how loss of the subunit manifests clinically.

1.2 *Caenorhabditis elegans*

Caenorhabditis elegans (*C. elegans*) is a species of free-living nematodes, established in the 1960s as a genetic model organism for understanding questions surrounding developmental biology and neurobiology by Sydney Brenner (Brenner, 1974). They have gone on to become an important organism in studying processes that go awry in human disease (Markaki and Tavernarakis, 2010).

1.2.1 *C. elegans* as a model organism

C. elegans has many attributes that make them an excellent model organism. These features include; a small size with an adult nematode reaching ≈1 mm in length, meaning that a large number of animals can be cultivated in a small space. They have a short life cycle, living on average three weeks but produce a high brood count of roughly 300 progeny. They have a transparent anatomy, so individual components and cells of the animal can easily be visualised under a light microscope (Shen et al., 2018).

The whole *C. elegans* genome was sequenced in 1998 (C. elegans Sequencing Consortium, 1998), at just over 100 million base pairs. Among the available *C. elegans* protein sequences (18,452), it has been suggested that at least 83% of the *C. elegans* proteome has a homologous human counterpart and nematode-specific genes contributing only 11% or less to the *C. elegans* proteome (Lai et al., 2000). In addition, approximately 40% of genes associated with human disease showing homologues in the *C. elegans* genome (Culetto and Sattelle, 2000), making them a suitable model organism for the study of human diseases and ageing. Genetic manipulation has been key in their use as a model organism, with both forward and reverse genetics utilised to address biological problems. Despite a well annotated genome, a number of the genes remain uncharacterised, due to low sequence homology and lack of functional evidence.

1.2.1.1 Animal development

One advantage of *C. elegans* is their short development time, as it allows rapid evaluation of genetic manipulation. The life cycle, Figure 1.14, shows the four larval stages (L1-L4) of development, before the animal enters adulthood after about 2.5 days when grown at 20ºC. The average lifespan of an N2 strain animal grown on non-pathogenic *E. coli* OP50 is 3 weeks, with lifespan being influenced by environmental and genetic factors (Riddle et al., 1997). Each development stage has defining features that allow the current growth stage to be distinguished (Shen et al., 2018).

If environmental factors such as population density, food supply and temperature are not favourable for the organism, a late L1 stage developmental decision to enter dauer arrest stage is taken. Animals in dauer stage undergo morphological changes, such as a dauer-specific cuticle, lack of pharyngeal pumping and a thinner, longer appearance (Golden and Riddle, 1984). They can exist for up to four months, and if environmental factors become more favourable then the animals will continue development from the L4 stage, as shown in Figure 1.14 (Cassada and Russell, 1975). It is also possible for *C. elegans* larvae to reversibly arrest development during the first larval stage (L1) (Baugh, 2013).

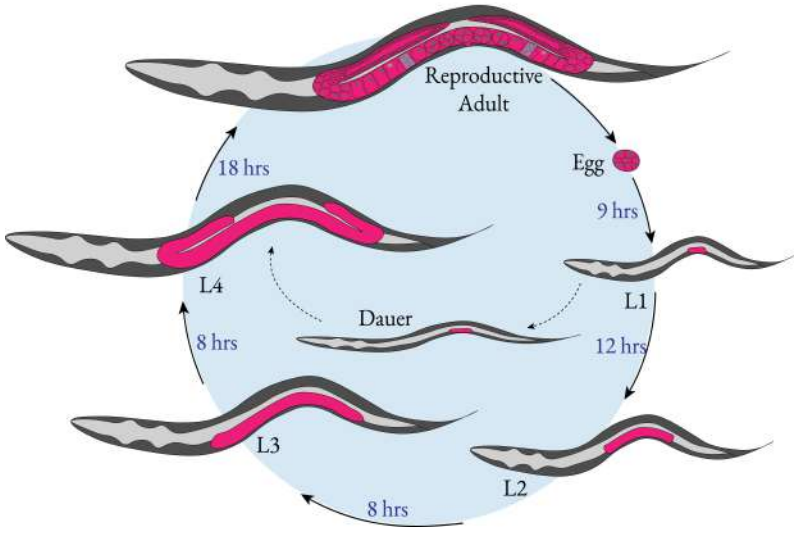

Figure 1.14: Life cycle of *C. elegans* - schematic representation of the life cycle of *C. elegans*, including the four larval stages (L1-L4) into a reproductively capable adult. The hours indicated in blue represent the average time it takes for an animal to develop from one stage to the next, when grown at 20ºC. The developmental decision to enter dauer stage occurs in late L1 stage, it is influenced by environmental parameters such as population density, food supply and temperature (Cassada and Russell, 1975)

C. elegans undergo a metabolic shift, between larval stages L1 and L2. Embryos and L1 larvae generate cellular energy using the glyoxylate cycle, a variation of the TCA cycle, it is an anabolic pathway that is generally assumed to be absent in animals, with the exception of nematodes in the early stages of development (Kondrashov et al., 2006; Wadsworth and Riddle, 1989). As *C. elegans* reach later stages of development, L2 and onwards, energy production shifts to occur preferentially through the TCA cycle, with a corresponding relative increase in TCA cycle activity (Wadsworth and Riddle, 1989). Discussed later in Section 1.2.2, this is an important feature to consider, as L2 arrest has previously been described as a phenotype in mitochondrial defective animals (Navarro-González et al., 2017), and is seen in RNAi animals investigated in this project. A phenotype likely due to the animals not having the functional respiratory machinery to produce sufficient cellular energy when the metabolic shift occurs.

1.2.1.2 Anatomy

An adult hermaphrodite *C. elegans* contains only 959 somatic cells and has a simple anatomy, with the structure of the animal essentially comprises a tube with two smaller tubes contained inside. The outer layer, the cuticle, is formed by an extracellular matrix composed for the most part of small, extensively crosslinked collagen-like proteins (Johnstone, 1994) forming a tough outer covering. Inside the walls of the cuticle, lies the first of the inner tubes containing the pharynx, intestine and rectum, making up the digestive tract of the worm (Kormish et al., 2010).

The second inner component is the reproductive system, which in a adult worm takes up a large majority of its volume. The system can be divided into three major parts; the somatic gonad and germ line which together form two symmetrical U-shaped arms that join to the third part, the egg-laying apparatus (Hubbard and Greenstein, 2000).

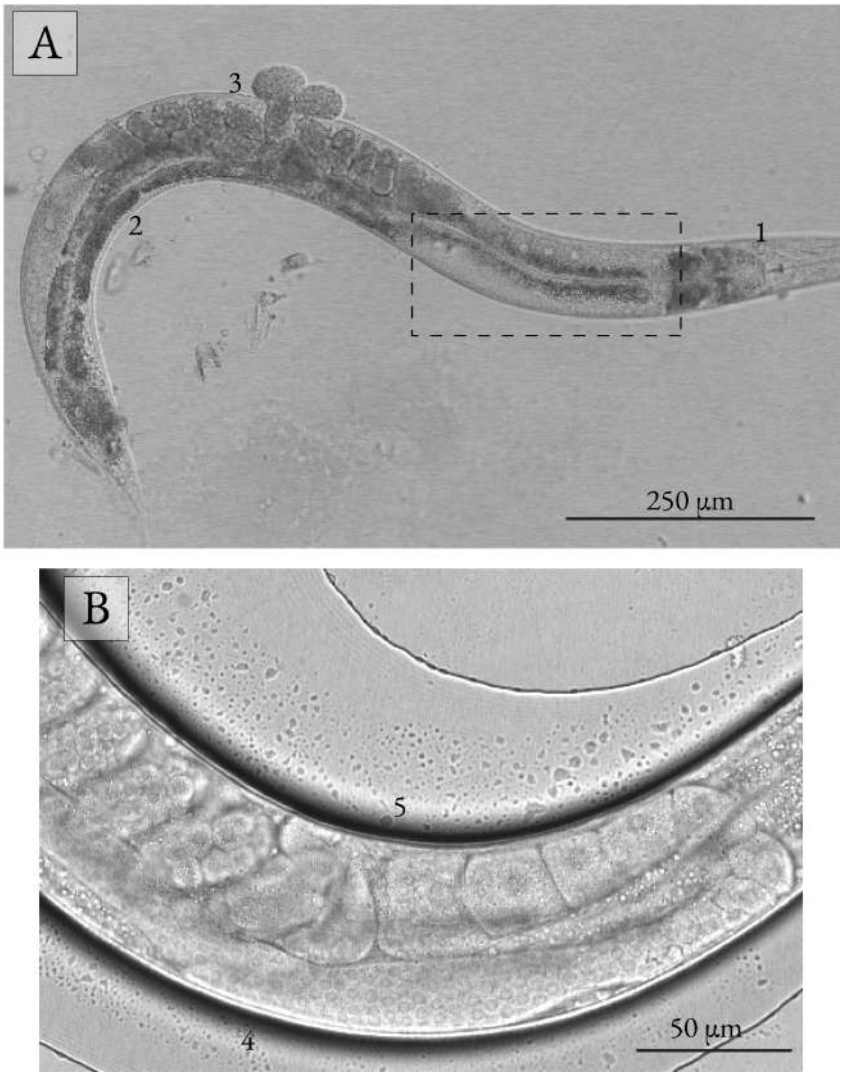

Figure 1.15: Representative image of an adult *C. elegans* - representative brightfield image of an N2 strain adult *C. elegans* animal taken through a **(A)** 20× glycerol immersion objective of whole worm, **(B)** 63× glycerol immersion objective focussing on one arm of the gonad. Two different worms feature in **A** and **B**, with the dashed line in **A** representing the general area shown in **B**. **(A1)** appears next to the pharynx, **(A2)**, the digestive tract, **(A3)** the vulva, **(B4)** the proximal gonad, showing germ line cells **(B5)** the distal gonad, showing developing oocytes, the spermatheca and embryos.

Figure 1.15 (A1) shows the pharynx, a highly active muscular structure, it is a mitochondrial rich area to facilitate a persistent pumping mechanism. The digestive tract can be seen close to (A2), appearing as a comparatively darker tract running the length of the animal and (A3) highlights the vulva, where the two arms of the gonad meet and from which fertilised embryos are laid as eggs. The

dashed line in (A) highlights one arm of the gonad, shown at a higher resolution in (B). Germ line cells can be seen in the distal gonad (B4), round to oocytes on the top of the arm in the promixal gonad (B5), followed by the spermatheca and fertilised embryos (Pazdernik and Schedl, 2013).

1.2.1.3 Genetics

C. elegans exist as either hermaphrodites or males, with hermaphrodites having the ability to either self-reproduce through internal self-fertilisation using their own sperm, features of which discussed above, or they can outcross with males. This means that growing isogenic populations from hermaphrodites is very straight forward, and in addition makes *C. elegans* a favourable organism for carrying out genetic screens. When required, matings with males can be used to obtain genetic crosses (Bahrami and Zhang, 2013). Males are found at low frequencies, about 0.1%, compared to hermaphrodites (Brenner, 1974). However, this number increases when if the progeny are from a male hermaphrodite mating.

1.2.2 *C. elegans* as a tool for mitochondrial research

C. elegans provide a multi-cellular, genetically tractable organism to study the mitochondrial respiratory chain, allowing analysis of mitochondria dysfunction on a whole animal and biochemical level. Other model organism systems have either been found to be unsuitable, or do not provide as advantageous system as *C. elegans*. Bacterial systems, such as *E. coli* do not contain mitochondria. In yeast, *S. cerevisiae*, the mitochondria do not have complex I. Human cell culture clearly provides the most direct way to study human genes, however, observations found often have limited application on a single cell system. On the other hand, a mouse model *M. musculus*, although evolutionary closer to humans and able to provide whole animal physiology, genetic manipulation is expensive and time consuming. Overall, *C. elegans* provides a balance between organismal complexity, able to provide a wide range of biological data, and ease of experimental workability, as they can be easily genetically manipulated on a large scale of animals.

1.2.2.1 Homology to the mammalian system

In addition to the general advantages of using *C. elegans* as a model organism, they share a significantly high percentage of homologous proteins with the mammalian ETC, specifically 84% in complex I (Falk et al., 2009), including all 14 core subunits. Using Wormbase, which provides information concerning the genetics, genomics and biology of *C. elegans*, and a protein abundance database, PaxDb (Wang et al., 2012), the current standings of *C. elegans* homologues of human mammalian proteins was established, summarised in Table 1.2.

ETC complex	Number of mammalian subunits	Number of homologous *C. elegans* subunits
Complex I	44	37
Complex II	4	4
Complex III	11	11
Complex IV	19	10
ATP synthase	20	13

Table 1.2: Mammalian OXPHOS subunits and *C. elegans* homologues - Each electron transport chain complex and ATP synthase detailed by the number of mammalian subunits, as determined by the National Human Genome Research Institute. Accompanied by the number of homologous subunits that are found in *C. elegans*, as determined by Wormbase and PaxDb (Wang et al., 2012). For this table, *C. elegans* protein B0491.5 has not been included as a homologue, as it is not yet recorded as such on *C. elegans* databases, although its homology to complex I NDUFA11 is outlined in this project.

It can be seen from Table 1.2 that *C. elegans* provides a highly homologous system to investigate the mitochondrial OXPHOS machinery. Many of the intermediary pathways of metabolism, such as the Krebs cycle, which has homologous proteins for every enzyme, are also conserved in *C. elegans* (O'Riordan and Burnell, 1989). Furthermore, within the respirasome ($CI_1CIII_2CIV_1$), sequence alignments of the binding motifs of proteins at the CI: CIII contact site, NDUFA11, NDUFB9 and UQCRC1, mentioned previously in Section 1.1.7.3, are highly conserved across species. This indicates

that the organisation of the ETC is likely to be highly conserved, and investigations in *C. elegans* may be able to elucidate understanding of the mammalian system (Gu et al., 2016).

1.2.2.2 Mitochondrial studies in *C. elegans*

C. elegans have already been established as a model organism to investigate a wide range of mitochondrial processes, particularly human mitochondrial-associated diseases. Studies have looked at ageing (Harman, 1972; Miquel et al., 1980; Kenyon, 2010), lifespan extension, (Van Raamsdonk et al., 2010; Butler et al., 2010; Dingley et al., 2010; Cho et al., 2011; Rea et al., 2007) and neurodegeneration (Maglioni and Ventura, 2016; Lin and Beal, 2006; Cho et al., 2010).

Ageing

The first mitochondrial theory of ageing was proposed by Denham Harman (Harman, 1972), suggesting that a maximum life span of a given mammalian species is largely influenced by the rate of oxygen consumption, linked to the rate of accumulation of mitochondrial damage produced by ROS, which ultimately causes death. This theory was reformulated (Miquel et al., 1980), presenting the "oxygen radical-mitochondrial injury hypothesis of ageing" which implicates mitochondria as the central target of radicals damage. It is suggested that mutations which disturb mitochondrial function could impact ageing, either by affecting the production of ROS or the antioxidant machinery that scavenges it. Furthermore, as the mtDNA is in close proximity to sources of ROS, this leaves it particularly vulnerable to ROS-mediated mutations (Maglioni and Ventura, 2016).

Lifespan extension

Despite mitochondria being essential elements of the cell, carrying out the critical function of OXPHOS, it has surprisingly been shown that partial mitochondrial respiration impairment has been shown to promote longevity in some organisms. Studies carried out in yeast, *C. elegans*, *Drosophila*

and mice have all shown increases in lifespan, with authors suggesting that diminished mitochondrial respiration, ultimately leads to a lower production of ROS which may be responsible for the extension of lifespan (Van Raamsdonk et al., 2010; Butler et al., 2010; Dingley et al., 2010; Cho et al., 2011; Rea et al., 2007; Hwang et al., 2012; Rea et al., 2007).

These findings suggest a lifespan extension is found with mild respiration impairment. Considering the studies above, that suggest age related decline may be attributed to ROS mediated damage, along with previous findings, discussed in Section 1.1.5.3, which suggests a 'mild uncoupling' can decrease ROS production, through reducing the membrane potential. This may suggest that the mild impairment of respiration discussed in this section, leads to a reduction in membrane potential, which in turn reduces ROS production and, as ROS has been attributed to aging, this reduction causes the lifespan extension.

1.3 Hypothesis and aims of the project

The existence of mitochondrial respiratory supramolecular structures has been reviewed in the introduction. The most extensively analysed mitochondrial supramolecular structure is the respirasome, which is composed of $CI_1CIII_2CIV_1$. Evidence supporting the composition of supercomplexes is based on structural data, which shows subunit conservation across multiple species. However, little is understood with certainty about the functional role of supercomplexes. It has been proposed that inter-complex interactions may be required to support the normal function of some respiratory complexes. Disruption within one of the complexes could further lead to the disruption of the larger respirasome supercomplex. A number of disease states are associated with the disruption of individual complexes, most commonly, complex I deficiency, which presents as a range of symptoms caused by leukodystrophy. It remains to be resolved whether a decrease in the activity of complex I alone is responsible for these symptoms, or whether disruption of supercomplex assembly is of greater significance in causing disease.

This project investigates how an integral accessory subunit of complex I, NDUFA11, affects mitochondrial complex I activity and supercomplex assembly. NDUFA11 has been proposed to participate in either the assembly or stabilisation of complex I. A reduction in NDUFA11 activity has been shown to decrease the amount of intact complex I, which results in a complex I deficiency disease state, as described in Sections 1.1.4.1 and 1.1.7.4. Within the respirasome structure, NDUFA11 makes contact with CIII subunits, suggesting a stabilisation role. To better understand how NDUFA11 might control and regulate mitochondrial function, I sought to analyse its activity in the genetically tractable model organism *C. elegans*.

Aim 1: To identify the *C. elegans* homologue of NDUFA11, allowing investigation of NDUFA11 in a genetically tractable model organism system with strong homology to the mammalian system, able to facilitate analyses on a whole animal and biochemical level. This aim is addressed in first results chapter, which provides bioinformatic data, supported by proteomic and computational evidence, of the homologous relationship.

Aim 2: To explore how a reduction in the activity of the *C. elegans* NDUFA11 homologue affects whole organism physiology. To address the second aim, the second results chapter utilises the *C. elegans* genetic toolkit, to explore partial and full loss of of the NDUFA11 homologue. Characterising the impact on organism lifespan, reproductive capabilities and developmental changes.

Aim 3: To confirm the existence of, and to characterise the composition of *C. elegans* mitochondrial respiratory complexes and supercomplexes. To understand the wild-type organisation of the respiratory chain, to be able to identify changes that occur with reduction of the NDUFA11 homologue. The first results chapter addresses this aim, using native protein separation techniques to establish the organisation of the respiratory complexes, including the existence of supercomplexes in wild type *C. elegans* mitochondria.

Aim 4: To examine how a reduction in the activity of the *C. elegans* NDUFA11 homologue affects mitochondrial organisation and function. This aim is addressed in both the second and third results chapters. Changes in the respiratory complex organisation are looked at with native protein separation, followed by proteome wide analysis of changes in protein expression. To understand how respiratory complex organisation influences mitochondrial physiology, oxygen consumption, membrane potential and ROS production assays were carried out. To explore the subsequent effect on mitochondrial morphology, in networks and on internal structure, imaging with mitochondrially targeted GFP, as well as electron microscopy techniques.

Underpinning all the results were techniques used to carry out the investigations. The technical developments chapter, presented first, outlines optimisation of the isolation of *C. elegans* mitochondria, crucial for all biochemical analysis. The chapter also covers development of RNAi techniques utilised in results chapters two and three, as the method of investigating loss of respiratory subunit. The final technique developed was BN PAGE, used to investigate complex organisation in results chapters one and two.

Chapter 2

Materials and Methods

2.1 Strains and plasmids

C. elegans strain Bristol N2 were used as the standard wild-type strain, from our laboratory collection. Transgenic strain SJ4103 (zcIs14 [*myo-3*::GFP(mit)]) carries a mitochondrially targetted GFP, under the control of a *myo-3* muscle promoter (used in Section 6.3, Figure 6.4). Transgenic strain CGC43 *unc-4*(e120)/*mnC1* [*dpy-10*(e128) *unc-52*(e444) umnIs32] II, used for balancing the CRISPR *b0491.5* knockout strain (used in Section 5.2.3). Both SJ4103 and CGC43 strains were provided by the Caenorhabditis Genetics Center (CGC) (University of Minnesota). CRISPR strain Δ*b0491.5* was made by Patty Kuwabara, used for this project from our laboratory collection (used in Section 5.2, Figures 5.1-5.5).

Bacterial strains used in worm maintenance and culturing included, *E. coli* strain OP50, used when culturing animals on NGM plate. OP50 is a uracil auxotroph, and NGM media is uracil-limited, preventing the bacterial lawn from overgrowing. The prototroph *E. coli* strain NA22 was used when growing worms in liquid culture. For RNAi experiments (used in Section 5.3 and then throughout), *E. coli* strain HT115 was used. All strains were from our laboratory collection.

2.2 Antibodies

The following antibodies were purchased from Abcam (Cambridge, United Kingdom). Complex I, anti-NDUFS3 antibody [17D95] (ab14711) and ATP synthase, anti-ATP5A antibody [15H4C4] (ab14748), used at a dilution of 1:1000. A custom antibody to B0491.5 was purchased from Cambridge Research Biochemicals (Billingham, United Kingdom), raised against a peptide from the N-terminal region of the protein sequence, used at a dilution of 1:500.

Fluorescent secondary antibodies (anti-mouse and anti-rabbit) were purchased from ThermoFisher Scientific (Waltham, Massachusetts, United States. HRP conjugated secondary antibodies (anti-mouse and anti-rabbit) were from our laboratory collection. All secondaries were used at a dilution of 1:10 000.

2.3 Chemicals and detergents

Digitonin was purchased from Millipore Sigma (Burlington, Massachusetts, United States) and Triton X-100 from Sigma-Aldrich (St. Louis, Missouri, United States). Gels for SDS-PAGE, BN-PAGE and 2D-PAGE were pre-cast, and purchased from ThermoFisher Scientific (Waltham, Massachusetts, United States), as were all of the equipment and reagents for immunoblotting. Unless otherwise stated all reagents were purchased from ThermoFisher Scientific (Waltham, Massachusetts, United States).

2.4 *C. elegans* methods

2.4.1 *C. elegans* maintenance

C. elegans were cultured at 20ºC, maintained by *C. elegans* methods previously described (Brenner, 1974), on 60 mm tissue culture plates. Worms were grown on NGM plates (Appendix I) seeded with *E. coli* OP50 as a food source. The plates were seeded with OP50 bacteria, then incubated overnight at 37ºC (stationary). Plates stored at 4ºC until use.

C. elegans stocks were maintained by either transferring ≈ten gravid adults to a fresh OP50 NGM plate, or, by chunking a section of agar and placing it onto a new OP50 NGM plate, allowing the worms to crawl out onto the fresh lawn of *E. coli*. When required, worms were transferred using a worm pick, a thin platinum wire fused to a glass Pasteur pipette.

2.4.2 Liquid culture

C. elegans were cultured in liquid medium when large quantities were required, rather than on plates as previously described in Section 2.5.1. Within this project, liquid culture preparations were used when growing gravid adults for bleaching to obtain a large number of synchronised L1 animals, and for growing adults for mitochondrial isolation.

For every 0.5 L of *C. elegans* liquid culture, a 1 L preparation of NA22 *E. coli* bacteria was grown as a food source. 1 L of 2xYT (Appendix I) was inoculated with 1 mL of NA22 bacteria and grown in 2 L Erlenmeyer flask overnight at 37ºC. Centrifuge pots were sterilised with a 20 minute incubation with 1:49 diluted bleach, followed by thorough washing with ultrapure water. The NA22 bacteria was centrifuged at 4000 rpm for 15 minutes to pellet, and the supernatent discarded, the pellet was then re-suspended in S-basal complete medium (Appendix I).

Worms were grown on NGM plates so that all bacteria had been depleted and a semi-synchronised population of L1 worms populated the plate, requiring five NGM plates per 0.5 L liquid culture. Worms were harvested from the plates using M9 (Appendix I) and added to the culture of NA22 bacteria and S-basal complete medium. Cultures were incubated at 20ºC, 200 rpm for three days to achieve adults.

To harvest the worms, the liquid culture was transferred to a measuring cylinder and incubated at 4ºC for one hour. The worms sank to the bottom of the cylinder, and the medium was aspirated. The last 100 mL, so to not risk aspirating the worms, was poured into two 50 mL Falcon tubes and centrifuged at 1200 rpm for 2 minutes. The remaining medium was then aspirated off, followed by

washing the worm pellet with M9 media, 3x. ≈5 mL of adult worms was obtained from a 0.5 L liquid culture.

2.4.3 RNA interference

The RNA interference (RNAi) technique used throughout this project was RNAi by feeding (Timmons and Fire, 1998). The RNAi clone for *b0491.5* was obtained from our laboratory collection, originally from the Ahringer *C. elegans* RNAi feeding library purchased from Source Bioscience (Nottingham, United Kingdom). *E. coli* strain HT115 (DE3), which is RNase III-deficient and carries an IPTG-inducible T7-polymerase was used, either transformed with the L4440 vector containing the *b0491.5* clone, or transformed with the "empty" L4440 RNAi vector, as a control.

2.4.4 RNAi feeding on NGM plates

For delivering RNAi on NGM plates, as used in Section 5.3 Figures 5.6-5.8, for characterising *b0491.5* RNAi. LB media supplemented with ampicillin (100 μg/mL) (Appendix I) + tetracycline (12 μg/mL) (Appendix I) was inoculated with a single colony of HT115 bacteria and grown at 37ºC overnight. NGM plates containing ampicillin (100 μg/mL) and IPTG (0.4 mM) (Appendix I) were then incubated overnight at room temperature, during which time the double-stranded RNA would be expressed.

Eggs were harvested from N2 OP50 fed worms by bleaching (see Section 2.4.6) and allowed to hatch overnight in M9 medium (in the absence of food). The synchronised L1 larvae were then transferred to the NGM plates expressing double-stranded RNAi, and grown to adulthood, to be used as required. If plates became contaminated, worms would need to be transferred to fresh NGM RNAi plates.

2.4.4.1 RNAi feeding in large scale liquid culture

To RNAi suppress large volumes of worms, as required for mitochondrial isolation, it was necessary to use the medium of liquid culture to deliver the HT115 RNAi bacteria for feeding. This technique was developed in Section 3.3, and for a schematic overview see Figure 3.6. The protocol spanned nine days for the *b0491.5(RNAi)* condition, and eight days for the control, detailed here is the method used to culture both conditions side by side, in preparation for isolating the mitochondria from both conditions on the same day.

Day 1: A 0.5 L liquid culture of N2 worms fed on NA22 bacteria was set up (see Section 2.4.2). **Day 2**: A second 0.5 L liquid culture of N2 worms fed on NA22 bacteria was set up (see Section 2.4.2). **Day 4**: Gravid adult worms were harvested from the Day 1 culture, and subjected to alkaline hypochlorite treatment (see Section 2.4.6). The eggs were allowed to hatch overnight in M9. Pre-cultures of *b0491.5(RNAi)* bacteria were set up by inoculating 2x 250 mL of LB media with a single colony of HT115 *b0491.5(RNAi)*, incubated overnight at 37ºC, 180 rpm. **Day 5 (part 1)**: Gravid adult worms were harvested from the Day 2 culture, and treated as in Day 4. Pre-cultures of empty vector control RNAi bacteria were set up as per the cultures in Day 4.

Day 5 (part 2): 4 L of 2xYT media, supplemented with ampicillin (100 μg/mL) is inoculated with the *b0491.5(RNAi)* pre-cultures from Day 4. The cultures are grown at 37ºC until to OD_{600} 0.4, then induced with 0.4 mM IPTG and incubated for a further 2 hours. Centrifuge pots were sterilised with a 20 minute incubation with 1:49 diluted bleach, followed by thorough washing with ultrapure water. Bacteria was harvested by centrifugation at 5000 rpm for 20 minutes at 4ºC. The supernatent was discarded, and the pellet re-suspended in S-basal complete medium, supplemented with ampicillin (100 μg/mL) and IPTG (0.4 mM). The eggs from Day 4 are now starved L1 larvae, which are roughly counted at $\approx$1 million are added to the medium in a 5 L Erlenmeyer flask. Worms are incubated at 20ºC, 200 rpm, for four days.

Day 6: 4 L of 2xYT media, supplemented with ampicillin (100 μg/mL) is inoculated with control RNAi pre-cultures from Day 5 and treated as per Day 5 (part 2). The eggs from Day 5 (part 1) are now

starved L1 larvae, and cultures are set up as per Day 5 (part 2), and grown for three days. **Day 9**: Both cultures are ready for mitochondrial isolation.

2.4.5 Worm matings

As detailed in Section 5.2, including a schematic overview in Figure 5.3, it was required to balance the CRISPR *b0491.5* deletion strain with strain *mnC1*. To generate large quantities of N2 males, two hermaphrodite N2 worms were set up with ten male N2 worms from the laboratory stock, generating a high number of males in the brood. These N2 males were then mated with *mnC1*/+ worms in the same format, and *mnC1*/+ males identified by the GFP marker. These *mnC1*/+ males were then set up in a third mating with Δ*b0491.5*/+ worms, as determined post mating by single worm PCR. The progeny were screened by GFP signal and single worm PCR to validate the balancing.

2.4.6 Alkaline hypochlorite treatment

Alkaline hypochlorite treatment (bleaching) was used to harvest eggs from gravid adults that had been grown in liquid culture (see Section 2.4.2). Adult worms were harvested from the liquid culture as per Section 2.4.2 and re-suspended in 10 mL H_2O per 2 mL of worms in a 50 mL Falcon tube. An equal volume of alkaline hypochlorite solution (Appendix I) was added. The worms were incubated in the solution for four minutes with constant inversion. Then checked under a light microscope for signs of breakage, if the majority showed signs of breaking open the process would be stopped, if not, the incubation time was extended for one more minute. After this extra minute the process was stopped, as excessive time in bleach harms the viability of the eggs.

The Falcon tube was topped up to 50 mL with M9 solution, to dilute the bleach. The samples were centrifuged for 1 minute at 1500 rpm, the supernatant taken off and egg pellet re-suspended in M9. The washing step was repeated 3x. The eggs were re-suspended in 10 mL M9 and transferred onto two 9 cm unseeded NGM plates, where they were incubated overnight, with gentle rocking. Synchronised, starved L1 larvae were be ready in the morning.

2.4.7 Brood count

A brood count of *b0491.5(RNAi)* and the control was carried out as part of characterisation of the *b0491.5(RNAi)* (Section 5.3, Figure 5.7). RNAi feeding was set up on plates as described in Section 2.4.4, with synchronised N2 L1 larvae, on either control or *b0491.5(RNAi)* bacteria. Worms were grown to L4 larval stage and then plated onto single NGM RNAi plates, before any progeny had been laid. Once egg laying began, worms were moved every 12 hours onto fresh RNAi plates. Progeny were counted in triplicate.

2.4.8 Lifespan

A lifespan assay for *b0491.5(RNAi)* and the control was carried out as part of characterisation of the *b0491.5(RNAi)* (Section 5.3, Figure 5.7). The lifespan assays were performed as previously described (Lithgow et al., 1995), with the addition of 80 μL of 0.2 mM (+)-5-fluorodeoxyuridine (FUdR) to the plates used during the reproductive phase. RNAi was introduced to worms at the old L4 larvae stage and carried out at 20ºC. Day 1 was counted as the first day of adulthood in the survival curves. Animals were scored on every other day (alive, dead or lost) using tactile stimulation. Once animals did not move in response to touching, they were scored as dead. Animals that were lost due to escape up the side of the plate or foraging were not included in the analysis, neither were worms that displayed vulval rupture, as in accordance with (Chen et al., 2007).

2.4.9 Sucrose flotation

Sucrose flotation was used in this project to clean worms prior to mitochondrial isolation, this step is included in the schematic in Figure 3.4. The worm pellet, harvested from a liquid culture, was re-suspended in 25 mL of cold M9. To that 25 mL of ice cold 60% sucrose was added and the solution inverted, followed by a centrifugation step at 2000 rpm for 5 minutes. From this the worms sat as a distinct phase, on top of the sucrose solution, with bacteria pelleted at the bottom. The top worm layer was poured off into a new 50 mL Falcon and topped up with cold M9, followed by centrifugation at 1500 rpm for 5 minutes. The supernatant was removed and the worms re-suspend in M9 and centrifuged at 1500 rpm for 2 minutes. The M9 wash step was repeated twice.

2.5 Single-worm polymerase chain reaction

Single worm (SW) polymerase chain reaction (PCR) was used to identify worms that were Δ*b0491.5* positive (Section 5.2, Figures 5.4, 5.5). A single worm was picked into a PCR tube containing 2.5 μL of single worm lysis buffer (Appendix I). The samples were either stored at -80ºC or immediately incubated at 60ºC for 1 h (lysis) followed by 95ºC 20 minutes (to deactivate the proteinase K).

PCR reaction reagents; 5x GoTaq buffer (Promega, Southampton, United Kingdom), 0.2 μM forward and reverse primers as indicated in Table 2.1, 0.2 mM dNTP, 0.62 U GoTaq enzyme (Promega, Southampton, United Kingdom) and H_2O to a total volume of 22.5 μL, were made up and added directly the worm lysis mix. The cycling conditions used were: 95ºC for 3 minutes; [95ºC for 40 seconds, 58ºC for 40 seconds, 72ºC for 1 minute] x 35 cycles; 72ºC for 10 minutes.

Primer	Sequence
Forward *b0491.5* screening primer	GGACGAAGTATGCGCTAAC
Reverse *b0491.5* screening primer	CAGCTCTCCTGGCTGATC

Table 2.1: Screening primers for *b0491.5* - the forward and reverse primers used in SW PCR to screen for Δ*b0491.5*

2.6 Mitochondrial isolation

A large proportion of the data collected in this project involved the isolation of mitochondria from *C. elegans* for analysis. This technique was developed in Section 3.2, and for a schematic overview see Figure 3.4. For isolation of wild-type N2 mitochondria, worms were grown in accordance to Section 2.4.2 and for isolation of RNAi mitochondria, worms were grown in accordance to Section 2.4.4.1. Adult worms were harvested for isolation, from the liquid culture as per Section 2.4.2. For the RNAi experiments, this method was carried out in parallel for both conditions. All steps were carried out

in the cold room or on ice.

The worms were cleaned by sucrose flotation, as per Section 2.5.4. After flotation the M9 was poured off and a worm pellet of 7.5 - 10 mL remained. This pellet was re-suspended in collagenase buffer (Appendix I), using 1U collagenase per 1 mL of worms, therefore a 1:1 ratio of worm pellet to collagenase buffer. The worms were gently agitated for 2 h at 20ºC, after which the collagenase was diluted out with basic STEG/M buffer (Appendix I), using rounds of centrifugation at 1200 rpm for 2 minutes and discarding of the supernatent.

Once the worms are fully exchanged out of the collagenase buffer, the final supernatent was removed and the worm pellet was then re-suspended in 10 mL of (+)STEG/M buffer (Appendix I). A fitted glass/Teflon power-driven Potter-Elvejhem homogeniser was used to carry out 30 strokes of homogenisation. An additional 10 mL of (+)STEG/M buffer was added and 10 more homogenisation stokes were carried out. The homogenate was centrifuged at 750 x g for 15 minutes at 4ºC on either Sorvall RC-6 Plus or Sorvall Evolution RC, SS-34 rotor, (ThermoFisher Scientific, Waltham, Massachusetts, United States) and the supernatent transferred to a new tube. The homogenisation and centrifugation step was then repeated for the pellet.

The resulting supernatent was then spun at 12'000 x g for 15 minutes at 4ºC. The pellet was re-suspended in 15 mL of basic STEG/M buffer, followed by centrifugation at 750 x g for 15 minutes at 4ºC. Again, with the resulting supernatent was then spun at 12'000 x g for 15 minutes at 4ºC. The supernatent was poured off and the pellet (isolated mitochondria) re-suspended in 150 μL of basic STEG/M buffer. The concentration of the mitochondria was then estimated (Section 2.6.1) and samples were then either used for physiology assays or frozen down immediately and stored at -80ºC.

2.6.1 Protein concentration estimations

Protein quantification assays, based on the use of bicinchoninic acid (BCA), were carried out following the manufacturer's instructions (Pierce™ BCA Protein Assay Kit, ThermoFisher Scientific, Waltham,

Massachusetts, United States). 5 μL of BSA standards or 1:50 diluted mitochondrial preparations were measured in triplicate. The BSA reagent was prepared with the ratio 50:1 or reagent A:B and added to each sample (100 μL). Samples were incubated at 37ºC for 30 minutes and the absorbance was read using a NanoDrop using the colour metrics function. A standard curve was calculated using the BSA standards and the concentration of the mitochondrial isolation determined.

2.7 Mitochondrial physiology

Mitochondrial physiology experiments, O_2 consumption, membrane potential and ROS production, were used to assess the respiratory function of *b0491.5(RNAi)* with isolated mitochondria (isolation protocol detailed in Section 2.6, physiology experiments in Section 6.2, Figure 6.1-6.3).

2.7.1 O_2 consumption

Oxygen consumption was measured by high-resolution respirometry on a Clark-type oxygen electrode (Oroboros O2k Series D). Mitochondria were suspended at a concentration of 0.25 mg/mL in KCl based respiration medium (Appendix I). Samples were kept at a constant 25ºC while in the chamber, and energisation was achieved with either 10 mM malate/5 mM pyruvate (complex I-linked respiration) or 5 mM succinate in the presence of 1 μM rotenone (complex II-linked respiration). State 3, coupled respiration was investigated with the addition of 1 mM ADP. Outer membrane integrity was investigated by the addition of 10 μM cytochrome c and ATP synthase was inhibited with 1 μM oligomycin to induce a pseudo-state 4 respiration. These parameters were influenced by a protocol from previously published respiration experiments in *C. elegans* (Wojtovich et al., 2008) as well as by standard protocols used in our laboratory.

Parameters associated with phosphorylation, such as oxidation rates and the RCR were determined according to classical techniques (Chance and Williams, 1956, 1955). In brief, the addition of ADP results in an increase of substrates oxidation rates, once ADP is phosphorylated to ATP, this ceases. The RCR the ratio between state 3 respiration, measured as maximal ATP synthesis, and state

4 respiration, in absence of ATP synthesis. In addition, the RCR provides an indication of the control efficiency exercised by phosphorylation on oxidation (Chance and Williams, 1956, 1955).

2.7.2 Membrane potential

Membrane potential assays were carried out with Tetramethylrhodamine Methyl Ester Perchlorate (TMRM) (Sigma-Aldrich), a cationic, cell permeable, red-orange fluorescent dye, that is sequestered by active mitochondria, based on of established protocols (Scaduto and Grotyohann, 1999). Assays were carried out using a Varian Cary 50 UV-Vis Spectrophotometer (Agilent Technologies, Santa Clara, California, United States), with manual mixing. The results were collected in quench mode, therefore a lower membrane potential is represented by a higher fluorescence. Mitochondria at a concentration of 0.25 mg/mL were added to a 2 mL cuvette in KCl based respiration medium (Appendix I), pre-incubated with either 10 mM malate/5 mM pyruvate (complex I-linked respiration) or 5 mM succinate in the presence of 1 μM rotenone (complex II-linked respiration) (State 2 respiration). Substrates were sequentially added as follows; coupled respiration was stimulated with the addition of 1 mM ADP (state 3 respiration), ATP synthase was inhibited with 1 μM oligomycin. Maximum depolarisation was achieved using 1 μM CCCP and 10 μM antimycin A.

2.7.3 ROS production

ROS production assays were carried out with Amplex red (Thermofisher), a sensitive and stable probe for H_2O_2, based on of established protocols (Wang et al., 2017). Assays were carried out using a Varian Cary 50 UV-Vis Spectrophotometer (Agilent Technologies, Santa Clara, California, United States), with manual mixing. Mitochondria at a concentration of 0.25 mg/mL were added to a 2 mL cuvette in KCl based respiration medium (Appendix I). Mitochondria were energised with either 10 mM malate/5 mM pyruvate (complex I-linked respiration) or 5 mM succinate (complex II-linked respiration)(State 2 respiration). Substrates were sequentially added as follows; 1 μM rotenone, 10 μM antimycin A.

2.8 Microscopy

All microscopy was carried out using the Wolfson Bioimaging Facility at the University of Bristol.

2.8.1 Brightfield

Brightfield microscopy was used to capture the anatomy of *b0491.5(RNAi)* animals, as compared to the control. (Section 5.2, Figures 5.2 and 5.8). Images were taken using a Leica TCS SP8 AOBS confocal laser scanning microscope, using the transmitted light detector for brightfield imaging. Using a combination of the 20x and 63x objective,

2.8.2 Confocal fluorescence microscopy

As a tool to investigate mitochondria morphology, transgenic *C. elegans* strain SJ4103, expressing a mitochondrial targetted GFP under the control of a *myo-3* muscle promoter, were grown on RNAi bacteria and the adult worms imaged by confocal microscopy (Section 6.3, Figure 6.4).

2.8.2.1 Sample preparation

4% w/v agarose was made using H_2O. One drop of agarose was placed on a glass slide and covered with a second slide. Spacers were used either side of the agarose glass slide to ensure that the agarose pad formed was consistent. Once set, the top slide was removed and microscopy pad was used immediately. 15A few drops of 15 μL 1 mM levamisole was then added to the agarose pad and worms were picked into the drop, anaesthetising them. A coverslip was then placed over the pad.

2.8.2.2 Confocal fluorescence imaging

Images of GFP expressing worms were taken using a Leica TCS SP8 AOBS confocal laser scanning microscope attached to a Leica DMi8 inverted epifluorescence microscope. Using a combination of the 20x and 63x objective, images were taken using Excitation: 470/40; Emission: 525/50.

2.8.3 Whole worm transmission electron microscopy

Whole worm transmission electron microscopy (TEM) was used to investigate the internal structure of whole worms (Section 6.3, Figures 6.5 and 6.6) in collaboration with Professor Paul Verkade (Professor of Bioimaging, University of Bristol) and Dr Chris Neal (Honorary Research Fellow, University of Bristol).

Worms were immersed in NA22 *E.coli* media in a 0.2 mm deep metal holder prior high pressure freezing with a Leica Empact 2 high pressure freezer (Leica Biosystems Lab Solutions, Wetzlar, Germany). This cooled the worms at 20-25,000ºC/second and raised the pressure during cooling to about 2,050 bar, ensuring that any ice crystals were smaller than EM resolution, or that water had been frozen in a vitrified form. The frozen worms were freeze substituted (fixed) for 2 hours at -90ºC with 1% osmium tetroxide and 0.1% uranyl acetate in acetone using a Leica EM AFS2 freeze substitutor (Leica Biosystems Lab Solutions, Wetzlar, Germany). After a temperature ramp to 0ºC, acetone was used to wash the specimens and worms were infiltrated with acetone/Epon Resin then Epon resin (x2). Followed by polymerisation at 60ºC between 2 Aclar (polychlorotrifluoroethylene) sheets. The Aclar sheets kept the worms flat so that longitudinal sectioning could be more easily achieved. Resin embedded worms were cut at 1 μm thickness and stained with Methylene Blue prior to ultrathin section cutting at 70 nm on a Reichert Ultracut S ultramicrotome (Leica Biosystems Lab Solutions, Wetzlar, Germany). Sections were stained with lead and uranyl salts and were imaged in a Tecnai T12 microscope (Thermofisher), magnifications used were x 440, x 1900 and x 9300.

2.8.4 Cryo-electron tomography

Cryo-electron tomography was carried out in isolated mitochondria to investigate the internal structure of the *b0491.5(RNAi* mitochondria in comparison with the control, (Section 6.3, Figures 6.7 - 6.10). All equipment used is part of the Wolfson Bioimaging Facility at the University of Bristol in collaboration with Dr. Vicki Gold (Senior Lecturer, Living Systems Institute, University of Exeter, United Kingdom)

2.8.4.1 Sample preparation

Mitochondria were re-suspended in basic STEG/M buffer at pH 7.4 at either 5 or 10 mg/mL. Holey carbon EM grids (Quantifoil, Jena, Germany) were glow-discharged using an ELMO TM Glow Discharge System (Cordouan Technologies, France), carbon side up, in a vacuum device according to manufacturer's instructions. Mitochondria were mixed 1:1 with 10 nm protein A-gold (Aurion, Wageningen, The Netherlands) as fiducial markers and immediately apply 3 μL to a glow-discharge EM grid held in tweezers. Grids were blotted for 1 - 1.5 s, followed by plunge-freezing in liquid ethane using a FEI Vitrobot (ThermoFisher Scientific, Waltham, Massachusetts, United States). Freezing occurred very fast, (105 ºC/sec), meaning that water remains in a vitrified state and does not crystallise. This was important as ice crystal formation can damage biological structures. Samples were placed in a grid storage box, and stored under liquid nitrogen until imaging.

2.8.4.2 Cryo-tomography imaging

Tomography was performed using a FEI™ Talos™ Arctica, equipped with a 200 kV X-FEG, Ceta 16 M CCD detector, Gatan K2 DED, and Gatan GIF Quantum LS energy filter (ThermoFisher Scientific, Waltham, Massachusetts, United States). Dose-fractionated tomograms were typically collected from +60ºto 60ºat tilt steps of two. Gold fiducial markers were used to align tomograms and volumes reconstructed using the IMOD software (Kremer et al., 1996). The contrast of the tomogram was enhanced by non-linear anisotropic diffusion (NAD) filtering on IMOD. Tomogram reconstructions were performed using AMIRA (ThermoFisher Scientific, Waltham, Massachusetts, United States).

2.9 Electrophoresis

2.9.1 DNA electrophoresis

DNA electrophoresis was used to analysis products from single-worm PCR (Section 2.11) (results found in Section 5.2, Figure 5.4 and 5.5).

PCR products were visualised on 1.5% agarose gels prepared with 1x TBE Buffer (Appendix I).

2 g agarose was dissolved in 200 mL of 1 X TBE Buffer, heated on full power in a microwave for approximately 3 minutes (until solution was seen to boil and turned clear), then cooled before use. 20 μL of 10'000x Gel Red (Cambridge Bioscience, Cambridge, United Kingdom) was added to the gel solution before pouring. The gel was submerged in 1x TBE buffer in the tank and 3.5 μL of PCR sample was loaded (loading dye already present in the PCR buffer). 5 μL of a 100 bp DNA Ladder was loaded as a marker. Gels were run at at constant voltage (65 V) for approximately one hour. Gels were visualised using the LI-COR Odysey FC imaging system at 600 nm.

2.9.2 SDS polyacrylamide gel electrophoresis

SDS polyacrylamide gel electrophoresis (SDS-PAGE) was used to determine the amount of B0491.5 protein in both whole worm and isolated mitochondria samples. (Section 5.3, Figures 5.6 and 5.9).

2.9.2.1 Sample preparation

For analysis of whole worms, ≈50 worms were picked into 15 μL of M9. Samples were mixed with 4x LDS NuPAGE sample buffer (Thermo) with 250 mM 1,4-Dithiothreitol (DTT) (Sigma-Aldrich, St. Louis, Missouri, United States) was added 1:1 to the worms. The sample was incubated at 60ºC for 25 minutes, then either centrifuged at 13k rpm for 1 minute, or frozen at -80ºC until use.

Isolated mitochondria samples were mixed with 4x LDS NuPAGE sample buffer) with 250 mM 1,4-Dithiothreitol (DTT) (Sigma-Aldrich, St. Louis, Missouri, United States). The sample was incubated at 60ºC for 10 minutes, then either centrifuged at 13k rpm for 1 minute, or frozen at -80ºC until use.

2.9.2.2 Running conditions

Samples were run on 4-12% Bolt Bis-Tris Plus Gels (ThermoFisher Scientific, Waltham, Massachusetts, United States) and a constant voltage (150 V) in a MOPS-running buffer for 30 minutes, or until the dye front had migrated to the bottom of the gel. Gels were removed from the cast for subsequent visualisation.

2.9.2.3 Visualisation

Coomassie

Coomassie staining was carried out using a Coomassie staining solution (Appendix I), gels were incubated for 20 minutes in the staining solution before background stain was removed using washes in de-staining buffer (Appendix I).

Silver stain

Silver staining was carried out with Silver Quest reagents (ThermoFisher Scientific, Waltham, Massachusetts, United States). Gels were first rinsed in distilled water, then fixed in 100 mL of fixative solution (40% ethanol, 10% acetic acid) for 20 minutes, followed by wash in 30% ethanol for 10 minutes. The gel was then incubated in 100 mL of sensitising solution (30% ethanol, 10% Silver Quest sensitiser solution) for 10 minutes, followed by two 10 minute washes in distilled water. Gels were stained with 100 mL of staining solution (1% Silver Quest stainer) for 15 minutes. Gels were briefly washed in distilled water before developed with 100 mL of developing solution (10% Silver Quest developer, 1 drop Silver Quest developer enhancer). The gel was agitated and observed continuously for development, once the desired intensity was achieved, 10 mL of Silver Quest stopper solution was immediately added. All steps were carried out a room temperature using an orbital shaker at 60 rpm.

2.9.3 Blue native polyacrylamide gel electrophoresis

Blue native polyacrylamide gel electrophoresis (BN PAGE) was used in Chapters 4 and 5, to investigate the organisation of the ETC complexes, (Figure 4.3 and 5.10). The technique was developed to optimise the protein load and resolution, see Section 3.4. Samples run on BN PAGE were isolated mitochondria, see Section 2.6. All reagents and equipment was purchased from (ThermoFisher Scientific, Waltham, Massachusetts, United States).

2.9.3.1 Sample solubilisation

Isolated mitochondria (1 or 2 mg) were defrosted, and centrifuged at 13k rpm for 15 minutes at 4ºC, the supernatent was discarded. Stocks of detergents (10% for digitonin and 20% for TX-100) were made up to use in the solubilisation buffers. Solubilisation buffer (Appendix I) at a concentration of

10 mg/mL with digitonin and 5 mg/mL with TX-100, was added to the samples. Mitochondria were solubilised for 20 minutes in the cold room, rotating at 20 rpm, followed by centrifugation at 13k rpm, for 15 minutes at 4ºC.

2.9.3.2 Running conditions

BN PAGE buffers were made up according to manufacturers protocols, 750 mL Native PAGE running buffer (20x Running Buffer) for the outer chamber and 200 mL Cathode buffer (Native PAGE 20x Running Buffer, Cathode Buffer Additive 1 mL) for the inner chamber. Buffers were chilled before use.

After solubilisation, samples were prepared according to manufacturers protocols, apart from a homemade 10% G-250 used in place of the commercially available 5% stock, which was added to a concentration 1/4 of the detergent % and added last, just before the samples were loaded. For 100 μL, sample preparation was as follows; digitonin samples (60 μL solubilised mitochondria, 25 μL 4x sample buffer, 15 μL 10% G-250). TX-100 samples (62.5 μL solubilised mitochondria, 25 μL 4x sample buffer, 12.5 μL 10% G-250).

Gels used were pre-cast 10 well gel (3-12%), the gel tank was set up with cathode buffer in the inner chamber and Native PAGE running buffer in the outer chamber. 25 μL of sample was loaded per well and 7.5 μL of Native protein ladder was used. Gels were run at constant voltage (30V) for 16 hours, or until the dye front had run off the gel. Gels were then either stained by Coomassie or Silver Stain (Section 2.9.2.3), used for in gel activity (Section 2.9.3.3) or 2D analysis (2.9.3.4).

2.9.3.3 Blue native PAGE in gel assays

In-gel activity assays were used to determine which bands within the blue native gel contained the complex in question, assays were carried out for CI, CIV and CV (Figures 4.4 and 5.11). Protocols were obtained from (Zerbetto et al., 1997; Celis and Carter, 2005).

Complex I

A complex I assay buffer was made up; 50 mM potassium phosphate buffer, NADH 0.1 mg/mL, Nitro blue Tetrazolium Chloride (NBT) 0.2 mg/mL and used immediately. The gel was incubated a room temperature using an orbital shaker at 60 rpm, for one hour, or until sufficient band development was seen.

Complex IV

A complex IV assay buffer was made up to 10 mL; 5 mg 3,3'-Diaminobenzidine (DAB), 10 mg cytochrome *c*, 0.75 g sucrose and 2 μg/mL catalase. Solution can be kept at -80ºC. The gel was incubated a room temperature using an orbital shaker at 60 rpm, for one hour, or until sufficient band development was seen.

Complex V

A complex V assay buffer was made up; 35 mM Tris-HCL, NADH 0.1 mg/mL, 270 mM glycine, 14 mM $MgSO_4$, 0.2% $Pb(NO_3)_2$ and 8 mM ATP. Solution can be kept at -80ºC. The gel was incubated a room temperature using an orbital shaker at 60 rpm, for one hour, or until sufficient band development was seen.

2.9.3.4 Blue native PAGE 2D analysis

To separate out the component subunits of the BN PAGE, 2D analysis was used (Figure 4.5 and 5.12). Gel system and pre-cast gels were purchased from ThermoFisher Scientific (Waltham, Massachusetts, United States).

BN PAGE gel was taken and trimmed to the appropriate size, so that it would fit in the loading area in the 2D gel. Gels were incubated in 10 mL reducing solution (Appendix I), for 30 minutes with agitation. Next, the reducing solution was discarded and gel rinsed with 1x Bolt buffer. The BN PAGE gel lane was inserted into the well of the pre-cast 2D gel. The well was overlaid with 1x LDS buffer.

The gel was run at constant voltage (150 V) for 40 minutes, or until the dye front reached the bottom of the gel. Once run, the 2D gels were either immunoblotted (Section 2.10) or visualised by Silver Stain (Section 2.9.2.3)

2.10 Immunoblot

2.10.1 PVDF transfer

Polyvinylidene difluoride (PVDF, 0.45 μm, Millipore, Burlington, Massachusetts, United States) was selected due to its high protein binding capacity, target retention and resistance to cracking. The hydrophobicity of the membrane meant it required a short pre-incubation step in methanol prior to equilibration in transfer buffer (Appendix I). Following SDS-PAGE, protein samples were transferred onto the PVDF membrane, sandwiched between between two sheets of Western blotting filter paper. The transfer system used was the Pierce G2 Fast Blotter (ThermoFisher Scientific, Waltham, Massachusetts, United States), transferred at a constant voltage of 25 V for 10 minutes.

2.10.2 Blocking and antibody incubation

Following transfer, the membrane was blocked in 5% milk in TBS-Tween (Appendix I) for a minimum of one hour at room temperature, using an orbital shaker at 60 rpm. Primary antibodies were diluted as appropriate in 2% milk in TBS-Tween, for incubation with the membrane for one hour at room temperature, shaking. The membrane was washed in TBS-Tween for 10 minutes, 3x. Conjugated secondary antibodies (HRP or fluorescent) were diluted as appropriate with 2% milk in TBS-Tween, and incubated with the membrane for one hour at room temperature, shaking. A further 3x wash steps for 10 minutes with TBS-Tween were carried out. Antibodies were used at the dilution stated in Section 2.2.

2.10.3 Imaging and visualisation of immunoblots

Immunoblots processed with a fluorescent-conjugated secondary antibody were imaged directly using the LI-COR Odyssey FC imaging system, at either 700 or 800 nm as required. HRP-conjugated secondary antibody processed blots were first incubated with Amersham ECL detection reagent (GE Healthcare, Chicago, Illinois, United States) for 1 minute. Images were then collected on the LI-COR under the Chemi channel. For intensity analysis on the antibody signal, the LI-COR image studio programme was used and subsequent intensity values plotted in Graphpad.

2.11 Mass spectrometry

Mass spectrometry techniques were used to locate *C. elegans* protein B0491.5 to complex I (Section 4.4, Figure 4.6) and to analyse proteomic changes under *b0491.5(RNAi)* conditions (Section 5.5, Figures 5.13-15).

2.11.1 Shotgun mass spectrometry

N2 isolated mitochondria (Section 2.5) solubilised with Triton X-100 were run on a blue native gel (Section 2.8.3) and an complex I activity assay carried out (2.8.3.2). Bands that showed complex I activity were excised and sent to Mark Skehel (Head of the Biological Mass Spectrometry and Proteomics Laboratory, Medical Research Council, Cambridge, United Kingdom). The exclusive spectrum count was used to identify proteins located within the band

2.11.2 Quantitative mass spectrometry

Quantitative mass spectrometry was carried out at the Univerity of Bristol Proteomics facility, Material and Methods were provided by Dr. Kate Heesom.

2.11.2.1 TMT labelling and high pH reversed-phase chromatography

Aliquots of 100 μg of each sample were digested with trypsin (2.5 μg trypsin per 100 μg protein; 37ºC, overnight), labelled with Tandem Mass Tag (TMT) ten plex reagents according to the manufacturer's protocol (Thermo Fisher Scientific, Loughborough, United Kingdom) and the labelled samples pooled. An aliquot of the pooled sample was evaporated to dryness, re-suspended in 5% formic acid and then desalted using a SepPak cartridge according to the manufacturer's instructions (Waters, Milford, Massachusetts, USA).

Eluate from the SepPak cartridge was again evaporated to dryness and re-suspended in buffer A (20 mM ammonium hydroxide, pH 10) prior to fractionation by high pH reversed-phase chromatography using an Ultimate 3000 liquid chromatography system (Thermo Scientific). In brief, the sample was loaded onto an XBridge BEH C18 Column (130Å, 3.5 μm, 2.1 mm X 150 mm, Waters, UK) in buffer A and peptides eluted with an increasing gradient of buffer B (20 mM Ammonium Hydroxide in acetonitrile, pH 10) from 0-95% over 60 minutes. The resulting fractions were evaporated to dryness and resuspended in 1% formic acid prior to analysis by nano-LC MSMS using an Orbitrap Fusion Lumos mass spectrometer (Thermo Scientific).

2.11.2.2 Nano-LC mass spectrometry

High pH RP fractions were further fractionated using an Ultimate 3000 nano-LC system in line with an Orbitrap Fusion Lumos mass spectrometer (Thermo Scientific). In brief, peptides in 1% (vol/vol) formic acid were injected onto an Acclaim PepMap C18 nano-trap column (Thermo Scientific). After washing with 0.5% (vol/vol) acetonitrile 0.1% (vol/vol) formic acid peptides were resolved on a 250 mm × 75 μm Acclaim PepMap C18 reverse phase analytical column (Thermo Scientific) over a 150 min organic gradient, using 7 gradient segments (1-6% solvent B over 1 min, 6-15% B over 58 min, 15-32%B over 58 min, 32-40%B over 5 min, 40-90%B over 1 min, held at 90%B for 6 min and then reduced to 1%B over 1 min) with a flow rate of 300 nL/min. Solvent A was 0.1% formic acid and Solvent B was aqueous 80% acetonitrile in 0.1% formic acid. Peptides were ionized by nano-electrospray ionization at 2.0 kV using a stainless steel emitter with an internal diameter of 30 μm (Thermo Scientific) and a capillary temperature of 275ºC.

All spectra were acquired using an Orbitrap Fusion Tribrid mass spectrometer controlled by Xcalibur 4.1 software (Thermo Scientific) and operated in data-dependent acquisition mode using an SPS-MS3 workflow. FTMS1 spectra were collected at a resolution of 120 000, with an automatic gain control (AGC) target of 200 000 and a max injection time of 50 ms. Precursors were filtered with an intensity threshold of 5000, according to charge state (to include charge states 2-7) and with monoisotopic peak determination set to Peptide. Previously interrogated precursors were excluded using a dynamic window (60s +/-10ppm). The MS2 precursors were isolated with a quadrupole isolation window of 0.7 m/z. ITMS2 spectra were collected with an AGC target of 10 000, max injection time of 70ms and CID collision energy of 35%. For FTMS3 analysis, the Orbitrap was operated at 50 000 resolution with an AGC target of 50 000 and a max injection time of 105ms. Precursors were fragmented by high energy collision dissociation (HCD) at a normalised collision energy of 60% to ensure maximal TMT reporter ion yield. Synchronous Precursor Selection (SPS) was enabled to include up to 5 MS2 fragment ions in the FTMS3 scan.

2.11.2.3 Data analysis

An additional note on the statistical interpretation of the mass spectrometry data can be found in Section 2.14.

The raw data files were processed and quantified using Proteome Discoverer software v2.1 (Thermo Scientific) and searched against the UniProt *Caenorhabditis elegans* database (downloaded December 2018: 27626 entries) using the SEQUEST algorithm. Peptide precursor mass tolerance was set at 10 ppm, and MS/MS tolerance was set at 0.6 Da. Search criteria included oxidation of methionine (+15.9949) as a variable modification and carbamidomethylation of cysteine (+57.0214) and the addition of the TMT mass tag (+229.163) to peptide N-termini and lysine as fixed modifications. Searches were performed with full tryptic digestion and a maximum of 2 missed cleavages were allowed. The reverse database search option was enabled and all data was filtered to satisfy false discovery rate (FDR) of 5%.

2.12 Bioinformatic tools

Bioinformatic tools were used within the project to explore the relationship between B0491.5 and NDUFA11 (Figures 4.1, 4.2 and 4.7).

Position-Specific Iterative Basic Local Alignment Search Tool (PSI-BLAST) was used to identify B0491.5, via searching the *Drosophila* homologue to NDUFA11. The database TreeFam, composed of phylogenetic trees inferred from animal genomes, was used to investigate the phylogenetic relationship between B0491.5 and NDUFA11. Clustal omega was used to create sequence alignments, and for the percentage identify calculations.

2.13 Homology modelling

Homology modelling was used to establish protein homology between *C. elegans* B0491.5 and mammalian NDUFA11 (Section 4.5, Figure 4.8-4.11). The model was built in Modeller (Sali and Blundell, 1993), using the NDUFA11 protein structure from respirasome structure 5GUP (Wu et al., 2016). 5000 individual models were constructed, and scored according to their Discrete Optimised Protein Energy (DOPE) value, and the top 1% were kept. These remaining models were analysed to identify clusters of well-scoring structures, using Gromacs gcluster tool, from this the best scoring model from the largest cluster was selected. All molecular models are represented using PyMOL.

2.13.1 Atomistic simulation of model

To investigate the stability of the homology model, an atomistic simulation was carried out by Dr Robin Corey (Oxford, United Kingdom). The simulation was then analysed (Section 4.5, Figure 4.9) looking at the root-mean-square deviation (RMSD) and root-mean-square fluctuation (RMSF) using tools within Gromacs.

2.14 Statistics

All statistical analyses were performed using GraphPad Prism 7.0 Software. For mitochondrial physiology analyses (Section 2.6), where experiments were carried out on the same day with parallel preparations, a paired two-tailed t-test was performed, using independent t-tests for each parameter within the assay. Where data is compared from experiments performed on different days, an unpaired, two-tailed t-test was used.

For analysis of worm length and size measurements were collected in ImageJ, and an unpaired, two-tailed t-test was calculate in Graphpad. To analyse the lifespan data of *C. elegans b0491.5(RNAi)* and control animals (Section 2.4.8), Kaplan-Meier analyses was used.

Statistical analysis for the quantitative mass spectrometry was carried out with guidance from Dr Philip Lewis through his role as bioinformatic support in the proteomics facility. The protein abundances were $\log_2$ transformed so that the data followed near normal distribution and skewness was reduced. The $\log_2$ fold change was then calculated between *b0491.5(RNAi)* and the control samples by subtracting the mean of the former from that of the latter. Unpaired, two-tailed t-tests were performed on the transformed data to calculate the *p*-values. The $\log_2$ fold change and $-\log_{10}$ of the p-values were then plotted on the volcano plots to show the distribution of the data (Figure 5.13-15). Although n of 2 t-tests are a valid method of establishing statistical significance, due to the low power of such a test, they are taken here as a guide to the degree and consistency of the difference between conditions, rather than inferring a strict statistical significance.

Chapter 3

Technique Development

3.1 Chapter introduction

Underpinning the coming results chapters are techniques which in themselves took development, analysis and moderation. Getting these techniques working was hugely valuable and the protocols can be applied extensively to a range of investigations in *C. elegans*. Although not novel in their conception, these techniques had to be adapted and optimised to fit the purpose of the project.

3.2 Mitochondrial isolation

One of the greatest technical challenges for the project was isolating respiratory competent mitochondria from *C. elegans*. There were two major elements to the challenge; the first was obtaining enough biological material, which will be addressed in more detail in Section 3.3, and the second was isolating mitochondria samples capable of collecting significant respiration data. The second part involved components such as creating a balance between successfully breaking open the tough worm cuticle, but not damaging the mitochondria and removing contaminating bacteria from the culture, these elements will be the focus of this section.

Mitochondria isolation is a well established protocol, first introduced by Chance and Williams, (Chance and Williams, 1956). The first isolation protocol used for this project was based on a combination of existing literature in *C. elegans* and established techniques in the laboratory isolating mitochondria from other biological samples, such as yeast and rat heart (Toth et al., 1986; Pedersen et al., 1978). The differential centrifugation steps within the protocol are standard across all protocols, however the techniques used to breakdown the cellular material prior to centrifugation were varied. Some used an enzymatic step, such as zymolyase for yeast, protease for heart tissue or collagenase in *C. elegans* in addition to a mechanical step, which predominately was homogenisation.

3.2.1 Outer membrane integrity

Within the mechanical homogenisation step, it became clear that the specification of the homogeniser was crucial to the success of the preparation, as too strong a mechanical disruption will compromise the integrity of the mitochondria outer membrane, but too weak will generate a low yield. When consulting the literature, only generic information regarding the type of homogeniser used was included, making it difficult to replicate the protocol precisely. The first aspect within the isolation which required optimisation, regardless of whether an enzymatic step prior to mechanical disruption would be used, was selecting the optimal homogeniser.

3.2.1.1 Mechanical disruption

Although the mechanical disruption stage of the isolation protocol chronologically falls after an enzymatic step, it was decided that the impact of the mechanical stage on the isolation was comparatively greater, therefore it was optimised first. A Potter-Elvehjem homogeniser with PTFE pestle works using shearing forces to disrupt the sample as it moves between the sides of the tube and the pestle, making the clearance between the tube and the pestle an important variable. Too large, and the material will pass through unaffected, but too tight and it will cause damage to the mitochondria.

Three different homogenisers with varying clearances were selected from the lab for testing, detailed in Table 3.1 with the greatest clearance represented with '+++' and the narrowest with '+'. The testing criteria were three fold; firstly, the worms were visually inspected under a light microscope for signs of breakage, as shown in Figure 3.1. Indicators that the worms are being disrupted included; release of eggs from their gonad into the surrounding media, the worms dying as indicted by them becoming rigid and straightened, and a loss of contrast in their cuticle. Secondly, the yield of mitochondria from the isolation was compared using a BCA assay to indicate total protein concentration.

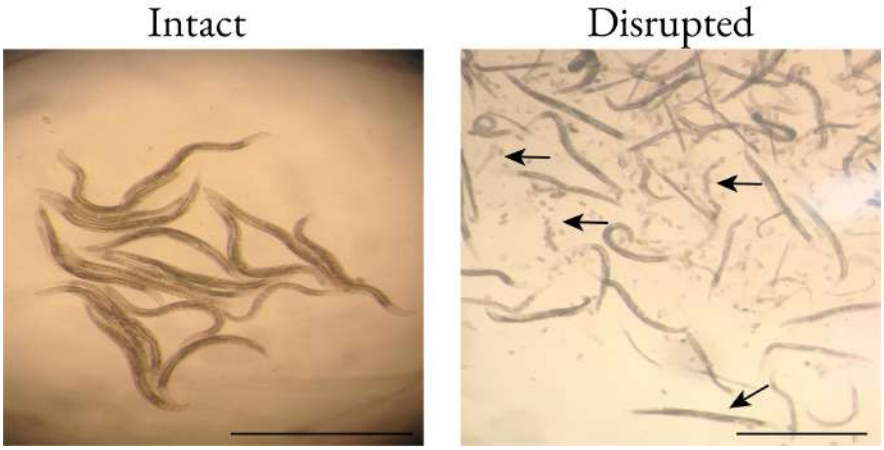

Figure 3.1: Mechanical disruption of *C. elegans* - Comparing intact adult worms with worms that have encountered mechanical disruption. In the image on the right you can see as indicated by the arrows, eggs released, worms rigid and straightened and loss of definition of the cuticle. Scale bar represents 1 mm.

Finally, ADP-dependent oxygen consumption in the presence of exogenous added cytochrome *c* was measured on the high-resolution respirometer (Oxygraph) (Table 3.1). Stimulation with cytochrome *c* is an effective parameter to test the integrity of the outer membrane, as if the outer membrane is damaged, cytochrome *c* is lost during the isolation protocol and washing steps. This leads to the pool of endogenous cytochrome *c* being reduced, allowing only sub-maximum levels of respiration, therefore, on the addition of exogenous cytochrome *c*, a proportionally high percentage increase was

seen in respiration for damaged mitochondria as it returns to maximum. If the membrane remains intact, there is no loss of endogenous cytochrome *c* and respiration stays unaffected. Then, if exogenous cytochrome *c* is added, it cannot cross the outer membrane, and therefore there is no further stimulation of the respiration, which is working at maximum capacity already.

Homogeniser	Homogeniser Clearance	Breakage	Yield	Stimulation with Cyt *c*
1	+++	Low	Low	Not Tested
2	++	Medium	Good	Low
3	+	High	Good	High

Table 3.1: Ranking of homogenisers - Three homogenisers were selected with a range of clearances. They were each used to homogenise *C. elegans* within an isolation protocol, that included no enzymatic step. The homogenisers were ranked on how well they broke the worms, the yield of mitochondria from the isolation and stimulation with cytochrome *c*. These measures were used as an indication of the best suited homogeniser for a *C. elegans* mitochondrial isolation.

The three homogenisers were ranked comparatively on each aspect. The results, compiled in Table 3.1, show that homogeniser number three produced the greatest level of breakage, however this led to a high cytochrome *c* stimulation, as compared to the first homogeniser, which did not disrupt enough material to produce a yield able to be measured on the Oxygraph. Going forward, homogeniser two (Kontes 100 mL, with teflon pestle) was found to be the best suited for disrupting *C. elegans*, as it provided a balance between a reasonable yield, and low cytochrome *c* stimulation.

3.2.1.2 Enzymatic disruption

Having established the best equipment for mechanically disrupting the samples, a different overview of the published protocols for purifying *C. elegans* mitochondria was carried out and is detailed below

in Table 3.2. This was done to see which additional steps could be taken to improve the quality of the mitochondria, and to understand the role they play with the isolation and quality of the samples.

Publication	Filtering	Enzymatic Step	Rupture Method
Methods in Molecular Biology™, vol 372, Gandre and van der Bliek (2007)	Sucrose flotation	No	Homogenisation
Analytical Chemistry, Joseph R Daniele et al. (2016)	No	Collagenase III	Homogenisation
Methods in Molecular Biology™, vol 372, Grad L.I., Sayles L.C., Lemire B.D. (2007)	No	Collagenase III	Homogenisation
Biochemical and biophysical research communications vol. 376,3 (2008), Wojtovich, Andrew P et al.	No	No	Sand
Molecular Basis of Cell and Developmental Biology: Sean P. Curran, (2004)	Sucrose flotation	protease inhibitor	Homogenisation

Table 3.2: Table of published mitochondrial preps - a summary of a range of published mitochondrial protocols in *C. elegans*, (Gandre and van der Bliek, 2007; Daniele et al., 2016; Grad et al., 2007; Wojtovich et al., 2008; Curran et al., 2004)

Based on protocols in Table 3.2, it was decided that an enzymatic step consisting of treatment of the worms with collagenase prior to homogenisation could improve the quality of the isolated mitochondria. It could compromise the integrity of the worm cuticle prior to mechanical disruption, therefore reducing force needed the expose to subcellular components. This could increase the yield of mitochondria obtained from the same amount of starting biological material and increase the integrity of the samples.

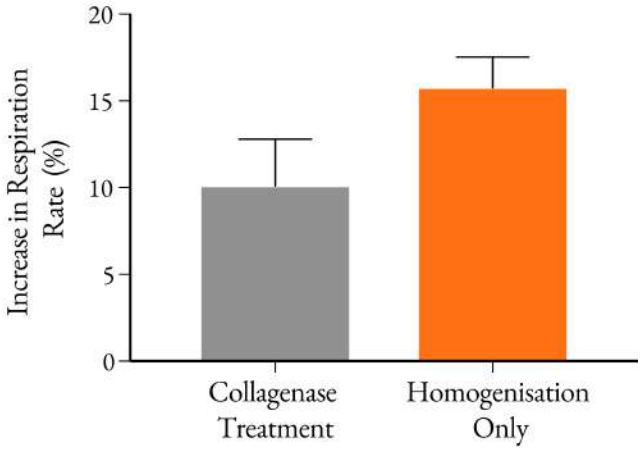

Figure 3.2: Testing the effect of collagenase treatment on outer membrane integrity using cytochrome *c* stimulation on the Oxygraph. The average percentage increase of the respiration rate was plotted. Statistics determined by a paired, two tailed t-test, n=2, 3 replicates for each condition, *p*-value=0.0739

When comparing two separate independent isolations for each condition, the protocol that included a two hour incubation with collagenase before homogenisation had a 16% increase in yield, data not shown. Respiration was tested on the Oxygraph, Figure 3.2, the collagenase treated preparation had an average increase of oxygen consumption of 10%, compared to 15.75% for the preparation which used homogenisation only, when the samples were stimulated with cytochrome *c*. This indicated that collagenase treatment of the worms prior to homogenisation was a beneficial step in the protocol and acted to increase yield and improve the integrity of the mitochondrial outer membrane.

3.2.2 Basal respiration

When analysing the oxygen consumption activity of the isolated mitochondria, a high basal rate of respiration was detected before the addition of substrates. It was hypothesised that bacterial contamination was coming across from the isolation, Figure 3.3, (-) sucrose condition.

When culturing worms on standard *E. coli* it is possible to grow the culture to the point of starvation, where the bacteria is highly depleted but the worms have not started to starve, making the impact of an additional step to remove bacteria from the culture minimal. However, when using RNAi bacteria strains, as in this project, it is essential that they never reach this point as the potential for the RNAi suppression to be weakened or varied if they are not consuming consistent levels of bacteria is detrimental to the experiment.

To test whether the basal rate could be reduced, an additional step was included to remove residual bacteria after culturing worms. The classic method for this is sucrose flotation, as used in some of the established protocols, which separates out adult animals, which float, from the bacteria that pellets upon centrifugation in 60% sucrose.

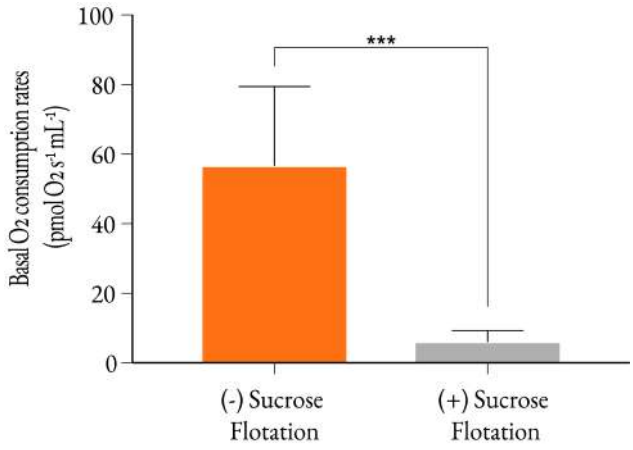

Figure 3.3: Comparative basal respiration rates - Data were collected from four different mitochondria isolation preparations, two preparations before the addition of sucrose flotation in the isolation protocol and two preparations after the addition of sucrose flotation. From each preparation the basal respiration was taken after the addition of mitochondria to the chamber containing respiration buffer and no other substrates. Statistics determined by t-test, n=2, 3 replicates for each condition, unpaired, two-tailed, *p*-value=0.0003

This resulted in a marked difference in basal respiration, shown in Figure 3.3, from an average of 56 pmol O_2/s/mL with no sucrose flotation to 6 pmol O_2/s/mL with the additional step. This was an important adaptation to the basic protocol, the elimination of contamination allows greater clarity when analysing experimental differences in respiration by significantly reducing the levels of basal respiration.

Overall, these modifications have created a more efficient and higher quality isolation protocol for mitochondria in *C. elegans*, particularly tailored towards collecting competent respiration data. An overview of the protocol is detailed in Figure 3.4, highlighted in blue are the reasoning behind the steps. Furthermore, this protocol could also be applied to experiments investigating protein import, where an intact outer membrane and low levels of contaminating bacteria are also important.

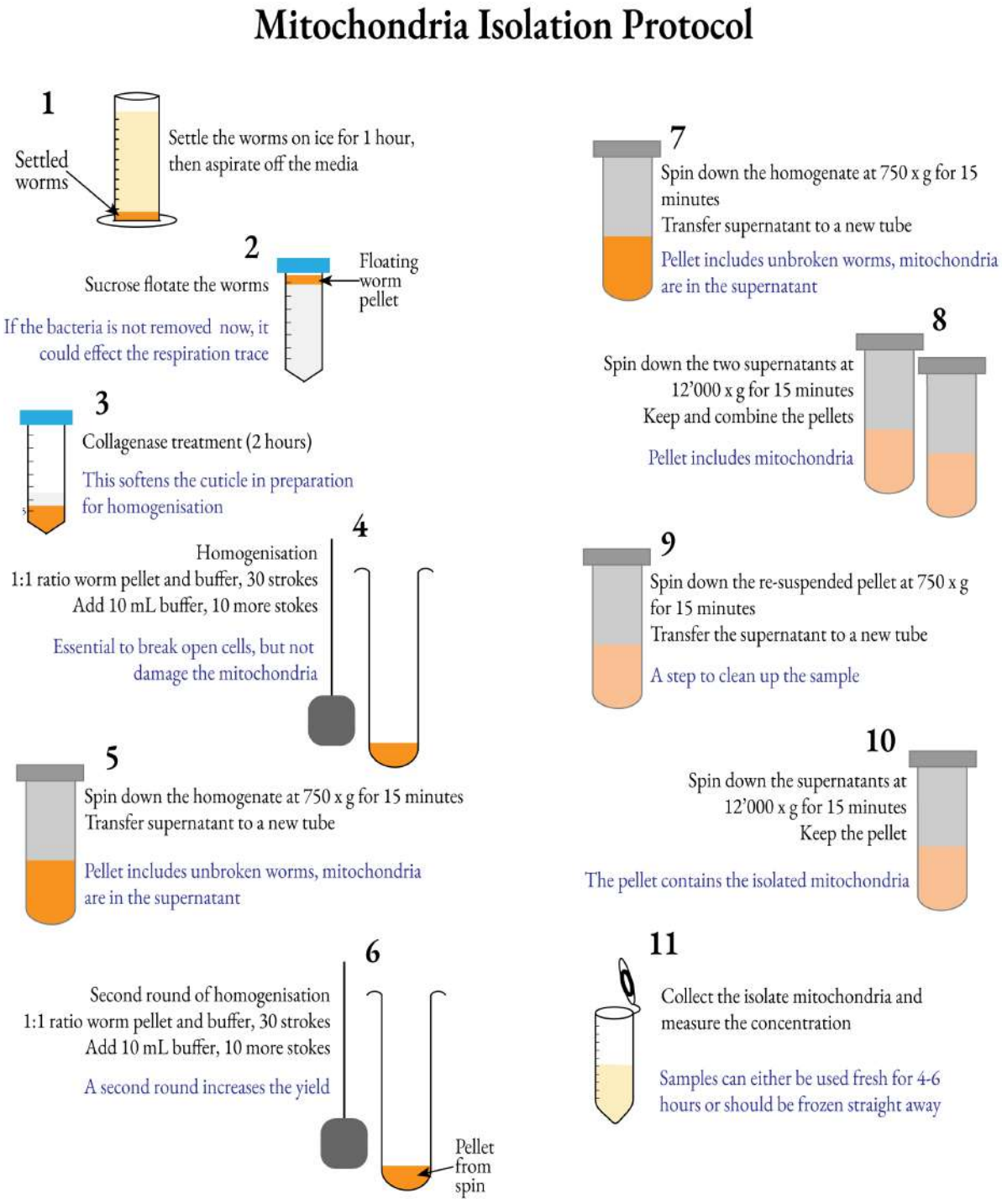

Figure 3.4: Mitochondria isolation protocol overview - An overview of the optimised mitochondria isolation protocol. Highlighted in blue are the reasoning behind the steps.

3.3 Large scale liquid culture RNAi

Within the *C. elegans* genetic toolkit is the highly valuable technique RNA interference (RNAi), developed by Fire and Mello in 1998. They discovered that the introduction of double stranded RNA (dsRNA) to worms led to degradation of the cognate mRNA, this created a tool that facilitates a targeted reduction in gene expression (Fire et al., 1998). The original discovery delivered the dsRNA by microinjection, a technique that is time consuming and has limited scalability; further developments found that dsRNA could be introduced by either soaking (Tabara et al., 1998) or feeding via bacteria engineered to produce dsRNA (Timmons and Fire, 1998).

It became apparent during the project, due to limitations with gene deletion of *b0491.5*, that RNAi would be the best suited technique to knockdown expression of *b0491.5*, allowing B0491.5 activity to be reduced, while retaining viability. As large quantities of worms would be required to obtain meaningful mitochondrial physiology and morphological data, the delivery of feeding RNAi was selected with a detailed description of the protocol in Section 2.4.3 of Materials and Methods

Initial experiments to establish the potency of *b0491.65(RNAi)*, characterisation of the knock down worms and resulting mitochondrial investigations are detailed in Section 5.3. In this section, the necessary developments made to scale up the technique to generate enough biological material for large scale mitochondria preparations are detailed, as the current literature describes smaller scale experimental protocols not fit for the purpose of this project (Hammell and Hannon, 2012; Lehner et al., 2006; Habig et al., 2008).

3.3.1 Scaling up the RNAi technique

One technique to deliver RNAi on a larger scale is to use large, 20 cm Petri dishes which are able to sustain large populations of worms, however it was found that the distribution of bacteria was unevenly depleted and this led to pockets of worms within the plate having reduced access to bacteria. As mentioned in Section 3.2, it is essential that worms have a consistent exposure to RNAi bacteria

to ensure even protein knockdown within the culture. Alternative to culturing *C. elegans* on plates, is to use a liquid medium, which is a standard protocol for normal growth, however is less common for RNAi, and the literature is focused on a 96-well plate small scale delivery (Lehner et al., 2006; Habig et al., 2008).

There are a few key variables within an RNAi protocol relating to bacteria growth and induction, such as culture growth phase, IPTG concentration and induction time, with variances in these potentially impacting on the potency of the RNAi. Reading published protocols found in relation to 96-well plate experiments (Lehner et al., 2006; Habig et al., 2008), it was decided to grow RNAi bacteria cultures to OD_{600} 0.4-0.6, induce the bacteria for 2 hours with 0.4 mM IPTG, then add the bacteria to the standard S-basal worm liquid culture medium with addition of 100 μg/mL ampicillin and 0.8 mM IPTG.

It was determined that 4 L of RNAi bacteria was needed to maintain 1 L of worm culture to adulthood, inoculated with $\approx$ 1 million worms. To determine if those RNAi conditions were sufficient, the isolated mitochondria were analysed by SDS-PAGE and an anti-B0491.5 antibody, shown in Figure 3.5. Full characterisation of *b0491.5(RNAi)* is detailed in Section 5.3, including phenotypical analysis. This section aimed to establish that this exact protocol of delivering RNAi does in fact lead to a successful knockdown of protein. The western blot shows a roughly three-fold decrease in the signal of B0491.5 for the *b0491.5(RNAi)* fraction, suggesting that the RNAi conditions in relation to bacterial growth and induction are suitable to be used at this scale.

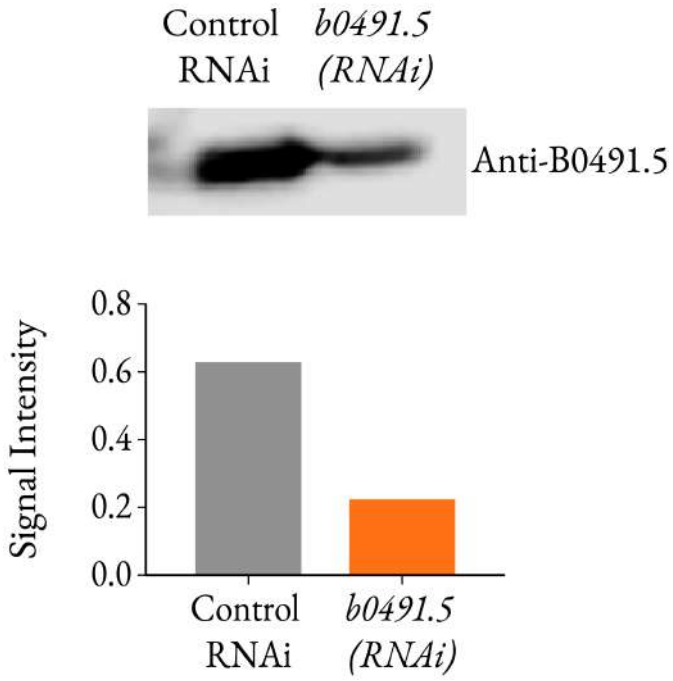

Figure 3.5: RNAi liquid culture knockdown analysis - The concentration of the isolated mitochondria was determined by a BCA assay and 60 μg of each condition loaded onto an SDS-PAGE gel and blotted with an anti-B0491.5 primary antibody and an anti-rabbit HRP secondary. Band signal intensity was determined in LI-COR Image Studio

3.3.2 Synchronising experimental cultures

Having established conditions suitable for delivery of RNAi bacteria on a large scale, optimisation was needed to synchronise the two experimental cultures, as the control and *b0491.5(RNAi)* worms grew at different rates. It was important that both cultures were grown to reach adulthood on the same day, so that the mitochondria isolations could be carried out simultaneously. Many of the physiology experiments required fresh mitochondria, as the freezing process can cause damage to the outer membrane, and variation arising from buffers or equipment meant that if collected on separate occasions it decreased the extent that the data from the two conditions could be compared.

The worms exposed to *b0491.5(RNAi)* grew slower, therefore to have both cultures reach adulthood on the same day for isolation the control was grown for three days, and the *b0491.5(RNAi)* culture for

four days, from starved L1 stage. Adulthood was determined on the control by a developed gonad with visible eggs, but animals were harvested before many second generation progeny entered the culture. For the *b0491.5(RNAi)* condition, as the treatment causes hindered reproductive development, indications that the culture had reached adulthood were size and looking for them to have grown passed the L4 'knotch stage'.

Optimising these two aspects, of scaling up the delivery of the RNAi producing bacteria to large quantities of worms and achieving synchronous cultures has created a consistent protocol, detailed in Figure 3.6, for supplying *b0491.5(RNAi)* animals for mitochondrial isolation and downstream biochemical analysis.

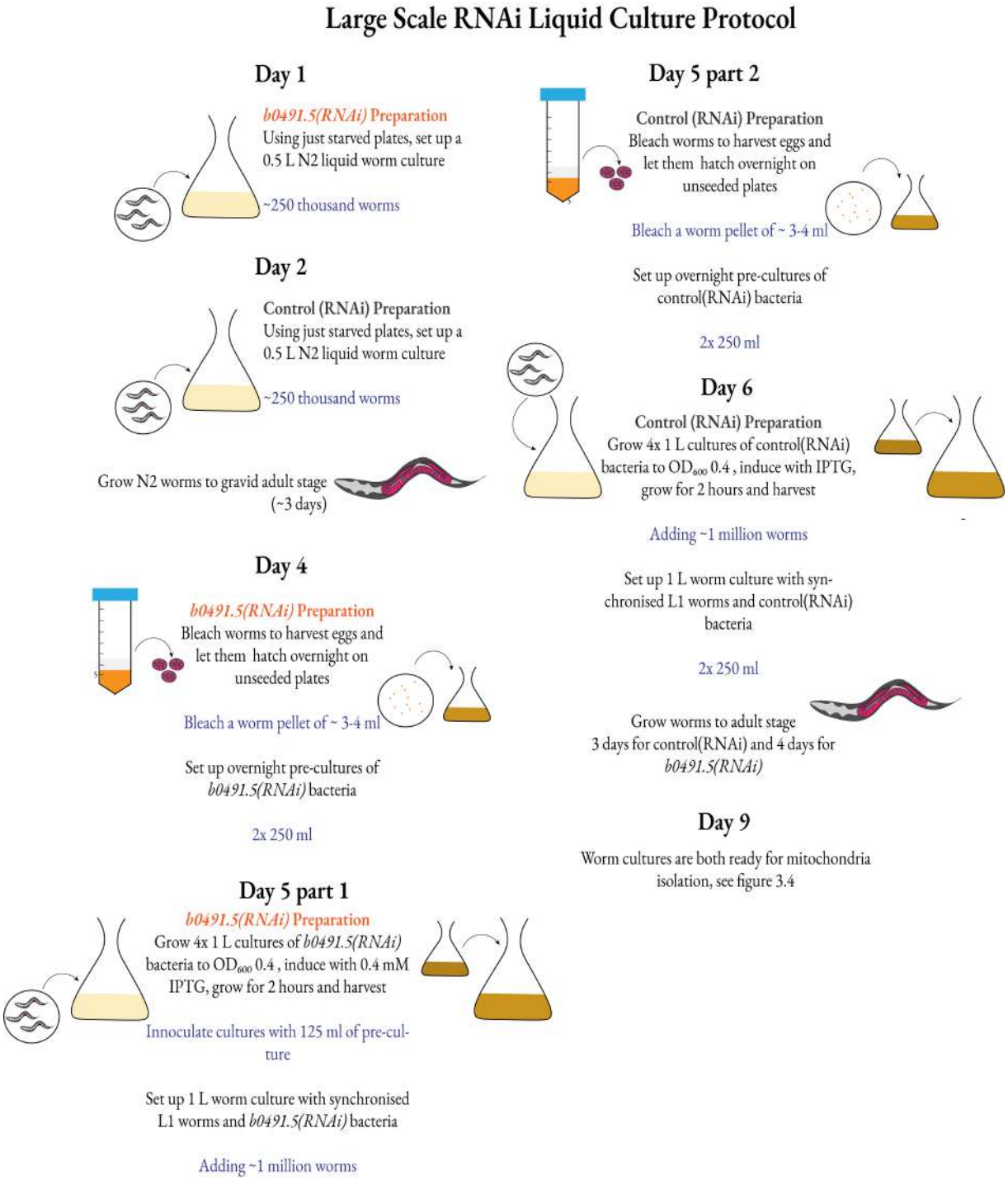

Figure 3.6: Large scale liquid culture RNAi protocol - A step by step overview of the protocol to achieve large volumes of *C. elegans* with RNAi suppression of *b0491.5* with a comparative control culture.

3.4 Blue native PAGE

Blue **N**ative **P**oly**a**crylamide **G**el **E**lectrophoresis (BN PAGE) is an established technique for examining mitochondrial protein complexes as it allows the native conformation and protein-protein interactions to be maintained (Wittig et al., 2006). The technique works through binding of anionic dye Coomassie blue G-250 (G-250), to solubilised mitochondria. The dye binds the membrane proteins due to its hydrophobic properties, leading to a charge shift on the proteins due to binding of a large number of dye molecules. Even basic proteins migrate to the anode, at pH 7.5 (Schagger et al., 1994). Proteins are separated according to size, in acrylamide gradient gels (Wittig et al., 2006). With this technique, as the membrane proteins are coated with negatively charged G-250, the tendency for them to aggregate is minimal. Furthermore, the dye converts membrane proteins into water-soluble molecules, losing their hydrophobic properties, meaning the risk of protein denaturation, even in the in-gel absence of detergent, is minimised (Wittig et al., 2006).

It is a technique that has developed over the years, and the quality of resulting gels has increased significantly. It has developed from gels where individual complex identification was unclear, (Grad and Lemire, 2006; van den Ecker et al., 2010), to systems showing clear separation of multiple supercomplexes (**??**). However, obtaining highly resolved bands often remains a challenge, and is affected by the detergent/protein ratio and concentrations for your sample. Furthermore, variables such as the parameters of the gel system can vary, therefore it is necessary to optimise the sample for the system in use.

3.4.1 Detergents

3.4.1.1 Digitonin

For running samples in their native conformation, two different detergents were used in complement with the BN system. Digitonin is a natural detergent obtained from the purple foxglove plant, it is used widely for mitochondrial solubilisation (Vercesi et al., 1991). Digitonin has a critical micelle con-

centration (CMC) value of 0.25–0.5 mM (Baker et al., 2015), the CMC describes the concentration that, once exceeded, the detergent begins to form micelles. In this project concentrations far exceeding the CMC were used, 1-6% (w/v), 8-49 mM and a detergent: protein ratio of 1:1 or 6:1, respectively. It is considered a 'mild' detergent and maintains larger complexes that have potentially weaker interactions, if the mitochondria samples contain supercomplexes, these should be able to be visualised with digitonin. Furthermore, it is thought that with digitonin, the majority of complex I is found in complex with complex III (Acín-Pérez et al., 2008).

3.4.1.2 Triton X-100

The other detergent used in this project was Triton X-100 (TX-100), a classical non-ionic detergent, and one of the oldest that is still in use. It has CMC value of 0.2 mM, and will be used in these experiments at 5% (w/v), 70 mM. A 'harsher' detergent, it solubilises proteins into smaller complexes, including individual complex I (Gurtubay, 1980).

3.4.2 Initial protocol

An initial protocol was established based on parameters described in (Jha et al., 2016), carried out with digitonin solubilised isolated mitochondria. The results (Figure 3.7) showed a presence of multiple higher bands, but only after silver staining. The resolution of bands was fairly sharp, suggesting that the detergent/protein ratio was suitable, but a weak signal indicates the amount of protein could be increased.

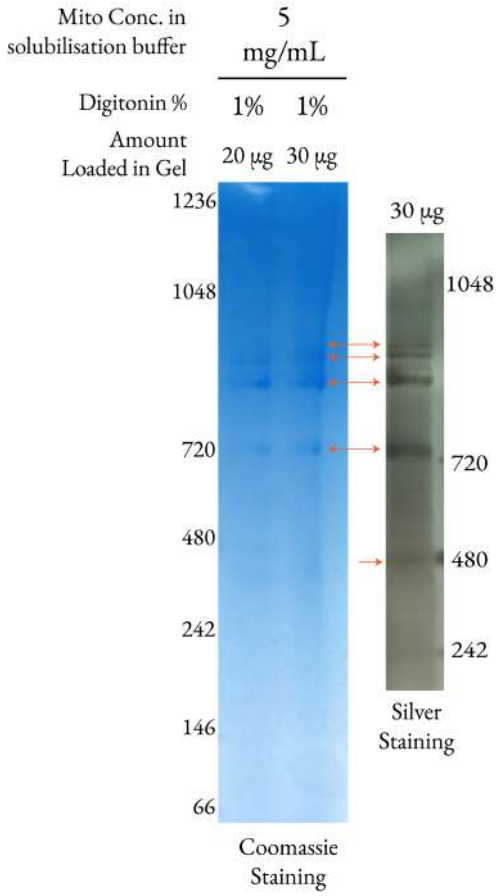

Figure 3.7: Blue Native PAGE - 1 mg of isolated N2 mitochondria was solubilised in 200 μL of 1% digitonin solubilisation buffer (concentration of 5 mg/mL), giving a detergent: protein ratio of 2:1. Loading samples were made up with 5% G-250 sample additive and either 100 μg or 50 μg of solubilised mitochondria in 30 μL, with 10 μL of each of those samples loaded on a 15 well 3-12% gel. Gels were stained with either Coomassie or silver stain, as indicated. Numbers to the side of the gel indicated protein size in kDa.

3.4.3 Protein and digitonin concentration optimisation

To address the issue of weak signal in the BN PAGE, the protein concentration was doubled at the solubilisation step, increasing from 5 mg/mL to 10 mg/mL. As the protein concentration increased, the digitonin concentration was also doubled to maintain the same digitonin: protein ratio of 2:1 as in the initial gel. An additional variable was tested, based on alternative published protocols (Suthammarak et al., 2009, 2010) which uses a digitonin: protein ratio of 6:1, therefore the same concentration of mitochondria were also solubilised at 6% digitonin.

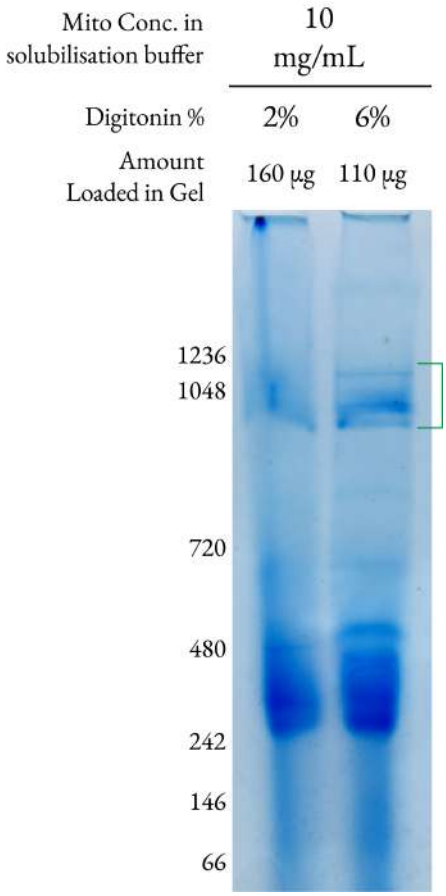

Figure 3.8: Protein and digitonin concentration optimisation in blue native PAGE - Mitochondria were solubilised at a concentration of 10 mg/mL and either 2% or 6% digitonin, to produce protein ratios of 2:1 and 6:1 respectively. Samples contained 10% G250 solution and solubilised mitochondria with 25 μL sample loaded on a 10 well 3-12% gel. Gels were stained with Coomassie. Numbers to the left indicated protein size in kDa.

There was a clear increase in the signal on the gel, particularly between the regions of 480-242 kDa, where in the initial gel no signal was detected here. Around 1048 kDa, where the respiratory complexes are expected, there was a ladder of 4-5 bands detectable under Coomassie staining, previously only detected with silver stain.

In terms of detergent concentrations, for the bands under a digitonin: protein ratio of 6:1 (6% digitonin), there was a noticeable increase in the resolution of the larger complexes, suggesting this condition was more suitable for solubilisation of mitochondria for the goals of this project. Therefore going forward, the protein will be solubilised at a concentration of 10 mg/mL with 6% digitonin.

3.4.4 Maximising protein loading

As the detergent concentration was increased, so does the amount of G-250 sample additive required, as it needs to be a 1/4th the detergent percentage. The consequence of this was that as more G-250 was required, there was a proportional decrease in the amount of solubilised mitochondria in the loading sample, reducing the amount of protein loaded on the gel and ultimately reducing the signal.

Supplied from Invitrogen is a 5% G-250 solution of a proprietary recipe, however to try and optimise this aspect, a 10% 'homemade' solution was made from Coomassie Brilliant Blue G-250 Dye, see materials and methods, to reduce the volume of G-250 required in preparing the loading sample. This was particularly important if a smaller sized gel system is being used, as the volume that can be loaded onto the gel is limited, at around 25 μL per well, and therefore if the protein concentration is low due to high volume of G-250, this cannot be countered with adding a large volume of sample to the well.

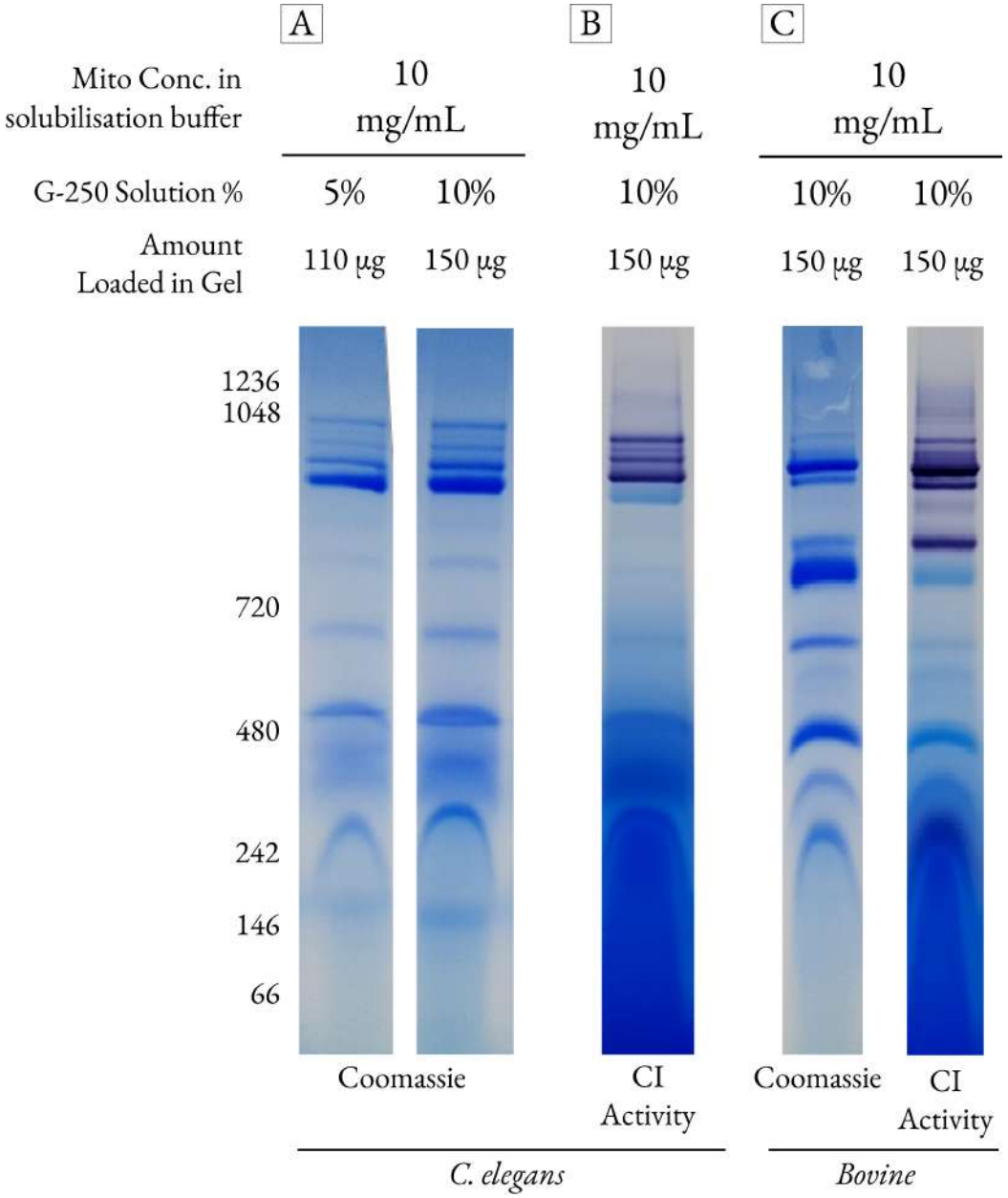

Figure 3.9: Optimisation of G-250 in BN PAGE - Mitochondria were solubilised at a concentration of 10 mg/mL and 6% digitonin. **A** Samples contained either 5% or 10% G250 solution and solubilised mitochondria, stained with Coomassie. **B** In-gel activity assay for complex I (see materials and methods for assay details). **C** *Bovine* mitochondria shown for comparison to *C. elegans*, stained with Coomassie or by complex I activity. For all lanes 25 μL sample was loaded on a 10 well 3-12% gel. Numbers to the left indicated protein size in kDa.

Figure 3.9 (A) shows that the 10% G-250 successfully solubilises the mitochondria to the same extent as the 5% commercial solution. Furthermore, raising the stock concentration of G-250 allowed an increase in the protein amount that was able to be loaded onto the gel, which improves the signal obtained under Coomassie staining. Figure 3.9 (B) shows complex I activity staining, identifying the bands that contain active complex I. In addition to this, mitochondria solubilised from *bovine* heart tissue are shown in Figure 3.9 (C) as a comparison to *C. elegans*. Overall the band patterning between the two species was similar, with interspaced single bands throughout the gel and a ladder of bands in the top region. However, in the *bovine* samples there are a greater number of higher order bands than with *C. elegans* mitochondria.

This adaptation concludes optimisation of the BN PAGE gels with digitonin detergent as the solubilisation agent. This technique was key in investigating mitochondrial respiratory complexes, with digitonin playing the role as a gentle detergent that maintains the integrity of larger protein complexes. With this optimised protocol, going forward a standard BN PAGE under digitonin conditions will have 150 μg of mitochondria in a lane solubilised with a digitonin: protein ratio of 6:1 and the loading sample made up with 10% G-250, a summary of the protocol can be seen in Figure 5.11.

3.4.5 Blue native PAGE with Triton X-100 detergent

Alongside digitonin, the detergent Triton X-100 (TX-100) was used as an investigative tool, the harsher nature of TX-100 allows investigation of complex I as an individual complex, as under digitonin it has been published that this maintains a large proportion of complex I: complex III supercomplexes (Acín-Pérez et al., 2008). Therefore the use of TX-100 allows an additional tool to look at complex I individually.

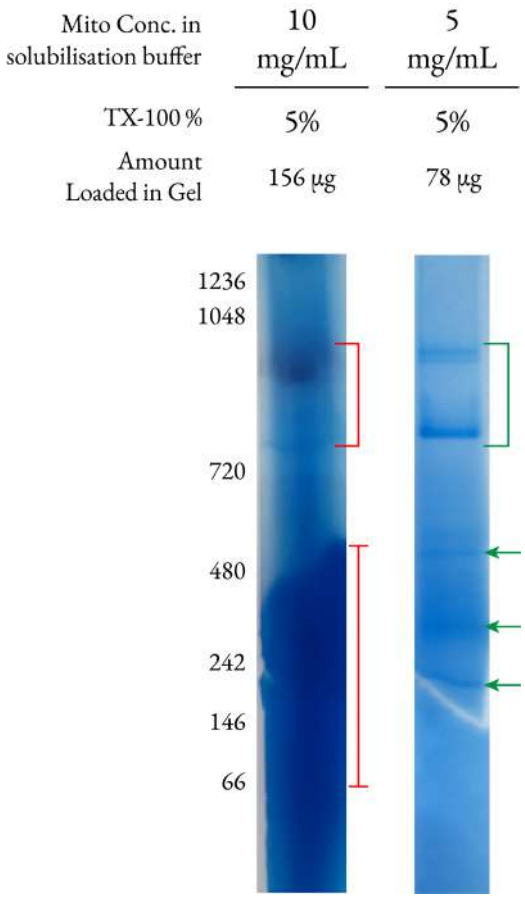

Figure 3.10: BN PAGE with Triton X-100 - The mitochondria were solubilised at a concentration of either 5 or 10 mg/mL in 5% TX-100; as indicated. Samples contained 10% G250 solution and solubilised mitochondria. 25 μL sample was loaded on a 10 well 3-12% gel. Gels were stained with Coomassie. Numbers to the left indicated protein size in kDa.

It was found that TX-100 solubilised the mitochondrial proteins into smaller complexes than those observed after digitonin extraction. It was also observed that large smear, thought to be caused by the accumulation of smaller complexes, appeared in the bottom half of the BN PAGE when using the same amount of protein. This can be seen in Figure 3.10, in the gel lane on the left from 480 kDa and below.

To reduce this aggregate, the mitochondria concentration used for solubilisation was halved to 5 mg/mL, with the same 5% TX-100 concentration used. Looking again at Figure 3.10 at the gel lane on

the right, this had a dramatic effect in reducing the smeared region, and in improving the resolution of the bands. As a result, it was concluded for investigating mitochondrial samples in BN PAGE under TX-100 conditions, these optimised conditions will be adopted and a lane will have 78 μg of mitochondria.

3.5 Chapter conclusion

Having an optimised toolkit of techniques was essential to meet the experimental aims of this project, and these techniques have facilitated a wide range of data collection across the project. Chapter four (Section 4.3 and 4.4) used isolated mitochondria (technique developed in Section 3.2) for Blue Native PAGE (technique developed in Section 3.4), to validate the wild type respiratory complex organisation and, crucially, facilitated the identification of B0491.5 in complex I. This was only possible due to high concentrations of mitochondria available for use in the BN PAGE and optimised protein loading for the gels, allowing detection of an antibody signal by second dimension analysis (Figure 4.5). Previous to optimisation, the protein amounts in the second dimension analysis from BN PAGE were too small to determine an antibody signal. Furthermore, the resolution achieved in the BN PAGE (Figures 4.3 and 4.4) allowed the determination of multiple supramolecular bands, previously indistinguishable in earlier protocols.

BN PAGE (technique developed in Section 3.3), was used in Chapter Five (Section 5.4, Figures 5.10, 5.11 and 5.12) to compare mitochondria purified from control and *b0491.5(RNAi)* animals. The technique allowed differences in the organisation of the respiratory complexes between the two conditions to clearly be visualised, allowing changes to be seen that otherwise could have gone undetected in an unoptimised system. Previous to scaling up the RNAi protocol, it would have been challenging to isolate enough *b0491.5(RNAi)* mitochondria for analysis by BN PAGE. Isolated mitochondria were analysed in Chapter Five (Section 5.5) for mass spectrometry, to investigate proteome changes in control and *b0491.5(RNAi)* samples. The removal of bacterial contamination prior to isolation (Section 3.2.2), allowed for high quality results, unencumbered by hits from bacterial proteins.

Data collection for mitochondria physiology experiments in Chapter Six (Section 6.2) was improved by the optimised mitochondria isolation protocol. The modifications carried out in Section 3.2, collagenase incubation and sucrose flotation, were designed to improve the quality of the O_2 consumption data (Section 6.2.1). Cleaning the worms by sucrose flotation significantly reduced the amount of background respiration from bacteria. Incubation in collagenase weakened the cuticle, which led to improved integrity of the outer membrane and increased the accuracy of the respiration data, as decreases in activity due to loss of cytochrome *c* are less prominent. Data collection from the other mitochondrial physiology experiments, analysing membrane potential (Section 6.2.2) and ROS production (Section 6.2.3) , were also improved for the same reasons. Large quantities of mitochondria were required to carry out these analyses, which was made possible by the scaled up growth of RNAi inhibited worms. In addition, it was essential the mitochondrial samples were fresh, therefore synchronisation of the two conditions (Section 3.3.2) was a crucial factor in allowing the most accurate comparisons between the control and *b0491.5(RNAi)* conditions. Cryo-electron tomography carried out on isolated mitochondria (Section 6.3.3), found that the mitochondrial samples showed consistently intact out membranes, which can be attributed to protocol development in Section 3.2.1.

Potential disadvantages of the sucrose flotation and collagenase incubation optimisation steps incorporated into the mitochondrial isolation, revolved predominately around the length of time an isolation would take. The addition of the sucrose flotation step (Section 3.2.2) added ≈30 minutes to the protocol, whereas the collagenase digestion was an additional ≈two and a half hours. These added time steps are particularly pertinent as, as previously discussed, this was necessary for the mitochondrial physiology experiments to take place directly after isolation, putting more of a time demand on the protocol to facilitate data collection on the same day. In total, the isolation and mitochondrial physiology experiments took 14 hours, with the modifications included. Furthermore, due to large variability in collagenase enzymatic activity in commercial batches, there is a wide range of reported incubation times with the enzyme, from 30 minutes to 36 hours. When optimising the protocol for the purpose of this project, a balance was struck between the time pressures associated with immediately carrying out physiology experiments, and sufficient incubation with collagenase for an effect to take place. When including a two hour incubation with collagenase, an increase of 16% in yield was found along with an increase in outer membrane integrity as indicated by a reduction in stimulation

with cytochrome *c*, suggesting the incubation was sufficient to make valuable improvements on the protocol.

Although none of the techniques incorporated into these protocols were novel, it was important to determine the impact each variable had on the data produced. In relation to the mitochondria isolation, some of the published protocols had included respiration studies (Wojtovich et al., 2008), however, it was difficult to assess the integrity of the preparations as they did not include data on stimulation with cytochrome *c*. Therefore, it was not possible to conclude if without these combined steps the competency of the mitochondria would be as high. The protocol optimisations detailed in this chapter have conclusively improved the data collection found in the forthcoming results chapters, and are valuable additions to the laboratory's protocol toolkit.

Chapter 4

Establishing B0491.5 as a homologue of mammalian NDUFA11

4.1 Chapter introduction

The first section of this study sets out to establish that *C. elegans* protein B0491.5 is the homologue of mammalian respiratory complex I protein NDUFA11. As detailed in Section 1.2.2, *C. elegans* has a significant number of electron transport chain proteins in common with mammals. In complex I, NDUFA11 was one of only seven subunits out of the forty-four in human complex I that did not have an identified *C. elegans* homologue. Despite the whole genome being sequenced, many proteins are still uncharacterised due to lack of functional data and low primary sequence homology, explaining why certain homologous genes, such as *b0491.5*, are currently not yet annotated. After an initial discovery by Patty Kuwabara, this project aimed to validate the discovery, with further bioinformatic and biochemical evidence.

This chapter provides bioinformatic, respiratory complex localisation and functional evidence that *b0491.5* is the homologue of mitochondrial respiratory complex I subunit NDUFA11. Furthermore, investigations into the composition of mitochondrial respiratory complexes not only serves to identify the subcellular location of B0491.5, but also to validate the organisation of respiratory complexes in *C. elegans*, which has been previously published (Suthammarak et al., 2009, 2010).

4.2 NDUFA11 bioinformatics

Researching *C. elegans* as a mitochondrial model organism and understanding how highly homologous their mitochondria composition is with mammalian counterparts, investigating the human subunits with no current homologous subunit in *C. elegans* was a natural progression. The original discovery regarding *C. elegans* protein B0491.5 as a homologue of mammalian NDUFA11, was made by Patty Kuwabara using psi-BLAST (Position-Specific Iterative Basic Local Alignment Search Tool) which can be used to find distant evolutionary relationships. The NDUFA11 homologue in *Drosophila*, *ND-B14.7*, was first used in psi-BLAST to identify *C. elegans b0491.5*. Following on from that discovery, TreeFam, a database developed to provide curated phylogenetic trees for animal gene families and also provide orthology/parology predictions (Ruan et al., 2008) was used to investigate the phylogenetic relationships of *b0491.5*. Searching NDUFA11 in the database brings up TreeFam family TF314729, consisting of 62 species. Looking within the family at model organisms, the cladogram of the family tree is shown in Figure 4.1. Furthermore, looking for B0491.5 in a proteomic paper which carried out a comprehensive proteomic analysis of *C. elegans* mitochondria (Li et al., 2009), it was found to be enriched in the mitochondria, providing confidence that B0491.5 could potentially be a homologue of NDUFA11.

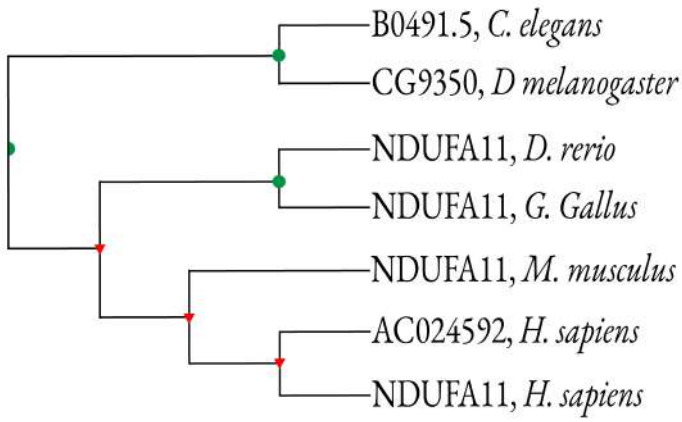

Figure 4.1: Cladogram of NDUFA11 - The TreeFam family TF314729 (NDUFA11) has 63 sequences from 62 species. The sequences were aligned using MCoffee. The final alignment was 675 AA long and on average 42% conserved. TreeBest (Ruan et al., 2008) was used to build a gene tree and reconciles it with the species tree. TreeBest build 5 source trees using nj and Phyml (Guindon et al., 2010). It then merges them into one tree trying to minimise the number of duplications using a species tree. Represented using a model tree type and cladogram branch length.

The bioinformatic data from the psi-BLAST search (not shown), and TreeFam phylogenetic relationships (Figure 4.1), led the project to *C. elegans* protein B0491.5. Figure 4.1 shows the gene tree for NDUFA11, focused on model organisms. The hit AC024592 refers to the genomic DNA region, where NDUFA11 resides. The *C. elegans* protein B0491.5 is currently classed as uncharacterised, and the gene has not been annotated with a known function. WormBase, an international consortium dedicated to providing accurate and current information regarding the model organism *C. elegans*, has information suggesting enrichment of B0491.5 in some neurons and the germ line as well as it being affected by several genes including *daf-2*, *daf-12*, and *let-7*. Carrying out a literature search, *b0491.5* can be found in one study which explores the impact of RNAi on lifespan for a range of proteins, and finds that suppression of *b0491.5* leads to small increase in lifespan (Chen et al., 2007). In addition, the proteomic paper (Li et al., 2009) discussed above, which showed enrichment of B0491.5 in the mitochondria, suggesting its subcellular location.

As the *C. elegans* genome is fully sequenced, both the gene and protein sequence were available from WormBase. Using The European Bioinformatics Institute (EMBL-EBI) multiple sequence alignment tool Clustal Omega (Madeira et al., 2019), the protein sequences of NDUFA11 from humans, pig and cow as well as the homologue CG9350 from fruit fly were compared to *C. elegans* B0491.5 shown in Figure 4.2.

An immediate observation was in relation to the length of the *C. elegans* protein B0491.5 in comparison to the other homologues. With a primary sequence of 327 amino acids, it was over double the length of the others, with the majority of the additional amino acids found at the beginning. This N-terminal region (amino acids 1-155) was investigated further by Basic Local Alignment Search Tool (BLAST), using the BLASTp algorithm (Altschul et al., 1990). All the hits were from the nematode phylum, with the top five being from other members of the *Caenorhabditis* genus, suggesting it was a nematode specific region (data not shown). The functional role, if any, the N-terminus region has to play was unclear; searching databases of protein families using EMBL-EBI tool Pfam (Bisseru, 1971) comes up with no functional annotation for the region.

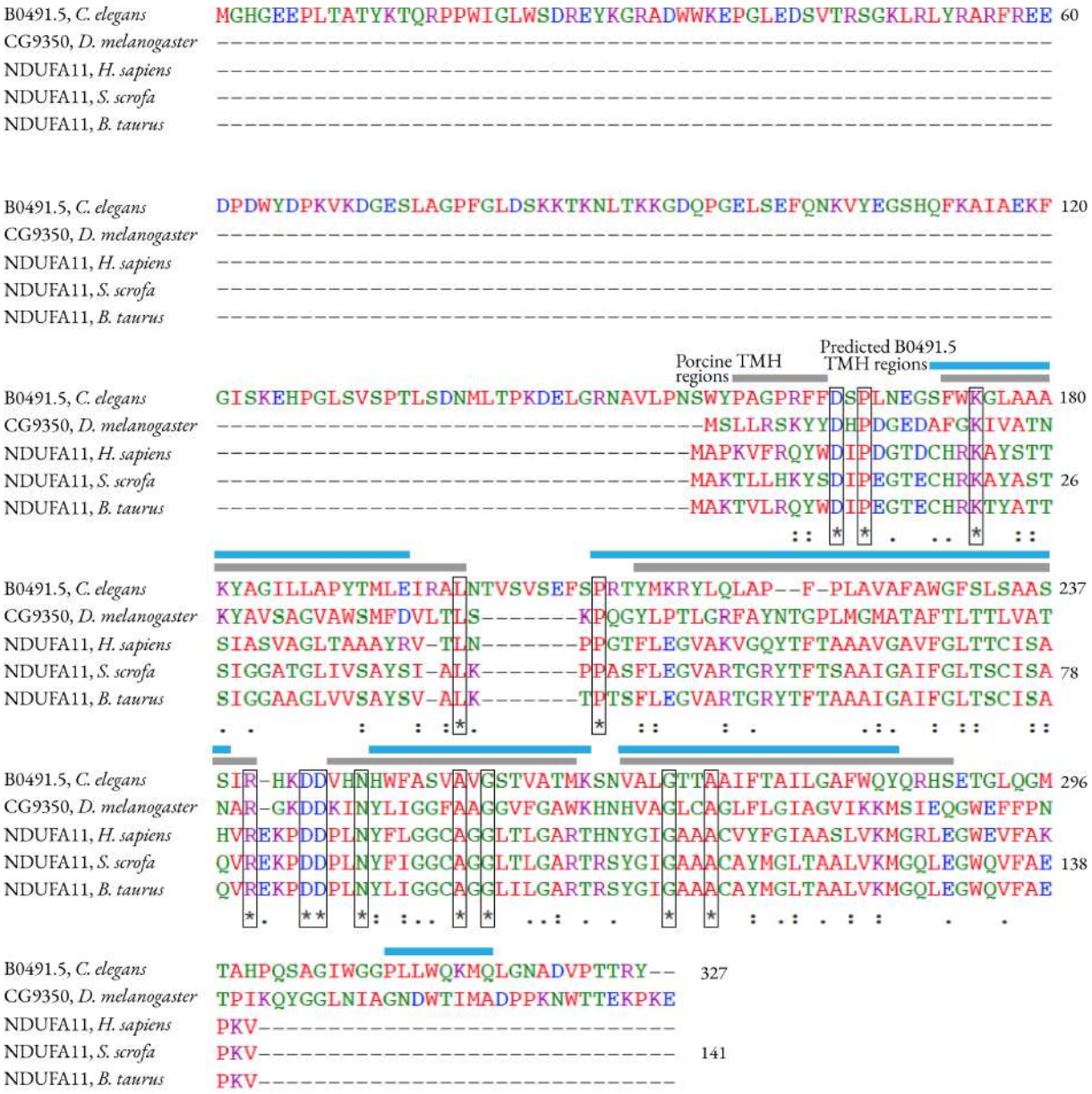

Figure 4.2: NDUFA11 multiple sequence alignment - Multiple sequence alignment generated on Clustal Omega (Madeira et al., 2019). The block colour regions above represent the TMH secondary structure regions for porcine NDUFA11, taken from the 5GUP structure (Wu et al., 2016) (grey) and predicted regions for *C. elegans* B0491.5 (blue) as determined in JPred4 (Kayser et al., 1989). The boxes surrounding the residues conserved across all five entries, and residues which hold similar properties are represented by : or . depending on the strength of similarity.

C. elegans protein B0491.5 alignment with the other sequences begins from amino acid 155, the alignment contains 13 highly conserved residues, marked with boxes in Figure 4.2, and a similar length C-terminal region with that of the fruit fly. The sequence shows low sequence similarity to all four other proteins, detailed in the table below in Table 4.1, as determined by Clustal Omega's percent identity matrix. Even when truncating the B0491.5 sequence, from just amino acid 155 onwards, the percent identity remained within one percent of the score with the full sequence.

Protein	**% Identity with *C. elegans* B0491.5**
CG9350, *D. melanogaster*	22.42%
NDUFA11, *H. sapiens*	16.79%
NDUFA11, *S. scrofa*	15.33%
NDUFA11, *B. taurus*	13.87%

Table 4.1: Percentage identity of B0491.5 to mammalian NDUFA11 - determined by Clustal Omega (REF-CLUS) percent matrix tool, based on the sequences shown in Figure 4.2.

The transmembrane helix (TMH) regions for the porcine protein were added to the sequence alignment using the solved structure 5GUP (Wu et al., 2016), to identify the primary sequence that corresponds to key structural regions of the protein. These regions are represented by the grey bars above the sequence in Figure 4.2. For B0491.5, TMH regions were predicted using Protein Secondary Structure Prediction server JPred (Kayser et al., 1989), and added in blue bars. The predicted B0491.5 secondary structure, to the most part, overlaps with the established porcine structure, indicating that despite a low primary sequence similarity, there was more prominent secondary sequence comparability.

As initial evidence investigating B0491.5 as a homologue of NDUFA11, the sequence alignment shows promising similarity in the second half of the protein sequence, with multiple highly conserved residues potentially clustered around the ends of the TMH regions. Therefore, the project aimed to provide biological evidence to validate the bioinformatic data.

4.3 Organisation of *C. elegans* mitochondrial respiratory complexes

Blue native PAGE (BN PAGE) is an established method for investigating the organisation of multi-subunit complexes, full development of the technique for this project is detailed in Section 3.4. In this section, BN PAGE was used to validate the organisation of the respiratory complexes in *C. elegans* mitochondria. Furthermore, it was used alongside second dimension analysis and antibody probing to investigate the subunit composition of the respiratory complexes, to provide evidence of the localisation of B0491.5 to complex I. Isolated mitochondria from N2 worms were separated using BN PAGE, the data presented in Figures 4.3 and 4.4, alongside published data, will work to support the identity of the respiratory complexes in each of the bands, before antibody data presented in Figure 4.5 localises protein B0491.5 specifically to complex I.

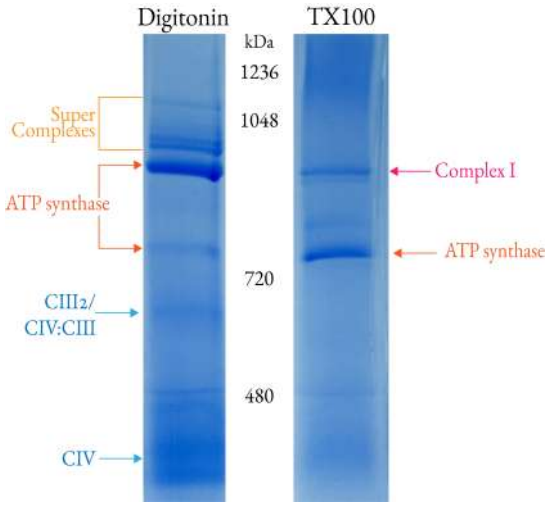

Figure 4.3: Blue native PAGE with N2 isolated mitochondria - Isolated mitochondria from N2 worms were solubilised with digitonin or TX-100 (see Materials and Methods Section 2.9.3 for full protocol), then electrophoresed in 4-16% gradient acrylamide gels under native conditions and visualised by staining with Coomassie Blue.

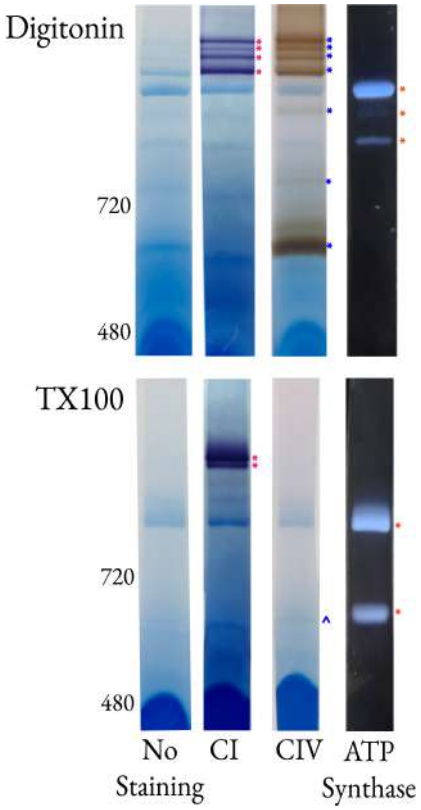

Figure 4.4: Blue native PAGE in-gel activity assays - Isolated Mitochondria from N2 worms solubilised with digitonin (A) or TX-100 (B), were electrophoresed in 4-16% gradient acrylamide gels under native conditions. In-gel activity assays show positions of complex I, IV or ATP synthase (see Materials and Methods Section 2.9.3.1 for full protocol)

When solubilised with digitonin, the supramolecular organisation of the respiratory complexes was kept intact, and can be seen stained in Figure 4.3. Combining data published previously (Sutham-marak et al., 2009, 2010), and in-gel activity assay data in Figure 4.4, it suggested the ladder of bands located at the top of the gel are varying arrangements of CI, III and IV. Other predominant bands on the gel include an ATP synthase dimer, and bands of either CIII:IV or $CIII_2$.

Solubilisation with TX-100, a 'harsher' detergent, disrupted the larger complexes, and maintained only those complexes which are bound tightly. This condition disassembled the supercomplexes and leaves complex I intact, which was in contrast to digitonin conditions, where the majority of the complex I was suggested to in a CI:III state (Schagger and Pfeiffer, 2000).

4.4 Locating B0491.5 within the respiratory supercomplexes

As a tool to determine if B0491.5 was located in the mitochondrial respiratory complexes, the BN gels were run on a second dimension in reducing conditions, allowing visualisation of the constituent subunits of each complex. Firstly, antibodies against the NDUFS3 subunit in complex I and ATP5 in complex V confirmed the in-gel activity assay data in Figure 4.4, then when blotted for B0491.5, it can be seen to co-localise with the NDUFS3 antibody, in both digitonin and TX-100 conditions. This is compelling evidence that B0491.5 is localised to respiratory complex I, and supports the bioinformatic data in Figure 4.1, that it is a homologue of NDUFA11.

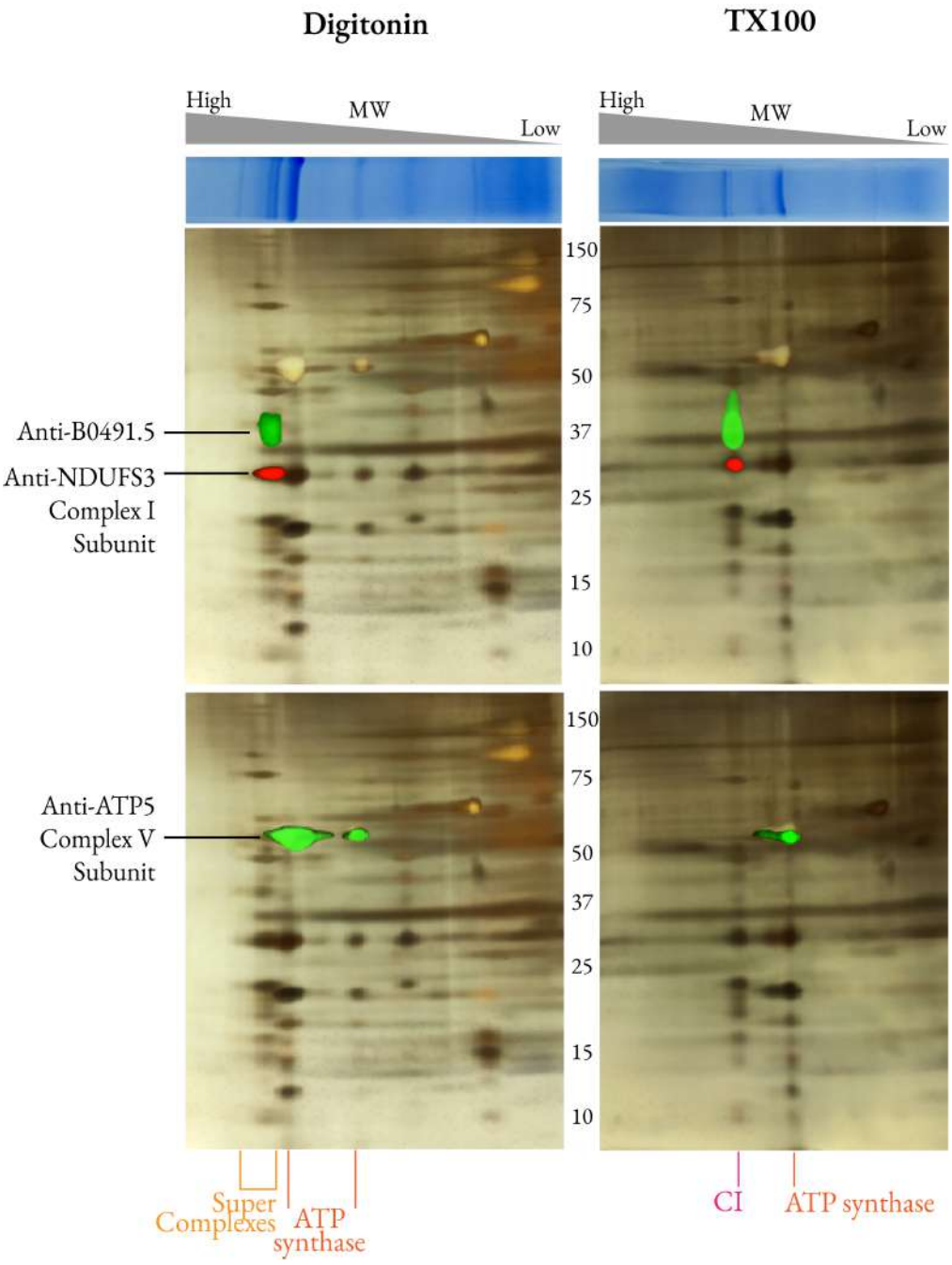

Figure 4.5: Two-dimensional analysis of BN PAGE - separated in reducing conditions on a 4-12% gel (see Materials and Methods 2.9.3.2 for full protocol). Superimposed on gels stained with silver stain are antibody signals for B0491.5 (green) and NDUFS3 (red) in the top panel, and ATP5 (green) in the bottom panel. Representative gel, n=3

To support the antibody data in Figure 4.5, and support the localisation of B0491.5 in complex I, the band in the BN gel under TX-100 conditions showing CI activity, was excised and analysed using shotgun mass spectrometry by Mark Skehel (Head of the Biological Mass Spectrometry and Proteomics Laboratory). The top twenty hits, as determined by the exclusive spectrum count, are shown in Figure 4.6. Predominately, the subunits detected are from complex I (10/20), however, there are also subunits from complex III (4/20), this could be due to remnant CI:III supercomplexes, or local contaminants. Within these hits was B0491.5, supporting the antibody data in Figure 4.5, and supporting prior evidence of the proteins localisation to mitochondrial respiratory complex I.

C. elegans gene	Human Ortholog	Respiratory Complex	Exclusive Spectrum Count
ucr-1	UQCRC1	Complex III	84
NUO-5	NDUFS1	Complex I	79
NUO-1	NDUFV1	Complex I	51
Y53G8AL.2	NDUFA9	Complex I	46
CYC-1	CYC1	Complex III	44
ANT-1.1	SLC25A4/5/6	-	43
icl-1	-	-	42
GAS-1	NDUFS2	Complex I	40
NUO-2	NDUFS3	Complex I	40
UCR-2.2	UQCRC2	Complex III	39
NUO-4	NDUFA10	Complex I	38
Vit-6	CTD-3088G3.8	-	37
UCR-2.1	UQCRC2	Complex III	36
B0491.5	NDUFA11	Complex I	36
atp-1	ATP5F1A	Complex V	32
Vit-5	CTD-3088G3.8	-	29
C16A3.5	NDUFB9	Complex I	29
F59C6.5	NDUFB10	Complex I	28
Vit-2	CTD-3088G3.8	-	27
F53F4.10	NDUFV2	Complex I	26

Figure 4.6: Shotgun mass spectrometry of BN PAGE complex I active band - Top twenty hits from mass spectrometry of the protein band excised from BN gel that showed in-gel complex I activity as determined by exclusive spectrum count. Mass spectrometry was carried out by Mark Skehel at Cambridge

4.5 Homology model of B0491.5

Having collected compelling BN PAGE antibody and in-gel activity data, supported by mass spectrometry, supporting the localisation of B0491.5 to the mitochondria, and more specifically to respiratory complex I, attention was turned back to the sequence alignment. The overlapping porcine and predicted B0491.5 TMH regions, as well as the number of residues conserved across all species, suggested likely secondary structure similarity between the two proteins. To investigate the structure of B0491.5 and to try and shine light on any structural similarity between NDUFA11 and B0491.5 the approach of homology modelling was taken.

This was carried out as the data collected so far locates B0491.5 to the same cellular location as NDUFA11, but does not provide evidence of them sharing the same function. If similarities could be shown between B0491.5 and NDUFA11 on a structural level, this would provide strong evidence, in combination with the bioinformatic and BN PAGE data, that they are homologous proteins. Furthermore, structural analysis could contribute to the understanding of the function of NDUFA11 within complex I, beyond the current suggestions of its role as an assembly or stabilisation subunit, discussed in Section 1.1.7.2.

The model was constructed using porcine NDUFA11, from the 5GUP respirasome structure as the model (Wu et al., 2016), this structure was chosen as it was determined at 3.6 Å for complex I with side chains, which at the time was the highest resolution structure available, furthermore, the structure was solved with cardiolipin bound to NDUFA11, which was of particular interest to this project. A comprehensive protocol of how the model was made can be found in Materials and Methods, Section 2.13. In short, an alignment of the sequence to be modelled was used, with a known structure, and Modeller calculates a model containing all non-hydrogen atoms, implementing spatial restraints and performing de novo modeling of loops, if necessary. Due to limitations within the homology modelling method, in the respect that it needs a solved structure to work from, and the fact that the N-terminal region only shares homology with other nematodes, the model was constructed using the region of B0491.5 that aligns with other species, and for which there are structures available.

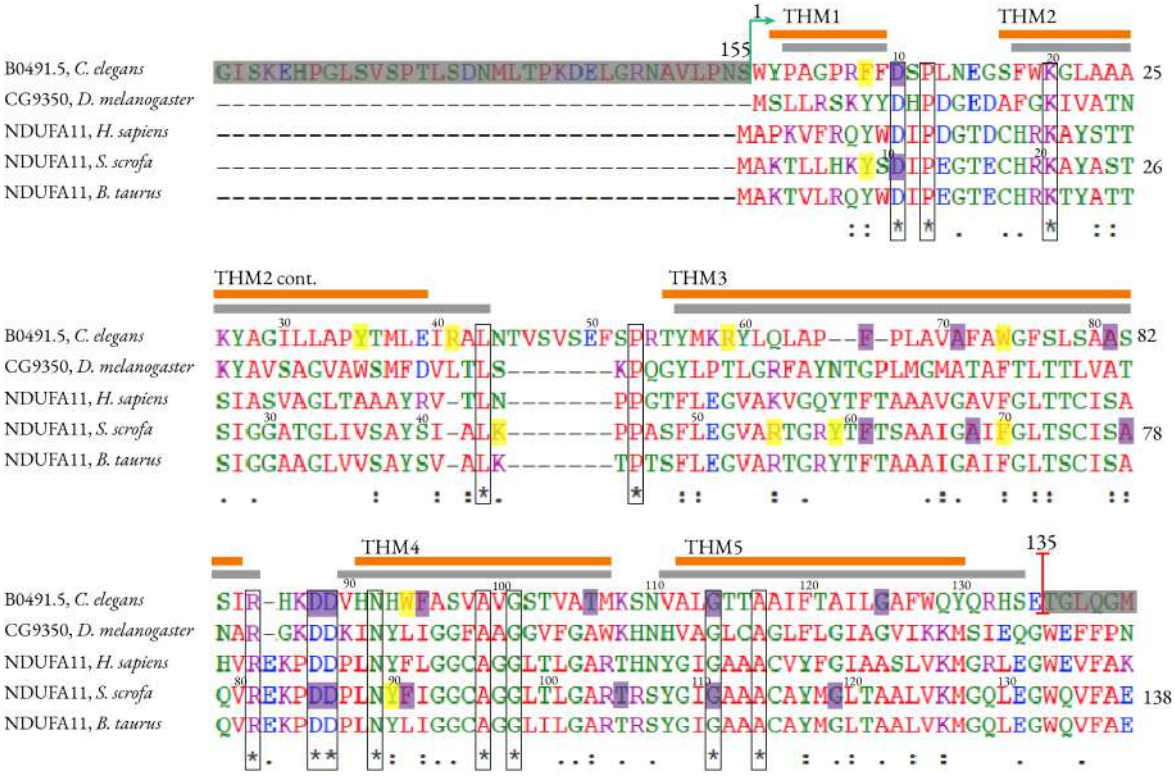

Figure 4.7: Homology model sequence alignment - multiple sequence alignment from Figure 4.2, highlighting only the residues for B0491.5 that are present in the homology model, residues not included in the homology model are either not shown or greyed over. The block colour regions above represent the TMH secondary structure regions for porcine NDUFA11, taken from the 5GUP structure (Wu et al., 2016) (grey) and predicted regions from the model of *C. elegans* B0491.5 (orange). As before, the boxes surrounding the residues conserved across all five entries, and residues which hold similar properties are represented by : or . depending on the strength of similarity. The residues highlighted in yellow are predicted to have cardiolipin interaction properties, and the residues highlighted in purple are conserved somatic mutations found in (Tate et al., 2019)

The region of the B0491.5 primary sequence that was included in the homology model is shown in the sequence alignment in Figure 4.7, from reside 155 onwards, consisting of 135 residues in total. Annotated on the alignment are the same TMH regions from porcine NDUFA11 as in Figure 4.2, shown in grey, however in regards to B0491.5 it is now annotated with the modelled TMH regions, represented as orange bars above the corresponding residues. Also shown on the sequence alignment, in yellow and purple, are residues that will be referenced back to as we look at the model, relating to residues of interest when looking at different aspects of the structure.

The model, shown in Figure 4.8 in orange, exhibits pronounced alignment with NDUFA11, in grey. Not only does the model fit with the same number of TMH regions, they are organised with similar trajectories, both a structure that sits off the side of the transmembrane arm of complex I and creates a 'channel' like structure that CL sits in. This 'channel' is most prominently displayed in Figure 4.8, in the left hand image, showing a top down view from the mitochondrial matrix. In addition, areas such as the region between TMH 2 and 3, where there is an insertion of residues for B0491.5, manifest as a longer loop in the model. That B0491.5 is modelled to conform to a four transmembrane structure is particularly interesting, as out of the complex I accessory subunits, twelve contain a single TMH, one contains two TMHs, and NDUFA11 uniquely has four (Wu et al., 2016). Suggesting that out of the complex I subunits B0491.5 could be homologous to, the structural conformation of four TMHs is strong evidence it is homologous to NDUFA11.

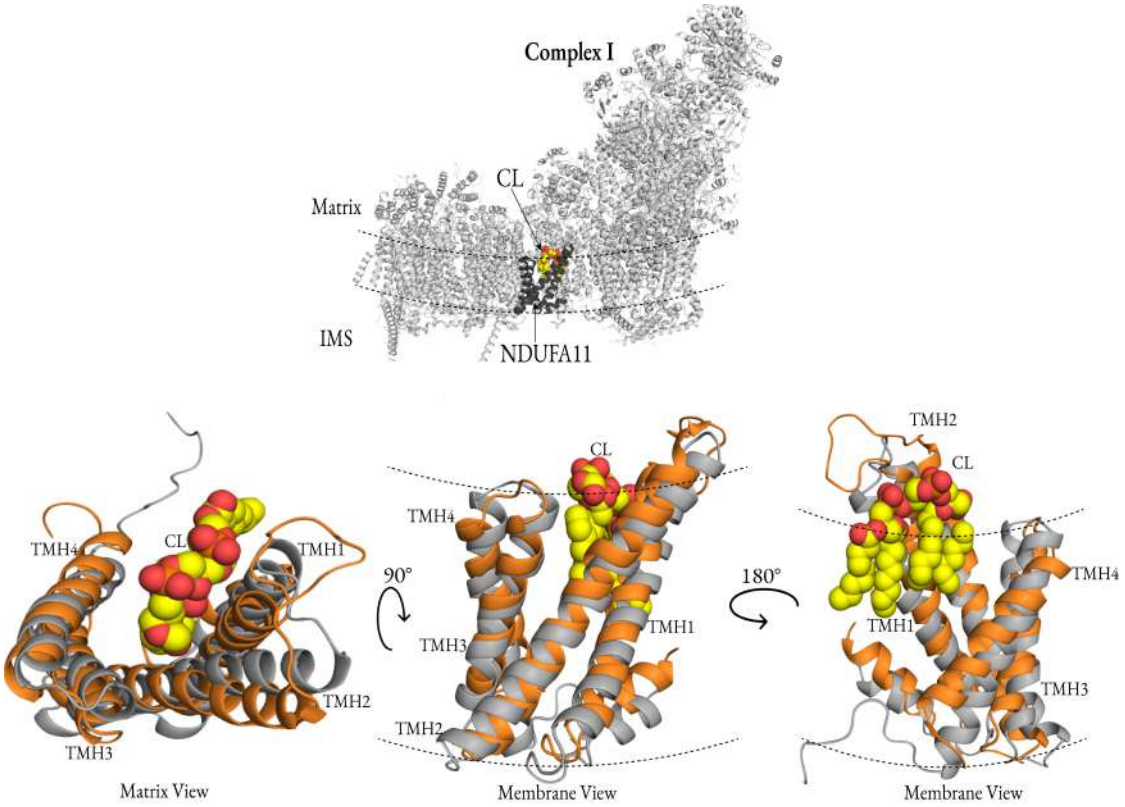

Figure 4.8: Introducing the B0491.5 homology model - top: structure of CI from porcine 5GUP respirasome structure (Wu et al., 2016) with NDUFA11 shown in a darker grey. bottom: three orientations of the model (orange) overlaid with NDUFA11 structure from 5GUP (grey). Cardiolipin is represented in yellow and the dotted lines represent the border of the membrane.

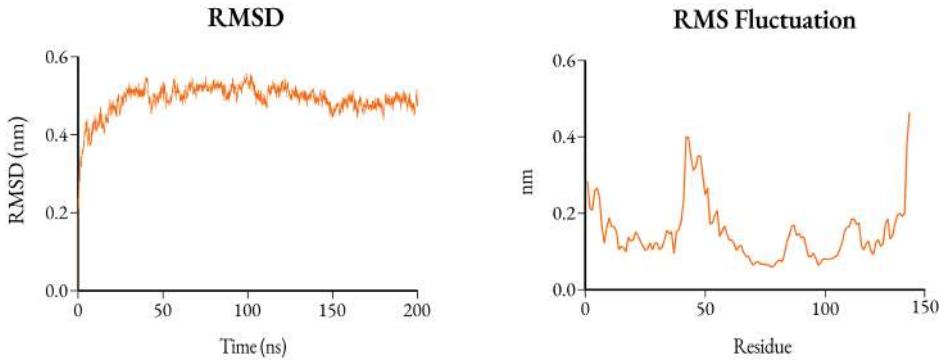

Figure 4.9: RMSD and RMSF values of the homology model in atomistic MD simulation - RMSD analyses based on Cα, calculated every 0.1 ns. RMSF calculated per residue

When evaluating the model, it was essential to take into account the parameters used when creating it. The input structure, NDUFA11, used to build the model had a large influence on the resulting output structure, B0491.5, so interpretations of the model should be made with the appropriate caution. To test the robustness of the model a 200 ns atomistic molecular dynamic (MD) simulation was run by Robin Corey. From this, analyses such as root-mean-square deviation (RMSD) and root-mean-square fluctuation (RMSF) were used to measure the spatial variations of the proteins within the simulation (Figure 4.9).

The RMSD was used as a quantitative measure looking at the similarity between two superimposed atomic coordinates (Kufareva and Abagyan, 2012), in this case the reference structure NDUFA11 and the model B0491.5. Whereas, the RMSF captured, for each residue, the fluctuation around its average position, giving a measure of the flexibility of regions of the peptide and showing regions of high flexibility as peaks in the plot.

The closer the RMSD value to zero the better, the model deviated by an average of 4.9 Å RMSD (0.49 nm) (Figure 4.9), this was a relatively high value, however, this could be due to multiple factors. The RMSD is thought to correlate inversely with the sequence similarity of the two structures (Smith, 1992), and as the primary sequences have significantly low identities of only 15.33% between B0491.5 and porcine NDUFA11, this could be a contributing factor to the high RMSD.

The regions of a protein model that are the most reliable are those directly conserved with the modelling template, whereas the regions that required building, such as non-conserved loops are a major contributor to model inaccuracy (Guex et al., 1999). The longer loop region between TMH2 and 3 could therefore be a contributing factor in increasing the RMSD value for the model. Furthermore, the RMSD value can be influenced by the fact that the reference structure was extracted as part of a larger complex (respirasome of CI, III and IV), which can increase the value due to artefacts.

The RMSD value was stable throughout the course of the simulation (200 ns) (Figure 4.9), suggesting that the model is consistent in relation to the reference structure. Taking into account the low

percentage identities between the two proteins, combined with the fact that the reference structure is from a larger complex and there is a disordered additional loop region on the model the RMSD value indicated reasonable similarity between NDUFA11 and the B0491.5 model.

The RMSF plot was a representation of molecule flexibility, in Figure 4.9 there are two distinct regions showing increased plasticity; the first was the long loop between TMH2 and 3, which corresponds to the fluctuation at around residue 50, and the second are the terminal regions. Overall the RMSF plot corresponds predictably with the secondary structure of the model, showing less flexibility in the TMH regions and increased flexibility in the loop and terminal regions. The combination of these analyses could be taken to suggest that B0491.5 was stable within the constraints of the modelled structure.

4.6 Investigating cardiolipin interactions

Cardiolipin (CL) is a lipid predominantly found in the inner mitochondria membrane (Paradies et al., 2014; Houtkooper and Vaz, 2008), where it is known to interact with the respiratory complexes (Jussupow et al., 2019; Arnarez et al., 2013; Duncan et al., 2016), but exact binding motifs have been hard to pinpoint. The structure of the respirasome (5GUP) (Wu et al., 2016) has a CL molecule bound at the site of the NDUFA11 'channel', between the TMH of the protein and the membrane arm of complex I. This can be seen from multiple angles in Figure 4.8, with the phospholipid head of the CL molecule facing up into the matrix.

When analysing the cryo-EM structure of NDUFA11, and the model of B0491.5, residues that potentially interact with CL were compared between the two structures, shown in Figure 4.10. These six residues from each structure are also highlighted in yellow in the sequence alignment in Figure 4.7. They were selected based on evidence from previously published literature regarding residues that bind CL (Jussupow et al., 2019; Arnarez et al., 2013), including specific residues in NDUFA11 identified by the authors that solved the 5GUP porcine respirasome (Wu et al., 2016), and proximity to the CL molecule.

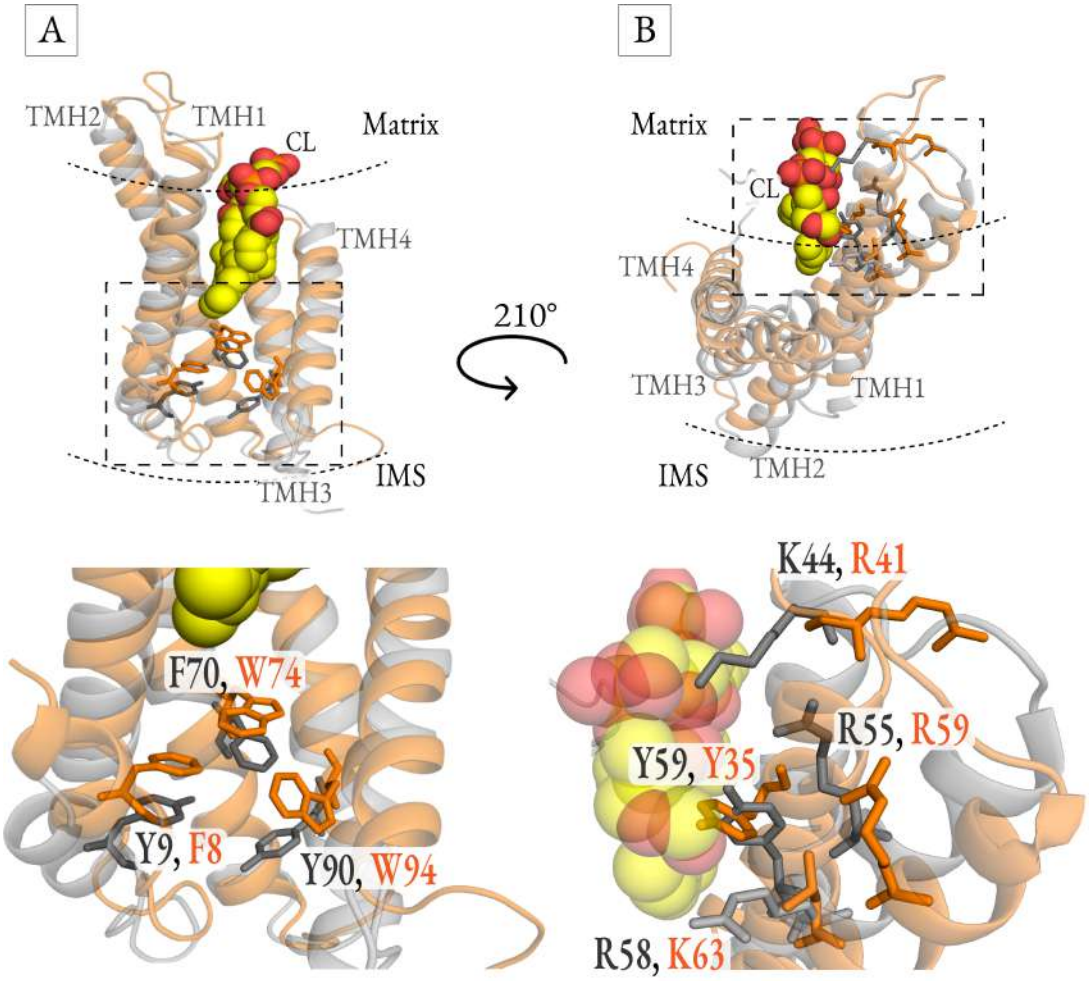

Figure 4.10: B0491.5 and cardiolipin interacting residues - B0491.5 homology model is shown in orange, NDUFA11 structure shown in grey, with CL in yellow/red. Dotted curved line represents the boundaries of the membrane. **Top panel:** membrane view of different orientations of a B0491.5 and NDUFA11 overlay. **Bottom panel:** zoomed in regions of the dotted box areas of the top panel. Residues labelled in the figure respond to the NDUFA11 structure (grey), B0491.5 homology model (orange).

Figure 4.10 (A) features three aromatic residues facing towards the IMS side of the protein, although not within a particularly close proximity to the CL molecule itself, they formed an interesting aromatic triad between CL and the IMS. Interest in the aromatic triad came from the nature of the three residues, which could potentially act to 'close off' the channel formed between NDUFA11 and the CI matrix arm from the IMS. Additionally, there was strong structural conservation between the model and NDUFA11 structure, with the three residues orientated in a similar manner, as well as amino acids with similar properties being conserved at those positions. This both suggests a functional role for the residues, as well as supporting B0491.5 and NDUFA11 being homologous.

The four residues highlighted in Figure 4.10 (B), likely make direct contact with the CL molecule. Three of the residues are referenced by the authors in relation to the porcine respirasome (Wu et al., 2016), suggesting that NDUFA11 forms four hydrogen bonds with CL via residues R58, Y59 and K44. Analysing the model, amino acids with similar properties are found to roughly overlay with these NDUFA11 residues. On the second TMH where R58 sits, a similarly basic lysine residue (L63) was found on THM2 of the B0491.5 model. NDUFA11 residue Y59 was located on TMH3, and on the model a tyrosine residue (Y35) was orientated towards to CL and occupying the same space, however, this residue was located on B0491.5 TMH2, suggesting that although variation has arisen in the primary sequence of the two homologous proteins, structural homology has been maintained in relation to lipid binding activity.

The third residue referenced in (Wu et al., 2016), NDUFA11 K44, was located at the end of TMH2 and was orientated towards the CL molecule. At the same position on the B0491.5 model was residue R41, however in the model the residue was facing away from the CL. This opens up the possibility of the CL binding residues operating in two binding states, in an on/off mechanism, however it also could be an artefact of the model.

When compared to the sequence alignment, there was not strict conservation in the primary sequence for the CL binding residues, which could potentially be surprising considering how crucial CL binding was likely to be in relation to the function of the protein. However, there was strong structural conservation, particularly when looking at Tyr(59) on the model, which structurally orientates

itself directly towards CL and occupies the same space as Tyr(35) in NDUFA11, despite them being on different helices. Additionally, in the comparative residues where the exact same residue was not conserved a residue with similar properties are found. Examples being lysine and arginine, and the aromatic residues phenylalanine, tryptophan and tyrosine.

4.7 Investigating additional conservation between B0419.5 and NDUFA11

In addition to the residues that may interact with CL, the structure of porcine NDUFA11 and model were analysed in relation to somatic mutations in NDUFA11 as determined by COSMIC: the Catalogue Of Somatic Mutations In Cancer (Tate et al., 2019). The COSMIC database was used to identify residues in NDUFA11 that had been found to be mutated in human cancers, as an indication that they potentially held an important function. Of these residues, it was found that of the 90% of mutations that are highly conserved in *S. scrofa*, 75% are also strictly conserved in *C. elegans*. Furthermore, they are within a close proximity to each other on the primary structure and overlay significantly structurally. These residues are highlighted on the sequence alignment in Figure 4.7 in purple. Of the ten conserved somatic mutations between the structure and model, three are strictly conserved in the primary sequence, see Figure 4.7, residues highlighted in purple surrounded by a black box. Furthermore, the observation that the residues, which are likely of functional importance, are similarly patterned between the two structures provides additional support for B0491.5 being a NDUFA11 homologue.

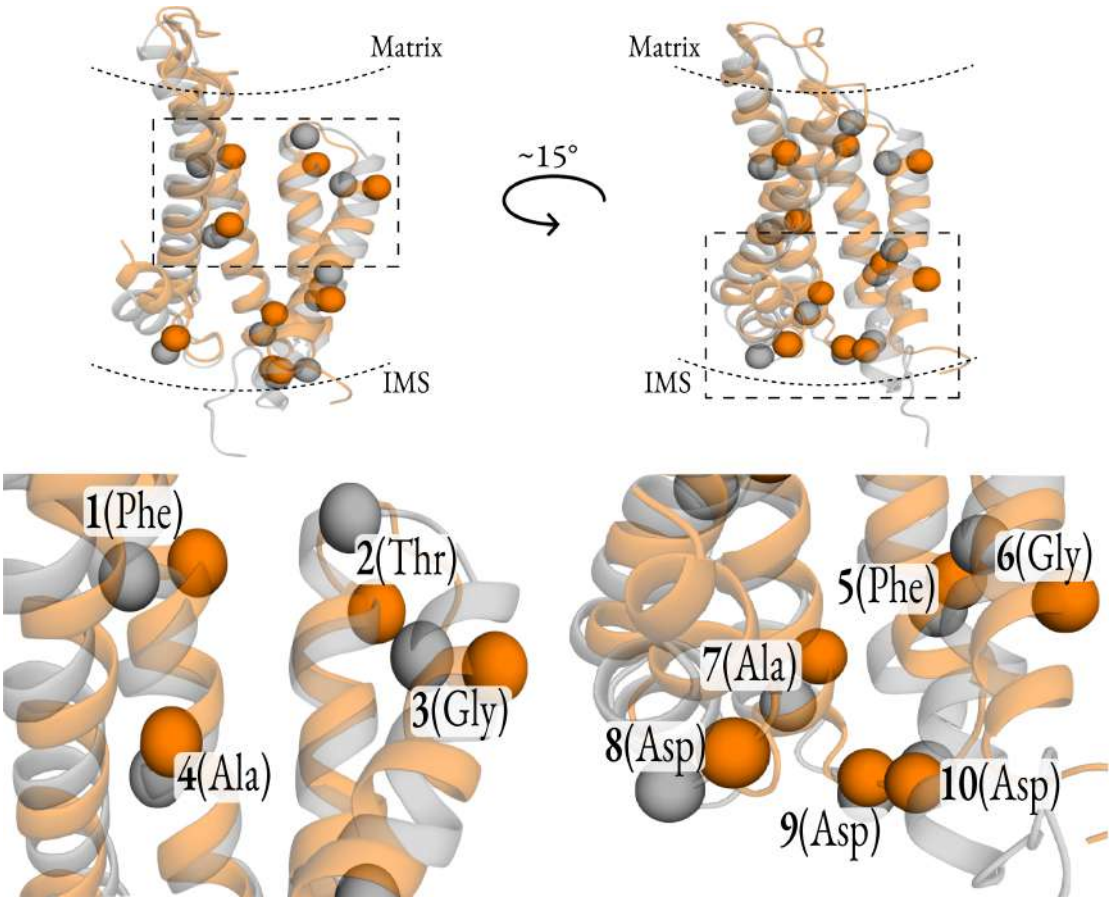

Figure 4.11: NDUFA11, the B0491.5 model and somatic mutations - B0491.5 homology model shown in orange, NDUFA11 structure shown in grey. Dotted curved line represents the boundaries of the membrane. **Top panel:** membrane view of different orientations of a B0491.5 and NDUFA11 overlay. **Bottom panel:** zoomed in regions of the dotted box areas of the top panel. Residues labelled in the figure respond to the residues that undergo somatic mutations in both the B0491.5 homology model and porcine NDUFA11

4.8 Chapter discussion

Bioinformatic data mining of mammalian NDUFA11 using psiBLAST and investigation of phylogenetic relationships using TreeFam, followed by a literature search which showed B0491.5 was enriched in the mitochondria, provided promising data suggesting *C. elegans* B0491.5 is a homologue of NDUFA11. The primary sequence showed low sequence identity, with a particularly long N-terminal region on B0491.5, that is not shared with mammalian NDUFA11 sequences. However, analysis of secondary structure looking at TMHs in NDUFA11, and predicted TMH regions in B0491.5 suggested that the proteins shared secondary structure homology. Furthermore, the proteins shared thirteen strictly conserved residues. The bioinformatic data provided enough evidence to warrant further investigation, using biological analyses to validate the finding.

Section 4.3 outlines the solubilisation of mitochondria in two contrasting detergents, and separation of the native respiratory complexes by BN PAGE. The composition of the complexes within the BN PAGE bands was established using in-gel complex activity data, 2D analysis and previously published data. This data served two purposes, firstly, it validated the organisation of *C. elegans* respiratory complexes, including supramolecular organisation. Secondly, it facilitated the investigation of the subcellular location and association to CI, of B0491.5. The 2D analysis, with accompanying antibody data localises B0491.5 to CI, in both digitonin conditions, and importantly, also in TX100, where CI was found as an individual entity. The antibody data was supported by in-gel assays identifying the same bands as complex I, and further corroborated with shotgun mass spectrometry. Together this data provides demonstrative evidence of localisation of B0491.5 to respiratory complex I.

To build on the affirmation of B0491.5 localisation to complex I, and to provide evidence of a homologous relationship specifically to NDUFA11, a homology model of B0491.5 was made. Although the model had to be taken with an understanding of its internal bias, it showed unmistakable comparability to NDUFA11. The fitting of B0491.5 to a four TMH structure, which the RMSD and RMSF data show could be a thermodynamically plausible conformation, provides strong evidence of homology to NDUFA11, as it is the only accessory subunit of CI with a four TMH structure. Furthermore, the model features a range of structurally and functionally conserved residues with NDUFA11, primarily

in relation to CL binding. As discussed in Section 1.1.1.2, it has been suggested that CL plays an important role within the respiratory complexes, both in their activity and structural integrity (Paradies et al., 2014; Zhang et al., 2002; Böttinger et al., 2012), but how this role is mediated is not currently well understood. As NDUFA11 is a CL binding subunit, it could provide an excellent opportunity for future research exploring the function CL plays in relation to complex I and the supercomplex, by investigating the impact of perturbing NDUFA11: CL interactions. As data from the model suggests that B0491.5 shows a similar CL interacting relationship as NDUFA11, the *C. elegans* model can confidently be used to carry out this experiments.

All together the bioinformatic, proteomic and computational data provides strong evidence of B0491.5 as an homologue of NDUFA11, the project can now utilise the *C. elegans* toolkit to investigate B0491.5 as a subunit of complex I, and extrapolate the findings accordingly.

Chapter 5

Utilising the *C. elegans* toolkit to investigate the loss of B0491.5

5.1 Chapter introduction

Chapter four has established B0491.5 as an homologue of NDUFA11, this chapter utilises the *C. elegans* toolkit to investigate the effect of losing NDUFA11 from the ETC. Two approaches are discussed in this chapter, firstly the genetic manipulation tool CRISPR was used to create a complete knockout (KO) of *b0491.5*. The second uses RNA interference (RNAi) to suppress expression. The impact of both methods on worm physiology are characterised in Sections 5.2 and 5.3 respectively. The chapter goes on to explore the effect of *b0491.5(RNAi)* on the immediate protein environment in ETC organisation, and on a whole proteome level with mass spectrometry.

The supramolecular organisation of the *C. elegans* mitochondrial ETC was validated through BN PAGE in Chapter 4, Figures 4.3 and 4.4, showing the existence of supercomplex entities under digitonin solubilisation. It has been suggested that NDUFA11 is integral in complex I assembly or stabilisation (Section 1.1.7), and loss of the subunit leads to a decrease in intact CI (Andrews et al., 2013). Moreover, the decrease in one of the ETC complexes is thought to impact on the supramolecular structure of the complexes (Section 1.1.6.2). An additional factor, is the location of NDUFA11 at the interface between CI and CIII in the respirasome, suggesting it could play a direct structural role within the respirasome. Therefore, the organisation of the respiratory complexes in B0491.5 deficient

mitochondria was explored (Section 5.4), to investigate the effect the loss of the subunit has on ETC protein organisation, either as a direct effect due to loss of contact points between CI and CIII, or as a consequence of decreased CI.

Finally, as mentioned above, changes in one ETC complex is thought to have an impact on other complexes in the system. Section 5.5 examines the expression level of mitochondria proteins using quantitative mass spectrometry, to explore if the changes in complex organisation, including loss of supercomplex formation, seen in Section 5.4 could be attributed to a general down regulation of the respiratory proteins, of if perhaps they are re-organised. The cytosolic proteome was briefly explored to determine if changes in the respiratory proteins has a wider cellular impact.

5.2 CRISPR knockout of B0491.5

The initial approach to investigate loss of B0419.5 was to edit the *C. elegans* genome using the CRISPR-Cas9 system, which uses a guide RNA sequence to the target gene to facilitate specific double-strand DNA cutting, allowing permanent genome wide removal of the gene. This relatively recent technique, implemented in the laboratory from 2015, revolutionised the ease at which gene manipulation could be achieved in *C. elegans*, particularly in relation to removing regions of genetic material. Previously, to reduce gene expression the tool available was RNA mediated interference (RNAi) which has variable levels of suppression.

5.2.1 Creation

The CRISPR mutant was created by cutting the *b0491.5* gene at two sites, then repairing with a template that created a frameshift deletion between residues 46 and 193, causing the protein to be reduced by 139 bp and to be non-functional. The CRISPR deletion of *b0491.5* was designed and carried out by Patty Kuwabara, unless otherwise indicated further work with the strain was my own.

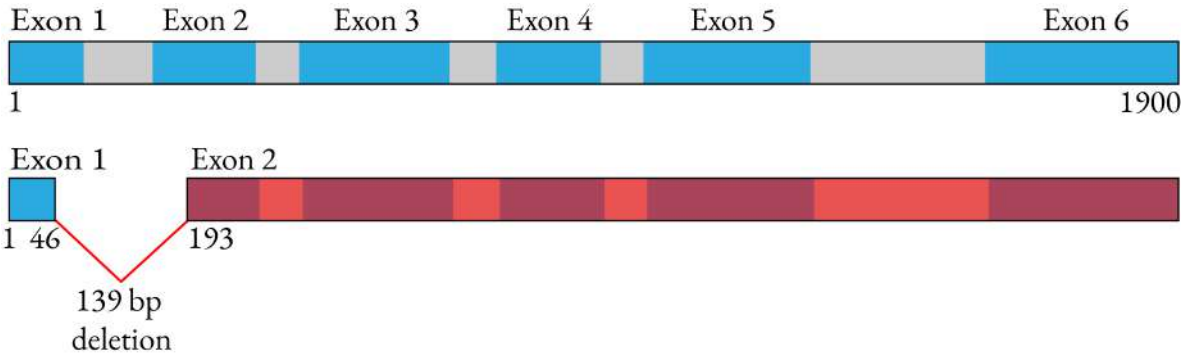

Figure 5.1: B0491.5 CRISPR mutant - schematic representation of the CRISPR mutation introduced to *b0491.5*. Caused a deleted region in between position 46 and 193, introducing a frameshift mutation which perturbs the rest of the sequence represented in red.

The CRISPR strain was screened using the co-CRISPR method, using *dpy-10* as the Co-CRISPR marker, as described previously (El Mouridi et al., 2017). The *dpy-10* mutation is indicative of a both a successful injection event and, also, active CRISPR protein which allows targetted screening for the desired CRISPR edit. Successful *b0491.5* deletion events were confirmed by PCR, see materials and methods Section 2.5 for full protocol on PCR for detecting *b0491.5* deletion.

5.2.2 Phenotype

The CRISPR mutant displays a common mitochondrial defect phenotype, where development arrests at L2 stage, highlighted in Figure 5.2. *C. elegans* undergo a metabolic shift at the L2 larval stage (Section 1.2.1.1), and this developmental defect may be representative of the animals not being capable of the increased demand on respiration through complex I. In addition to a developmental arrest, preliminary analysis in ImageJ on balanced *b0491.5* KO worms suggested that *b0491.5* KO worms also display anatomical changes, being slimmer and longer. Measurements of the KO strain averaged a length of 323μm and width of 15.45μm, compared to a length of 287μm and width of 21μm in N2 L2 worms, however to be confident in the observations, more repeats would be necessary as the analysis was generated from an n of 3.

The phenotype of L2 larval arrest can be distinguished from animals entering the dauer stage, as although animals enter dauer formation from L2 stage, animals in this state develop a distinctive anatomy, predominately appearing very thin, with a length-width ratio of 30: 1. It was possible to detect by eye that the B0491.5 CRISPR mutant does not enter a dauer state, and the preliminary measurement data supported this, with a suggested length-width ratio of 21: 1. Somewhere in between dauer and the control, which has a length-width ratio of 13.5: 1. This was important to distinguish, as the causative factors behind the different states, either dauer or L2 arrest, are different, as discussed in Section 1.2.1.1.

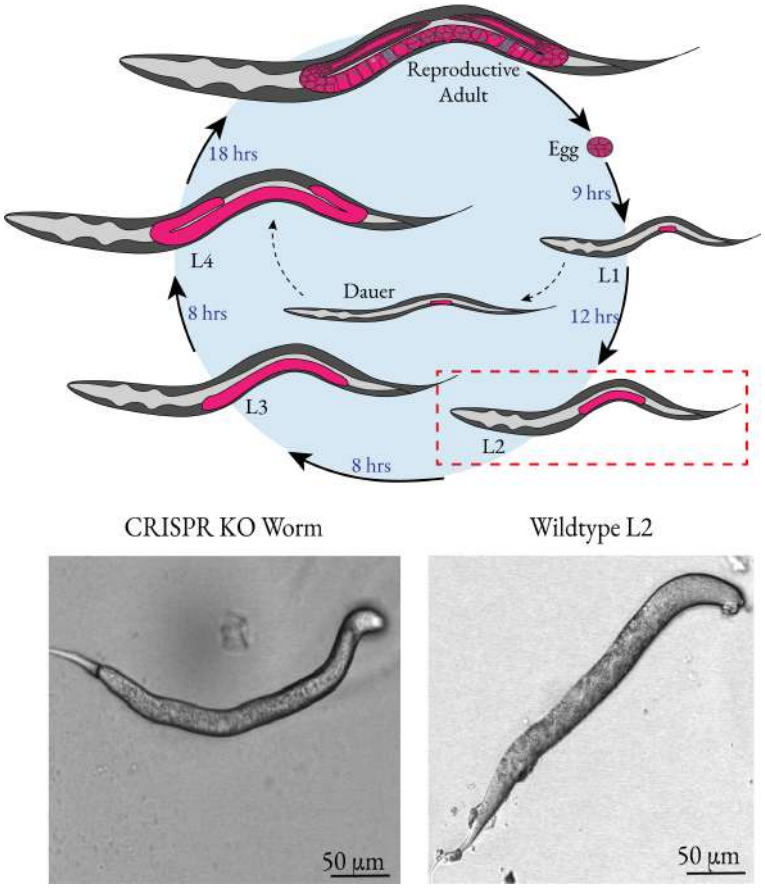

Figure 5.2: Characterising the B0491.5 knockout phenotype - **Top panel:** repeat of schematic of *C. elegans* lifespan used in Figure 1.14, with the developmental stage L2 highlighted by dotted red box. **Bottom panel:** Brightfield images of B0491.5 KO worm (left) and a comparative N2 L2 worm (right). Scale bar: 50 μm.

Arresting at L2 stage, and not developing to an egg-laying adults meant the homozygote Δ*b0491.5* animals would lay no progeny and the strain was lethal, where lethal is defined as any mutation that prevents survival or reproduction (Edgley et al., 2006).

5.2.3 Maintenance and balancing

Due to the lethality of the homozygote Δ*b0491.5* mutant, to be maintained, the strain needed to be balanced. A balancer is a genetic construct or chromosomal rearrangement that allows stable maintenance of lethal or sterile mutations in heterozygotes (Edgley et al., 2006). An appropriate balancer needed to be selected for the mutation; balancer *mnC1* (strain CGC43) was chosen as it featured an inverted chromosome II, and had an integrated GFP construct under the control of a pharynx specific promoter (see Section 2.1 for full annotation). This allowed Δ*b0491.5* homozygotes to be distinguished from the population by a lack of GFP signal.

Furthermore, the co-CRISPR marker method introduced a *dpy-10* mutation in the strain. The *dpy-10* gene was edited to the dominant *dpy-10(cn64)* mutation, giving a homozygote dumpy phenotype and heterozygote roller phenotype. This could be seen in the (Δ*b0491.5*/N2) heterozygote strain as a roller, however the homozygote phenotype was masked by phenotype created by an absence of *b0491.5*. Therefore, in addition to balancing the strain, the *dpy-10* mutation needed to be crossed out of the Δ*b0491.5* strain.

It was desirable to remove the *dpy-10* mutation from the *b0491.5* KO strain before moving forward, to allow the effects of the Δ*b0491.5* to be clearly distinguished from a potential combined effect of having a *dpy-10* homozygote mutation. As *b0491.5* and *dpy-10* were both on chromosome II, a recombination event was required to out cross the *dpy-10* mutation. *dpy-10* was located at position 0 on chromosome 2, and *b04915* was at position 3.5, creating a distance of ≈3.5 map units from each other. Therefore it was estimated that ≈3.5 in every 100 *b0491.5*/+ animals would experience a recombination event, where by the *dpy-10* mutation would recombine away from the allele carrying the *b0491.5* mutation, producing a *b0491.5*/+ genotype with a WT phenotype.

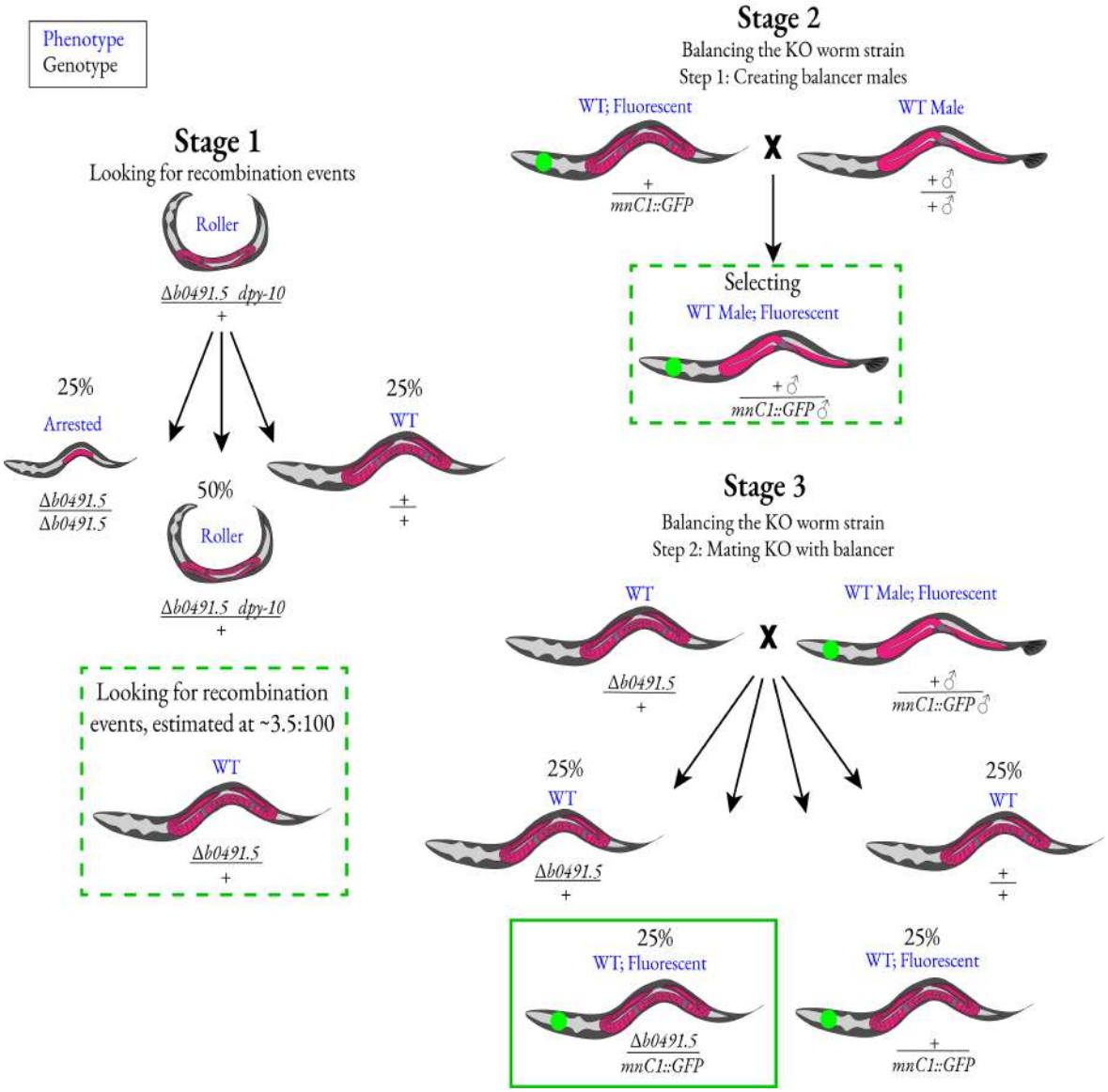

Figure 5.3: Balancing the *b0491.5* CRISPR KO strain - A schematic representation of the stages required to cross out the *dpy-10* mutation and balance the Δ*b0491.5* gene. **Stage 1**: looking for recombination events to cross out *dpy-10* from Δ*b0491.5*, expected to find 3.5 recombination events in every 100 animals due to the two genes (*dpy-10* and *b0491.5*) being 3.5 map units from each other. 40 WT animals were single plated and screened by PCR to determine *b0491.5* genotype (Figure 5.4). **Stage two**: generating balancer (mnc1::GFP) males for mating with *b0491.5*/+ **Stage 3**: mating the *b0491.5* deletion strain with the balancer (mnc1::GFP), successful matings can be determined by a WT:GFP phenotype and PCR screened for *b0491.5* genotype (Figure 5.5)

Figure 5.3, stage 1, outlines how the recombination event was identified. Picking WT phenotype progeny from an individual heterozygote (Δ*b0491.5*;*dpy-10*/+) animal, and screening the progeny by PCR to identify WT worms with a Δ*b0491.5* genotype. At this stage 40 WT worms were picked and single plated, once they had laid progeny, thus securing the line, they were screened by single worm PCR for the *b0491.5* deletion (Figure 5.4).

There was one clear recombination event, animal 25, indicated in Figure 5.4 by a green box, which presented a non-roller WT phenotype, and producing two bands in the screening PCR, with the lower 502 bp band indicative of the *b0491.5* deletion. There were two other double bands (gel lanes 7 and 39), however they were not as conclusive due to the band appearing larger than 502 bp. Based on the screening in Figure 5.4, the progeny of animal 25 were selected to balance the deletion strain.

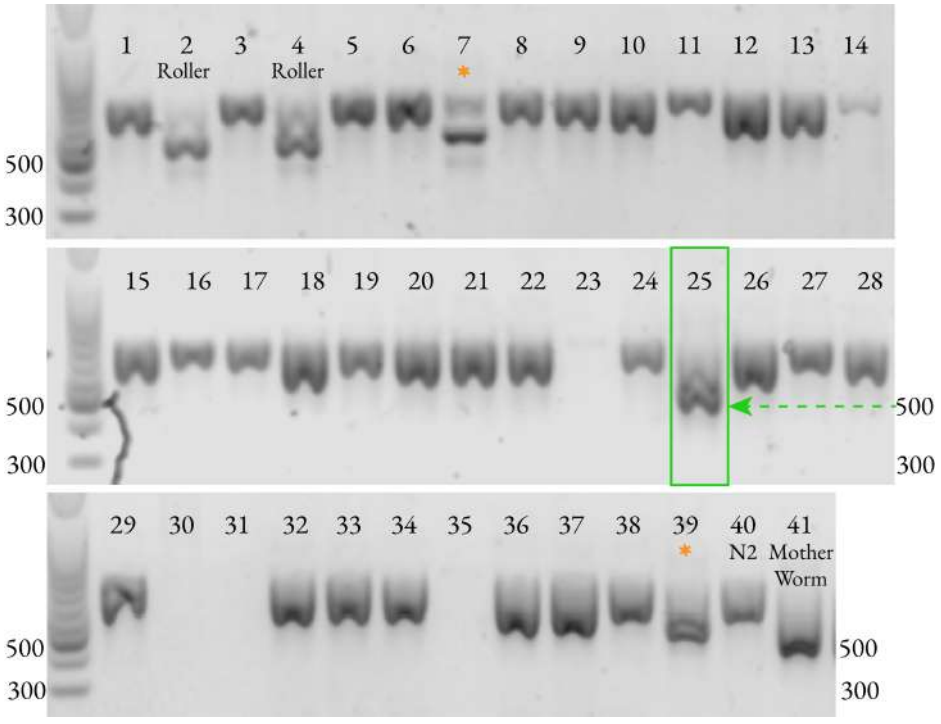

Figure 5.4: Screening for recombinant events in Δ*b0491.5* strain - SW PCR results for 39 phenotypically WT worms, progeny of a single Δ*b0491.5*, *dpy-10*/+ animal. A double band with the smaller product at 500 bp was indicative of Δ*b0491.5*/+, whereas one band at 660 bp was representative of WT *b0491.5*, +/+. Successful recombination events are marked with a green box. Control is lane 40, N2.

As Δ*b0491.5* homozygotes are lethal, arresting at larval stage 2, and producing no progeny, the deletion alone was prone to being selected out and cannot be maintained as Δ*b0491.5*/+. Additionally, the Δ*b0491.5*/+ strain was susceptible to recombination events and loss of the Δ*b0491.5* deletion. Therefore, to maintain the strain, the balancer *mnC1* was selected for mating with Δ*b0491.5*/+, full annotation of the balancer can be found in Materials and Methods Section 2.1.

A classical crossover suppressor allele, the *mnC1* strain featured an inverted chromosome II, which made the balanced Δ*b0491.5* less prone to recombination events. It also contains a GFP marker on chromosome II, driven by a pharynx promoter, which allowed straight forward identification of Δ*b0491.5* homozygote worms through identifying non-GP animals (Dejima et al., 2018). The *mnC1* strain had further additions of *dpy-10* and *unc-52* mutations, meaning homozygote balancer worms (*mnC1*/*mnC1*) are also easily identifiable from the brood, as they presented with a stick unc phenotype. This made the Δ*b0491.5*/*mnC1* balanced strain helpful in two ways, it divided the population up into easy to identify phenotypes, but in addition the stick unc *mnC1* homozygotes are sterile. Therefore, the Δ*b0491.5*/*mnC1* animals were easy to select for, allowing stable propagation of the Δ*b0491.5* mutation.

As shown in Figure 5.3, achieving the balanced strain required mating Δ*b0491.5*/+ hermaphrodites with *mnC1*/+ males, a full protocol can be found in Materials and Methods 2.4.5. Figure 5.5 details the PCR screening required during stage 3 in Figure 5.3, as the brood to select mating Δ*b0491.5*/+ hermaphrodites contains both Δ*b0491.5*/+ and +/+ animals which are phenotypically identical. Therefore, to identify the matings carried out with Δ*b0491.5*/+ animals, after exposure to *mnC1*/+ males and subsequent progeny were laid the hermaphrodites were screened for Δ*b0491.5*.

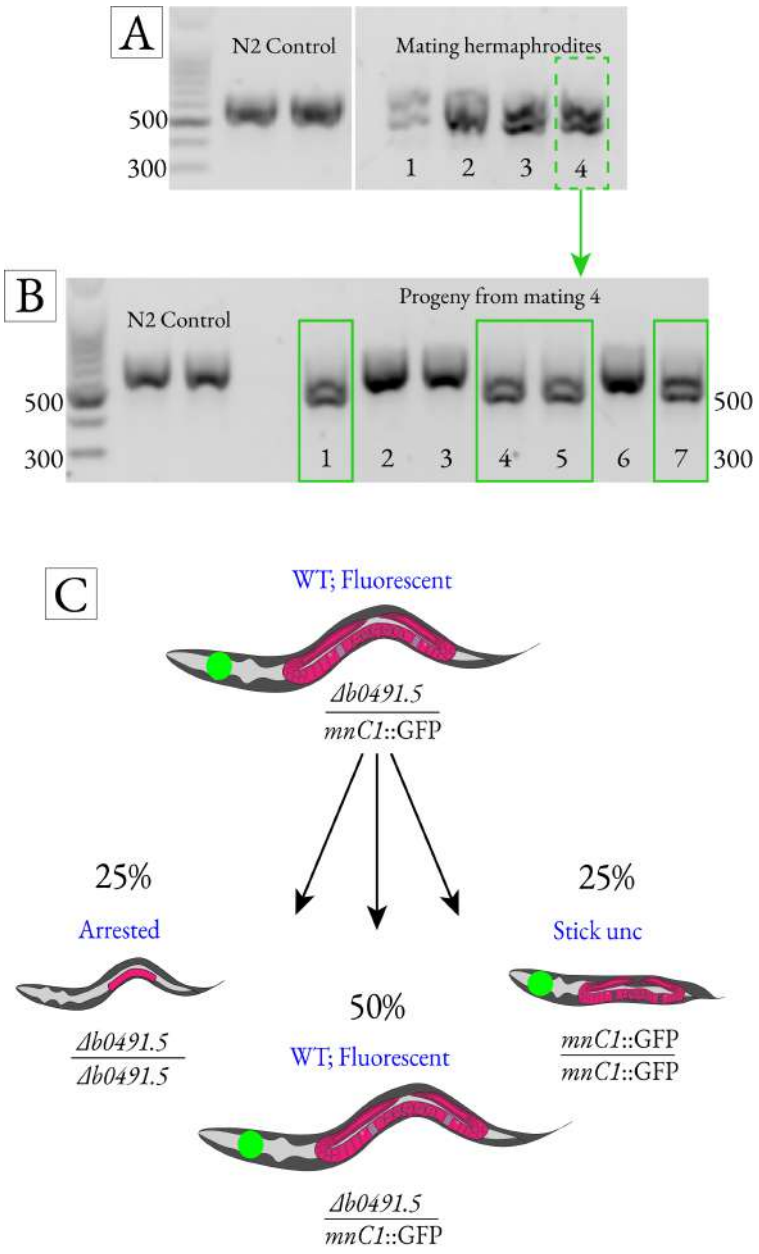

Figure 5.5: PCR screening for matings and balancer and strain phenotypes - matings between potential Δ*b0491.5*/+ hermaphrodites and *mnC1*/+ males and the subsequent progeny were screened for identification of the deletion, see materials and methods Section 2.5 for full experimental details.

Figure 5.5 (A) shows that of four matings set up, all were Δ*b0491.5*/+ hermaphrodites. Seven progeny from mating number four, indicated with the green dashed box, were single plated and screened for the *b0491.5* deletion. Four of the progeny were positive for the deletion, indicated with a solid green box.

This successful mating concluded the balancing of the *b0491.5* deletion strain, where Δ*b0491.5*/*mnC1* animals have a WT phenotype and are identifiable by a GFP signal, the strain was there on in maintained by picking WT GFP worms. As seen in Figure 5.5 (C), the homozygote Δ*b0491.5* animals could be identified as the non-GFP population, distinct from homozygote *mnC1* animals.

This section has outlined the process of creating a stable Δ*b0491.5* strain that can be maintained and, in addition, Δ*b0491.5* homozygote worms can be easily identified to further analyse in future experiments.

5.3 Establishing *b0491.5 RNAi*

The CRISPR Δ*b0491.5* strain displays a severe developmental arrest phenotype, suggesting that B0491.5 is essential for normal development. However, as Δ*b0491.5* worms arrest at L2, it was therefore difficult to obtain large volumes of material, and this was a barrier to further biochemical analysis.

To overcome this, an alternative genetic approach, RNAi, was used to suppress expression of *b0491.5* in large volumes of animals. The impact of RNAi varies from gene to gene, so it was necessary to establish the level of knockdown achieved for *b0491.5*. The control used throughout the RNAi experiments was an 'empty' feeding vector, fully described in Materials and Methods 2.4.3.

5.3.1 Initial investigation

RNAi was carried out by feeding bacteria producing *b0491.5* dsRNA (Timmons and Fire, 1998) to starved L1 larval animals (see Section 2.4.4 for full experimental details). Visual observations were carried out, in addition to whole worms taken for immunoblotting, after intervals of four and eight days (Section 2.9.2).

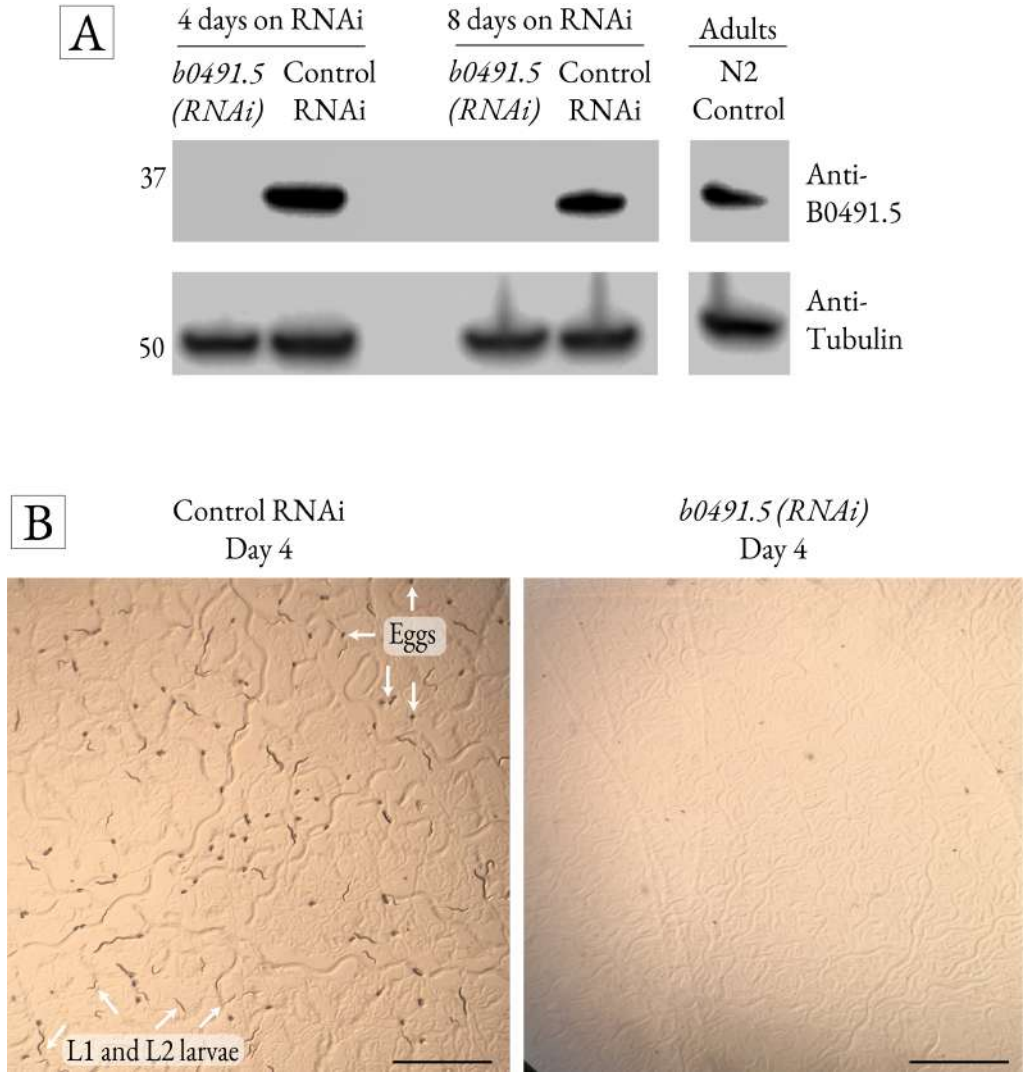

Figure 5.6: Establishing *b0491.5 RNAi* - **(A)** Immunoblot of whole worms grown on *b0491.5 RNAi* from L1 larval stage, for four or eight days, as indicated. Blotted against B0491.5, or tubulin as a control, as indicated. **(B)** RNAi plates viewed through the dissecting microscope on day 4, scale bar is 1 mm. Eggs, L1 and L2 larvae are present in the control RNAi condition, as labelled, but not in *b0491.5(RNAi)* condition

Figure 5.6 (A) indicated that there was a significant reduction in the protein levels of B0491.5, showing no detectable signal from the *b0491.5(RNAi)* samples. As a control, the blot was also probed for tubulin, showing even loading in each lane.

There was also a marked difference in animal development. In the first two days the animals developed at similar rates, however, as they entered post-embryonic development pronounced differences could be seen. By day four, control animals had begun to lay eggs and the second generation were hatching, whereas, under *b0491.5 RNAi* the animals displayed little to no egg laying, shown in Figure 5.6 (B). The animals were however growing to reach adulthood, not shown. This provided evidence that the *b0491.5 RNAi* was working, and furthermore that it had a significant impact on animal development.

5.3.2 Characterising *b0491.5 RNAi*

As initial observations showed a marked difference in reproductive capacity, a brood count of *b0491.5(RNAi)* animals was carried out. In addition, to validate previous findings in *b0491.5(RNAi)* (Chen et al., 2007), the lifespan of *b0491.5(RNAi)* animals was established, see Material and Methods Section 2.4.8 for the full protocol.

Figure 5.7 shows a significant decrease in brood count for *b0491.5(RNAi)* animals, with a near complete reduction in progeny compared to the control. Furthermore, of the few progeny laid from a *b0491.5(RNAi)* parent, they were observed to arrest at the L2 larval stage, the same phenotype as the *b0491.5* CRISPR KO strain, detailed in Figure 5.2. This was in conjunction with an observed slower rate of development for the *b0491.5(RNAi)* animals, reaching adulthood after four days as compared to three days for the control. Adulthood was determined based on worm size and gonad development.

A

	Average Total Brood Count	Developmental stage of the 2nd generation				
		L1	L2	L3	L4	Adult
Control	282	-	-	-	-	100%
b0491.5 (RNAi)	1.9	12%	88%	-	-	-

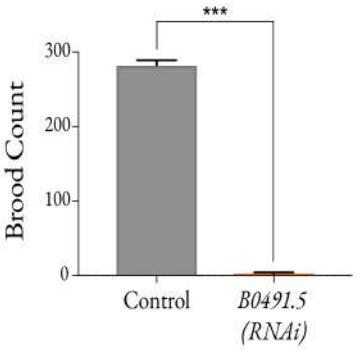

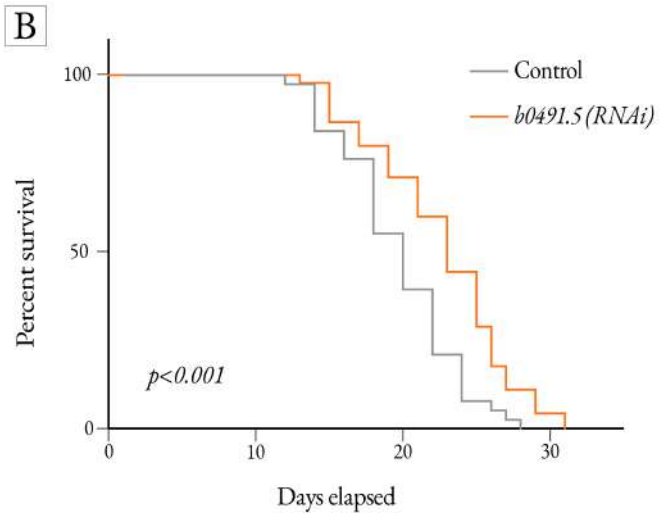

Figure 5.7: Characterisation of *b0491.5(RNAi)* I - **(A)** Brood count for *b0491.5(RNAi)* and control under RNAi suppression from hatching, n=6 for control, n=10 for *b0491.5(RNAi)*, $p < 0.001$. **(B)** Lifespan measurements were carried out on animals under RNAi feeding from L4 stage, full protocol in Materials and Methods 2.4.8. n=45 for *b0491.5(RNAi)* and n=38 for control, $p < 0.001$.

The survival curve, Figure 5.7 (B), showed an increase in lifespan of *b0491.5(RNAi)* animals, from an average lifespan of 18.7 days for the control, to 22.6 days under *b0491.5(RNAi)*. This was consistent with other published findings, in relation to mitochondrial knockdowns in general (as discussed in Section 1.2.2.2) and specifically in *b0491.5* (Chen et al., 2007).

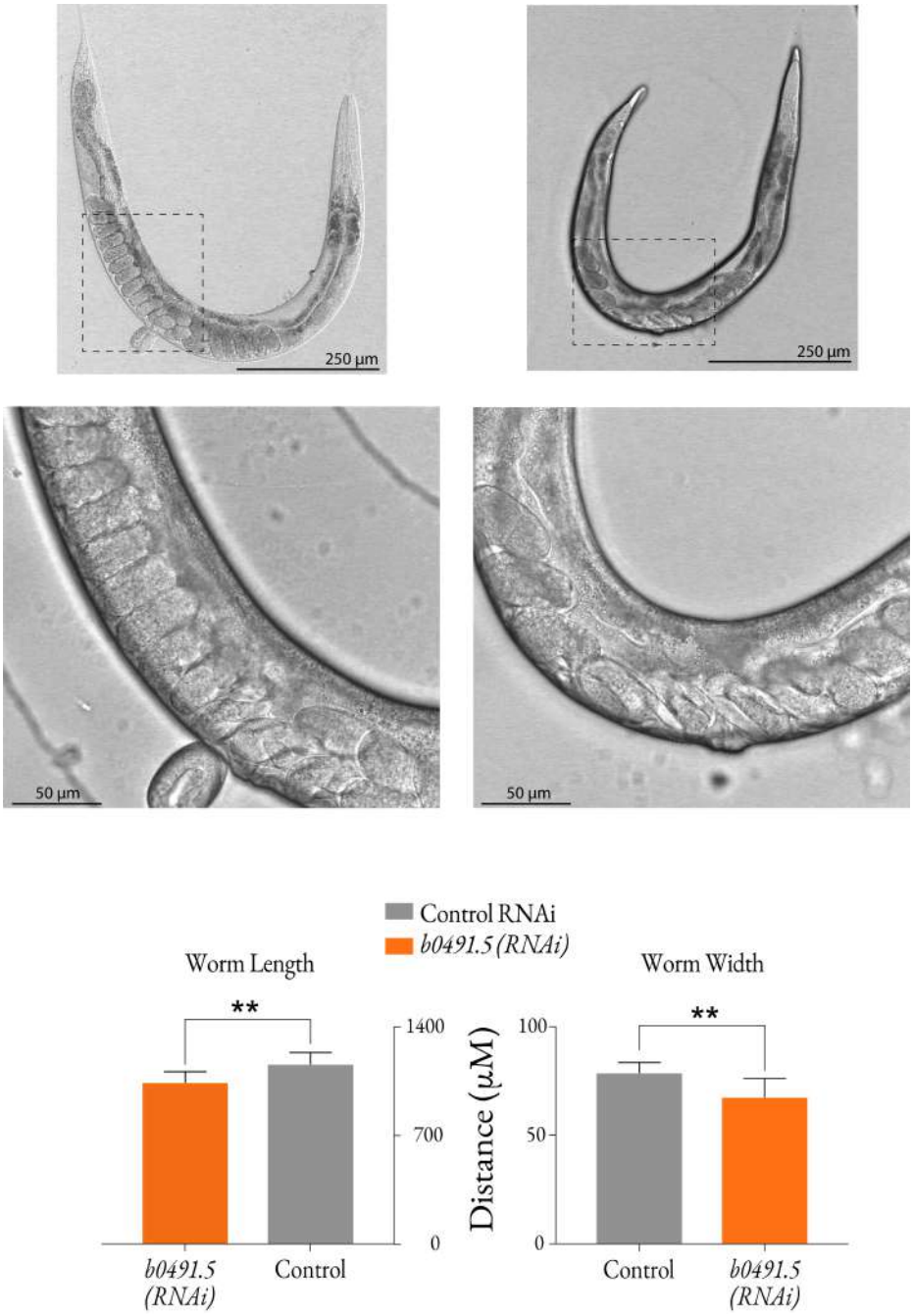

Figure 5.8: Characterisation of B0491.5(RNAi) - **Top panel**: brightfield images of either control RNAi or *b0491.5(RNAi)* adult worms, as indicated. Control and *b0491.5(RNAi)* animals were grown for three and four days respectively to reach adulthood. **Middle panel**: zoomed in brightfield image of the boxed area in the top panel focusing on the gonad area of the worm. **Bottom panel**: graphs representing the width and length 25 μm of the two worm populations, control n= 11, *b0491.5(RNAi)* = 8, two-tailed, unpaired t-test p-value < 0.05 in both conditions.

Analysis of the phenotype (Figure 5.8), shows the *b0491.5(RNAi)* knockdown worms to be slightly slimmer and shorter than the control; average widths of 79 μm and 68 μm were measured for the control and *b0491.5(RNAi)* respectively, and, average lengths of 1162 μm and 1104 μm were measured for the control and *b0491.5(RNAi)* respectively. These differences are small but consistent across the population, analysed with statistical analysis of $p < 0.05$ for both length and width measurements.

All animals included in phenotypical analysis showed some development of eggs in the gonad, indicating that the *b0491.5(RNAi)* animals were reaching adulthood. However, as shown in Figure 5.8 the gonad was less full and appears disordered. This could suggest either a defect in an egg laying, as some embryos are developing, or a defect in the animals ability to produce eggs.

5.3.3 *b0491.5(RNAi)* mitochondrial isolations

The RNAi technique was scaled up to harvest enough material to isolate mitochondria for further analysis. Significant work went into scaling up the RNAi process to knockdown a sufficient biomass of worms, see Section 3.3 in the Technique Development Chapter. Having established a protocol, it was important to determine the level of B0491.5 knockdown was consistent throughout different mitochondrial isolations.

Figure 5.9 (A) shows immunoblot data for five mitochondrial preparations, it was noted that a small signal for B0491.5 can be detected in the isolated mitochondria samples, and that this result differs marginally from the whole worm Western blot in Figure 5.6, where there was no signal at all in the *b0491.5(RNAi)* samples. It is likely that remnant levels of B0491.5 were present in the whole worm samples in Figure 5.6, but, were too low to be detected by the antibody. However, due to enrichment in the isolated mitochondria samples, they appeared in the blots in Figure 5.9 (A).

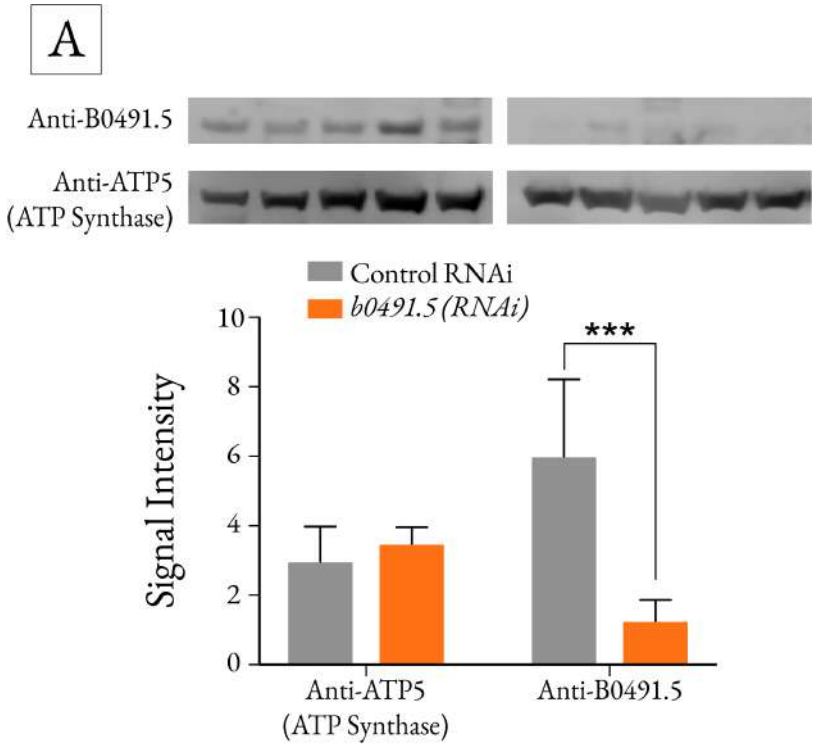

B

	Quantative Mass Spec Log2(Abundance)	Log2FC
Control	8.18	2.52
b0491.5 (RNAi)	5.66	

Figure 5.9: Quantification of *b0491.5(RNAi)* knockdown in mitochondrial isolations - **(A)** immunoblot blot of five mitochondrial isolations. 50 μg of isolated mitochondria was loaded on an SDS-PAGE gel (Section 2.9.2) and transferred to a PVDF membrane (Section 2.10.1), the membrane was blotted with B0491.5 and ATP synthase subunit ATP5 primary antibodies and fluorescent-conjugated secondaries. Band intensities were determined by LI-COR software Image Studio and plotted in Graphpad. The data indicates a knockdown of 84% of B0491.5 protein levels (6-fold decrease). **(B)** Analysis of B0491.5 protein expression levels, from quantitative mass spectrometry analysis of *b0491.5(RNAi)* (Materials and Methods, Section 2.11, and results Section 5.5) were used as a measure of RNAi knockdown, a $\log_2$FC of 2.52 is equivalent to a knockdown to 83% of control levels (5.74-fold decrease)

Figure 5.9 shows consistent protein knockdown across multiple isolations, the extent of the reduction was assessed by immunoblot blot and quantified by fluorescent secondary antibody, determining an average reduction of 84% of B0491.5 protein levels. Additionally, two isolations were analysed by quantitative mass spectrometry, shown in Figure 5.9 (B), which determines a $Log_2(2.5)$ fold decrease in the amount of B0491.5 protein in the *b0491.5(RNAi)* isolated mitochondria as compared to the control, equivalent to a 83% reduction in expression. This data demonstrated consistent protein knockdown throughout different mitochondrial isolations, and the extent of protein knockdown was validated by immunoblot and mass spectrometry data.

5.4 Investigating ETC organisation and activity

As discussed in the Section 1.1.7 and the chapter introduction Section 5.1, complex I accessory subunit NDUFA11 has been shown to be integral in the assembly and stabilisation of the complex, with loss of the subunit leading to complex disassembly (Andrews et al., 2013). In addition, structural data has shown the subunit is located at the interface of CI and CIII in the respirasome, however, its role within the supramolecular organisation of the respiratory complexes has not been defined. The organisation of the respiratory complexes in mitochondria with reduced NDUFA11 homologue B0491.5 was explored using BN PAGE and second dimension analysis. Section 4.3 validated the organisation of the *C. elegans* ETC, this section details data from control and *b0491.5(RNAi)* isolated mitochondria investigated with the two detergents previously discussed, digitonin and TX-100.

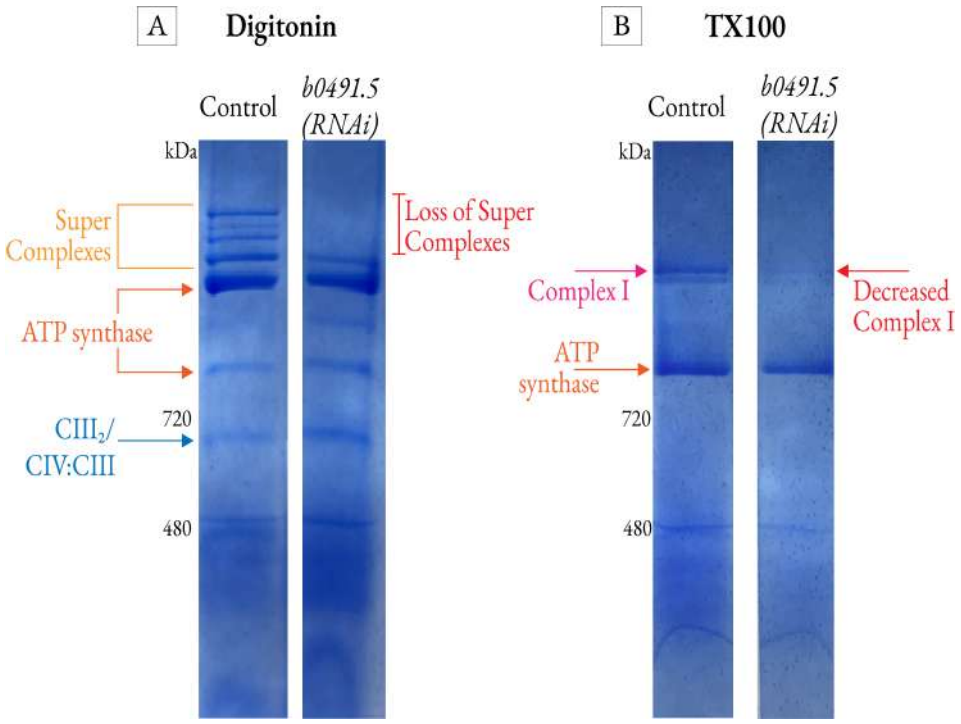

Figure 5.10: ETC organisation with suppressed B0491.5 - Isolated mitochondria from adult *C. elegans* grown on either control or *b0491.5* RNAi bacteria (Materials and Methods, Section 2.4.4.1), as indicated. Solubilised with either digitonin **(A)** or TX100 **(B)**. Gels are stained by Coomassie Blue. Annotations of the bands presenting on the gel are as decided in Figure 4.3

Figure 5.10 (A) shows that under solubilisation with digitonin there was a distinct loss of the higher order supercomplex structures in the *b0491.5(RNAi)* condition, as compared to the control. Other complexes shown on the gel, such as ATP synthase and smaller bands of CIV/CII, appear to remain constant. Under TX100 solubilisation, Figure 5.10 (B), a reduction in the amount of complex I was observed, with the other prominent band on the gel, ATP synthase, remaining constant.

Using an in-gel assay the activity of complex I was investigated, shown in Figure 5.11, this analysis supports the protein staining data in Figure 5.10. Under digitonin stabilisation, Figure 5.11 (A), *b0491.5(RNAi)* conditions show only one band with complex I activity, potentially individual complex I, but no CI activity from higher order structures, as compared with the control, which shows four distinct bands. Figure 5.11 (B) TX-100 solubilisation shows a clearly observable decrease in the activity of CI.

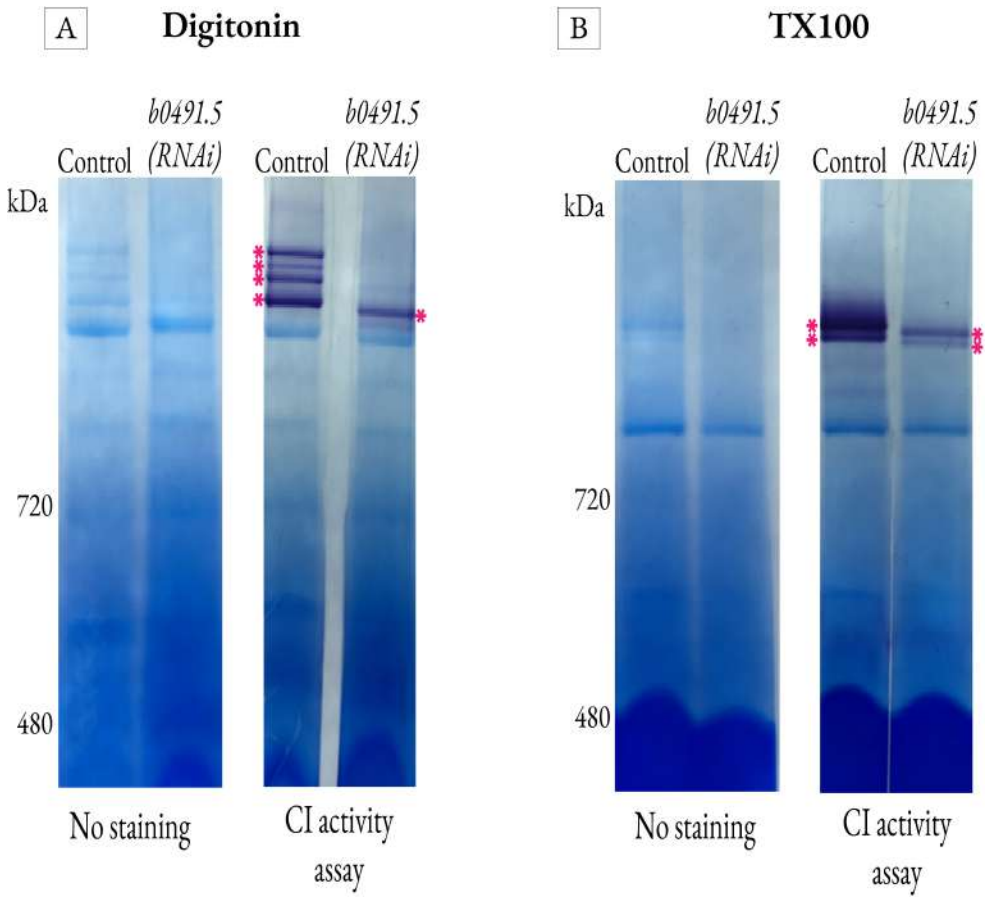

Figure 5.11: BN PAGE in-gel CI activity with suppressed B0491.5 - Isolated mitochondria from adult *C. elegans* grown on either control or *b0491.5 RNAi* bacteria, as indicated. Solubilised with either digitonin **(A)** or TX100 **(B)**. CI in-gel activity assay was carried out where indicated.

Second dimension analysis of the BN PAGE gels allowed visualisation of the subunit composition within the native complexes, shown in Figure 5.12. Again, the loss of supercomplexes was clearly observed under digitonin solubilisation for *b0491.5(RNAi)*, as compared to control conditions. Furthermore, the decrease in complex I in *b0491.5(RNAi)* with TX100 was clearly visualised, showing a reflective decrease in CI activity to the decrease in amount of CI show in in 5.10 (B). From this analysis, smaller changes in the protein amount in each BN band can be detected, and this potentially reveals an increase in the amount of $CIII_2$ or CIII: CIV supercomplexes, that was not detectable from observing the BN PAGE. The change was not as distinctive as the variations in the supercomplexes and CI, but, it could indicate an increase in CIII: CIV supercomplexes as an alternative organisation, when, due to reduced B0491.5 and CI, they are unable to form respirasome structures.

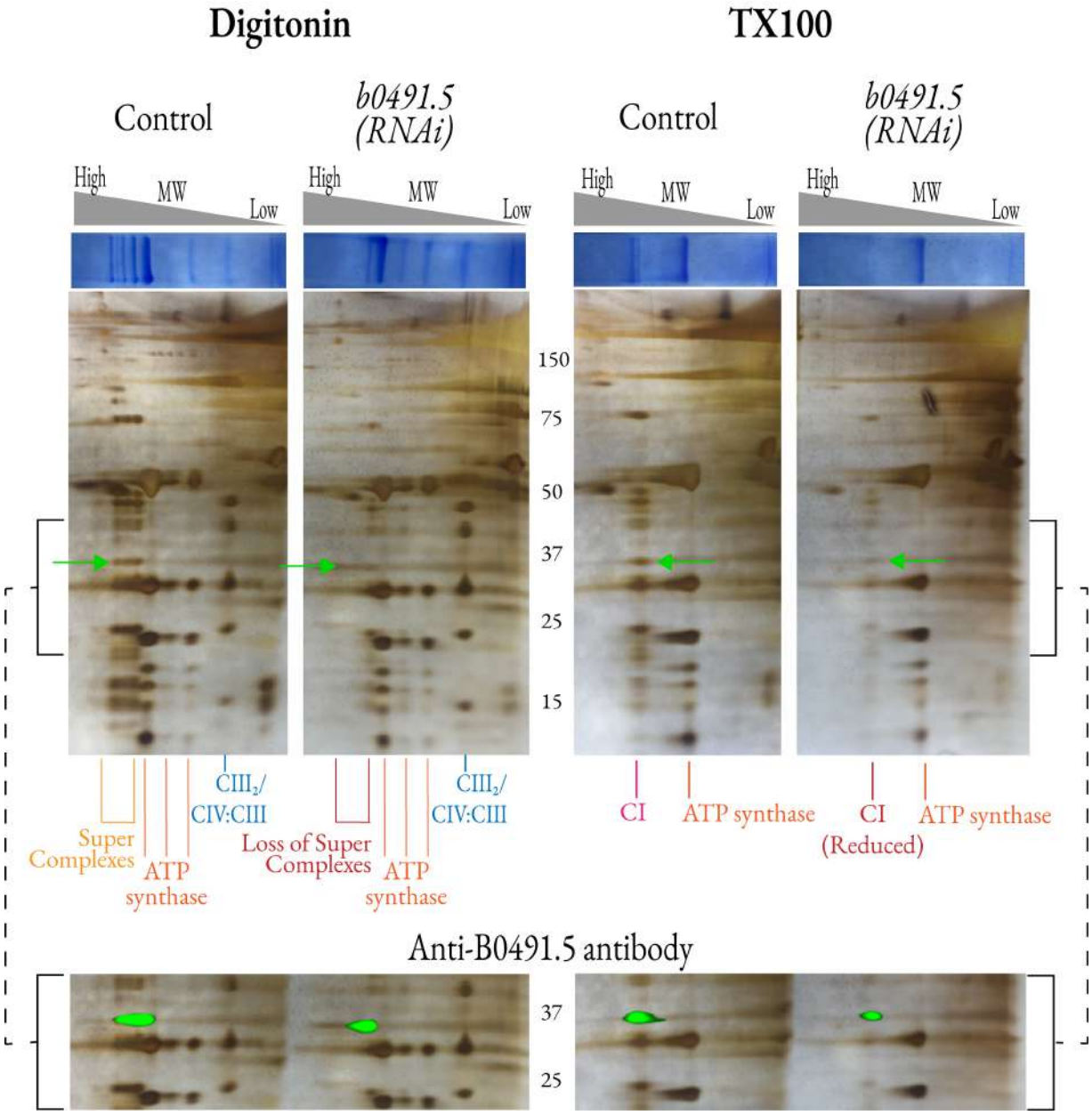

Figure 5.12: 2D analysis of ETC organisation with suppressed B0491.5 - **Top panel:** BN PAGE 2D protein separation in reducing conditions (Materials and Methods Section 2.9.3.2). Green arrows indicate the position of the B0491.5 band on the silver stained 2D gel. **Bottom panel:** Duplicate view of the area indicated on the top panel, showing the antibody signal for B0491.5, superimposed on silver stained gel.

5.5 Quantitative mass spectrometry

In Section 5.4, the effect of B0491.5 suppression on the organisation of the ETC complexes was investigated, showing that under conditions with lower B0491.5 levels, there was a severe impact on the supramolecular organisation of the ETC, showing a reduction in both intact complex I and higher order supercomplex structures.

To explore the impact B0491.5 suppression had on the protein expression of the ETC subunits, and additional key mitochondrial proteins, quantitative mass spectrometry was carried out. The aim of the analysis was to investigate if the loss of supercomplexes was representative of an overall reduction in expression of the respiratory complexes, or, if they were perhaps being re-organised. Cytosolic fractions were also investigated, to make preliminary explorations into the wider cellular effects these changes in respiratory organisation could be having.

The quantitative proteomic approach, Tandem Mass Tagging (TMT), was carried out by the proteomic facility at the University of Bristol and guidance was received from Philip Lewis in the analysis, though his role in Bioinformatics Support at the facility. The technique was carried out in an 8-plex format, and data was collected from two repeats of each sample; control isolated mitochondria and cytosolic fractions and *b0491.5 RNAi* mitochondria and cytosolic fractions. The consequence of having an n of 2 is detailed in Materials and Methods Section 2.14, and although it is a valid method of establishing statistical significance, due to the low power of an n of 2, the results are taken here as a guide to the degree of change and the consistency of that change, rather than inferring statistical significance.

Over 5000 proteins were identified with high confidence from the analysis, Figure 5.13 looks at changes in protein expression levels for specific groups of mitochondrial proteins, firstly subunits that comprise the complexes of the ETC, and also proteins associated with the function of the ETC. Figures 5.14 and 5.15 look at the proteins that show the largest changes in expression, using a $\log_2$FC of +/- 1 and p<0.01 as a guide to indicate the proteins that likely have a degree of change greater than double or less than half, and that this change was consistent.

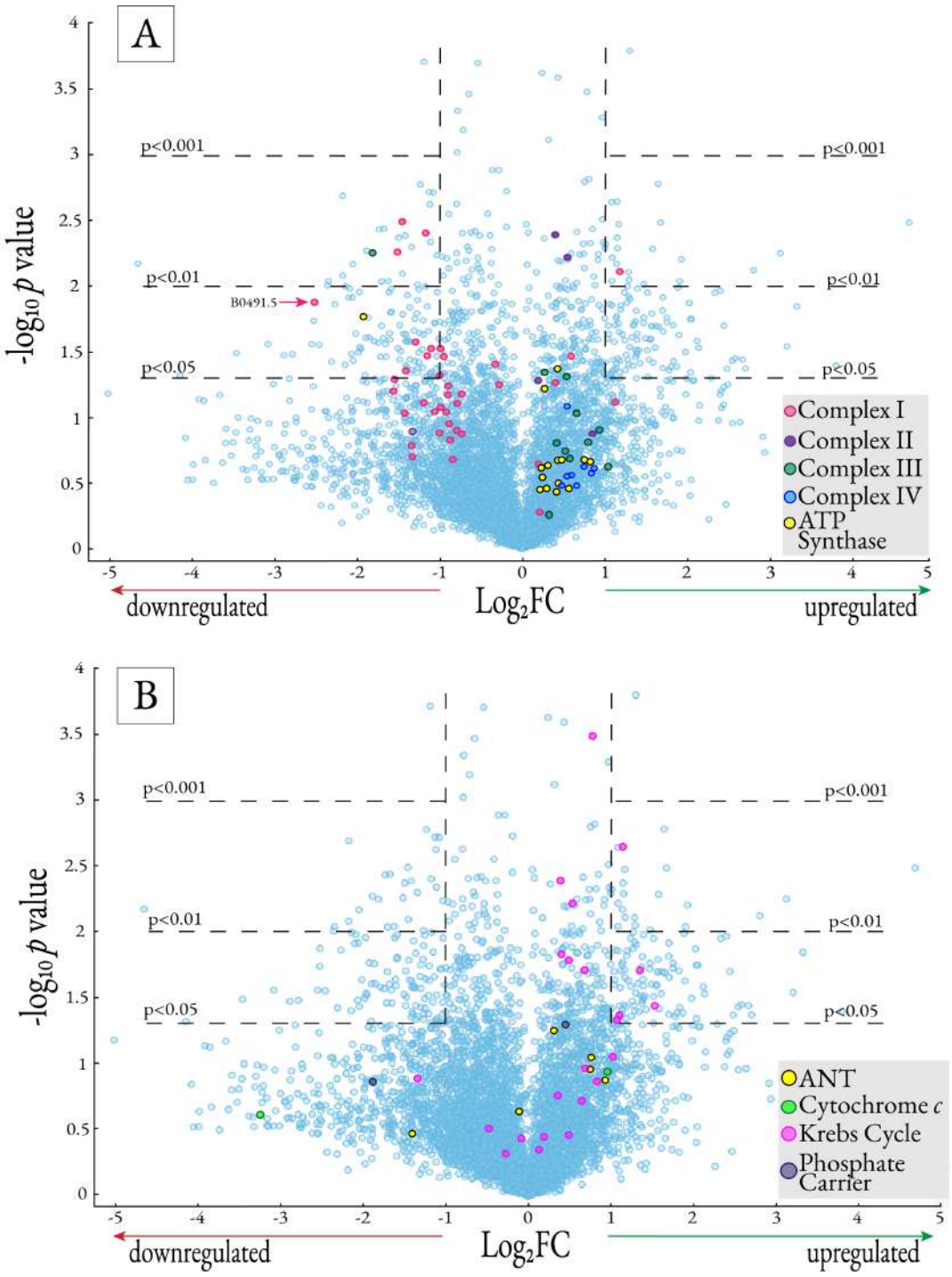

Figure 5.13: Mass spectrometry to analyse changes in protein expression of respiration related proteins - The same data is represented in both volcano plots, showing the changes protein expression of proteins in *b0491.5(RNAi)* mitochondria compared to control mitochondria. The vertical dashed line on the graphs indicate +/- 1 $\log_2$FC and the horizontal lines p<0.01, 0.01 and 0.05 as indicated. **(A)** Subunits of the ETC are highlighted on the plot, as indicated by the legend on the graph. **(B)** Subunits of proteins associated with the function of the ETC are highlighted on the plot, as indicated by the legend on the graph

Looking at Figure 5.13 (A), the ETC proteins have a general distribution away from the centre of the volcano plot, however, only eleven subunits out of over eighty which comprise the ETC show changes greater than log_2FC and p<0.05, indicators of proteins which are consistently changed, these subunits are detailed below in Table 5.1.

Downregulated Proteins	**Human Homologue**	**ETC Complex**	***p*-value**	**log_2FC**
Q9TZ33	UQCRC2	CIII	0.0056	-1.81
Q17880	NDUFV1	CI	0.0032	-1.46
Q9N4Y8	NDUFS1	CI	0.0055	-1.51
Q93831	NDUFB10	CI	0.0040	-1.17
Q17512	**NDUFA11**	**CI**	**0.013**	**-2.52**
Q20053	ATP5PB	CV	0.017	-1.92
Q9N2W7	NDUFA12	CI	0.027	-1.29
Q23098	NDUFB4	CI	0.029	-1.11
O44509	NDUFB11	CI	0.034	-1.15
Q22800	NDUFS2	CI	0.044	-1.42
Upregulated Proteins	**Human Homologue**	**ETC Complex**	***p*-value**	**log_2FC**
Q17439	NDUFA4	CIV	0.0078	1.18

Table 5.1: Up and down regulated ETC subunits - Proteins highlighted in Figure 5.13 (A) from the mitochondrial fractions that have a log_2FC +/- 1 and p<0.05. *C. elegans* proteins annotated by accession number

The data presented in Table 5.1 and Figure 5.13 (A) show that the majority of the ETC components which undergo a consistent change are from CI, furthermore the general distribution in the volcano plot suggests the CI subunits are generally downregulated, whereas the majority of the subunits from complexes II-V showed tendencies towards upregulation. The exceptions to that pattern are a complex

III subunit, homologue of UQCRC2, which was consistently downregulated. The only subunit to show consistent upregulation, NDUFA4, interestingly, was originally classified as a CI subunit, but was later found to be a component of CIV (Balsa et al., 2012).

In addition to components of the ETC, changes in proteins associated with the function of the respiratory complexes were also explored, Figure 5.13 (B). These proteins included the Adenine Nucleotide Transporter (ANT), cytochrome *c*, components of the Krebs cycle and the phosphate carrier protein. It was found that in *C. elegans* there are multiple proteins suggested to be homologous to mammalian cytochrome *c* and the phosphate carrier, all of which are plotted in Figure 5.13 (B). The general pattern was an overall trend towards upregulation, with the components of the Krebs cycle undergoing the most observable changes. In fact, the only consistently upregulated proteins are from the Krebs cycle, as determined by the guide $\log_2$FC and *p*-values, detailed in Table 5.2.

Upregulated proteins	**human homologue**	**Krebs cycle component**	***p*-value**	**$\log_2$FC**
O17643	IDH2	isocitrate dehydrogenase	0.0023	1.15
P34455	ACO2	aconitase	0.019	1.36
P34575	CS	citrate synthase	0.036	1.54
O02640	MDH2	malate dehydrogenase	0.043	1.11
O17214	FH	fumarase	0.046	1.083

Table 5.2: Upregulated Krebs cycle proteins - Proteins highlighted in Figure 5.13 (B) from the mitochondrial fractions that have a $\log_2$FC +/- 1 and $p<0.05$. *C. elegans* proteins annotated by accession number

In addition to investigating specific mitochondrial proteins, the volcano plots were also analysed in relation to the proteins most consistently changed to the greatest degree, in both the mitochondrial (Figure 5.14) and cytosolic fractions (Figure 5.15).

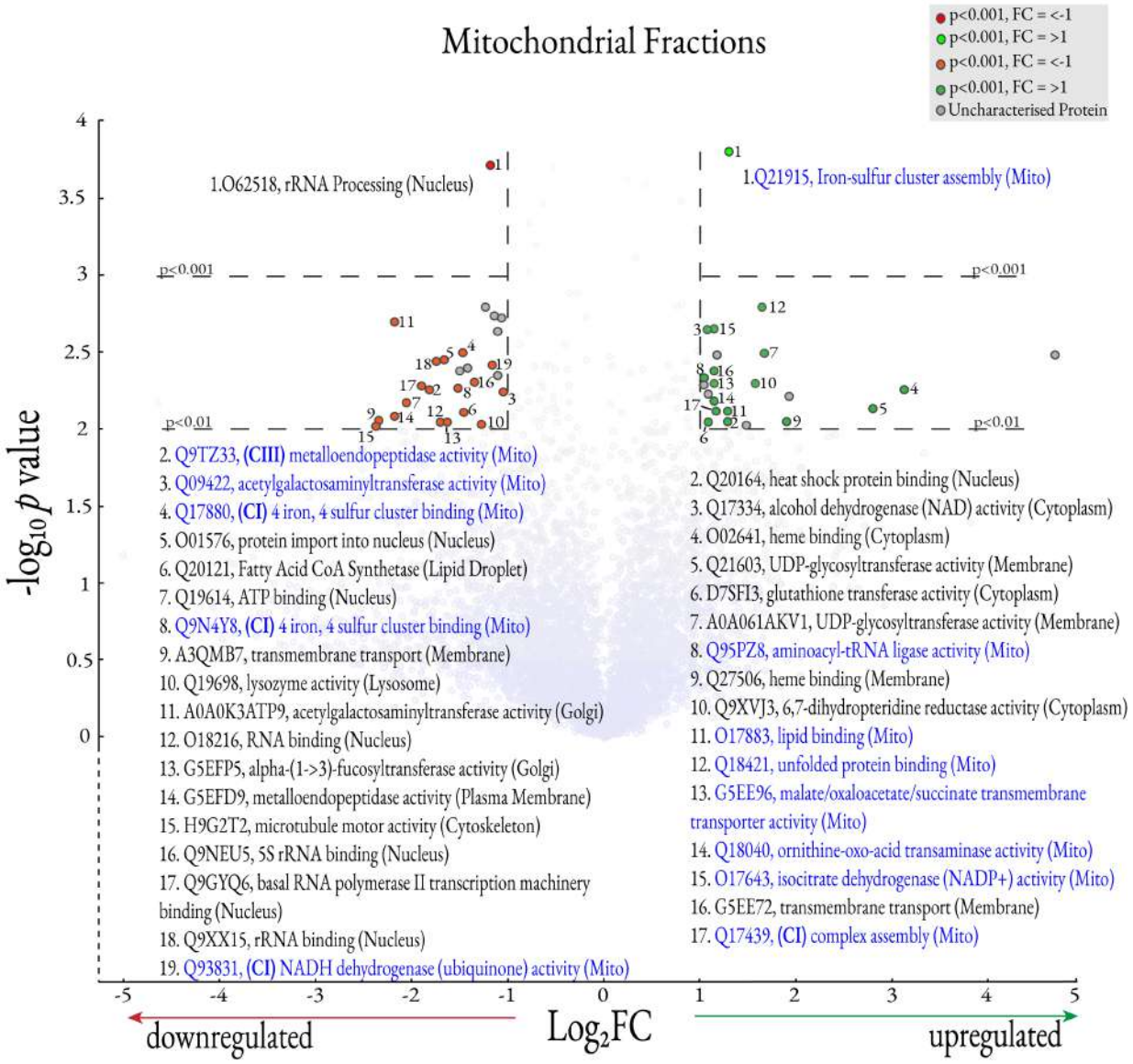

Figure 5.14: Consistently changed mitochondrial proteins as determined by mass spectrometry - Subunits that consistently changed to the greatest degree in the mitochondrial fractions using a $\log_2$FC off of +/- 1 and p<0.01 as a guide. Proteins with a mitochondrial subcellular location are annotated in blue.

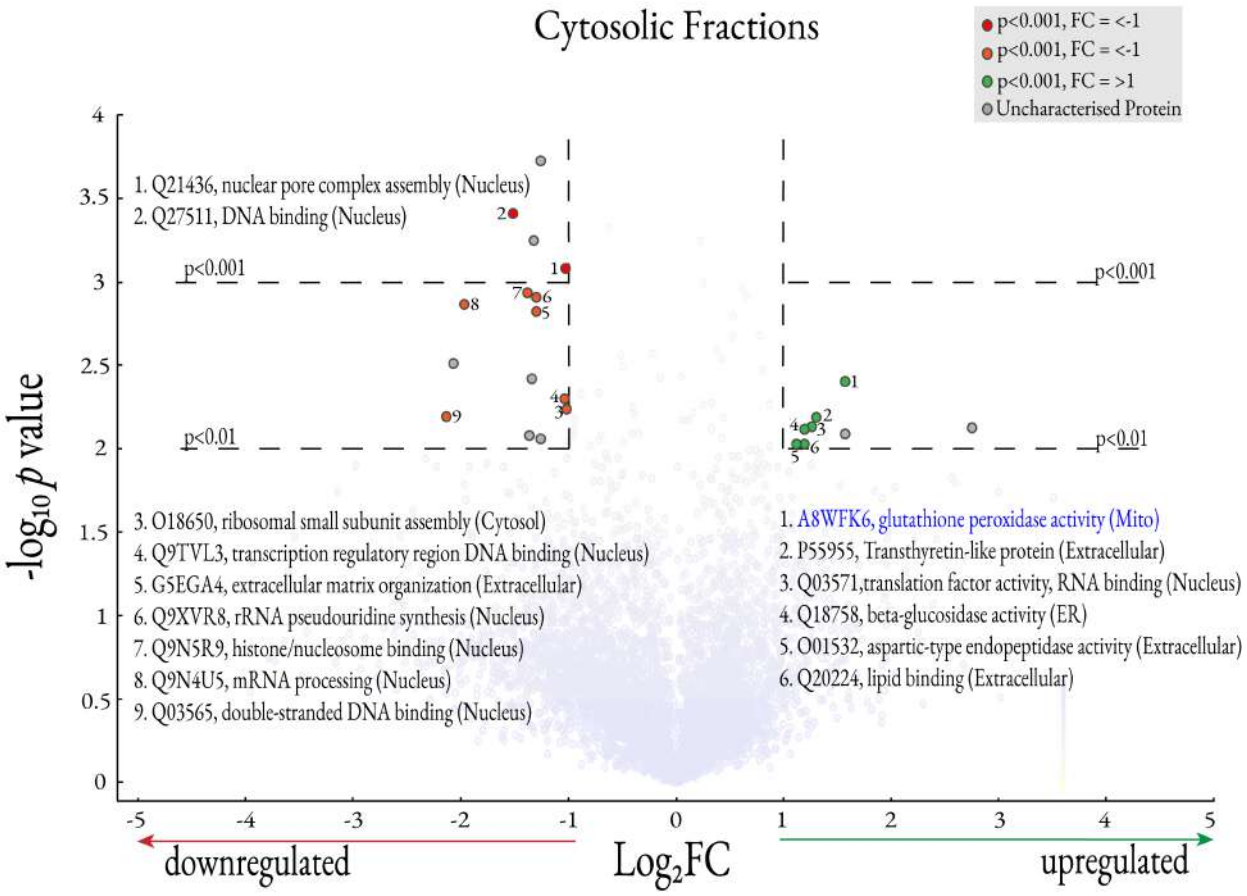

Figure 5.15: Consistently changed cytosolic proteins as determined by mass spectrometry - Subunits that are consistently changed to the greatest degree in the cytosolic fractions using a log_2FC off of +/- 1 and p<0.01 as a guide. Proteins with a mitochondrial subcellular location are annotated in blue.

Looking at the consistently changed proteins, there are unsurprisingly observable differences between the types of proteins up and down regulated in the mitochondrial fractions to the cytosolic. The cytosolic fraction (Figure 5.15), has only one mitochondrially located protein, with the majority of the proteins being either nuclear or extracellular. There are also notably fewer consistently changed proteins in the cytosolic fraction, suggesting fewer proteins have been impacted by the changes in the respiratory machinery.

Whereas although the mitochondrial fraction (Figure 5.14), has a higher number of mitochondrial proteins that are consistently changed, including the ETC subunits already mentioned in Table 5.1, they are still not in the majority. Furthermore, the consistently changed proteins come from a wide range of subcellular locations, particularly in comparison to the cytosolic fraction, perhaps suggesting an organelle wide impact of suppression of B0491.5 that is not limited to the respiratory machinery.

5.6 Chapter discussion

This chapter set out to utilise the genetically tractable qualities of *C. elegans* to investigate the protein B0491.5, established as a homologue of mammalian complex I protein NDUFA11 in Chapter 4. Section 5.2 establishes that if B0491.5 is removed from the genome, this causes a lethal phenotype due to the animals arresting at the L2 larval stage, indicating that B0491.5 is essential for normal animal development. Previous studies that have suppressed NDUFA11 in mammalian cell culture (Andrews et al., 2013), were able to carry out biochemical analysis, finding that the suppression led to a decrease in intact complex I, mitochondrial fragmentation and decreased CI-linked respiratory activity. However due to limitations in the experimental model, the impact of NDUFA11 suppression on complex multi-cellular processes was not able to be investigated, making this a valuable experimental model. Section 5.2.3 details outcrossing and balancing carried out to maintain the strain for future experiments, the strain will be an excellent tool to carry out further analysis of the impact of complete loss of B0491.5, such as investigating the mitochondrial morphology and profiling the respiration activity.

Due to limitations in cultivating large volumes of B0491.5 knockout animals for mitochondrial isolation, Section 5.3 outlines the development of RNAi as a technique to suppress B0491.5 expression and facilitate investigation of the impact of loss of the complex I subunit on whole animal physiology and directly on the mitochondrial respiratory system. Initial experiments (Figure 5.6) validated B0491.5 knockdown through RNAi, and indicated the *b0491.5(RNAi)* animals were showing a developmental delay phenotype and reduced brood counts. Full characterisation of *b0491.5 RNAi* (Figures 5.7 and 5.8) validated the initial findings, showing a severe decrease in the brood count, alongside a

lethal phenotype of *b0491.5 RNAi* second generation animals, which arrest at L2 stage predominantly. This was interesting, as it was the same phenotype as the *b0491.5* CRISPR KO strain, suggesting that the second generation RNAi animals are potentially not able to respond to the L2 metabolic shift discussed previously (Section 1.2.1.1). There is a second hypothesis as to why L2 arrest occurs, which is the maternal effect; whereby the mother passes on sufficient levels of mitochondria to sustain the first stages of growth, but if they animals are not able to produce their own functional mitochondria they then arrest. B0491.5 suppressed animals were also shown to develop slower, taking an extra day to reach adulthood and to be slightly smaller in size (Figure 5.8). Potentially suggesting they are less able to keep up with the energetic demands of development.

Further investigation of the phenotype, Figure 5.8, shows embryos developing in the gonad however, the structure of the gonad appears atypical and disorganised, suggesting potentially an embryo development or egg laying defect, further work would need to be undertaken to distinguish between the two. Reproduction places a large energetic demand on an organism, extending the suggestion that the RNAi animals develop slower due to a reduced capacity to produce the energy required for development, perhaps they lack sufficient energy production capabilities to carry out reproductive activities or are carrying them out significantly slower.

The lifespan of *b0491.5 RNAi* animals was established, showing an increase of an average of ≈4 days (Figure 5.7), as previously discussed in the introduction, Section 1.2.2.2, this corroborates other studies which have found that reduction in mitochondrial function can lead to longevity in model organisms. Furthermore, the findings are consistent with previous lifespan assays conducted with *b0491.5 RNAi* (Chen et al., 2007). Also discussed in Section 1.2.2.2, it has been suggested that ageing is linked to ROS production, and that a lifespan extension is caused by a reduction in the levels of respiration, leading to the levels mitochondrial ROS also reducing. To determine if this was the cause in the *b0491.5(RNAi)* animals, more investigations were carried out in Chapter 6.

Section 5.4 investigates respiratory complex organisation in *b0491.5(RNAi)* animals, where it was found that supercomplex formation was severely disrupted, suggesting that either the supercomplexes are not able to assemble, or potentially, that they are not stable and a lack of B0491.5 causes disas-

sembly. This could be due to a direct role B0491.5 has assembling or stabilising the supercomplexes, but, it could also be that loss of B0491.5 causes a subsequent decrease in intact CI, and it was the lack of CI which leads to supercomplex loss. Support for the latter was that in Figure 5.10 (B), it can be seen that the amount of CI was dramatically reduced in the B0491.5 deficient system. However, this hypothesis does not factor in the position of B0491.5 between CI and CIII and the role that may play in supercomplex interactions, but from this data it was not possible to distinguish between the two hypotheses. All other complexes on the BN gels appear to be fairly constant, confirmed by visualisation of their component subunits in Figure 5.12. A reduction in complex I, with no discernible change in the other ETC was comparable to the results seen in NDUFA11 suppression in human cell culture (Andrews et al., 2013), suggesting a similar response was happening in the two systems.

Mass spectrometry provides a large data set to extract information from, so far this project has used the data to explore how the ETC and associated mitochondrial protein levels change under B0491.5 suppression, and examined the proteins which have consistently changed to a large degree, in mitochondrial and cytosolic fractions. Section 5.3 has shown that *b0491.5(RNAi)* animals experience developmental delays and reproduction inhibition, providing evidence of an impact on a whole animal level. Section 5.4 showed that there are significant changes in the local environment of B0491.5, with significant disruption to ETC organisation. Investigating protein expression changes can indicate what impact B0491.5 suppression, and the resulting ETC organisation disruption, has on an organelle and cellular level. As the data presented was based on an n of two, that does limit its power in making statistically significant conclusions, however, it is still a valid analysis and can be used as a guide until an n of at least three is obtained.

The volcano plots (Figures 5.13-5.15) suggest that the predominant changes within the ETC are to CI, where the majority of the subunits show a trend towards downregulation, which is consistent with the BN PAGE data showing decreased CI. Additionally, the mass spectrometry data shows a very mild trend towards upregulation for OXPHOS complexes II-IV and ATP synthase. This is interesting when considering the BN PAGE data, which shows a loss of the supercomplexes, with only a minor indication of an increase in CIII: CIV supercomplexes. Therefore, if there is the same, if not slightly more, CIII and CIV OXPHOS subunits found in the *b0491.5(RNAi)* mitochondria, but only a small

potential increase in smaller complex formations on the BN PAGE when complex III and IV is not formed into supercomplexes, this may suggest that in the absence of B0491.5 and CI, there is reduced assembly of CIII and CIV. However, it could be that the limit of detection in the BN PAGE is not enough give an accurate indication of supercomplex organisation changes. To investigate further, individual complex assays would provide data to suggest if there was a reduction in assembled and active complex III and IV, or whether it has been re-organised from the supercomplexes, but remains intact.

Figure 5.13 (B) shows the Krebs cycle proteins also showing a general trend towards upregulation, as the Krebs cycle is interlinked with respiration, this is interesting that an upregulation is seen in these proteins, when respiration levels show an overall reduction (Section 6.2). However, the mass spectrometry data does not take into account the activity of the cycle, so despite an increase in enzyme amount, the activity could be decreased. To investigate this further respiration studies with whole worms could be carried out to validate the in vitro respiration data and metabolomics, to explore the metabolites present within the mitochondria.

Chapter 6

Impact of reduced B0491.5 on mitochondrial activity and morphology

6.1 Chapter introduction

Chapter five investigated the effect of B0491.5 knockdown on the assembly of the respiratory chain supercomplexes, and established that loss of B0491.5 caused them to be unformed or disassembled. Mass spectrometry also showed that there were wide scale protein expression changes within the mitochondria, suggesting that the effect of loss of B0491.5 was not limited to the respiratory chain. Chapter six looks at the effect B0491.5 reduction has on mitochondrial physiology and morphology.

Several aspects of mitochondria physiology were investigated, using in vitro assays on isolated mitochondria, looking at differences between *b0491.5(RNAi)* and control mitochondria through both complex I-linked and complex II-linked respiration. Firstly, respiration rates were measured via oxygen consumption, followed by membrane potential using TMRM and finally, ROS production via hydrogen peroxide levels. These experiments were carried out to explore how the changes in ETC organisation impacts the respiratory function of the mitochondria. Additionally, increased lifespan, shown in Section 5.3.2, is an established phenotype when there is impairment in mitochondrial function, discussed in Section 1.2.2.2. This phenotype is potentially linked to changes in membrane potential and ROS production, therefore it was pertinent to explore this in *b0491.5(RNAi)* mitochondria.

As mitochondrial physiology and morphology are intrinsically linked, the morphology of *b0491.5 RNAi* mitochondria was investigated on multiple levels. Firstly, by looking at mitochondrial ultra structure in live worms using a *C. elegans* strain expressing a mitochondrial targeted GFP, allowing visualisation of mitochondrial networks. Secondly, whole worms were prepared for electron microscopy (EM) to visualise in situ mitochondria in more detail. Finally, cryo-electron tomography (cryo-ET) was used as it is an accurate method to deliver three-dimensional (3D) volumes of mitochondria at molecular resolution. To the author's knowledge, this presented the first tomograms of isolated mitochondria from *C. elegans*. Furthermore, reconstructions of the tomograms allowed 3D visualisation of the internal cristae structure.

6.2 Mitochondrial physiology

Physiology can be defined as the study of how living systems function, often with a focus on how chemical and physical functions are carried out. This section explores the physiology of mitochondria in relation to their function in cellular respiration, including the bioenergetic activity of the ETC machinery, membrane potential and respiration driven ROS production.

6.2.1 Mitochondrial bioenergetics

Serious perturbation of the respiratory chain complexes was found with loss of B0491.5; supramolecular organisation of the ETC was abolished and intact CI was also significantly reduced (Section 5.4). Despite this, *b0491.5(RNAi)* animals were found to reach adulthood, albeit with some developmental delays and reproductive inhibition (Section 5.3), suggesting they were still capable of meeting a minimum energy requirement, but perhaps had a reduced capacity to respond to greater energetic demands. Furthermore, as discussed in Section 5.6, *b0491.5(RNAi)* animals were found to have a lifespan extension, a phenomenon also seen in other mitochondrial impairment studies. It has been suggested that this could be linked to a reduction in respiration activity, and subsequent reduction in

ROS production. Therefore, to investigate if this might be the case in *b0491.5(RNAi)* animals and to understand the impact of complex organisation disruption, a more detailed investigation into the respiration activity of the *b0491.5(RNAi)* mitochondria compared to the control was conducted.

Figure 6.1 shows average traces for the rate of O_2 consumption over time, along with a bar chart representing the value of the plateau after addition of each substrate indicated, for three respiratory conditions. Complex I-linked respiration (A) uses substrates pyruvate and malate, which feed electrons into the ETC at complex I via electron carrier NADH, complex II-linked respiration (B) uses succinate and feeds electrons into complex II via electron carrier $FADH_2$. Finally, 'combined' respiration was carried out consisting of complex I-linked sequentially followed by complex II-linked respiration (C), this more represents in vivo conditions and also acted to rescue poor complex I activity that was observed in the B0491.5 knockdown condition.

After the addition of the indicated substrate, before ADP, the mitochondria are defined as being in state 2 respiration. Mitochondrial respiration states based on Chance and Williams nomenclature and calculations made in this section are according to classical techniques (Chance and Williams, 1955, 1956; Brand and Nicholls, 2011). For an overview of the OXPHOS system and ETC mechanisms, see Figures 1.4, 1.5 and 1.6, this section measures the consumption of oxygen as a measure of the activity of ETC which pumps protons driven by the transfer of electrons to a final acceptor of molecular oxygen.

The addition of ADP drives substrate oxidation and subsequently increases the rate of O_2 consumption, mimicking an increase in workload, during this ADP-stimulated phase the mitochondria are in state 3 respiration. After ADP phosphorylation, the ETC enters a steady-state, deemed state 4. The ratio between state 3 respiration, representing maximum ATP synthesis, and state 4, which is in the absence of ATP synthesis is called the respiratory control ratio (RCR). A high RCR is representative of a high capacity for substrate oxidation and ATP turnover; suggesting a strong coupling between respiration and ATP synthesis. The RCR value varies between different tissues and environments, however a lower RCR can be indicative of mitochondrial dysfunction (Brand and Nicholls, 2011).

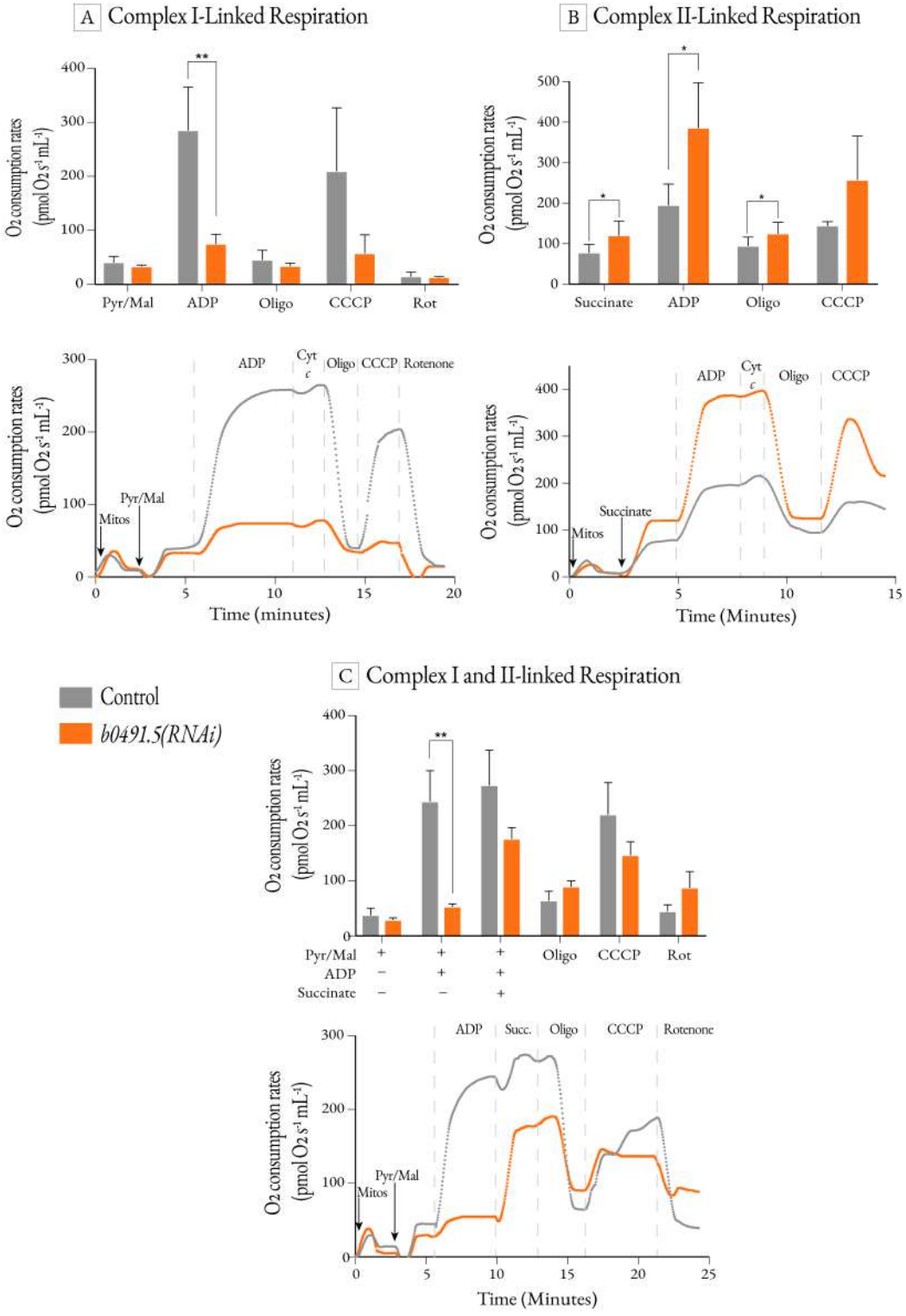

Figure 6.1: Mitochondrial bioenergetics of B0491.5 suppressed mitochondria - Assays were carried out on Oroboros O2k Oxygraph at 25°C. Full protocol in Section 2.7.1, substrates indicated were added to mitochondria and the rate of oxygen consumption recorded. Abbreviations used include; pyruvate (pyr), malate (mal), oligomycin (oligo), rotenone (rot). n=4 for each condition, statistics performed were paired, two tailed t-test, (A) ADP p=0.00214, (B) succinate p=0.0341, ADP p= 0.0208, oligomycin p=0.0489 (C) p=0.004

The data shown in Figure 6.1 shows distinct differences between the control and *b0491.5(RNAi)* mitochondria in all conditions. In complex I-linked respiration (A), state 2 respiration rates are similar, however upon the addition of ADP (state 3) significant differences appear with a 2.8-fold decrease in oxygen consumption in the B0491.5 knockdown. Upon addition of oligomycin, which induced a pseudo-state 4 both conditions slow to the same steady-state rate. To establish the cause of reduced respiration through complex I the mitochondrial uncoupler CCCP was used to assess maximal respiration capacity. As shown in Figure 6.1 (A), under these conditions the respiration remains impaired in the B0491.5 knockdown suggesting a specific effect on the electron transport chain rather than the phosphorylative system.

Conversely, complex II-linked respiration Figure 6.1 (B) shows significant variance in state 2 respiration, with *b0491.5(RNAi)* mitochondria demonstrating higher rates. This pattern was repeated in pseudo-state 4, with higher respiration in the steady states possibly indicative of higher proton leak across the IMM. Upon addition of ADP, there was a 1.43-fold increase in ADP sustained respiration for *b0491.5(RNAi)* mitochondria. The addition of oligomycin to induce pseudo-state 4 respiration was used to calculate the RCR values for each respiration condition, shown in Table 6.1. These values further validated findings from Figure 6.1 showing that *b0491.5(RNAi)* mitochondria have impaired respiration through the complex I pathway, and that have increased respiration activity through complex II-linked respiration, potentially acting as a compensatory measure.

Condition	**RCR**
Complex I-Linked Control	6.2
Complex I-Linked *b0491.5(RNAi)*	2.2
Complex II-Linked Control	2.1
Complex II-Linked *b0491.5(RNAi)*	3
'Combined' Control	4.2
'Combined' *b0491.5(RNAi)*	2

Table 6.1: Mitochondrial bioenergetics RCR values - the RCR values calculated from Figure 6.1. For Complex I-Linked (Figure 6.1 A) and Complex II-Linked (Figure 6.1 B) respiration the RCR was calculated by state 3 (ADP stimulated respiration)/state 4 (oligomycin induced steady state), for 'combined' respiration of Complex I + II-Linked, the value taken after the addition of succinate was taken as stage 3.

Figure 6.1 (C), 'combined' respiration was investigated to explore if a subsequent delivery of succinate could rescue poor CI-inked respiration in the *b0491.5(RNAi)* mitochondria condition by bypassing complex I, it also provided in vitro conditions that are more representative of the in vivo environment with substrates feeding electrons into the ETC at both CI and CII. The same severely reduced activity was seen in the ADP-linked state 3 respiration for the protein knockdown, upon addition of succinate respiration was partially rescued, reducing the RCR difference from a 2.8-fold decrease in complex I only respiration to 2.1-fold reduction when supplemented with succinate. It should be noted that in this system, oxaloacetate, produced in the Krebs cycle from malate, inhibits succinate dehydrogenase (Wojtczak et al., 1969), which may impact the extent of succinate driven respiration following pyruvate and malate. Higher respiration rates are also seen again in pseudo-state 4 respiration with oligomycin for B0491.5 suppressed mitochondria, indicating as in in Figure 6.1 (B) that higher rates of proton leak are occurring.

6.2.2 Membrane potential

As discussed in Section 1.1.3, the PMF is made up of two components, the membrane potential ($\Delta\Psi$) and ΔpH, generated by the ETC pumping protons into the IMS. The membrane potential is the majority contributor to the PMF and is created by the charge difference between the mitochondrial IMS and matrix, as an electrochemical gradient of positively charged protons accumulates in the IMS as an energy store to drive ATP synthesis. The membrane potential and O_2 consumption rates are explicitly linked, reduction of the PMF drives the ETC, as it works to pump protons back into the IMS and re-establish the PMF. Therefore at high rates of O_2 consumption you would expect the membrane potential to be reduced, and in steady rates of respiration, the membrane potential to be at full capacity of about -180 mV (Liberman et al., 1969).

As Figure 6.1 shows significantly varying respiration rates between the two conditions, with decreased C I-linked respiration and increase CII-linked respiration in *b0491.5(RNAi)* mitochondria, the membrane potential was investigated to explore if the respiration rates where acting as expected in relation to the membrane potential, shown in Figure 6.2. Experiments were carried out using tetramethylrhodamine methyl ester (TMRM), which accumulates in the matrix of polarised mitochondria and gives off a measurable fluorescent signal. On depolarisation of the membrane potential, the TMRM signal is reduced, see Section 2.7.2 for a full protocol. The results were collected in quench mode, therefore a lower membrane potential is represented by a higher fluorescence. The uncoupler CCCP and mitochondrial poison AA are used to fully depolarise the membrane, with similar signals in the two conditions indicating that comparable concentrations of mitochondria were present in the assay.

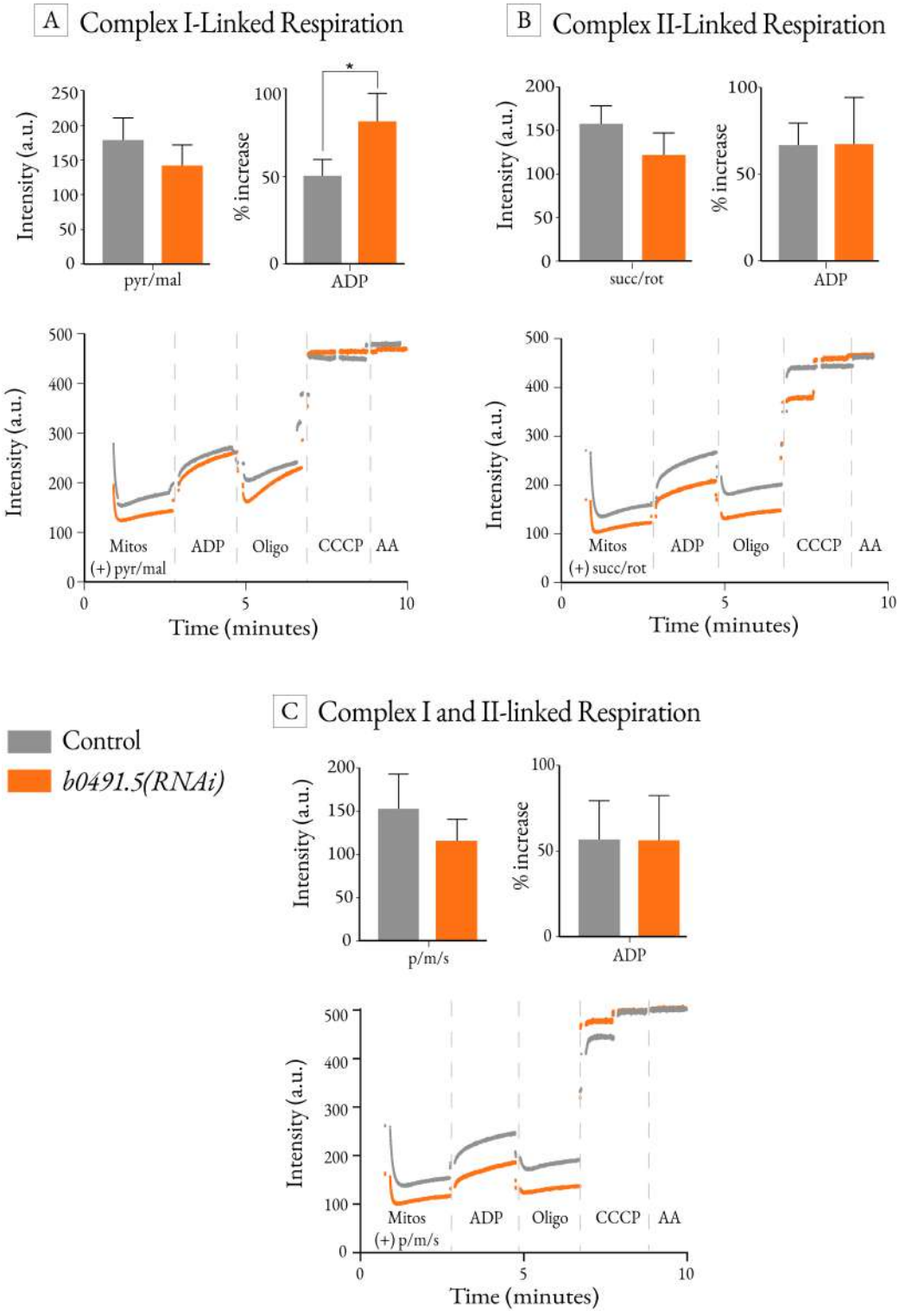

Figure 6.2: Investigating membrane potential in B0491.5 suppressed mitochondria - Assays were carried out with TMRM on a UV-Vis Spectrometer, full protocol in Section 2.7.2. Substrates indicated were added to mitochondria and intensity recorded. Abbreviations used include; pyruvate (pyr), malate (mal), oligomycin (oligo), antimycin A (AA). n=4 for each condition, statistics performed were paired, two tailed t-test, (A)p=0.0301

When conducting complex I-linked only respiration, Figure 6.2 (A), it can be seen that upon the addition of ADP there was a 81% change in membrane potential in relation to the state 2 steady-state for the *b0491.5(RNAi)* condition, as opposed to a change of only 50% from state 2 to state 3 in the control. When looking at both the respiration trace from Figure 6.1 (A) and TMRM traces in Figure 6.2 (A), this was representative of membrane depolarisation on the addition of ADP, as ATP synthase utilises the PMF to drive ATP synthesis. In the control the ETC was stimulated to pump protons to maintain the PMF in state 3 respiration, consuming oxygen and preventing a large reduction in potential in the PMF. In the B0491.5 suppressed mitochondria, there was reduced ability to respire through complex I, which leads to a greater reduction in membrane potential as the ETC pumps less protons in comparison to the control. In addition to the significantly increased reduction in the membrane potential under reduced B0491.5 conditions, when observing the TMRM data for CI-linked respiration, Figure 6.2 (A), upon the addition of oligomycin the *b0491.5(RNAi)* trace can be seen to dip prominently and then recover to a similar position as the control, his could potentially indicate proton leak in the membrane.

For complex II-linked respiration, when considering the significantly higher respiration rates for the *b0491.5(RNAi)* condition (Figure 6.1 (B), you would expect the corresponding membrane potential in Figure 6.2 (B) to be lower, driving greater electron flux through the ETC. However, what was observed in Figure 6.2 (B) was that the control and *b0491.5(RNAi)* conditions have the same percentage decrease in membrane potential in relation to state 2 (steady state), with succinate. This suggests that the B0491.5 suppressed mitochondria are working at a 1.43 fold greater respiration rate than the control, to maintain the same level of membrane potential. A suggested reason for this could be that the *b0491.5(RNAi)* mitochondria have increased ETC activity due to increased proton leak compared to the control, supported by the higher state 2 and stage 4 respiration rates seen in Figure 6.1 (B).

Under 'combined' respiration conditions Figure 6.2 (C), with pyruvate, malate and succinate added simultaneously not sequentially as in the O_2 consumption experiments, there was again a similar change in membrane potential as in the complex II-linked respiration, (B). This suggests that the addition of succinate rescues the reduced membrane potential observed in Figure 6.2 (A). In addition,

proton leak is not observed under these conditions the TMRM traces, in state 4.

6.2.3 Impact of B0491.5 reduction on ROS production

Section 6.1 showed significant changes in mitochondrial respiration between the control and *b0491.5(RNAi)* conditions, with a decreased ability to respire through complex I, and increased complex II-linked respiration rates for the B0491.5 suppressed mitochondria. In addition, investigation into the organisation of the respiratory complexes in Section 5.4 showed a lack of supramolecular organisation and decreased complex I. Supercomplexes have been hypothesised to have a preventative role in ROS production (discussed in Section 1.1.6.3), therefore, a consequence of their disassembly may be increased mitochondrial ROS production. Conversely, the lifespan extension seen in *b0491.5(RNAi)* animals, previously discussed, could be a consequence of reduced ROS due to impaired respiration. Therefore, ROS production was investigated to determine if the *b0491.5(RNAi)* mitochondria exhibited any changes.

As discussed in Section 1.1.5.1, mitochondrial ETC ROS are generated predominately by complex I and complex III, by the partial reduction of an oxygen molecule due to electron slip, producing superoxide anions which are rapidly converted to hydrogen peroxide by superoxide dismutase. Production of ROS was measured detecting hydrogen peroxide levels using Amplex Red reagent, shown in Figure 6.3.

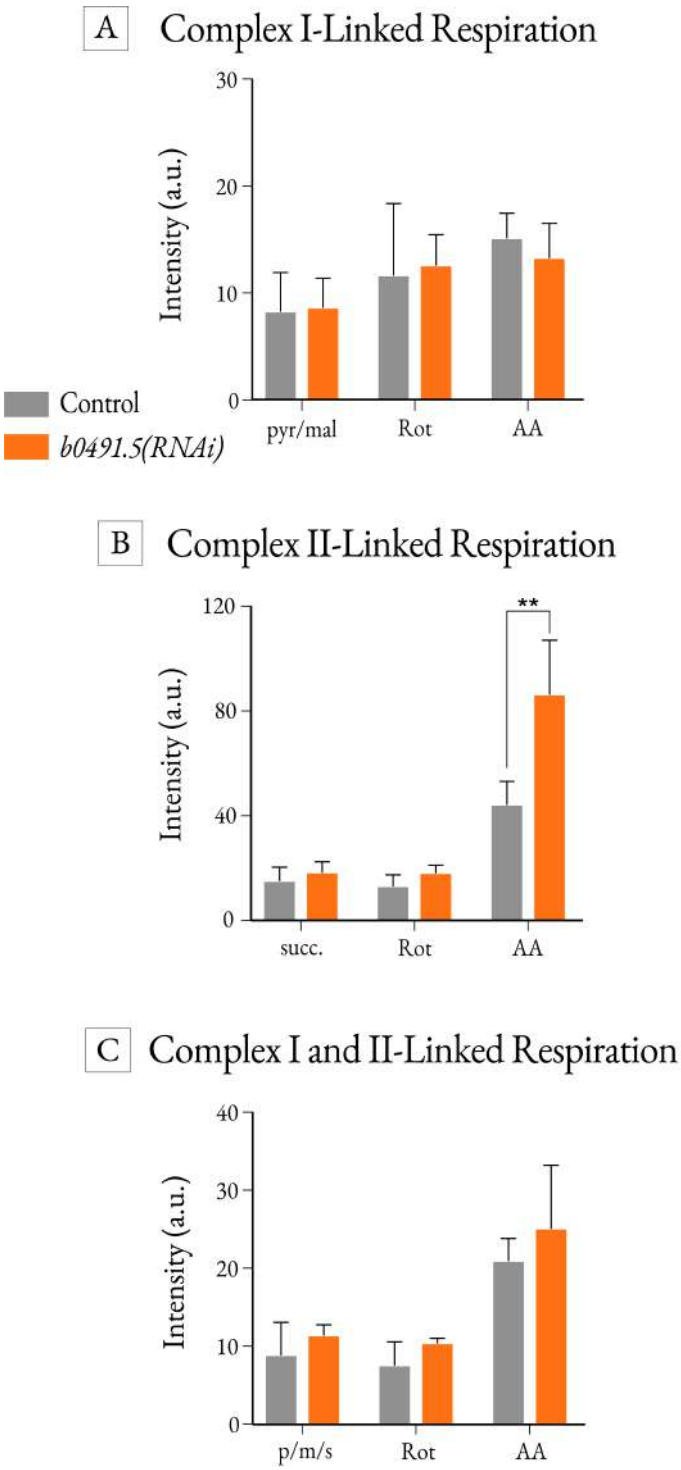

Figure 6.3: Impact of B0491.5 reduction on ROS production - Assays were carried out using Amplex Red reagent in a spectrophotometer at 585 nm. Full protocol in Section 2.7.3, substrates indicated were added to mitochondria and the OD recorded. Abbreviations used include; pyruvate (pyr), malate (mal), oligomycin (oligo), rotenone (rot), antimycin A (AA). n=4 for each condition, statistics performed were paired, two tailed t-test, (B) p= 0.00942

In the ROS assays, mitochondria were stimulated through either complex I-linked, complex II-linked or 'combined respiration' as in the oxygen consumption assay. However, 'combined' respiration conditions were carried out with pyruvate, malate and succinate added together as opposed to subsequently. The mitochondrial poisons rotenone and antimycin A (AA) were used as mitochondria stressors, with rotenone blocking respiration at complex I and AA at complex III.

For complex I-linked respiration (Figure 6.3 (A), although significant differences are seen between the control and B0491.5 knockdown (Figure 6.1), hydrogen peroxide production remains consistent regardless of the mitochondrial poison (rotenone ± AA). On the other hand, in complex II-linked respiration (Figure 6.3 (B), on the addition of AA a significant increase in hydrogen peroxide production was seen in the B0491.5 knockdown. As AA inhibits complex III, this increase could be caused due to the increased activity through complex II, as the electron flux is greater through the ETC at this entry point to generate the same PMF. Once complex III is blocked, a larger proportion of these electrons leave III as ROS.

In Figure 6.3 (C) addition of all three substrates stimulating respiration through both entry complexes (I and II), mimicking the rescue experiment in Figure 6.1 (C), was used to determine if this condition reduced ROS production. The results shown confirm that under these conditions there was no statistically significant difference in ROS production between the two conditions.

6.3 Morphological changes

The mitochondrial morphology is dynamic; altered by fission, fusion and branching events in response to multiple variables such as oxidative metabolism and membrane potential (Ishihara et al., 2003; Youle and van der Bliek, 2012; Zhan et al., 2013). There is a wide variety of mitochondrial morphologies across different cell types, from long filaments ranging from 1 to 10 μm in length, to more uniform spheres (Youle and van der Bliek, 2012). It has been found that during cell injury, mi-

tochondria have been observed to undergo mitochondrial fragmentation, which may not only be a morphological change, but could potentially contribute to mitochondrial membrane leakage (Zhan et al., 2013). It has also been found that oxidative stress increased mitochondria fragmentation, and these morphological changes were preceded by a reduction in membrane potential (Iqbal and Hood, 2014). Furthermore, studies have found that upon oxidative stress, mitochondria have been found to experience a loss of matrix density, and disorganisation of IMM cristae. However, when the oxidative stress was relieved, these changes were rapidly reversed, suggesting ROS specific morphology changes (Cole et al., 2010).

This project has found that *b0491.5(RNAi)* mitochondria have distinctly altered physiology, shown in Section 6.2, finding altered rates of respiration and indicators of increased proton leak in the IMM (Figure 6.1 (B) and 6.2(A)). In addition, there are clear protein organisation differences in the respiratory chain in the IMM, shown in Section 5.4. Therefore, to investigate if morphological changes are present in *b0491.5(RNAi)* mitochondria, a multifaceted experimental approach across a range of resolutions was undertaken as discussed in the chapter introduction (Section 6.1). All images were collected on microscopes in the Wolfson Bioimaging Facility at the University of Bristol.

6.3.1 Mitochondrially expressed GFP in whole worms

To observe the mitochondria network in vivo, the worm strain, SJ4103 [myo-3::GFP(mit)], was obtained from the Caenorhabditis Genetics Center (CGC). The strain expressed a mitochondrial GFP marker in the body wall muscle, using the muscle-specific *myo-3* promoter (Fire and Waterston, 1989). The muscle cells in the body wall are elongated, with a flat layer of myofibrils on the side of the body wall (Francis and Waterston, 1985). The body wall muscle was chosen to investigate the mitochondrial network, due to the normally organised, linear formation of the mitochondria. Worms were grown to adulthood on either control (empty vector) or *b0491.5(RNAi)* and images taken on a confocal laser scanning microscope, representative images shown in Figure 6.4.

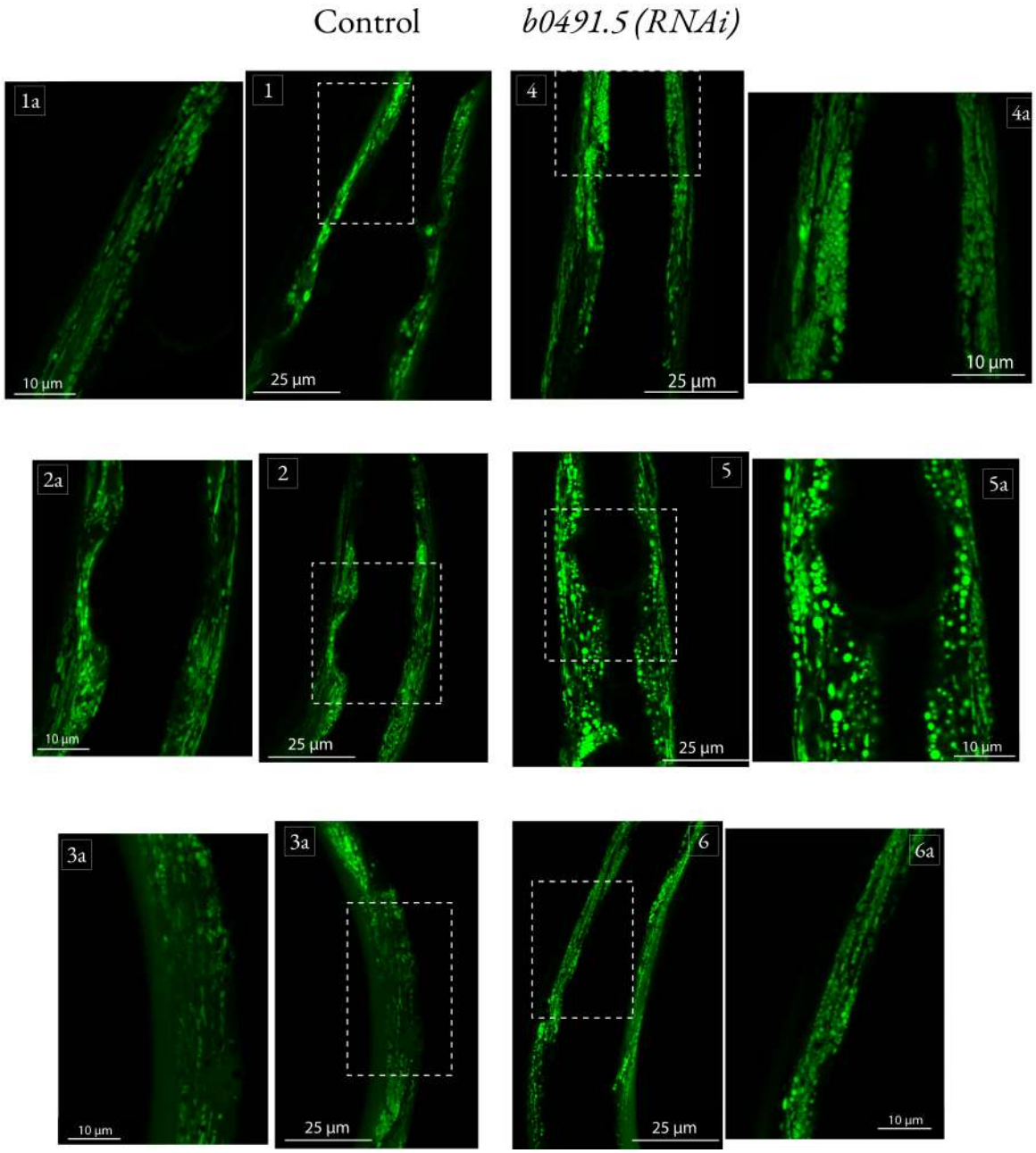

Figure 6.4: Mitochondrial targeted GFP images in live worms - Representative confocal fluorescent images to investigate mitochondrial morphology using Pmyo-3::mito::GFP reporter, which expresses a mitochondrial targeted GFP under the control of muscle specific *myo-3* promoter, in either control or *b0491.5(RNAi)* fed animals. Images annotated with Xa represent digital zooms of the white boxed in area of the main image. **(1, 1a, 2, 2a)** muscle surrounding the pharynx in control animals **(3, 3a)** body wall muscle in control animals **(4, 4a, 5, 5a)** muscle surrounding the pharynx in *b0491.5(RNAi)* animals **(6, 6a)** body wall muscle in *b0491.5(RNAi)* animals. Images are taken through a 63× glycerol immersion objective, representative images shown, n=5.

Observational analysis of the images in Figure 6.4 was made using three major mitochondrial phenotypic classifications of linear, intermediate and fragmented (Sarasija and Norman, 2018), in *C. elegans* body wall muscle mitochondria. The images suggests that *b0491.5(RNAi)* mitochondria are more fragmented in their appearance, and appear in clusters of highly fragmented and rounder mitochondria, as opposed to longer more interconnected morphology of the control. Whereas, the control mitochondria would seem to grouped with a phenotype of either linear or intermediate, predominately in the former, and show a more uniform, interconnected morphology.

6.3.2 Whole worm transmission electron microscopy

To build on the findings in Section 6.3.1, that *b0491.5(RNAi)* appear to have a more fragmented mitochondrial network, whole worm EM was used to explore the mitochondrial morphology in situ. EM also potentially allows the investigation of cristae structure within the mitochondria. As the organisation of the respiratory complexes has been shown to differ in B0491.5 suppressed worms from the control (Figure 5.4), it would be interesting to determine if this has had a structural impact on the IMM. Worms were grown under the same conditions as for the mitochondrial GFP experiments and imaged by Transmission electron microscopy (TEM) on a FEI Tecnai 12 TEM, representative images shown in Figures 6.5 and 6.6. Whole worm EM was carried out with the help of Prof. Paul Verkade and Dr. Chris Neal in the bioimaging department, at the University of Bristol.

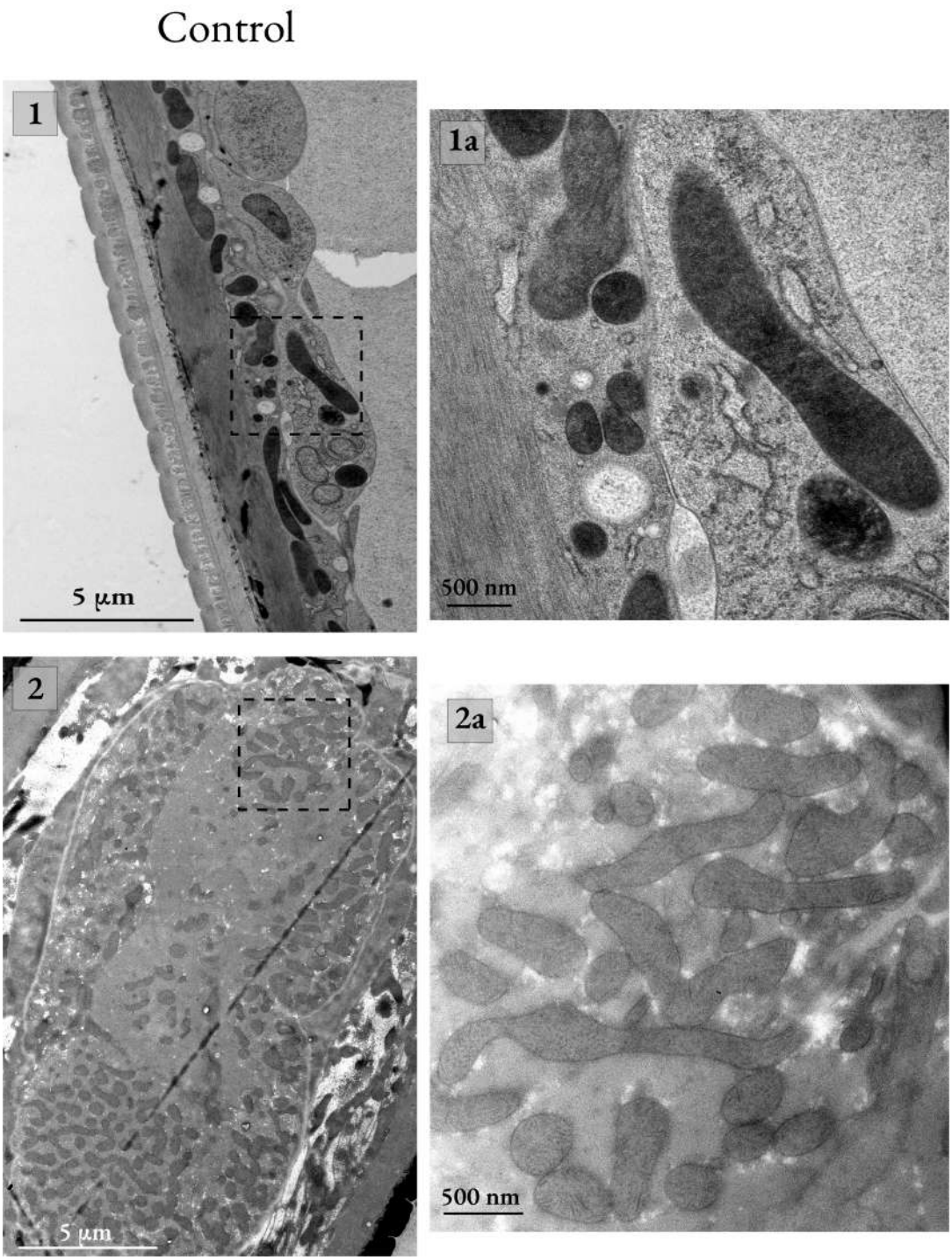

Figure 6.5: Electron microscopy with control mitochondria - Electron micrographs of control animals, looking at mitochondria in the body wall **(1, 1a)** and the pharynx **(2, 2a)**. The images on the right (1a and 2a) are digital zooms of the area indicated in the box on **1** and **2**.

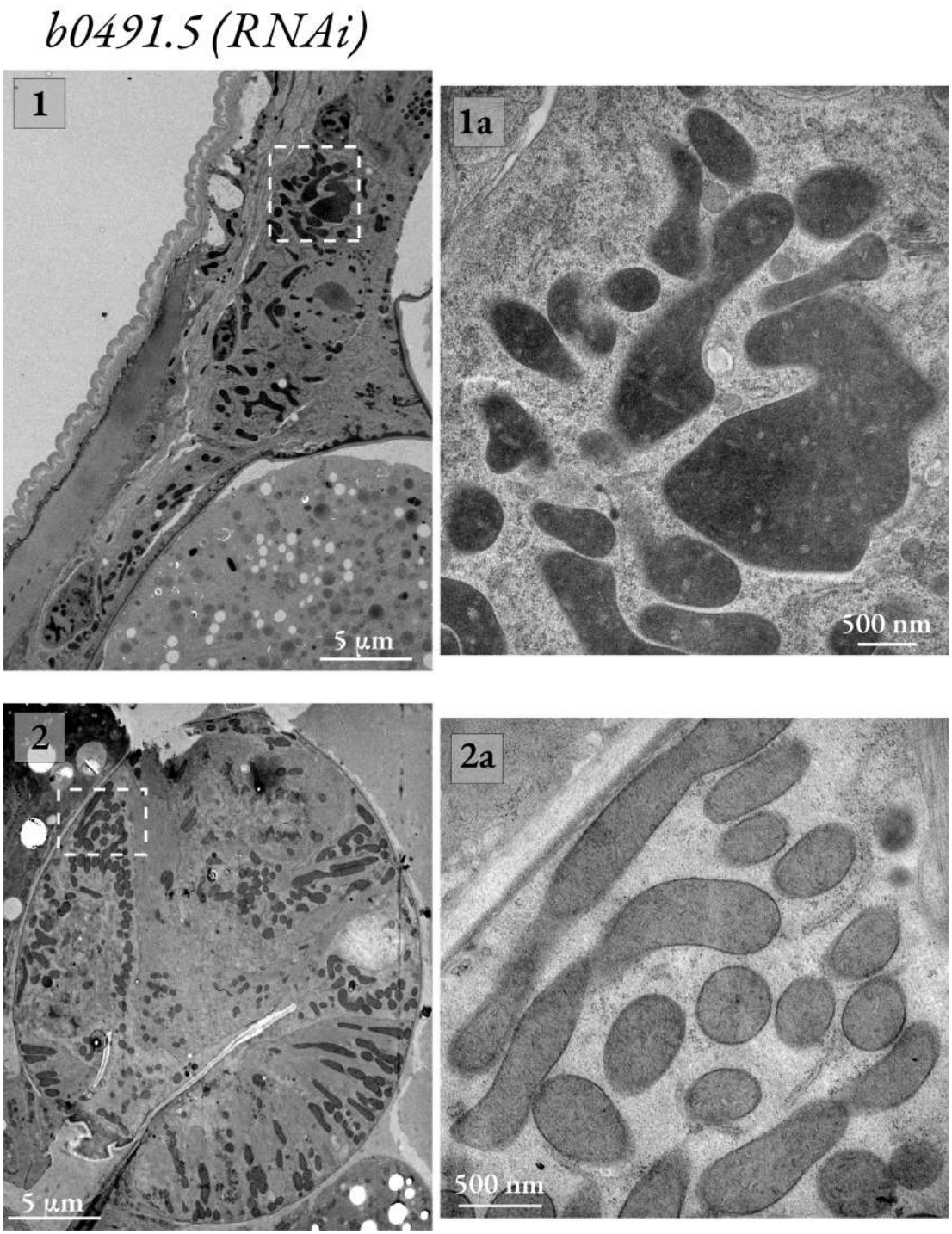

Figure 6.6: Electron microscopy with *b0491.5(RNAi)* mitochondria - Electron micrographs of (*b0491.5(RNAi)* animals, looking at mitochondria in the body wall **(1, 1a)** and the pharynx **(2, 2a)**. The images on the right **(1a and 2a)** are digital zooms of the area indicated in the box on **1** and **2**.

Looking at the TEM images in Figure 6.5 of the control mitochondria, a combination of linear (>1 μm) and smaller, rounder mitochondrions can be seen. Where as in the *b0491.5(RNAi)* conditions, Figure 6.6, the mitochondria appear to show observational differences, such as a greater number of smaller (<1 μm) round organelles, although not exclusively. The body wall muscle of the animals was looked at, 1 and 1a in both Figure 6.5 and 6.6, to make comparative observations between the mito::GFP (Figure 6.4) and EM images. Both sets of images show similar findings, with the control mitochondria showing a more linear morphology, organised in line with the body wall. Conversely, the *b0491.5(RNAi)* mitochondria display a wide variety of morphologies, and appear disorganised in their arrangement.

The pharynx was also looked at, chosen due to its high mitochondrial content. In this location, there appears to be a wider variety of morphologies, within both samples. This could be due to the different tissue type, where the body wall muscle promotes more linear organisation. It does appear that the proportion of smaller, more fragmented mitochondria was higher in *b0491.5(RNAi)*, with smaller mitochondria sporadically distributed in the control. but large groups of them appearing together in the *b0491.5(RNAi)* animals.

The staining conditions used across the images are varied, in some images the IMM and cristae are pronounced and identifiable but in others they cannot be distinguished. However it cannot be concluded whether this was due to a genuine difference between the conditions or whether it was an artefact of staining. This section therefore provides high resolution visualisation of mitochondria in situ, with the potential to extend to cristae analysis once homogeneous staining was applied across future samples. Furthermore, statistical analysis could be used to analyse the size and number of mitochondria to see if there are significant differences.

6.3.3 Cryo-electron tomography

Electron cryo-tomograms of mitochondria were used to reveal the 3D morphology of the organelle and investigate the internal structure of the mitochondria, allowing higher resolution of the membranes than achieved in TEM with whole worms. Samples were prepared and images collected using the Wolfson Bioimaging Facility at the University of Bristol, in collaboration with Dr. Vicki Gold (Senior Lecturer, Living Systems Institute, University of Exeter, United Kingdom)

Isolated mitochondria, free of the cytoskeleton, can adopt different, more spherical shapes (Claude and Fullam, 1945), as indeed they appear here, (Figures 6.7 and 6.8). This feature was not taken into account when interpreting the images, as it was an artefact of the isolation process and conditions of imaging. Instead, the higher resolution analysis was used to explore the internal ultra-structures of the mitochondria and membrane morphology.

6.3.3.1 Tomograms

The cryo-ET images show consistent observational differences in the mitochondrial morphology when B0491.5 was depleted (Figure 6.8, as compared to control mitochondria, Figure 6.7). These differences included a less dense interior, a phenomenon seen in other conditions where mitochondria have come under oxidative stress (Cole et al., 2010). This was in contrast to the high mitochondrial matrix density often having the disadvantage of obscuring internal detail, as seen in the control mitochondria (Figure 6.7).

The tomographic slices of control mitochondria are homogeneous in their appearance, consistently dense with the cristae hard to distinguish, however, those that can be seen are narrow and ordered. In comparison, the *b0491.5(RNAi)* mitochondria look irregular, and significantly less dense, with the internal structure more visible than the control. This allows the observation to be made that the reduction of B0491.5 seems to have induced the formation of wide gaps between the outer and inner membranes, as well as between the cristae. These observations are similar to those found in

previous studies examining the impact of oxidative stress (Cole et al., 2010), however, from the morphology alone it was not possible to determine if oxidative stress was the cause of the changes in this instance.

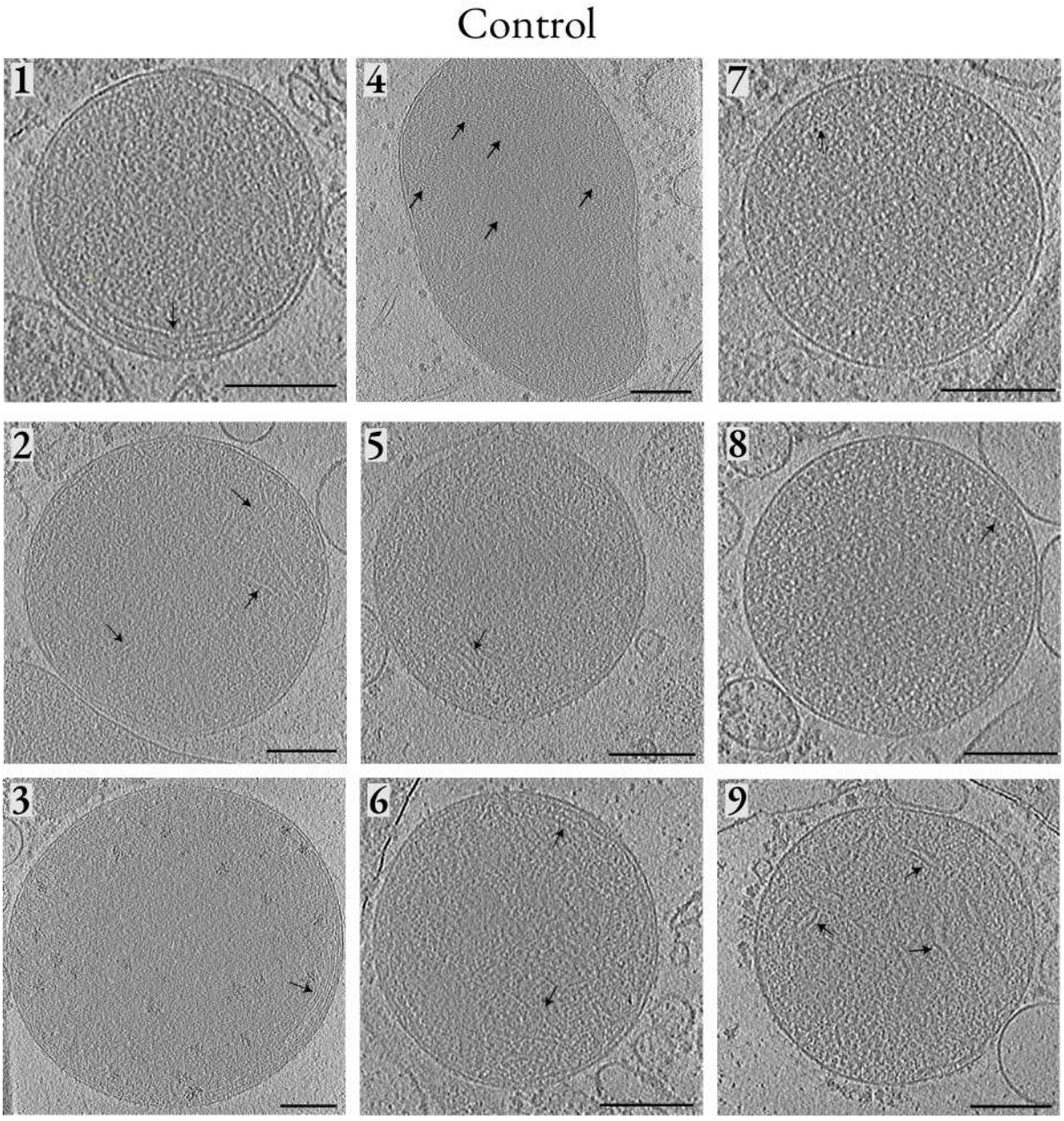

Figure 6.7: Tomographic slices of control mitochondria - isolated mitochondria from control animals were processed for cryo-ET, images were collected on a tilt series from +60°to 60°and images realigned using gold fiducials as markers, full protocol in Materials and Methods 2.8.4. Shown in this figure is a representative tomographic slice from the series, with each image from a different mitochondrion imaged. Scale bar 150 nm.

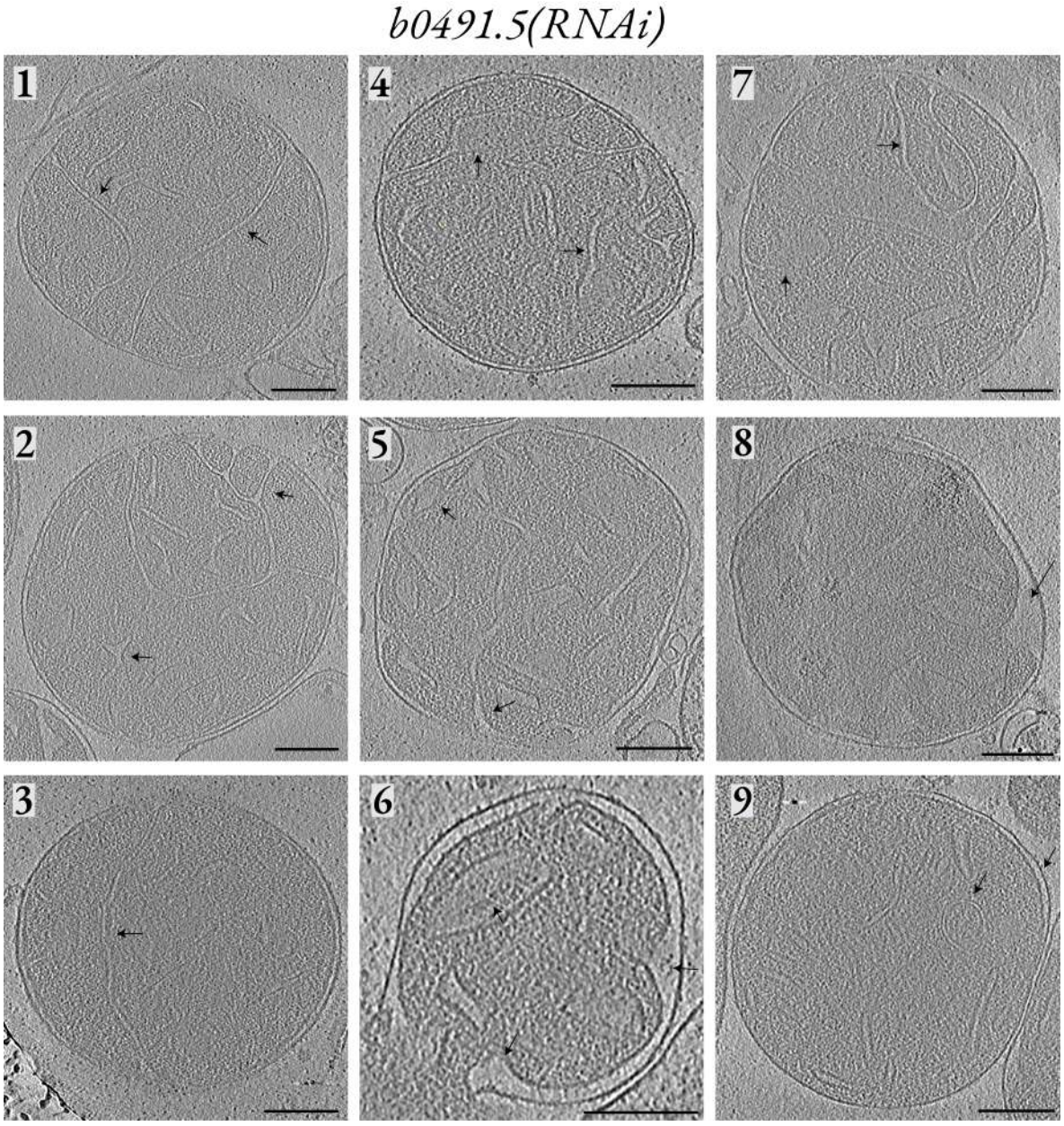

Figure 6.8: Tomographic slices of *b0491.5(RNAi)* mitochondria - isolated mitochondria from *b0491.5(RNAi)* animals were processed for cryo-ET, images were collected on a tilt series from +60ºto 60ºand images realigned using gold fiducials as markers, full protocol in Materials and Methods 2.8.4. Shown in this figure is a representative tomographic slice from the series, with each image from a different mitochondrion imaged. Scale bar 150 nm.

6.3.3.2 Tomogram reconstructions

Significant differences between the tomographic slices shown in Figures 6.7 and 6.8 were observed, to analyse the internal structure of the isolated mitochondria in greater detail, one mitochondrion from each condition was selected for 3D reconstruction, Figures 6.9 and 6.10. A series of tomographic slices from the mitochondrion selected (shown in the top panel (A) of each figure), can be used to observe how the cristae 'move' though the tomogram. However, to see the full tomogram, the QR code (B), links to a video.

When compared with the control, the mitochondria from *b0491.5(RNAi)* conditions lack the normal lamellar cristae of wild-type mitochondria. Although the density of the control mitochondria made reconstruction challenging, the cristae that were reconstructed show homogeneous lamellar morphology. In comparison, the membranes of the RNAi mitochondria were easily identifiable, due to the reduced matrix density. The cristae in the knockdown lose their lamellae like structure, and become flattened, taking up a lot more of the interior space. The 3D images compound the observations seen in the tomographic slices, and highlight significant alterations in membrane morphology due to reduction of B0491.5. Constructing 3D models of a larger sample size will increase confidence in these findings, however, as there are striking differences observed in the tomographic slices between the two conditions, this suggests similar observations will be found in further reconstructions.

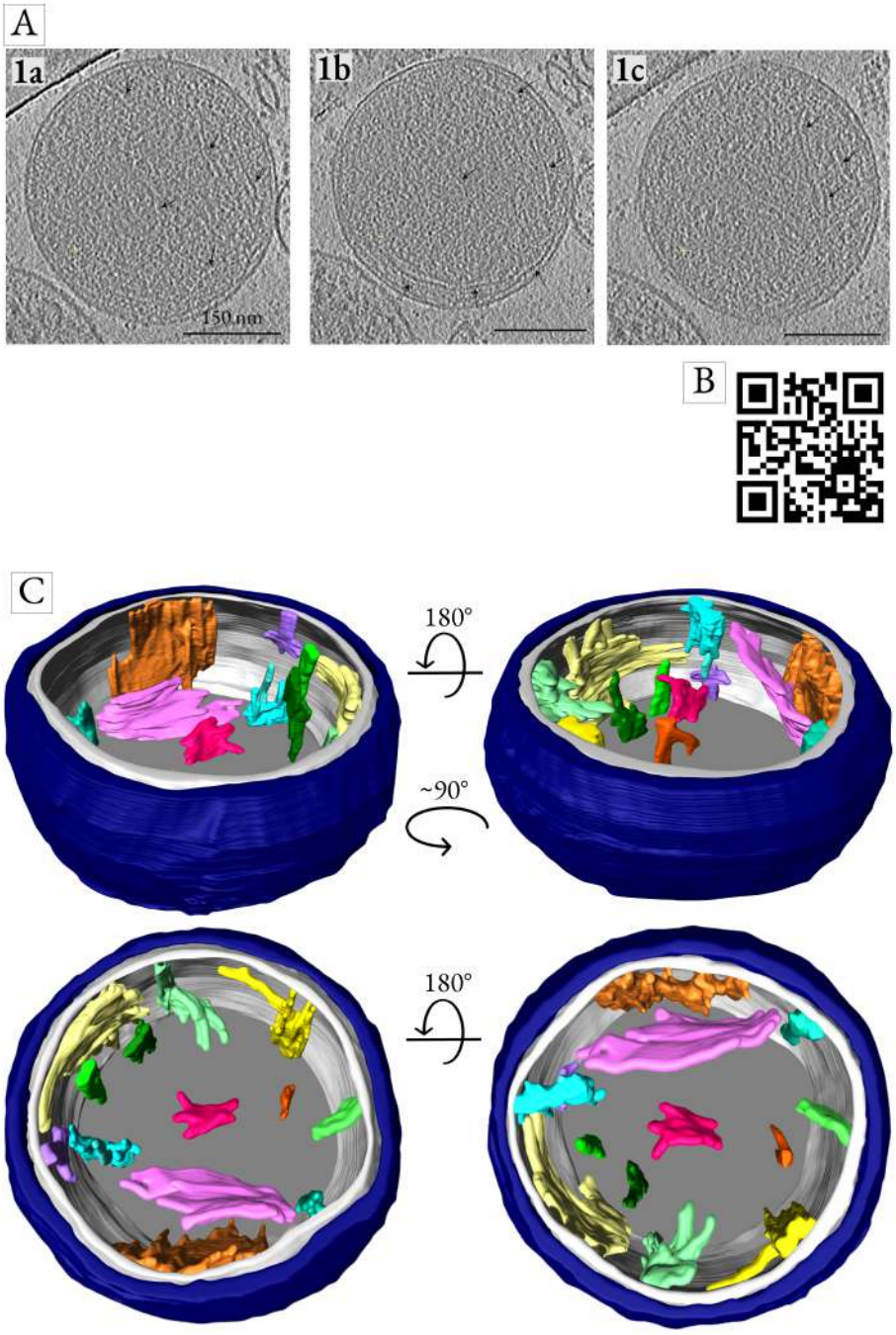

Figure 6.9: Tomogram reconstructions of control mitochondria - A representative mitochondrion from the control samples was selected **(A)** shows a series of three representative tomographic slices from the chosen mitochondrion **(B)** QR code which links to a video of the full tomogram, the QR code can be accessed by scanning with the camera on a smart phone, or via a dedicated application. **(C)** different orientations of the reconstructed mitochondria, as indicated in the figure, reconstructions were made in the 2D-5D visualisation and analysis software Amira.

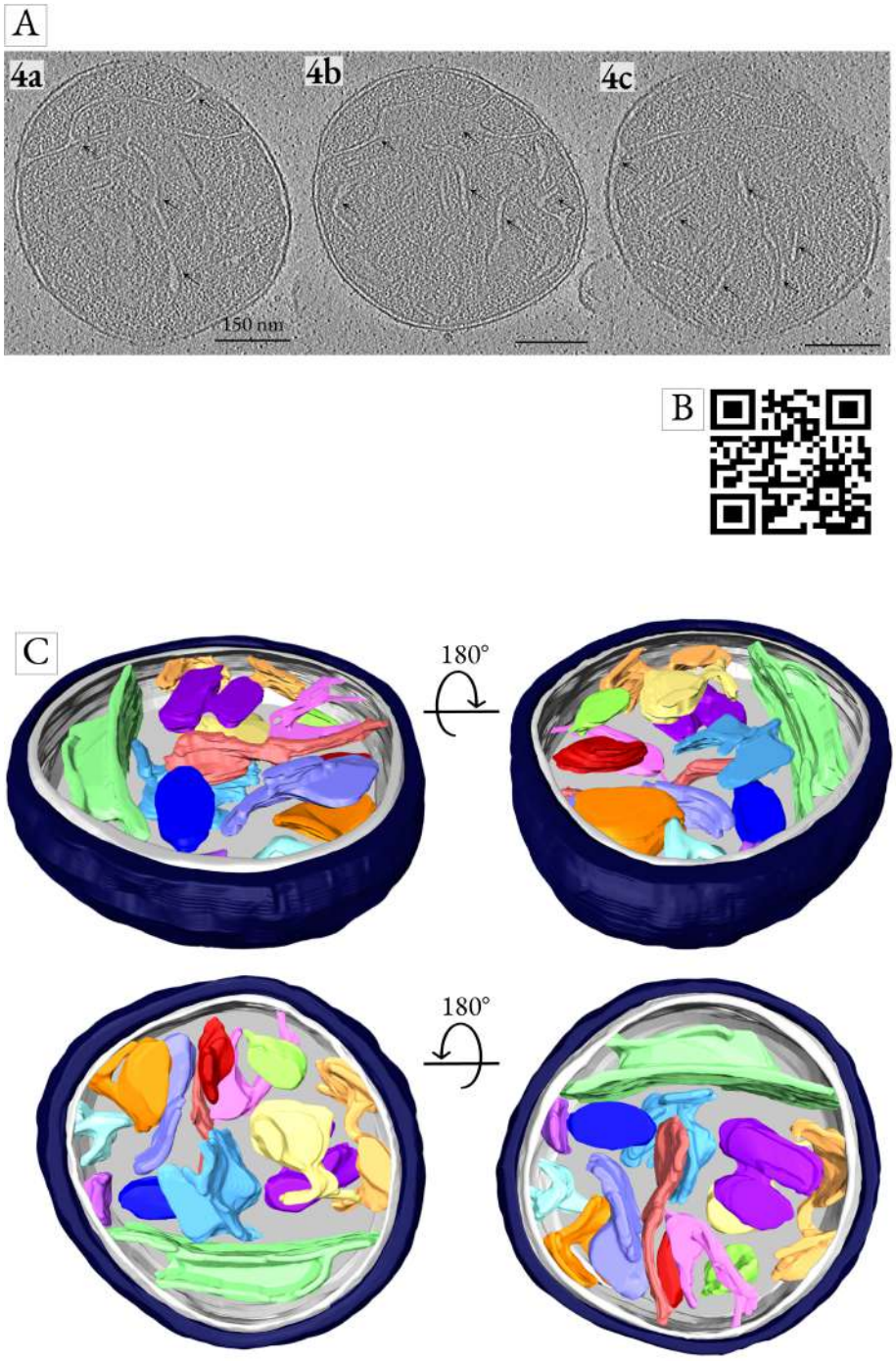

Figure 6.10: Tomogram reconstructions of *b0491.5(RNAi)* mitochondria - A representative mitochondrion from the *b0491.5(RNAi)* samples was selected **(A)** shows a series of three representative tomographic slices from the chosen mitochondrion **(B)** QR code which links to a video of the full tomogram, the QR code can be accessed by scanning with the camera on a smart phone, or via a dedicated application. **(C)** different orientations of the reconstructed mitochondria, as indicated in the figure, reconstructions were made in the 2D-5D visualisation and analysis software Amira.

6.4 Chapter discussion

Mitochondrial physiology was investigated due to the impact *b0491.5(RNAi)* had in whole animals, causing a developmental delay, along with a reduction in fertility, but an increase in lifespan (Section 5.3). Furthermore, investigating isolated mitochondria from *b0491.5(RNAi)* animals, the organisation of the respiratory complexes was shown to be disrupted, with significantly reduced complex I and complete loss of all supercomplexes (Section 5.3). Reduction of B0491.5 has had a significant physiological impact on respiration, through both the CI-linked and CII-linked pathways. In addition, changes in membrane potential reflect those seen in respiration, but little difference was found when measuring ROS production.

The respiration data, when energising the mitochondria through complex I, Figure 6.1 (A), shows a significant decrease in the respiration activity of the *b0491.5* mitochondria. This decrease was corroborated by the TMRM data, which suggests that the mitochondria are not able to maintain the PMF during state 3 respiration. During state 2 respiration, the two conditions are respiring at similar rates, but, upon the addition of ADP, and the transition to state three respiration, a significant difference was seen observed between the conditions. The RCR of the *b0491.5(RNAi)* mitochondria was 2.2, compared the control, which had an RCR of 6.2. Although the RCR generally cannot be used as a standalone measure, as it varies across different tissues and cell types, using it as a comparative measure in this case against the control mitochondria, could help characterise respiration in B0491.5 reduced mitochondria. A 2.8-fold reduction in respiration activity was suggestive that in the *b0491.5(RNAi)* respiratory system, not only was there less complex I, as shown by the BN PAGE gels (Figure 5.4) and mass spectrometry (Figure 5.5), but that the complex that remains has a reduced respiration capacity. Furthermore, this reduced respiration capacity could potentially be a causative factor in the developmental delay seen in RNAi animals, as the *b0491.5(RNAi)* mitochondria are producing less ATP from comparative amounts of substrate and ADP. It could also explain the severe reduction in fertility seen in RNAi animals, as they are not able to meet the energetic demands required.

The caveat when suggesting the reduced respiration capacity of complex I could be linked to the animal development phenotype seen in B0491.5 suppressed animals, was that in Figure 6.1 B, it shows that when energised with succinate, the RNAi mitochondria have greater respiration activity than the control. However, when analysing the mass spectrometry data in Figure 5.5, the subunits of CII did not appear to be upregulated. Complex II was also not the predominant entry site for OXPHOS, so it was unlikely that this represents physiological conditions. Furthermore, when looking at Figure 6.1 (C), it suggests that CII can partially rescue the complex I decreased respiration, however, further investigation would be needed to determine if this represented energetic conditions in vivo.

The TMRM data, Figure (6.2), combined with state 4 respiration data in Figure 6.1, suggests that the *b0491.5(RNAi)* mitochondria have increased proton leak. This gentle dissipation of the PMF, potentially mimics the action of uncoupler proteins described by the 'mild uncoupler' theory. Furthermore, impairment in respiration has been shown to cause an increase in lifespan, which was seen in the *b0491.5(RNAi)* animals. These theories hypothesise a reduction in mitochondrial ROS production. However, the ROS assay in Figure 6.3 shows little significant change. In contrast, an increase in ROS in *b0491.5(RNAi)* mitochondria was seen during complex II-linked respiration, when inhibited with antimycin A. However, this likely represents the increased proton flux due to highly active complex II. As discussed above, this condition was unlikely to represent physiological conditions. ROS can be difficult to measure accurately, as the antioxidant machinery, discussed in Section 1.1.5.3, acts rapidly. However, as the control and RNAi mitochondria are observed under the same experimental parameters, this should not inhibit changes was ROS production from being observed. Therefore, the mitochondrial physiology data may provide evidence towards a reduced respiration capacity linked phenotype in whole animals, but, the data does not corroborate theories relating to a lifespan increase linked to ROS reduction.

When looking at changes in the ultrastructure of the mitochondria, the morphology in the *b0491.5(RNAi)* condition showed fragmentation. A larger number of the RNAi mitochondria appeared as small and rounded mitochondria, compared to the control, which showed more linear structures. A similar pattern was seen in the EM images, although there was heterogeneity in both samples, the *b0491.5(RNAi)* mitochondria did appear to have a great number of smaller, rounded mitochondria. However, when

looking at the internal morphology of the mitochondria in the EM images, no significantly differences were observed. It has been suggested that this increased fragmentation state could be due to oxidative stress, however when analysing the ROS data from Figure 6.3, there does not appear to be a significant increase in mitochondrial ROS production.

This was in contrast to what was observed in the cryo-electron tomography images, here, striking differences can be seen the two populations of mitochondria. Most noticeable are the wide gaps appearing between both the IMM and OMM, and within the cristae, highlighted further by the reconstructions. The mitochondria also appear less dense, this was potentially interesting as it could suggest a lower protein concentration in the matrix of the *b0491.5(RNAi)* mitochondria. However, the mass spectrometry results (Section 5.5), did not display a significant global decrease in expression of mitochondrial proteins, in fact, a number of Krebs cycle proteins, found in the mitochondrial matrix, showed upregulation. There was scope for the mass spectrometry data set to be analysed with a focus on all mitochondrial matrix proteins, to investigate this further.

Chapter 7

Conclusion and Future Directions

NDUFA11 has proven to be a captivating focus for this project. Associated with complex I, supercomplexes and cardiolipin, all complex entities in themselves, the scope for investigating the role the protein plays was vast.

From initial bioinformatic data, this project was able to identify *C. elegans* protein B0491.5 as a homologue of NDUFA11. Using BN PAGE and second dimension analysis, the constituent subunits of the mitochondrial respiratory complexes were investigated, allowing B0491.5 to be localised within complex I. Modelling data then allowed the structural characteristics of B0491.5 to be explored, and provided evidence that suggested specific homology to NDUFA11. This work laid the foundations for the project, and identifying a *C. elegans* homologue opened up a plethora of experimental opportunities to explore the role of NDUFA11.

Extension of this work could be carried out using the *b0491.5* knockout model to explore the cardiolipin binding sites. Firstly, rescue of the knockout strain would need to be established, to show that the addition of *b0491.5* by extrachromosomal array rescued the lethal phenotype of the worm. Once rescue is established, various mutants, perturbing binding of specific cardiolipin sites, could be characterised in the knockout strain. This could provide insight into the role of cardiolipin and NDUFA11, and how their interactions are mediated.

Full advantage was taken of the experimental tools available using *C. elegans* as a model organism. A genetic knockout showed B0491.5 was an essential gene, and RNAi allowed the phenotype of worms with suppressed B0491.5 activity to be established. Delayed development and severely inhibited reproduction suggested that the animals had reduced energetic capabilities. Lifespan analysis showed the *b0491.5(RNAi)* animals to have increased longevity, a phenomenon seen in other mitochondrial impairment phenotypes. This linked the energetics of the mitochondria with whole animal physiology, as impairments in respiration have been linked to increased lifespan, due to reductions in mitochondrial ROS production.

Future directions could investigate the impact external stressors, such as heat or heavy metal stress, has on *b0491.5(RNAi)* animals. If the suggestion that RNAi animals are working at an energetic capacity only able to fulfil minimum energy requirements is correct, this would suggest that they would be less able to respond to stressors. Furthermore, the RNAi animals could be exposed to oxidative stressors, such as paraquat or hydrogen peroxide, and investigate if this reduces the increases in longevity seen. This would be able identify if a reduction in ROS was playing a role in the lifespan extension.

Blue native PAGE was a powerful tool throughout the project. Firstly, it allowed the visualisation of wild-type mitochondria respiratory complexes. Confirming the existence of a supramolecular organisation of the electron transport chain in *C. elegans*. As discussed above, the characterisation of the complexes allowed the localisation of B0491.5 to complex I, and supercomplex entities to be shown. The system was then used to investigate the organisation of the respiratory complexes in conditions of reduced B0491.5, the clarity and strength of the protein bands on the blue native gels, and corresponding second dimension analysis, allowed the changes to be seen in great detail. The loss of supercomplex structures, and reduction in complex I was evident, however, minor increases in complex III: complex IV entities were more subtle, but noticeable on the gels.

Extension of this work could look to characterise the in-gel activity of the other ETC complexes in *b0491.5(RNAi)* mitochondria, in addition to the complex I activity that was carried out. This could elucidate information as to whether there are changes in complex activity, as well as organisation.

Throughout the project, a wide range of investigations were carried out to understand the impact reducing B0491.5 had on mitochondrial organisation and function. As discussed above, a dramatic change in the organisation of the respiratory complexes was seen. Proteomic analysis of the respiratory complexes showed changes in expression for complex I that reflected the blue native PAGE data. However, the expression changes for the other complexes, showing a mild trend towards upregulation, which was not clearly demonstrated on the blue native gels. The physiology data showed a marked reduction in complex I-linked respiration for the *b0491.5(RNAi)* animals, with a corresponding increase in complex II-linked respiration. The TMRM data reflected the reduced respiration capacity of RNAi mitochondria through complex I, showing a decrease in membrane potential, reflective of the ETC being unable to maintain the PMF to the same extent when ATP synthase is active. Together, the O_2 consumption and TMRM traces, suggested increased proton leak in the RNAi mitochondria.

There was no significant basal increase, or decrease, in ROS production in the *b0491.5(RNAi)* mitochondria. Oxidative stress was an interesting component within the project, it has been suggested that supercomplexes provide protection against the production of ROS, therefore their loss in the reduced B0491.5 environment suggested an increase in ROS may be expected. On the other hand, impairment of mitochondrial respiration, and the resulting reduction in membrane potential, which was observed for RNAi mitochondria in complex I-linked respiration, is suggested to reduce mitochondrial ROS, and induce longevity. Which as discussed, was a phenotype of the *b0491.5(RNAi)* animals. It is possible that the experimental system is not sensitive enough to detect the level of changes that happened in this 'mild uncoupling' effect.

Extension of this work could include characterising the activity of the individual respiratory complexes, within the control and *b0491.5(RNAi)* environments. Understanding if a reduction in B0491.5 leads to decreased activity in the complexes individually, could potentially distinguish between whether the effects seen under *b0491.5(RNAi)* are due to the proteins role within complex I, and the decrease in intact complex I alone, which is causing mitochondrial perturbation, or whether a decrease in supercomplexes may be responsible.

Finally, when investigating the impact reduction of B0491.5 had on mitochondrial morphology, distinct differences were observed in the RNAi mitochondria. Along the body wall muscle, a mitochondrial GFP reporter showed fragmentation of the mitochondrial networks, corroborated by

electron microscopy where it was observed that RNAi mitochondria were irregularly shaped. Cryo-electron microscopy analysis displayed the greatest differences between the conditions. Evidence from previous studies suggest that oxidative stress can lead to similar phenotypes as the ones observed. As discussed above, the ROS data does not support that occurring in *b0491.5(RNAi)* mitochondria, as there was no discernible increase in ROS production detected.

Future experiments could carry out statistical analysis on the images collected, to determine if there are significant differences between the conditions. Furthermore, the proteomic data could be analysed to determine if there are changes in expression in the mitochondrial fission or fusion proteins, to better understand the morphological changes.

Chapter 8

Appendix I - buffers, solutions, media and antibiotics

8.1 Buffers and solutions

Unless otherwise stated, all buffers and solutions are made up in ultra-pure water.

2xYT

16 g/L Tryptone

10 g/L Yeast Extract

5.0 g/L NaCl

5% Triton X-100 solubilisation buffer

20 mM, Tris pH 7.5

50 mM NaCl

10% Glycerol

1 mM PMSF

5% Triton X-100

6% digitonin solubilisation buffer

20 mM Tris, pH 7.5

50 mM NaCl

10% Glycerol

1 mM PMSF

6% Digitonin

Alkaline hypochlorite solution

Makes 10 mL

4 mL sodium hypochlorite

5 mL 2 M sodium hydroxide

1 mL H_2O.

Basic STEG/M buffer

220 mM mannitol

70 mM sucrose

5 mM Tris-HCL

1 mM EGTA

STEG/M (+) buffer

1 mM PMSF

1% (fatty acid free) BSA

Collagenase buffer

100 mM Tris-HCl, pH 7.4

1 mM $CaCl_2$

collagenase enzyme (1U/mL)

Coomassie staining solution

50% v/v methanol

10% v/v acetic acid

0.5% Coomassie G-250

Davids M9

Makes 2 L

12 g disodium hydrogen phosphate (Na_2HPO_4)

6 g potassium dihydrogen phosphate (KH_2PO_4)

10 g sodium chloride (NaCl)

2 mL 1 M Magnesium sulphate ($MgSO_4$)

De-staining solution

10% v/v methanol

10% v/v acetic acid

Freezing medium

200 mL in H_2O)

20 mL 1 M NaCl

10 mL 1 M KH2PO4 (pH 6.0)

60 mL 100% glycerol

Add H_2O, autoclave, then add:

0.6 mL sterile 0.1 M MgSO4

LB (Luria-Bertani) Medium

Makes 1 L

10 g Tryptone

5 g Yeast Extract

10 g NaCl

Add H_2O, adjust pH to 7.5 with NaOH and autoclave

NGM agar

1 L in H_2O)

3 g NaCl

20 g Agar

2.5 g Peptone

Autoclave, then add the following sterile solutions:

1mL 1 M $CaCl_2$

1mL 1 M $MgSO_4$

1mL 5 mg/mL cholesterol

25mL 1M KH_2PO_4 (pH 6.0)

Reducing solution

1x LDS sample buffer

250 mM DTT

Respiration medium

125 mM KCl

10 mM Tris

20 mM MOPS

2.5 mM KH_2PO_4

2.5 mM $MgCl_2$

pH to 7.3

S-basal complete

Makes 1 L

5.9 g NaCl

50 mL 1 M KH_2PO_4, pH 6

1 mL 96% cholesterol

Autoclave, cool and add under sterile conditions;

10 mL 1 M potassium citrate, pH 6

10 mL trace metals solution

3 mL 1 M $CaCl_2$

3 mL 1 M $MgSO_4$

Single worm lysis buffer

50 mM KCl

10 mM Tris, pH 8.3

2.5 mM $MgCl_2$

0.45% Nonidet P-40

0.045% Tween-20

0.01% (w/v) gelatinin

Autoclave and store at -20ºC, before use add 60 μg/mL proteinase K

TBE Buffer

Makes 1 L of 5X stock solution

54 g Tris base

27.5 g boric acid

20 mL of 0.5 M EDTA, pH 8.0

TBS-Tween

50 mM Tris, pH 7.6

150 mM NaCl

0.05% Tween20

Transfer buffer

25 mM Tris

190 mM glycine

20% methanol

8.2 Antibiotics

Ampicillin

Makes a 100 mg/mL stock:

1 g ampicillin, made up to 10 mL with H_2O

Filter sterilise with a 0.22 μm syringe filter

Tetracycline

Makes a 12 mg/mL stock:

120 mg tetracycline, made up to 10 mL in 70% ethanol

Bibliography

Acín-Pérez, R., Bayona-Bafaluy, M. P., Fernández-Silva, P., Moreno-Loshuertos, R., Pérez-Martos, A., Bruno, C., Moraes, C. T. and Enríquez, J. A. (2004), 'Respiratory complex III is required to maintain complex I in mammalian mitochondria.', *Molecular cell* **13**(6), 805–815.

Acín-Pérez, R. and Enríquez, J. A. (2014), 'The function of the respiratory supercomplexes: the plasticity model.', *Biochimica et biophysica acta* **1837**(4), 444–450.

Acín-Pérez, R., Fernández-Silva, P., Peleato, M. L., Pérez-Martos, A. and Enriquez, J. A. (2008), 'Respiratory active mitochondrial supercomplexes.', *Molecular Cell* **32**(4), 529–539.

Akram, M. (2014), 'Citric acid cycle and role of its intermediates in metabolism.', *Cell biochemistry and biophysics* **68**(3), 475–478.

Althoff, T., Mills, D. J., Popot, J.-L. and Kühlbrandt, W. (2011), 'Arrangement of electron transport chain components in bovine mitochondrial supercomplex I1III2IV1.', *The EMBO journal* **30**(22), 4652–4664.

Altschul, S. F., Gish, W., Miller, W., Myers, E. W. and Lipman, D. J. (1990), 'Basic local alignment search tool.', *Journal of Molecular Biology* **215**(3), 403–410.

Andrews, B., Carroll, J., Ding, S., Fearnley, I. M. and Walker, J. E. (2013), 'Assembly factors for the membrane arm of human complex I.', *Proceedings of the National Academy of Sciences of the United States of America* **110**(47), 18934–18939.

Andreyev, A. Y., Kushnareva, Y. E. and Starkov, A. A. (2005), 'Mitochondrial metabolism of reactive oxygen species.', *Biochemistry. Biokhimiia* **70**(2), 200–214.

Antico Arciuch, V. G., Elguero, M. E., Poderoso, J. J. and Carreras, M. C. (2012), 'Mitochondrial regulation of cell cycle and proliferation.', *Antioxidants & Redox Signaling* **16**(10), 1150–1180.

Aon, M. A., Cortassa, S. and O'Rourke, B. (2010), 'Redox-optimized ROS balance: a unifying hypothesis.', *Biochimica et biophysica acta* **1797**(6-7), 865–877.

Arnarez, C., Marrink, S. J. and Periole, X. (2013), 'Identification of cardiolipin binding sites on cytochrome c oxidase at the entrance of proton channels.', *Scientific reports* **3**(1), 1263.

Bahrami, A. K. and Zhang, Y. (2013), 'When females produce sperm: genetics of C. elegans hermaphrodite reproductive choice.', *G3 (Bethesda, Md.)* **3**(10), 1851–1859.

Baker, M. R., Fan, G. and Serysheva, I. I. (2015), 'Single-Particle Cryo-EM of the Ryanodine Receptor Channel in an Aqueous Environment.', *European journal of translational myology* **25**(1), 4803–48.

Balsa, E., Marco, R., Perales-Clemente, E., Szklarczyk, R., Calvo, E., Landázuri, M. O. and Enriquez, J. A. (2012), 'NDUFA4 is a subunit of complex IV of the mammalian electron transport chain.', *Cell Metabolism* **16**(3), 378–386.

Baugh, L. R. (2013), 'To grow or not to grow: nutritional control of development during Caenorhabditis elegans L1 arrest.', *Genetics* **194**(3), 539–555.

Berger, I., Hershkovitz, E., Shaag, A., Edvardson, S., Saada, A. and Elpeleg, O. (2008), 'Mitochondrial complex I deficiency caused by a deleterious NDUFA11 mutation.', *Annals of neurology* **63**(3), 405–408.

Bianchi, C., Genova, M. L., Parenti Castelli, G. and Lenaz, G. (2004), 'The mitochondrial respiratory chain is partially organized in a supercomplex assembly: kinetic evidence using flux control analysis.', *The Journal of biological chemistry* **279**(35), 36562–36569.

Bisseru, B. (1971), 'The prevalence of Angiostrongylus cantonensis larvae collected from the giant African snail, Achatina fulica in west Malaysia and Singapore.', *The Southeast Asian journal of tropical medicine and public health* **2**(4), 523–526.

Böttinger, L., Horvath, S. E., Kleinschroth, T., Hunte, C., Daum, G., Pfanner, N. and Becker, T. (2012), 'Phosphatidylethanolamine and cardiolipin differentially affect the stability of mitochondrial respiratory chain supercomplexes.', *Journal of molecular biology* **423**(5), 677–686.

Boumans, H., Grivell, L. A. and Berden, J. A. (1998), 'The respiratory chain in yeast behaves as a single functional unit.', *The Journal of biological chemistry* **273**(9), 4872–4877.

Brand, M. D. and Esteves, T. C. (2005), 'Physiological functions of the mitochondrial uncoupling proteins UCP2 and UCP3.', *Cell Metabolism* **2**(2), 85–93.

Brand, M. D. and Nicholls, D. G. (2011), 'Assessing mitochondrial dysfunction in cells.', *The Biochemical journal* **435**(2), 297–312.

Brenner, S. (1974), 'The genetics of Caenorhabditis elegans.', *Genetics* **77**(1), 71–94.

Brown, G. C. and Borutaite, V. (2012), 'There is no evidence that mitochondria are the main source of reactive oxygen species in mammalian cells.', *Mitochondrion* **12**(1), 1–4.

Butler, J. A., Ventura, N., Johnson, T. E. and Rea, S. L. (2010), 'Long-lived mitochondrial (Mit) mutants of Caenorhabditis elegans utilize a novel metabolism.', *FASEB journal : official publication of the Federation of American Societies for Experimental Biology* **24**(12), 4977–4988.

C. elegans Sequencing Consortium (1998), 'Genome sequence of the nematode C. elegans: a platform for investigating biology.', *Science* **282**(5396), 2012–2018.

Cassada, R. C. and Russell, R. L. (1975), 'The dauerlarva, a post-embryonic developmental variant of the nematode Caenorhabditis elegans.', *Developmental biology* **46**(2), 326–342.

Celis, J. E. and Carter, N. (2005), *Cell Biology: A Laboratory Handbook*, Cell Biology, Elsevier Science.

Chance, B. and Williams, G. R. (1955), 'Respiratory enzymes in oxidative phosphorylation. I. Kinetics of oxygen utilization.', *The Journal of biological chemistry* **217**(1), 383–393.

Chance, B. and Williams, G. R. (1956), 'Respiratory enzymes in oxidative phosphorylation. VI. The effects of adenosine diphosphate on azide-treated mitochondria.', *The Journal of biological chemistry* **221**(1), 477–489.

Chen, D., Pan, K. Z., Palter, J. E. and Kapahi, P. (2007), 'Longevity determined by developmental arrest genes in Caenorhabditis elegans.', *Aging cell* **6**(4), 525–533.

Chen, Q., Vazquez, E. J., Moghaddas, S., Hoppel, C. L. and Lesnefsky, E. J. (2003), 'Production of reactive oxygen species by mitochondria: central role of complex III.', *The Journal of biological chemistry* **278**(38), 36027–36031.

Chicco, A. J. and Sparagna, G. C. (2007), 'Role of cardiolipin alterations in mitochondrial dysfunction and disease.', *American journal of physiology. Cell physiology* **292**(1), C33–44.

Cho, D.-H., Nakamura, T. and Lipton, S. A. (2010), 'Mitochondrial dynamics in cell death and neurodegeneration.', *Cellular and molecular life sciences : CMLS* **67**(20), 3435–3447.

Cho, J., Hur, J. H. and Walker, D. W. (2011), 'The role of mitochondria in Drosophila aging.', *Experimental gerontology* **46**(5), 331–334.

Clancey, C. J., Chang, S. C. and Dowhan, W. (1993), 'Cloning of a gene (PSD1) encoding phosphatidylserine decarboxylase from Saccharomyces cerevisiae by complementation of an Escherichia coli mutant.', *The Journal of biological chemistry* **268**(33), 24580–24590.

Claude, A. and Fullam, E. F. (1945), 'An electron microscope study of isolated mitochondria : method and preliminary results.', *The Journal of experimental medicine* **81**(1), 51–62.

Cole, L. A. (2016), Chapter 10 - adenosine triphosphate energetics, *in* L. A. Cole, ed., 'Biology of Life', Academic Press, pp. 65 – 77.

Cole, N. B., Daniels, M. P., Levine, R. L. and Kim, G. (2010), 'Oxidative stress causes reversible changes in mitochondrial permeability and structure.', *Experimental gerontology* **45**(7-8), 596–602.

Crofts, A. R. (2004), 'The cytochrome bc1 complex: function in the context of structure.', *Annual Review of Physiology* **66**(1), 689–733.

Culetto, E. and Sattelle, D. B. (2000), 'A role for Caenorhabditis elegans in understanding the function and interactions of human disease genes.', *Human molecular genetics* **9**(6), 869–877.

Curran, S. P., Leverich, E. P., Koehler, C. M. and Larsen, P. L. (2004), 'Defective mitochondrial protein translocation precludes normal Caenorhabditis elegans development.', *The Journal of biological chemistry* **279**(52), 54655–54662.

Daniele, J. R., Heydari, K., Arriaga, E. A. and Dillin, A. (2016), 'Identification and Characterization of Mitochondrial Subtypes in Caenorhabditis elegans via Analysis of Individual Mitochondria by Flow Cytometry.', *Analytical Chemistry* **88**(12), 6309–6316.

Daum, G. and Vance, J. E. (1997), 'Import of lipids into mitochondria.', *Progress in Lipid Research* **36**(2-3), 103–130.

David L Nelson, M. M. C. (2017), Lehninger principles of biochemistry, *in* M. M. C. David L Nelson, ed., 'Lehninger principles of biochemistry', Macmillan Learning, pp. 65 – 77.

de Kroon, A. I., Dolis, D., Mayer, A., Lill, R. and de Kruijff, B. (1997), 'Phospholipid composition of highly purified mitochondrial outer membranes of rat liver and Neurospora crassa. Is cardiolipin present in the mitochondrial outer membrane?', *Biochimica et biophysica acta* **1325**(1), 108–116.

Dejima, K., Hori, S., Iwata, S., Suehiro, Y., Yoshina, S., Motohashi, T. and Mitani, S. (2018), 'An Aneuploidy-Free and Structurally Defined Balancer Chromosome Toolkit for Caenorhabditis elegans.', *Cell reports* **22**(1), 232–241.

Dekker, P. J., Ryan, M. T., Brix, J., Müller, H., Hönlinger, A. and Pfanner, N. (1998), 'Preprotein translocase of the outer mitochondrial membrane: molecular dissection and assembly of the general import pore complex.', *Molecular and Cellular Biology* **18**(11), 6515–6524.

Diaz, F., Fukui, H., Garcia, S. and Moraes, C. T. (2006), 'Cytochrome c oxidase is required for the assembly/stability of respiratory complex I in mouse fibroblasts.', *Molecular and Cellular Biology* **26**(13), 4872–4881.

Dickinson, B. C. and Chang, C. J. (2011), 'Chemistry and biology of reactive oxygen species in signaling or stress responses.', *Nature chemical biology* **7**(8), 504–511.

Dienhart, M. K. and Stuart, R. A. (2008), 'The yeast Aac2 protein exists in physical association with the cytochrome bc1-COX supercomplex and the TIM23 machinery.', *Molecular biology of the cell* **19**(9), 3934–3943.

Dingley, S., Polyak, E., Lightfoot, R., Ostrovsky, J., Rao, M., Greco, T., Ischiropoulos, H. and Falk, M. J. (2010), 'Mitochondrial respiratory chain dysfunction variably increases oxidant stress in Caenorhabditis elegans.', *Mitochondrion* **10**(2), 125–136.

Dudek, J., Rehling, P. and van der Laan, M. (2013), 'Mitochondrial protein import: common principles and physiological networks.', *Biochimica et biophysica acta* **1833**(2), 274–285.

Dudkina, N. V., Eubel, H., Keegstra, W., Boekema, E. J. and Braun, H.-P. (2005), 'Structure of a mitochondrial supercomplex formed by respiratory-chain complexes I and III.', *Proceedings of the National Academy of Sciences of the United States of America* **102**(9), 3225–3229.

Dudkina, N. V., Kouril, R., Peters, K., Braun, H.-P. and Boekema, E. J. (2010), 'Structure and function of mitochondrial supercomplexes.', *Biochimica et biophysica acta* **1797**(6-7), 664–670.

Duncan, A. L., Robinson, A. J. and Walker, J. E. (2016), 'Cardiolipin binds selectively but transiently to conserved lysine residues in the rotor of metazoan ATP synthases.', *Proceedings of the National Academy of Sciences of the United States of America* **113**(31), 8687–8692.

Echtay, K. S., Roussel, D., St-Pierre, J., Jekabsons, M. B., Cadenas, S., Stuart, J. A., Harper, J. A., Roebuck, S. J., Morrison, A., Pickering, S., Clapham, J. C. and Brand, M. D. (2002), 'Superoxide activates mitochondrial uncoupling proteins.', *Nature* **415**(6867), 96–99.

Edgley, M. L., Baillie, D. L., Riddle, D. L. and Rose, A. M. (2006), 'Genetic balancers.', *WormBook : the online review of C. elegans biology* pp. 1–32.

El Mouridi, S., Lecroisey, C., Tardy, P., Mercier, M., Leclercq-Blondel, A., Zariohi, N. and Boulin, T. (2017), 'Reliable CRISPR/Cas9 Genome Engineering in Caenorhabditis elegans Using a Single Efficient sgRNA and an Easily Recognizable Phenotype.', *G3 (Bethesda, Md.)* **7**(5), 1429–1437.

Esterbauer, H. (1993), 'Cytotoxicity and genotoxicity of lipid-oxidation products.', *The American journal of clinical nutrition* **57**(5 Suppl), 779S–785S– discussion 785S–786S.

Falk, M. J., Rosenjack, J. R., Polyak, E., Suthammarak, W., Chen, Z., Morgan, P. G. and Sedensky, M. M. (2009), 'Subcomplex Ilambda specifically controls integrated mitochondrial functions in Caenorhabditis elegans.', *PLoS ONE* **4**(8), e6607.

Fassone, E. and Rahman, S. (2012), 'Complex I deficiency: clinical features, biochemistry and molecular genetics.', *Journal of medical genetics* **49**(9), 578–590.

Feissner, R. F., Skalska, J., Gaum, W. E. and Sheu, S.-S. (2009), 'Crosstalk signaling between mitochondrial Ca2+ and ROS.', *Frontiers in bioscience (Landmark edition)* **14**, 1197–1218.

Finkel, T. and Hwang, P. M. (2009), 'The Krebs cycle meets the cell cycle: mitochondria and the G1-S transition.', *Proceedings of the National Academy of Sciences of the United States of America* **106**(29), 11825–11826.

Fire, A. and Waterston, R. H. (1989), 'Proper expression of myosin genes in transgenic nematodes.', *The EMBO journal* **8**(11), 3419–3428.

Fire, A., Xu, S., Montgomery, M. K., Kostas, S. A., Driver, S. E. and Mello, C. C. (1998), 'Potent and specific genetic interference by double-stranded RNA in Caenorhabditis elegans.', *Nature* **391**(6669), 806–811.

Flis, V. V. and Daum, G. (2013), 'Lipid transport between the endoplasmic reticulum and mitochondria.', *Cold Spring Harbor perspectives in biology* **5**(6), a013235–a013235.

Forkink, M., Smeitink, J. A. M., Brock, R., Willems, P. H. G. M. and Koopman, W. J. H. (2010), 'Detection and manipulation of mitochondrial reactive oxygen species in mammalian cells.', *Biochimica et biophysica acta* **1797**(6-7), 1034–1044.

Francis, G. R. and Waterston, R. H. (1985), 'Muscle organization in Caenorhabditis elegans: localization of proteins implicated in thin filament attachment and I-band organization.', *The Journal of Cell Biology* **101**(4), 1532–1549.

Gandre, S. and van der Bliek, A. M. (2007), 'Mitochondrial division in Caenorhabditis elegans.', *Methods in molecular biology (Clifton, N.J.)* **372**(Chapter 34), 485–501.

Gao, X., Wen, X., Esser, L., Quinn, B., Yu, L., Yu, C.-A. and Xia, D. (2003), 'Structural basis for the quinone reduction in the bc1 complex: a comparative analysis of crystal structures of mitochondrial cytochrome bc1 with bound substrate and inhibitors at the Qi site.', *Biochemistry* **42**(30), 9067–9080.

Gasanov, S. E., Kim, A. A., Yaguzhinsky, L. S. and Dagda, R. K. (2018), 'Non-bilayer structures in mitochondrial membranes regulate ATP synthase activity.', *BBA - Biomembranes* **1860**(2), 586–599.

Golden, J. W. and Riddle, D. L. (1984), 'The Caenorhabditis elegans dauer larva: developmental effects of pheromone, food, and temperature.', *Developmental biology* **102**(2), 368–378.

Gómez, L. A. and Hagen, T. M. (2012), 'Age-related decline in mitochondrial bioenergetics: does supercomplex destabilization determine lower oxidative capacity and higher superoxide production?', *Seminars in cell & developmental biology* **23**(7), 758–767.

Grad, L. I. and Lemire, B. D. (2006), 'Riboflavin enhances the assembly of mitochondrial cytochrome c oxidase in C. elegans NADH-ubiquinone oxidoreductase mutants.', *Biochimica et biophysica acta* **1757**(2), 115–122.

Grad, L. I., Sayles, L. C. and Lemire, B. D. (2007), 'Isolation and functional analysis of mitochondria from the nematode Caenorhabditis elegans.', *Methods in molecular biology (Clifton, N.J.)* **372**(Chapter 4), 51–66.

Granatiero, V., De Stefani, D. and Rizzuto, R. (2017), 'Mitochondrial Calcium Handling in Physiology and Disease.', *Advances in experimental medicine and biology* **982**(4), 25–47.

Gu, J., Wu, M., Guo, R., Yan, K., Lei, J., Gao, N. and Yang, M. (2016), 'The architecture of the mammalian respirasome.', *Nature* **537**(7622), 639–643.

Guerrero-Castillo, S., Baertling, F., Kownatzki, D., Wessels, H. J., Arnold, S., Brandt, U. and Nijtmans, L. (2017), 'The Assembly Pathway of Mitochondrial Respiratory Chain Complex I.', *Cell Metabolism* **25**(1), 128–139.

Guex, N., Diemand, A. and Peitsch, M. C. (1999), 'Protein modelling for all', *Trends in Biochemical Sciences* **24**(9), 364 – 367.

Guindon, S., Dufayard, J.-F., Lefort, V., Anisimova, M., Hordijk, W. and Gascuel, O. (2010), 'New algorithms and methods to estimate maximum-likelihood phylogenies: assessing the performance of PhyML 3.0.', *Systematic biology* **59**(3), 307–321.

Guo, R., Zong, S., Wu, M., Gu, J. and Yang, M. (2017), 'Architecture of Human Mitochondrial Respiratory Megacomplex I2III2IV2.', *Cell* **170**(6), 1247–1257.e12.

Gurtubay, J. I. (1980), 'Solubilization of inner mitochondrial membranes by triton X-100. Effect of ionic strength and temperature.', *Revista espanola de fisiologia* **36**(1), 83–87.

Haack, T. B., Haberberger, B., Frisch, E.-M., Wieland, T., Iuso, A., Gorza, M., Strecker, V., Graf, E., Mayr, J. A., Herberg, U., Hennermann, J. B., Klopstock, T., Kuhn, K. A., Ahting, U., Sperl, W., Wilichowski, E., Hoffmann, G. F., Tesarova, M., Hansikova, H., Zeman, J., Plecko, B., Zeviani, M., Wittig, I., Strom, T. M., Schuelke, M., Freisinger, P., Meitinger, T. and Prokisch, H. (2012), 'Molecular diagnosis in mitochondrial complex I deficiency using exome sequencing.', *Journal of medical genetics* **49**(4), 277–283.

Habig, J. W., Aruscavage, P. J. and Bass, B. L. (2008), 'In C. elegans, high levels of dsRNA allow RNAi in the absence of RDE-4.', *PLoS ONE* **3**(12), e4052.

Hackenbrock, C. R., Chazotte, B. and Gupte, S. S. (1986), 'The random collision model and a critical assessment of diffusion and collision in mitochondrial electron transport.', *Journal of bioenergetics and biomembranes* **18**(5), 331–368.

Hammell, C. M. and Hannon, G. J. (2012), 'Inducing RNAi in C. elegans by feeding with dsRNA-expressing E. coli.', *Cold Spring Harbor protocols* **2012**(12).

Harman, D. (1972), 'The biologic clock: the mitochondria?', *Journal of the American Geriatrics Society* **20**(4), 145–147.

Hatefi, Y. (1985), 'The mitochondrial electron transport and oxidative phosphorylation system', *Annual Review of Biochemistry* **54**(1), 1015–1069. PMID: 2862839.

Heinemeyer, J., Braun, H.-P., Boekema, E. J. and Kouril, R. (2007), 'A structural model of the cytochrome C reductase/oxidase supercomplex from yeast mitochondria.', *The Journal of biological chemistry* **282**(16), 12240–12248.

Herrmann, J. M. and Riemer, J. (2010), 'The intermembrane space of mitochondria.', *Antioxidants & Redox Signaling* **13**(9), 1341–1358.

Hirst, J. (2013), 'Mitochondrial complex I.', *Annual Review of Biochemistry* **82**(1), 551–575.

Hirst, J., Carroll, J., Fearnley, I. M., Shannon, R. J. and Walker, J. E. (2003), 'The nuclear encoded subunits of complex i from bovine heart mitochondria', *Biochimica et Biophysica Acta (BBA) - Bioenergetics* **1604**(3), 135 – 150.

Hirst, J., King, M. S. and Pryde, K. R. (2008), 'The production of reactive oxygen species by complex I.', *Biochemical Society transactions* **36**(Pt 5), 976–980.

Hoefs, S. J. G., Dieteren, C. E. J., Distelmaier, F., Janssen, R. J. R. J., Epplen, A., Swarts, H. G. P., Forkink, M., Rodenburg, R. J., Nijtmans, L. G., Willems, P. H., Smeitink, J. A. M. and van den Heuvel, L. P. (2008), 'NDUFA2 complex I mutation leads to Leigh disease.', *American journal of human genetics* **82**(6), 1306–1315.

Horvath, S. E. and Daum, G. (2013), 'Lipids of mitochondria.', *Progress in Lipid Research* **52**(4), 590–614.

Houtkooper, R. H. and Vaz, F. M. (2008), 'Cardiolipin, the heart of mitochondrial metabolism.', *Cellular and molecular life sciences : CMLS* **65**(16), 2493–2506.

Hubbard, E. J. and Greenstein, D. (2000), 'The Caenorhabditis elegans gonad: a test tube for cell and developmental biology.', *Developmental dynamics : an official publication of the American Association of Anatomists* **218**(1), 2–22.

Hwang, A. B., Jeong, D.-E. and Lee, S.-J. (2012), 'Mitochondria and organismal longevity.', *Current genomics* **13**(7), 519–532.

Iqbal, S. and Hood, D. A. (2014), 'Oxidative stress-induced mitochondrial fragmentation and movement in skeletal muscle myoblasts.', *American journal of physiology. Cell physiology* **306**(12), C1176–83.

Ishihara, N., Jofuku, A., Eura, Y. and Mihara, K. (2003), 'Regulation of mitochondrial morphology by membrane potential, and DRP1-dependent division and FZO1-dependent fusion reaction in mammalian cells.', *Biochemical and biophysical research communications* **301**(4), 891–898.

Jang, S. and Javadov, S. (2018), 'Current challenges in elucidating respiratory supercomplexes in mitochondria: Methodological obstacles', *Frontiers in Physiology* **9**, 238.

Jastroch, M., Divakaruni, A. S., Mookerjee, S., Treberg, J. R. and Brand, M. D. (2010), 'Mitochondrial proton and electron leaks.', *Essays in biochemistry* **47**, 53–67.

Jha, P., Wang, X. and Auwerx, J. (2016), 'Analysis of Mitochondrial Respiratory Chain Supercomplexes Using Blue Native Polyacrylamide Gel Electrophoresis (BN-PAGE).', *Current protocols in mouse biology* **6**(1), 1–14.

Johnstone, I. L. (1994), 'The cuticle of the nematode Caenorhabditis elegans: a complex collagen structure.', *BioEssays : news and reviews in molecular, cellular and developmental biology* **16**(3), 171–178.

Joshi, A. S., Zhou, J., Gohil, V. M., Chen, S. and Greenberg, M. L. (2009), 'Cellular functions of cardiolipin in yeast.', *Biochimica et biophysica acta* **1793**(1), 212–218.

Jussupow, A., Di Luca, A. and Kaila, V. R. I. (2019), 'How cardiolipin modulates the dynamics of respiratory complex I.', *Science advances* **5**(3), eaav1850.

Kadenbach, B., Kuhn-Nentwig, L. and Büge, U. (1987), Evolution of a regulatory enzyme: Cytochrome-c oxidase (complex iv), *in* C. LEE, ed., 'Current Topics in Bioenergetics', Vol. 15 of *Current Topics in Bioenergetics*, Elsevier, pp. 113 – 161.

Kayser, K., Gabius, H. J., Ciesiolka, T., Ebert, W. and Bach, S. (1989), 'Histopathologic evaluation of application of labeled neoglycoproteins in primary bronchus carcinoma.', *Human pathology* **20**(4), 352–360.

Kenyon, C. J. (2010), 'The genetics of ageing.', *Nature* **464**(7288), 504–512.

Kirby, D. M., Crawford, M., Cleary, M. A., Dahl, H. H., Dennett, X. and Thorburn, D. R. (1999), 'Respiratory chain complex I deficiency: an underdiagnosed energy generation disorder.', *Neurology* **52**(6), 1255–1264.

Kirby, D. M., Salemi, R., Sugiana, C., Ohtake, A., Parry, L., Bell, K. M., Kirk, E. P., Boneh, A., Taylor, R. W., Dahl, H.-H. M., Ryan, M. T. and Thorburn, D. R. (2004), 'NDUFS6 mutations are a novel cause of lethal neonatal mitochondrial complex I deficiency.', *The Journal of clinical investigation* **114**(6), 837–845.

Kondrashov, F. A., Koonin, E. V., Morgunov, I. G., Finogenova, T. V. and Kondrashova, M. N. (2006), 'Evolution of glyoxylate cycle enzymes in Metazoa: evidence of multiple horizontal transfer events and pseudogene formation.', *Biology direct* **1**(1), 31.

Kormish, J. D., Gaudet, J. and McGhee, J. D. (2010), 'Development of the C. elegans digestive tract.', *Current opinion in genetics & development* **20**(4), 346–354.

Korshunov, S. S., Skulachev, V. P. and Starkov, A. A. (1997), 'High protonic potential actuates a mechanism of production of reactive oxygen species in mitochondria.', *FEBS letters* **416**(1), 15–18.

Kremer, J. R., Mastronarde, D. N. and McIntosh, J. (1996), 'Computer visualization of three-dimensional image data using imod', *Journal of Structural Biology* **116**(1), 71 – 76.

Kufareva, I. and Abagyan, R. (2012), 'Methods of protein structure comparison.', *Methods in molecular biology (Clifton, N.J.)* **857**(Chapter 10), 231–257.

Kühlbrandt, W. (2015), 'Structure and function of mitochondrial membrane protein complexes.', *BMC biology* **13**(1), 89.

Kulawiak, B., Höpker, J., Gebert, M., Guiard, B., Wiedemann, N. and Gebert, N. (2013), 'The mitochondrial protein import machinery has multiple connections to the respiratory chain.', *Biochimica et biophysica acta* **1827**(5), 612–626.

Kussmaul, L. and Hirst, J. (2006), 'The mechanism of superoxide production by NADH:ubiquinone oxidoreductase (complex I) from bovine heart mitochondria.', *Proceedings of the National Academy of Sciences of the United States of America* **103**(20), 7607–7612.

Lai, C. H., Chou, C. Y., Ch'ang, L. Y., Liu, C. S. and Lin, W. (2000), 'Identification of novel human genes evolutionarily conserved in Caenorhabditis elegans by comparative proteomics.', *Genome research* **10**(5), 703–713.

Lambert, A. J. and Brand, M. D. (2009), 'Reactive oxygen species production by mitochondria.', *Methods in molecular biology (Clifton, N.J.)* **554**(Chapter 11), 165–181.

Lapuente-Brun, E., Moreno-Loshuertos, R., Acín-Pérez, R., Latorre-Pellicer, A., Colás, C., Balsa, E., Perales-Clemente, E., Quirós, P. M., Calvo, E., Rodríguez-Hernández, M. A., Navas, P., Cruz, R., Carracedo, Á., López-Otín, C., Pérez-Martos, A., Fernández-Silva, P., Fernández-Vizarra, E. and Enríquez, J. A. (2013), 'Supercomplex assembly determines electron flux in the mitochondrial electron transport chain', *Science* **340**(6140), 1567–1570.

Lebon, S., Chol, M., Benit, P., Mugnier, C., Chretien, D., Giurgea, I., Kern, I., Girardin, E., Hertz-Pannier, L., de Lonlay, P., Rötig, A., Rustin, P. and Munnich, A. (2003), 'Recurrent de novo mitochondrial DNA mutations in respiratory chain deficiency.', *Journal of medical genetics* **40**(12), 896–899.

Lehner, B., Tischler, J. and Fraser, A. G. (2006), 'RNAi screens in Caenorhabditis elegans in a 96-well liquid format and their application to the systematic identification of genetic interactions.', *Nature Protocols* **1**(3), 1617–1620.

Lemasters, J. J. (2007), 'Modulation of mitochondrial membrane permeability in pathogenesis, autophagy and control of metabolism.', *Journal of gastroenterology and hepatology* **22 Suppl 1**(s1), S31–7.

Letts, J. A., Fiedorczuk, K. and Sazanov, L. A. (2016), 'The architecture of respiratory supercomplexes.', *Nature* **537**(7622), 644–648.

Levine, T. (2004), 'Short-range intracellular trafficking of small molecules across endoplasmic reticulum junctions.', *Trends in cell biology* **14**(9), 483–490.

Li, J., Cai, T., Wu, P., Cui, Z., Chen, X., Hou, J., Xie, Z., Xue, P., Shi, L., Liu, P., Yates, J. R. and Yang, F. (2009), 'Proteomic analysis of mitochondria from Caenorhabditis elegans.', *Proteomics* **9**(19), 4539–4553.

Liberman, E. A., Topaly, V. P., Tsofina, L. M., Jasaitis, A. A. and Skulachev, V. P. (1969), 'Mechanism of coupling of oxidative phosphorylation and the membrane potential of mitochondria.', *Nature* **222**(5198), 1076–1078.

Lin, M. T. and Beal, M. F. (2006), 'Mitochondrial dysfunction and oxidative stress in neurodegenerative diseases.', *Nature* **443**(7113), 787–795.

Lithgow, G. J., White, T. M., Melov, S. and Johnson, T. E. (1995), 'Thermotolerance and extended lifespan conferred by single-gene mutations and induced by thermal stress.', *Proceedings of the National Academy of Sciences of the United States of America* **92**(16), 7540–7544.

Lobo-Jarne, T. and Ugalde, C. (2018), 'Respiratory chain supercomplexes: Structures, function and biogenesis.', *Seminars in cell & developmental biology* **76**, 179–190.

Lombardi, A., Silvestri, E., Cioffi, F., Senese, R., Lanni, A., Goglia, F., de Lange, P. and Moreno, M. (2009), 'Defining the transcriptomic and proteomic profiles of rat ageing skeletal muscle by the use of a cDNA array, 2D- and Blue native-PAGE approach.', *Journal of proteomics* **72**(4), 708–721.

Loschen, G., Flohé, L. and Chance, B. (1971), 'Respiratory chain linked H(2)O(2) production in pigeon heart mitochondria.', *FEBS letters* **18**(2), 261–264.

Lunt, S. Y. and Vander Heiden, M. G. (2011), Aerobic glycolysis: Meeting the metabolic requirements of cell proliferation, Vol. 27, pp. 441–464. PMID: 21985671.

Madeira, F., Park, Y. M., Lee, J., Buso, N., Gur, T., Madhusoodanan, N., Basutkar, P., Tivey, A. R. N., Potter, S. C., Finn, R. D. and Lopez, R. (2019), 'The EMBL-EBI search and sequence analysis tools APIs in 2019.', *Nucleic acids research* .

Maglioni, S. and Ventura, N. (2016), 'C. elegans as a model organism for human mitochondrial associated disorders.', *Mitochondrion* **30**, 117–125.

Mailloux, R. J. and Harper, M.-E. (2011), 'Uncoupling proteins and the control of mitochondrial reactive oxygen species production.', *Free radical biology & medicine* **51**(6), 1106–1115.

Maranzana, E., Barbero, G., Falasca, A. I., Lenaz, G. and Genova, M. L. (2013), 'Mitochondrial respiratory supercomplex association limits production of reactive oxygen species from complex I.', *Antioxidants & redox signaling* **19**(13), 1469–1480.

Markaki, M. and Tavernarakis, N. (2010), 'Modeling human diseases in Caenorhabditis elegans.', *Biotechnology journal* **5**(12), 1261–1276.

McFarland, R., Kirby, D. M., Fowler, K. J., Ohtake, A., Ryan, M. T., Amor, D. J., Fletcher, J. M., Dixon, J. W., Collins, F. A., Turnbull, D. M., Taylor, R. W. and Thorburn, D. R. (2004), 'De novo mutations in the mitochondrial ND3 gene as a cause of infantile mitochondrial encephalopathy and complex I deficiency.', *Annals of neurology* **55**(1), 58–64.

McLean, L. R., Hagaman, K. A. and Davidson, W. S. (1993), 'Role of lipid structure in the activation of phospholipase A2 by peroxidized phospholipids.', *Lipids* **28**(6), 505–509.

Mesmin, B. (2016), 'Mitochondrial lipid transport and biosynthesis: A complex balance.', *The Journal of Cell Biology* **214**(1), 9–11.

Meyer, E. H., Welchen, E. and Carrie, C. (2019), 'Assembly of the complexes of the oxidative phosphorylation system in land plant mitochondria', *Annual Review of Plant Biology* **70**(1), 23–50. PMID: 30822116.

Milenkovic, D., Blaza, J. N., Larsson, N.-G. and Hirst, J. (2017), 'The Enigma of the Respiratory Chain Supercomplex.', *Cell Metabolism* **25**(4), 765–776.

Mileykovskaya, E. and Dowhan, W. (2014), 'Cardiolipin-dependent formation of mitochondrial respiratory supercomplexes.', *Chemistry and physics of lipids* **179**, 42–48.

Mimaki, M., Wang, X., McKenzie, M., Thorburn, D. R. and Ryan, M. T. (2012), 'Understanding mitochondrial complex I assembly in health and disease.', *Biochimica et biophysica acta* **1817**(6), 851–862.

Miquel, J., Economos, A. C., Fleming, J. and Johnson, J. E. (1980), 'Mitochondrial role in cell aging.', *Experimental gerontology* **15**(6), 575–591.

Mitchell, P. (1961), 'Coupling of phosphorylation to electron and hydrogen transfer by a chemiosmotic type of mechanism.', *Nature* **191**(4784), 144–148.

Mitchell, P. (2011), *Chemiosmotic coupling in oxidative and photosynthetic phosphorylation. 1966.*, Vol. 1807.

Mordas, A. and Tokatlidis, K. (2015), 'The MIA pathway: a key regulator of mitochondrial oxidative protein folding and biogenesis.', *Accounts of chemical research* **48**(8), 2191–2199.

Murphy, M. P. (2009), 'How mitochondria produce reactive oxygen species.', *The Biochemical journal* **417**(1), 1–13.

Musatov, A. (2006), 'Contribution of peroxidized cardiolipin to inactivation of bovine heart cytochrome c oxidase.', *Free radical biology & medicine* **41**(2), 238–246.

Navarro-González, C., Moukadiri, I., Villarroya, M., López-Pascual, E., Tuck, S. and Armengod, M.-E. (2017), 'Mutations in the Caenorhabditis elegans orthologs of human genes required for mitochondrial tRNA modification cause similar electron transport chain defects but different nuclear responses.', *PLoS genetics* **13**(7), e1006921.

Nehls, U., Friedrich, T., Schmiede, A., Ohnishi, T. and Weiss, H. (1992), 'Characterization of assembly intermediates of NADH:ubiquinone oxidoreductase (complex I) accumulated in Neurospora mitochondria by gene disruption.', *Journal of Molecular Biology* **227**(4), 1032–1042.

Nicholls, D. G. (2010), 'Mitochondrial ion circuits.', *Essays in biochemistry* **47**, 25–35.

Nicholls, D. G. and Ferguson, S. J. (2013), Bioenergetics 4, *in* D. G. Nicholls and S. J. Ferguson, eds, 'Bioenergetics 4', fourth edition edn, Academic Press, california, pp. 1058 – 1072.

Ogilvie, I., Kennaway, N. G. and Shoubridge, E. A. (2005), 'A molecular chaperone for mitochondrial complex I assembly is mutated in a progressive encephalopathy.', *The Journal of clinical investigation* **115**(10), 2784–2792.

O'Riordan, V. B. and Burnell, A. M. (1989), 'Intermediary metabolism in the dauer larva of the nematode caenorhabditis elegans— 1. glycolysis, gluconeogenesis, oxidative phosphorylation and the tricarboxylic acid cycle', *Comparative Biochemistry and Physiology Part B: Comparative Biochemistry* **92**(2), 233 – 238.

Osellame, L. D., Blacker, T. S. and Duchen, M. R. (2012), 'Cellular and molecular mechanisms of mitochondrial function.', *Best practice & research. Clinical endocrinology & metabolism* **26**(6), 711–723.

Palmer, J. W., Tandler, B. and Hoppel, C. L. (1977), 'Biochemical properties of subsarcolemmal and interfibrillar mitochondria isolated from rat cardiac muscle.', *Journal of Biological Chemistry* **252**(23), 8731–9.

Paradies, G., Paradies, V., De Benedictis, V., Ruggiero, F. M. and Petrosillo, G. (2014), 'Functional role of cardiolipin in mitochondrial bioenergetics.', *Biochimica et biophysica acta* **1837**(4), 408–417.

Paradies, G., Petrosillo, G., Pistolese, M., Di Venosa, N., Federici, A. and Ruggiero, F. M. (2004), 'Decrease in mitochondrial complex I activity in ischemic/reperfused rat heart: involvement of reactive oxygen species and cardiolipin.', *Circulation research* **94**(1), 53–59.

Paradies, G., Petrosillo, G., Pistolese, M. and Ruggiero, F. M. (2001), 'Reactive oxygen species generated by the mitochondrial respiratory chain affect the complex III activity via cardiolipin peroxidation in beef-heart submitochondrial particles.', *Mitochondrion* **1**(2), 151–159.

Paradies, G., Petrosillo, G., Pistolese, M. and Ruggiero, F. M. (2002), 'Reactive oxygen species affect mitochondrial electron transport complex I activity through oxidative cardiolipin damage.', *Gene* **286**(1), 135–141.

Patil, V. A., Fox, J. L., Gohil, V. M., Winge, D. R. and Greenberg, M. L. (2013), 'Loss of cardiolipin leads to perturbation of mitochondrial and cellular iron homeostasis.', *The Journal of biological chemistry* **288**(3), 1696–1705.

Pazdernik, N. and Schedl, T. (2013), 'Introduction to germ cell development in Caenorhabditis elegans.', *Advances in experimental medicine and biology* **757**(5955), 1–16.

Pedersen, P. L., Greenawalt, J. W., Reynafarje, B., Hullihen, J., Decker, G. L., Soper, J. W. and Bustamente, E. (1978), 'Preparation and characterization of mitochondria and submitochondrial particles of rat liver and liver-derived tissues.', *Methods in cell biology* **20**, 411–481.

Petrosillo, G., Ruggiero, F. M., Pistolese, M. and Paradies, G. (2001), 'Reactive oxygen species generated from the mitochondrial electron transport chain induce cytochrome c dissociation from beef-heart submitochondrial particles via cardiolipin peroxidation. Possible role in the apoptosis.', *FEBS letters* **509**(3), 435–438.

Peverelli, L., Legati, A., Lamantea, E., Nasca, A., Lerario, A., Galimberti, V., Ghezzi, D. and Lamperti, C. (2019), 'New missense variants of NDUFA11 associated with late-onset myopathy.', *Muscle & nerve* **49**(7623), 277.

Pfeiffer, K., Gohil, V., Stuart, R. A., Hunte, C., Brandt, U., Greenberg, M. L. and Schägger, H. (2003), 'Cardiolipin stabilizes respiratory chain supercomplexes.', *The Journal of biological chemistry* **278**(52), 52873–52880.

Phaniendra, A., Jestadi, D. B. and Periyasamy, L. (2015), 'Free radicals: properties, sources, targets, and their implication in various diseases.', *Indian journal of clinical biochemistry : IJCB* **30**(1), 11–26.

Porcelli, A. M., Ghelli, A., Zanna, C., Pinton, P., Rizzuto, R. and Rugolo, M. (2005), 'pH difference across the outer mitochondrial membrane measured with a green fluorescent protein mutant.', *Biochemical and biophysical research communications* **326**(4), 799–804.

Porras, C. A.-M. and Bai, Y. (2015), 'Respiratory supercomplexes: plasticity and implications.', *Frontiers in bioscience (Landmark edition)* **20**, 621–634.

Rahman, S., Blok, R. B., Dahl, H. H., Danks, D. M., Kirby, D. M., Chow, C. W., Christodoulou, J. and Thorburn, D. R. (1996), 'Leigh syndrome: clinical features and biochemical and DNA abnormalities.', *Annals of neurology* **39**(3), 343–351.

Raja, V., Joshi, A. S., Li, G., Maddipati, K. R. and Greenberg, M. L. (2017), 'Loss of Cardiolipin Leads to Perturbation of Acetyl-CoA Synthesis.', *The Journal of biological chemistry* **292**(3), 1092–1102.

Rathore, S., Berndtsson, J., Marin-Buera, L., Conrad, J., Carroni, M., Brzezinski, P. and Ott, M. (2019), 'Cryo-EM structure of the yeast respiratory supercomplex.', *Nature Structural & Molecular Biology* **26**(1), 50–57.

Ray, P. D., Huang, B.-W. and Tsuji, Y. (2012), 'Reactive oxygen species (ROS) homeostasis and redox regulation in cellular signaling.', *Cellular signalling* **24**(5), 981–990.

Rea, S. L., Ventura, N. and Johnson, T. E. (2007), 'Relationship between mitochondrial electron transport chain dysfunction, development, and life extension in Caenorhabditis elegans.', *PLoS Biology* **5**(10), e259.

Rich, P. R. and Maréchal, A. (2010), 'The mitochondrial respiratory chain.', *Essays in biochemistry* **47**, 1–23.

Riddle, D. L., Blumenthal, T., Meyer, B. J. and Priess, J. R. (1997), 'C. elegans II'.

Rodenburg, R. J. (2016), 'Mitochondrial complex I-linked disease.', *Biochimica et biophysica acta* **1857**(7), 938–945.

Ruan, J., Li, H., Chen, Z., Coghlan, A., Coin, L. J. M., Guo, Y., Hériché, J.-K., Hu, Y., Kristiansen, K., Li, R., Liu, T., Moses, A., Qin, J., Vang, S., Vilella, A. J., Ureta-Vidal, A., Bolund, L., Wang, J. and Durbin, R. (2008), 'TreeFam: 2008 Update.', *Nucleic acids research* **36**(Database issue), D735–40.

Ruiter, E. M., Siers, M. H., van den Elzen, C., van Engelen, B. G., Smeitink, J. A. M., Rodenburg, R. J. and Hol, F. A. (2007), 'The mitochondrial 13513G > A mutation is most frequent in Leigh syndrome combined with reduced complex I activity, optic atrophy and/or Wolff-Parkinson-White.', *European journal of human genetics : EJHG* **15**(2), 155–161.

Rutter, J., Winge, D. R. and Schiffman, J. D. (2010), 'Succinate dehydrogenase - Assembly, regulation and role in human disease.', *Mitochondrion* **10**(4), 393–401.

Sali, A. and Blundell, T. L. (1993), 'Comparative protein modelling by satisfaction of spatial restraints.', *Journal of Molecular Biology* **234**(3), 779–815.

Sánchez-Caballero, L., Guerrero-Castillo, S. and Nijtmans, L. (2016), 'Unraveling the complexity of mitochondrial complex I assembly: A dynamic process.', *Biochimica et biophysica acta* **1857**(7), 980–990.

Sarasija, S. and Norman, K. R. (2018), 'Analysis of Mitochondrial Structure in the Body Wall Muscle of Caenorhabditis elegans.', *Bio-protocol* **8**(7).

Sazanov, L. A. (2015), 'A giant molecular proton pump: structure and mechanism of respiratory complex I.', *Nature reviews. Molecular cell biology* **16**(6), 375–388.

Scaduto, R. C. and Grotyohann, L. W. (1999), 'Measurement of mitochondrial membrane potential using fluorescent rhodamine derivatives.', *Biophysical journal* **76**(1 Pt 1), 469–477.

Schäfer, E., Seelert, H., Reifschneider, N. H., Krause, F., Dencher, N. A. and Vonck, J. (2006), 'Architecture of active mammalian respiratory chain supercomplexes.', *The Journal of biological chemistry* **281**(22), 15370–15375.

Schagger, H. (2001), 'Respiratory chain supercomplexes.', *IUBMB life* **52**(3-5), 119–128.

Schägger, H. (2002), 'Respiratory chain supercomplexes of mitochondria and bacteria.', *Biochimica et biophysica acta* **1555**(1-3), 154–159.

Schagger, H., Cramer, W. A. and von Jagow, G. (1994), 'Analysis of molecular masses and oligomeric states of protein complexes by blue native electrophoresis and isolation of membrane protein complexes by two-dimensional native electrophoresis.', *Analytical Biochemistry* **217**(2), 220–230.

Schagger, H. and Pfeiffer, K. (2000), 'Supercomplexes in the respiratory chains of yeast and mammalian mitochondria.', *The EMBO journal* **19**(8), 1777–1783.

Scharwey, M., Tatsuta, T. and Langer, T. (2013), 'Mitochondrial lipid transport at a glance.', *Journal of cell science* **126**(Pt 23), 5317–5323.

Schlame, M. (2008), 'Cardiolipin synthesis for the assembly of bacterial and mitochondrial membranes.', *Journal of lipid research* **49**(8), 1607–1620.

Schug, Z. T. and Gottlieb, E. (2009), 'Cardiolipin acts as a mitochondrial signalling platform to launch apoptosis.', *Biochimica et biophysica acta* **1788**(10), 2022–2031.

Schägger, H. (2002), 'Respiratory chain supercomplexes of mitochondria and bacteria', *Biochimica et Biophysica Acta (BBA) - Bioenergetics* **1555**(1), 154 – 159. 12th European Bioenergetics Conference.

Shen, P., Yue, Y., Zheng, J. and Park, Y. (2018), 'Caenorhabditis elegans: A convenient in vivo model for assessing the impact of food bioactive compounds on obesity, aging, and alzheimer's disease', *Annual Review of Food Science and Technology* **9**(1), 1–22. PMID: 29261338.

Smith, G. R. (1992), 'The epidemiology and treatment of depression when it coexists with somatoform disorders, somatization, or pain.'.

Sousa, J. S., Mills, D. J., Vonck, J. and Kühlbrandt, W. (2016), 'Functional asymmetry and electron flow in the bovine respirasome.', *eLife* **5**, 805.

Srinivasan, S. and Avadhani, N. G. (2012), 'Cytochrome c oxidase dysfunction in oxidative stress.', *Free radical biology & medicine* **53**(6), 1252–1263.

Starkov, A. A. (1997), '"Mild" uncoupling of mitochondria.', *Bioscience reports* **17**(3), 273–279.

Stroud, D. A., Surgenor, E. E., Formosa, L. E., Reljic, B., Frazier, A. E., Dibley, M. G., Osellame, L. D., Stait, T., Beilharz, T. H., Thorburn, D. R., Salim, A. and Ryan, M. T. (2016), 'Accessory subunits are integral for assembly and function of human mitochondrial complex I', *Nature* **538**(7623), 123–126.

Suthammarak, W., Morgan, P. G. and Sedensky, M. M. (2010), 'Mutations in mitochondrial complex III uniquely affect complex I in Caenorhabditis elegans.', *The Journal of biological chemistry* **285**(52), 40724–40731.

Suthammarak, W., Yang, Y.-Y., Morgan, P. G. and Sedensky, M. M. (2009), 'Complex I function is defective in complex IV-deficient Caenorhabditis elegans.', *The Journal of biological chemistry* **284**(10), 6425–6435.

Taanman, J.-W. (1999), 'The mitochondrial genome: structure, transcription, translation and replication', *Biochimica et Biophysica Acta (BBA) - Bioenergetics* **1410**(2), 103 – 123.

Tabara, H., Grishok, A. and Mello, C. C. (1998), 'RNAi in C. elegans: soaking in the genome sequence.', *Science* **282**(5388), 430–431.

Tate, J. G., Bamford, S., Jubb, H. C., Sondka, Z., Beare, D. M., Bindal, N., Boutselakis, H., Cole, C. G., Creatore, C., Dawson, E., Fish, P., Harsha, B., Hathaway, C., Jupe, S. C., Kok, C. Y., Noble, K., Ponting, L., Ramshaw, C. C., Rye, C. E., Speedy, H. E., Stefancsik, R., Thompson, S. L., Wang, S., Ward, S., Campbell, P. J. and Forbes, S. A. (2019), 'COSMIC: the Catalogue Of Somatic Mutations In Cancer.', *Nucleic acids research* **47**(D1), D941–D947.

Timmons, L. and Fire, A. (1998), 'Specific interference by ingested dsRNA.', *Nature* **395**(6705), 854–854.

Toth, P. P., Ferguson-Miller, S. M. and Suelter, C. H. (1986), 'Isolation of highly coupled heart mitochondria in high yield using a bacterial collagenase.', *Methods in enzymology* **125**, 16–27.

Tsukihara, T., Aoyama, H., Yamashita, E., Tomizaki, T., Yamaguchi, H., Shinzawa-Itoh, K., Nakashima, R., Yaono, R. and Yoshikawa, S. (1996), 'The whole structure of the 13-subunit oxidized cytochrome c oxidase at 2.8 A.', *Science* **272**(5265), 1136–1144.

van den Ecker, D., van den Brand, M. A., Bossinger, O., Mayatepek, E., Nijtmans, L. G. and Distelmaier, F. (2010), 'Blue native electrophoresis to study mitochondrial complex I in C. elegans.', *Analytical Biochemistry* **407**(2), 287–289.

Van Raamsdonk, J. M., Meng, Y., Camp, D., Yang, W., Jia, X., Bénard, C. and Hekimi, S. (2010), 'Decreased energy metabolism extends life span in Caenorhabditis elegans without reducing oxidative damage.', *Genetics* **185**(2), 559–571.

Vercesi, A. E., Bernardes, C. F., Hoffmann, M. E., Gadelha, F. R. and Docampo, R. (1991), 'Digitonin permeabilization does not affect mitochondrial function and allows the determination of the mitochondrial membrane potential of Trypanosoma cruzi in situ.', *The Journal of biological chemistry* **266**(22), 14431–14434.

Wadsworth, W. G. and Riddle, D. L. (1989), 'Developmental regulation of energy metabolism in Caenorhabditis elegans.', *Developmental biology* **132**(1), 167–173.

Wang, C. and Youle, R. J. (2009), 'The role of mitochondria in apoptosis*.', *Annual review of genetics* **43**, 95–118.

Wang, N., Miller, C. J., Wang, P. and Waite, T. D. (2017), 'Quantitative determination of trace hydrogen peroxide in the presence of sulfide using the Amplex Red/horseradish peroxidase assay.', *Analytica chimica acta* **963**, 61–67.

Wang, Y., Carrie, C., Giraud, E., Elhafez, D., Narsai, R., Duncan, O., Whelan, J. and Murcha, M. W. (2012), 'Dual location of the mitochondrial preprotein transporters B14.7 and Tim23-2 in complex I and the TIM17:23 complex in Arabidopsis links mitochondrial activity and biogenesis.', *The Plant cell* **24**(6), 2675–2695.

Wiedemann, N. and Pfanner, N. (2017), 'Mitochondrial machineries for protein import and assembly', *Annual Review of Biochemistry* **86**(1), 685–714. PMID: 28301740.

Wiedemann, N., van der Laan, M., Hutu, D. P., Rehling, P. and Pfanner, N. (2007), 'Sorting switch of mitochondrial presequence translocase involves coupling of motor module to respiratory chain.', *The Journal of Cell Biology* **179**(6), 1115–1122.

Wiemerslage, L. and Lee, D. (2016), 'Quantification of mitochondrial morphology in neurites of dopaminergic neurons using multiple parameters.', *Journal of neuroscience methods* **262**, 56–65.

Wilkins, A. S. and Holliday, R. (2009), 'The evolution of meiosis from mitosis', *Genetics* **181**(1), 3–12.

Wittig, I., Braun, H.-P. and Schägger, H. (2006), 'Blue native PAGE.', *Nature Protocols* **1**(1), 418–428.

Wojtczak, L., Wojtczak, A. and Ernster, L. (1969), 'The inhibition of succinate dehydrogenase by oxaloacetate', *Biochimica et Biophysica Acta (BBA) - Enzymology* **191**(1), 10 – 21.

Wojtovich, A. P., Burwell, L. S., Sherman, T. A., Nehrke, K. W. and Brookes, P. S. (2008), 'The C. elegans mitochondrial K+(ATP) channel: a potential target for preconditioning.', *Biochemical and biophysical research communications* **376**(3), 625–628.

Wu, M., Gu, J., Guo, R., Huang, Y. and Yang, M. (2016), 'Structure of Mammalian Respiratory Supercomplex I1III2IV1.', *Cell* **167**(6), 1598–1609.e10.

Yankovskaya, V., Horsefield, R., Törnroth, S., Luna-Chavez, C., Miyoshi, H., Léger, C., Byrne, B., Cecchini, G. and Iwata, S. (2003), 'Architecture of succinate dehydrogenase and reactive oxygen species generation.', *Science* **299**(5607), 700–704.

Yin, H. and Zhu, M. (2012), 'Free radical oxidation of cardiolipin: chemical mechanisms, detection and implication in apoptosis, mitochondrial dysfunction and human diseases.', *Free radical research* **46**(8), 959–974.

Youle, R. J. and van der Bliek, A. M. (2012), 'Mitochondrial fission, fusion, and stress.', *Science* **337**(6098), 1062–1065.

Žárský, V. and Doležal, P. (2016), 'Evolution of the Tim17 protein family.', *Biology direct* **11**(1), 54.

Zerbetto, E., Vergani, L. and Dabbeni-Sala, F. (1997), 'Quantification of muscle mitochondrial oxidative phosphorylation enzymes via histochemical staining of blue native polyacrylamide gels.', *Electrophoresis* **18**(11), 2059–2064.

Zhan, M., Brooks, C., Liu, F., Sun, L. and Dong, Z. (2013), 'Mitochondrial dynamics: regulatory mechanisms and emerging role in renal pathophysiology.', *Kidney international* **83**(4), 568–581.

Zhang, M., Mileykovskaya, E. and Dowhan, W. (2002), 'Gluing the respiratory chain together. Cardiolipin is required for supercomplex formation in the inner mitochondrial membrane.', *The Journal of biological chemistry* **277**(46), 43553–43556.

Zhu, J., Vinothkumar, K. R. and Hirst, J. (2016), 'Structure of mammalian respiratory complex I.', *Nature* **536**(7616), 354–358.

Zimmerman, J. J., von Saint André-von Arnim, A. and McLaughlin, J. (2011), Chapter 74 - cellular respiration, *in* B. P. Fuhrman and J. J. Zimmerman, eds, 'Pediatric Critical Care (Fourth Edition)', fourth edition edn, Mosby, Saint Louis, pp. 1058 – 1072.

Zinser, E., Sperka-Gottlieb, C. D., Fasch, E. V., Kohlwein, S. D., Paltauf, F. and Daum, G. (1991), 'Phospholipid synthesis and lipid composition of subcellular membranes in the unicellular eukaryote Saccharomyces cerevisiae.', *Journal of bacteriology* **173**(6), 2026–2034.

Zorov, D. B., Juhaszova, M. and Sollott, S. J. (2014), 'Mitochondrial reactive oxygen species (ROS) and ROS-induced ROS release.', *Physiological reviews* **94**(3), 909–950.